I. PALEOMAGNETISM AND CRUSTAL ROTATIONS ALONG A SHEAR ZONE, LAS VEGAS RANGE, SOUTHERN NEVADA

II. SEISMOTECTONICS OF THE TIEN SHAN, CENTRAL ASIA

by

Michael Roy Nelson

B. S., California Institute of Technology (1981)

SUBMITTED IN PARTIAL FULFILLMENT
OF THE REQUIREMENTS FOR THE DEGREE OF
DOCTOR OF PHILOSOPHY

in

GEOPHYSICS

at the

MASSACHUSETTS INSTITUTE OF TECHNOLOGY

February, 1988

Signature of Author . . . . . .
Department of Earth, Atmospheric, and Planetary Sciences
January, 1988

Certified by . . . . . .
Thesis Supervisor

Accepted by . . . . . .
Chairman, Departmental Committee on Graduate Students

I. PALEOMAGNETISM AND CRUSTAL ROTATIONS ALONG A SHEAR ZONE, LAS VEGAS RANGE, SOUTHERN NEVADA

II. SEISMOTECTONICS OF THE TIEN SHAN, CENTRAL ASIA

by

Michael Roy Nelson

Submitted to the Department of Earth, Atmospheric, and Planetary Sciences in partial fulfillment of the requirements for the degree of Doctor of Philosophy in Geophysics

ABSTRACT

The first chapter of this thesis consists of a paleomagnetic study of crustal rotations along the Las Vegas Valley Shear Zone in the Basin and Range of western North America. In southern Nevada, Paleozoic isopachs, Mesozoic structures, and mountain ranges trend north-south, but as they approach the right-lateral, west-northwest-trending Las Vegas Valley Shear Zone (LVVSZ), they are bent clockwise up to 90° in oroflexes 30 km long. In the Las Vegas Range the declination of the characteristic magnetization of the Cambrian Bonanza King Formation has likewise been rotated clockwise more than 50°. For samples from eight sites (13-23 samples per site) in the Las Vegas Range and in its extension south of the LVVSZ, stepwise thermal demagnetization to 600° C removed recent and Tertiary overprints, revealing a nearly horizontal, late Paleozoic viscous partial thermoremanent magnetization (VPTRM) which predates both the Tertiary oroflexural bending and the Sevier thrusting in the area. The declination of the characteristic magnetization (after correcting for the dip of bedding) varies from 133° ± 2° at a site 24 km north of the shear zone to 196° ± 4° 13 km north of it and 204° ± 4° 11 km south of the shear zone. This parallels a similar change in the structural trend. The paleomagnetic data indicate that the Las Vegas Range is broken into rather small blocks (<5 km) which rotate in response to more continuous deformation at depth. This deformation of the upper crust can be modelled using a thin non-Newtonian viscous plate model, which when applied to the Las Vegas Valley Shear Zone predicts rotations similar to those seen in the Las Vegas Range.

The second and third chapters of this thesis contain the results of seismological studies of the tectonics and structure of the Tien Shan mountain belt of Central Asia. The Tien Shan was formed in late Paleozoic time and reactivated in Tertiary time following the collision of India with Eurasia, more than 1500 km to the south. To study the style and distribution of faulting occurring today in the Tien Shan, I digitized long-period World-Wide Standard Seismograph Network P and SH waveforms of 11 of the largest Tien Shan earthquakes between 1965 and 1982 and then used a least squares inversion routine to constrain their fault plane solutions and depths. Four of the earthquakes occurred near the southern edge of the Tien Shan, and two occurred in the intermontane Fergana Basin. These earthquakes occurred at depths of 10-20 km and are associated with thrust faulting on east-west to southwest-northeast striking fault planes

that dip moderately (35°-55°). The other five earthquakes, in the northern Tien Shan, were mostly deeper (15-44 km), and the fault plane solutions of four of them are similar to the events farther south. The exception, an event on June 2, 1973, probably occurred on a gently northward dipping, east-west striking fault plane. All events occur within the basement at depths of 10 km or greater. Waveforms for earthquakes near the edges of the Dzungarian, Fergana, and Kucha basins are fit best using velocity structures with thick sediment layers, implying that sediments from these basins have been and are being underthrust beneath the neighboring mountains. I examined only the relatively small (m_b = 5.5-6.2) events after 1965 and did not study any of the largest events (M_s > 8) that occurred in the Tien Shan earlier in this century. Still, we can conclude that north-south shortening is presently occurring in the Tien Shan, with the formation of basement uplifts flanked by moderately dipping thrust faults. The present-day tectonics of the Tien Shan seem to be analogous to those of the Rocky Mountains in Colorado, Wyoming, and Utah during the Laramide orogeny in Late Cretaceous and Early Tertiary time.

Since the uplift of the Tien Shan began in Oligocene time, there has been more than 100 km of north-south shortening across the belt, resulting in elevations of over 7 km and numerous east-west trending thrust faults. The relatively simple, linear geometry and Tertiary history of the eastern Tien Shan make it an excellent place to study the effects of crustal shortening on the upper mantle. In the third chapter, a number of seismological techniques are used to determine whether shortening in the eastern Tien Shan has resulted in the thickening of the mantle lithosphere and the formation of a "lithospheric root" beneath the mountain belt. Thickening the mantle lithosphere will reduce the geothermal gradient, resulting in lower temperatures, and thus higher seismic velocities, in the upper mantle. Previous studies of P wave and S wave station corrections have found larger delays in the eastern Tien Shan than in the Siberian Shield to the north. Soviet refraction profiles indicate that P_n velocities in the eastern Tien Shan are neither exceptionally high nor exceptionally low. These observations, along with heat flow measurements, indicate that the upper mantle beneath the Tien Shan is warmer than the upper mantle beneath the shield regions that flank it.

By matching synthetic seismograms to long-period World-Wide Standard Seismograph Network (WWSSN) seismograms, I measured P and S arrival times at teleseismic distances for eleven earthquakes in the Tien Shan. By using synthetic seismograms for both P and SH waves, it is possible to alleviate many of the problems with travel-time residual studies caused by hypocenter mislocations and the misidentification of S arrivals. The P and S arrival times were used to calculate "S-P residuals", which are less affected by mislocation errors than P wave or S wave residuals alone. To correct for variations in the seismic velocity structure beneath the WWSSN stations, the P wave station corrections of Dziewonski and Anderson [1983] were used along with S wave station corrections equal to 3 times the P wave corrections. These corrections significantly reduce the scatter in the S-P residuals. For the Tien Shan, mean S-P residuals for individual earthquakes fall between -0.2 and -1.8 s, slightly less negative than mean S-P residuals measured in shield regions.

In order to estimate P wave velocities in the uppermost mantle, seven travel-time plots for raypaths from earthquakes in the Tien Shan to

stations in the Tien Shan were constructed, using arrival times measured from seismograms from the Toktogul Reservior seismic network and arrival times reported to the International Seismological Centre (ISC) by Soviet and Chinese seismograph stations. For epicentral distances of 300-1700 km, the first-arriving P wave is the P_n phase, which travels in the uppermost mantle. The travel-time plots yielded P_n velocities of between 8.12 and 8.30 km/s (with typical 1 σ uncertainties of 0.1 km/s). Such velocities are lower than those measured for the Indian, Canadian, and Siberian shields and higher than those measured in regions of crustal extension, like the Basin and Range of western North America or the East African Rift.

Both the S-P residuals and the P_n velocities indicate that the upper mantle beneath the Tien Shan is warmer and the lithosphere thinner than beneath the shields that flank it. It is possible that the lithosphere beneath the Tien Shan was originally thicker, but that crustal shortening created a lithospheric root that dropped off, driving convection that heated the upper mantle beneath the range. Alternatively, the upper mantle beneath the Tien Shan may have been warmer than the upper mantle beneath the surrounding regions when shortening began, and has simply remained that way.

Thesis Supervisor: Dr. Peter Molnar

Title: Senior Research Scientist

TABLE OF CONTENTS

To My Mother and Father

PREFACE

Since its inception more than twenty years ago, plate tectonics has greatly increased our understanding of how oceanic crust is created, evolves, and is destroyed. According to plate tectonics, the earth is covered by rigid, lithospheric plates formed at spreading centers, sliding past one another at transform faults, and slipping beneath one another in subduction zones. Hundreds of studies of earthquake fault plane solutions have helped us understand how these plates are moving. The mapping of marine magnetic anomalies has enabled workers to determine the rates of relative motion and the past positions of the various oceanic plates. Due to the uniform composition and relatively uncomplicated history of the oceanic crust, simple models of the cooling oceanic lithosphere can successfully predict how bathymetry and heat flow will vary with the age of the oceanic crust [Parsons and Sclater, 1977]. The thermal structure of the oceanic crust seems to be well-constrained.

Plate tectonics has been less successful when applied to the continents. Continental crust is much more heterogeneous and much older than the oceanic crust. Compared to the oceans, it is much more difficult to determine how continental crust is created and how it deforms. Whereas the oldest oceanic crust is less than 200 million years old, the oldest continental crust is almost 4 billion years old. Most of the continental crust has been heated and deformed repeatedly by orogenic events. Neither the composition of the subcrustal mantle nor the thermal structure of the continents is well-understood [Jordan, 1981].

Deformation of the continents is complicated due to the heterogeneous nature of the continental crust. In the oceans, deformation and seismicity are typically restricted to narrow (<50 km) fault zones. On the continents, deformation may be distributed across zones hundreds or even thousands of kilometers wide.

My thesis consists of studies of distributed continental deformation in two very different tectonic settings, the Basin and Range of western North America and the Tien Shan mountains of Central Asia. The first chapter consists of an investigation of large-scale deformation along the Las Vegas Valley Shear Zone in southern Nevada and was recently published [Nelson and Jones, 1987]. Clark Burchfiel first suggested to me the possibility of studying rotations along the Las Vegas Valley Shear Zone. My advisor, Peter Molnar, helped me pose the problem. Geologic mapping and satellite photos along the shear zone indicate that mountain ranges on either side of the shear zone have been bent like giant drag folds. It appears that deformation is not restricted to a narrow fault zone, but instead is spread across a zone more than 40 km wide. The excellent exposure and geologic mapping that has been done in the Las Vegas Range make it a particularly good place to study the deformation along the shear zone.

With Peter Molnar and Craig Jones, I collected and analyzed paleomagnetic samples from the Las Vegas Range in January, 1982. After the first discouraging results, I returned to the field with Craig, sampled a different formation, and found a consistent paleomagnetic direction that could be used as a structural marker. I collected more samples on two subsequent trips.

I used the results from these paleomagnetic samples, along with previous geologic mapping, to determine how the rocks of the Las Vegas Range have been rotated due to movement along the Las Vegas Valley Shear Zone. I found crustal rotations of more than 60° near the shear zone with the amount of rotation decreasing away from the shear zone. Rocks ≈20 km from the shear zone have been rotated more than 20°.

The gradual decrease in the amount of crustal rotation away from the shear zone is similar to that predicted by numerical experiments on a strike-slip fault in a thin viscous plate [England et al., 1985]. England et al. [1985] have applied their results to the San Andreas Fault system where deformation is distributed across a zone hundreds of kilometers wide. It appears that their results can be applied at a smaller scale as well.

The second and third chapters of my thesis deal with the Tien Shan mountain range in Central Asia. The ongoing deformation of Central Asia caused by the collision of India with Eurasia make it an obvious place to study how continents deform. Although it is a major mountain chain, the Tien Shan has been somewhat overshadowed by the Himalaya and the Tibetan Plateau. Peaks in the Tien Shan reach elevations of over 7 km and there have been numerous large earthquakes in the Tien Shan in this century. In contrast, the Tarim Basin and the Siberian Shield, which flank the Tien Shan are low-lying and relatively undeformed. As part of my thesis work, I have studied the largest, recent earthquakes in the Tien Shan and put constraints on the seismic velocity structure of the upper mantle beneath the Tien Shan, in an effort to understand how deformation is occurring in the Tien Shan and why it is concentrated there.

My advisor, Peter Molnar, first got me interested in the Tien Shan. Unfortunately, due to the difficulties in working in the Soviet Union and China, we were not able to go to the Tien Shan and so I studied the tectonics of the region at a distance. Using seismograms recorded at teleseismic distances, I determined fault plane solutions for eleven earthquakes in the Tien Shan. I worked closely with Rob McCaffrey, who taught me how to use the software he had developed for inverting long-period WWSSN waveforms to determine the fault plane solutions and focal depths of teleseismic earthquakes. The results of this study comprise the second chapter of my thesis, which was recently published [Nelson et al., 1987].

The third chapter of my thesis places constraints on the upper mantle velocity structure of the Tien Shan. Using the focal mechanisms and waveforms from the eleven earthquakes studied in the second chapter, I determined P and S arrival times and calculated "S-P residuals" for the Tien Shan. The S-P residuals for the Tien Shan indicate that seismic velocities in the upper mantle beneath the Tien Shan are not quite as high as those beneath shield regions but are much higher than those beneath regions known to be underlain by warmer-than-average mantle. A study of P_n velocities using arrival times measured from seismograms from the Toktogul Reservior seismic network and arrival times reported to the International Seismological Centre also provided evidence that seismic velocities in the upper mantle beneath the Tien Shan are lower than those beneath shields.

The relatively low seismic velocities inferred for the upper mantle beneath the Tien Shan indicate that the upper mantle beneath the Tien Shan is not as cool as the upper mantle beneath shields. Such a difference in temperature may lead to a difference in strength, which could explain why the Tien Shan is deforming so much more than the shields that adjoin it. This inferred difference in temperature provides an important constraint on the evolution of the Tien Shan and of the mantle which underlies it.

References

England, P., G. Houseman, and L. Sonder, Length scales for continental deformation in convergent, divergent, and strike-slip environments: Analytical and approximate solutions for a thin viscous sheet model, J. Geophys. Res., 90, 3551-3557, 1985.

Jordan, T. H., Continents as a chemical boundary layer, Phil. Trans. R. Soc. Lond. A, 301, 359-373, 1981.

Nelson, M. R., and C. H. Jones, Paleomagnetism and crustal rotations along a shear zone, Las Vegas Range, southern Nevada, Tectonics, 6, 13-33, 1987.

Nelson, M. R., R. McCaffrey, and P. Molnar, Source parameters for 11 earthquakes in the Tien Shan, Central Asia, determined by P and SH waveform inversion, J. Geophys. Res., 92, 12,629-12,648, 1987.

Parsons, B., and J. G. Sclater, An analysis of the variation of ocean floor bathymetry and heat flow with age, J. Geophys. Res., 82, 803-827, 1977.

ACKNOWLEDGMENTS

In a page or two, it is impossible for me to say thank you to all of the people who have helped me during the six years that I have spent at MIT. Without the help of many of them, this thesis could never have been written. They have given me ideas, advice, programs, references, and many of the other ingredients needed to make a thesis. I have been lucky enough to have collegues always eager to share a new joke, new discovery, or a new idea. Most importantly, I have received lots of encouragement from friends who always seemed to know when I needed some.

Because of the wide scope of my work I have spent a lot of time on several different floors in Building 54, from the tenth down to the second. Both on the tenth floor and in the field, Clark Burchfiel has provided me with insight and encouragement. I never ceased to be amazed at how much he could remember about the Cordillera, the Alps, or any other mountain belt you might name. I thank the rest of the crew on the tenth floor for all the help they've given me, whether it be with a cross-section or the Kroy lettering machine.

I have also done my best to pester the inhabitants of the eighth floor. During the many hours I spent learning to use the Apollo, I got a lot of answers to my stupid questions about why my programs wouldn't work. I am especially grateful that Carolyn Ruppel was there to help when nothing seemed to work.

Likewise, I am glad that the computer pros on the fifth floor were so willing to help. Without Lind Gee, Dave Krowitz, and Justin Revenaugh I doubt that any of us would get much computing done. I thank Ken Creager and Karen Fischer for teaching me the art of residual spheres and for writing so much useful software. I am grateful that Paul Huang and Eric Bergman were always willing to share their expertise and results. And I thank Tom Jordan and Sean Solomon for their enthusiasm, their advice, and their parties.

The librarians on the second floor are probably glad to see me graduate. Jean Eaglesfield, Laura Feld, and Amy Ferguson have each helped me chase down dozens of obscure references, many of them written in Russian.

Of course, I spent most of my time on the seventh floor and I am glad I could. Day in and day out, Yves Bernabe, Brian Evans, Joanne Fredrich, Sheila Gardner, Randy Hay, Hélène Lyon-Caen, and Jean Titillah were there to help. Steve Hickman has been a good friend. Geoff Abers taught me that waveforms can be fun.

Without Rob McCaffrey's help I could never have writen chapter two. His programs and his suggestions made it possible. Rob showed just how much an IBM PC can do. And he has been a mentor, who helped me cope with the inevitable frustrations of writing a Ph.D. thesis.

My advisor, Peter Molnar, has given me the opportunity and the freedom to explore a number of different problems in India, Alaska, Oregon, California, and Nevada. Along the way, I have learned, with Peter's help, how to evaluate the work of others and how to pose a good problem. Just as importantly, he's helped me become a better writer, both by his example and by editing hundreds of pages of my work.

I am also grateful for having had the chance to work with Craig Jones. For ten years, I've enjoyed Craig's enthusiasm of all things geological and his unique sense of humor. Talking with Craig helped me make sense of much of the data presented in this thesis. He's been an office-mate, a co-author, and a very good friend.

There are also many people not at M.I.T. who have helped make this thesis possible. I did much of the work for chapter one at Caltech in Joe Kirschvink's paleomagnetism lab, where I always felt welcome. And I will never forget the friendship and sashimi Atsuko Kirschvink provided. Martin and Alison Ruzek gave me a home away from home in Pasadena. I thank Dave Van Alstine for the chance to work in Alaska and for all that he taught me about paleomagnetism.

Dave Simpson gave me free access to his seismograms from the Toktogul seismograph network and made it easy for me to work at Lamont. He and Christina Boyko made my visits to Lamont both fun and productive.

Throughout my graduate career, I have been helped along by the love and support of my parents. They have always been there, ready to help. I hope that they take pride in my accomplishment, it would not have been possible without them.

My wife, Anne, deserves all the gratitude I can give her. When my work was not going well, she helped me maintain my perspective. When I dwelled on my shortcomings, she reminded me of my achievements. When I wasn't working, she did her best to help me relax. Graduate students do not make ideal husbands. I'm fortunate to be married to such an understanding wife.

CHAPTER 1

PALEOMAGNETISM AND CRUSTAL ROTATIONS ALONG A SHEAR ZONE, LAS VEGAS RANGE, SOUTHERN NEVADA

Michael R. Nelson and Craig H. Jones

Department of Earth, Atmospheric, and Planetary Sciences,
Massachusetts Institute of Technology, Cambridge

ABSTRACT

In southern Nevada, Paleozoic isopachs, Mesozoic structures, and mountain ranges trend north-south, but as they approach the right-lateral, west-northwest-trending Las Vegas Valley Shear Zone (LVVSZ), they are bent clockwise up to 90° in oroflexes 30 km long. In the Las Vegas Range the declination of the characteristic magnetization of the Cambrian Bonanza King Formation has likewise been rotated clockwise more than 50°. For samples from eight sites (13-23 samples per site) in the Las Vegas Range and in its extension south of the LVVSZ, stepwise thermal demagnetization to 600° C removed recent and Tertiary overprints, revealing a nearly horizontal, late Paleozoic viscous partial thermoremanent magnetization (VPTRM) which predates both the Tertiary oroflexural bending and the Sevier thrusting in the area. The declination of the characteristic magnetization (after correcting for the dip of bedding) varies from 133° ± 2° at a site 24 km north of the shear zone to 196° ± 4° 13 km north of it and 204° ± 4° 11 km south of the shear zone. This parallels a similar change in the structural trend. The

paleomagnetic data indicate that the Las Vegas Range is broken into rather small blocks (<5 km) which rotate in response to more continuous deformation at depth. This deformation of the upper crust can be modelled using a thin non-Newtonian viscous plate model, which when applied to the Las Vegas Valley Shear Zone predicts rotations similar to those seen in the Las Vegas Range.

INTRODUCTION

The Las Vegas Valley Shear Zone (LVVSZ) is a major right-lateral fault zone trending northwest from Las Vegas, Nevada. Movement along the fault has offset the north-south trending mountain ranges of southern Nevada (Figure 1) and bent them into large "oroflexes," which superficially resemble giant drag folds. The oroflex at the southern end of the Las Vegas Range north of the shear zone is particularly striking. Within 30 km the range bends almost 90° clockwise, its trend changing from north-south to roughly east-west near the fault. This area provides an excellent setting for an investigation of oroflexural bending and large-scale deformation in general. Previous paleomagnetic work has shown that the rocks of the Cambrian Bonanza King Formation acquired a stable remanent magnetization in late Paleozoic time, long before the deformation associated with the Miocene movement along the LVVSZ [Gillett and Van Alstine, 1979, 1982]. The direction of this magnetization can thus be used as a marker to determine how the Las Vegas Range has been deformed.

In this study we not only document structural rotation but also use paleomagnetism to try to understand the extent and mechanism of that rotation. Researchers frequently report rotated paleomagnetic declinations from a few sites and conclude that terranes several tens or hundreds of kilometers in extent have been similarly rotated. In areas

where the geologic structure is well exposed and well mapped and where more thorough paleomagnetic sampling has been done, rotations due to local structures (≈10 km in size) have been documented [e.g. Channell et al., 1978; Grubbs and Van der Voo, 1976; Reidel et al., 1984]. Studies of rotations in areas where the geologic structure is well-known, like the Las Vegas Range, are essential if we are to evaluate estimates of rotations in poorly exposed, less well-understood areas. In addition, the data presented here provide a test of recently published models for deformation near shear zones [Ron et al., 1984; McKenzie and Jackson, 1983; England et al., 1985].

GEOLOGIC SETTING

Structural trends, facies boundaries, and Paleozoic isopachs are all bent and offset right-laterally across the LVVSZ [Stewart et al., 1968]. Longwell [1974] showed that the shear zone offsets the Miocene (≈17 Ma) Thumb Formation right-laterally more than 64 km. Ekren et al. [1968] concluded from their work on the Nevada Test Site that much of the movement on the LVVSZ has occurred since 17 Ma. Movement must have ended by early Pliocene time when deposition of the Muddy Creek Formation began, since it is not cut by the shear zone [Longwell, 1974].

Burchfiel [1965] correlated the Gass Peak Thrust in the Las Vegas Range with the Wheeler Pass Thrust, east of Indian Ridge, south of the LVVSZ (Figure 1). Both thrusts put Precambrian Stirling Quartzite on the late Paleozoic Bird Spring Formation. The shear zone offsets the thrust 22 km, and bending north of the shear zone accounts for 21 km of additional displacement, for a minimum of 43 km of offset. In contrast, about 80 km to the west of the Las Vegas Range, in the Specter Range, Burchfiel found that movement along the shear zone was taken up entirely by bending, not

by faulting. The shear zone does not cut the Specter Range at the surface and is not continuous with the Walker Lane to the northwest.

The LVVSZ is thought to be an intracontinental transform separating regions of differential extension [Davis and Burchfiel, 1973; Anderson, 1973; Wernicke et al., 1982]. Detailed mapping by Guth [1981] in the Sheep, Desert, and Las Vegas ranges indicates that the region north of the shear zone and west of the Las Vegas Range has undergone almost 100% extension in Miocene time. The Spring Mountains, south of the shear zone, have not undergone any significant extension [Burchfiel et al., 1974].

Landsat images of southern Nevada show that mountain ranges along the Las Vegas Valley have been bent into "oroflexes," arcuate ranges suggesting giant drag folds [Albers, 1967; Burchfiel, 1965] caused by right-lateral movement across the LVVSZ. The most striking oroflex along the LVVSZ occurs at the southern end of the Las Vegas Range (Figure 1). At the southernmost end of the range, 30 km north of the city of Las Vegas, the range trends roughly east-west. Farther away from the shear zone, structures trend more northeasterly, and by 30 km north from the shear zone the range runs north-south, following the regional trend of nearby ranges. The structural geology and stratigraphy of the Las Vegas Range have been described in detail by Guth [1980] and Ebanks [1965].

The Las Vegas Range consists of a 6-km-thick section of uppermost Precambrian to Permian miogeosynclinal sedimentary rocks, which are exposed continuously along the range to within 5 km of the LVVSZ. They include thick sections of shallow marine limestones such as the Cambrian Bonanza King, the Cambrian Nopah, and the Permo-Pennsylvanian Bird Spring Formations. Higher up in the section is a regional unconformity due to widespread uplift in late Permian time. The Mesozoic section consists mostly of continental red beds and sandstones.

During the Mesozoic Sevier orogeny, the Gass Peak Thrust and several other eastward-directed thrusts (Figure 1) became active. The Gass Peak Thrust runs along the axis of the Las Vegas Range and places uppermost Precambrian Stirling Quartzite on the Bird Spring Formation. Guth [1980] documented 5900 m of stratigraphic displacement on the Gass Peak Thrust and thought that horizontal displacement on it exceeded 30 km. A number of folds with horizontal axes parallel to the Gass Peak Thrust formed during thrusting, especially in the Bird Spring Formation of the lower plate.

During Neogene time, extension of the Basin and Range was accompanied by listric normal faulting, creating the north-south mountain ranges that we see today. The Mormon Pass Fault, a major, west dipping normal fault, runs along the western edge of the Las Vegas Range, separating the Las Vegas Range, which was relatively unaffected by Basin and Range faulting, from the Desert and Sheep ranges which have undergone ≈100% east-west extension [Guth, 1980, 1981]. Alluvial conglomerates, lacustrine limestones, and rhyolitic tuffs of the Miocene Horse Spring Formation were deposited in the valleys between the ranges. During Miocene time, movement of the LVVSZ offset and deformed both the Tertiary normal faults and earlier Sevier age thrusts and folds. Basin and Range extension continued both during and after movement along the LVVSZ.

Gillett and Van Alstine [1979, 1982] and Van Alstine and Gillett [1979] studied the latest Precambrian and earliest Paleozoic strata of the Desert Range, 25 km west of the Las Vegas Range (Figure 1). They found that the rocks of the Upper Cambrian Bonanza King Formation have a characteristic magnetization (southeasterly declination, I ≈ -20°) apparently due to remagnetization during the late Paleozoic. A less stable Tertiary or late Cretaceous component was removed using thermal demagnetization. The

declination of the characteristic component varied between sites, suggesting that the rocks of the northern end of the Desert Range have been rotated 44° ± 5° counterclockwise with respect to those 30 km to the south.

PRESENT STUDY

Methodology

The Cambrian Bonanza King Formation in the Las Vegas Range consists of 900 m [Guth, 1980] of shallow marine limestones and dolomites and is exposed along most of the length of the Las Vegas Range. Dark gray lime mudstone, often mottled due to bioturbation, is the predominant rock type. Siltier, limonite-stained limestone commonly occurs as stringers or wavy laminae in the dark limestone. The rock commonly contains stylolites and calcite-filled fractures, which were not sampled when possible. Most samples were taken from the dark grey limestone, which also gave the most consistent paleomagnetic results.

Samples were taken from sixteen sites in the Las Vegas Range. In addition, samples were collected at one site at Indian Ridge (IR), 25 km west of the Las Vegas Range, about 10 km south of the LVVSZ (Figure 1). Care was taken to sample at well-exposed sites away from major faults and folds associated with Sevier age thrusting and other structural complications. Between 13 and 23 samples were collected at each site. Samples were usually spaced 1-3 m apart and typically spanned 10-20 m of stratigraphic section.

At most sites, samples were collected using a gasoline-powered core drill. Cores were oriented with a Brunton compass. At six sites (IR, PC, MR, QS, BL, and GV), block samples were collected using the technique described by Gillett and Van Alstine [1979]. Cores were drilled from the

block samples using a drill press in the lab. Each core, 2.5 cm in diameter, was cut into specimens 2 to 3 cm long, which were then rinsed in dilute HCl for 5-10 s to remove any metallic contamination from the drill bit or the rock saw used to trim the specimens. This is particularly important because these weakly magnetized rocks have natural remanent magnetization (NRM) intensities of $\approx 5 \times 10^{-5}$ Am^2/kg.

All measurements were made in the paleomagnetism lab at the California Institute of Technology using an ScT cryogenic magnetometer in a shielded room where the strength of the ambient field was ≈100 nT. All specimens were measured and thermally demagnetized inside the shielded room. Data collection and reduction were done with an Apple IIe computer interfaced to the magnetometer.

In addition to measuring the remanent magnetization of the specimens, isothermal remanent magnetization acquisition studies were done to determine the magnetic minerals present in selected samples. An impulse magnetizer was used to magnetize samples using progressively higher fields, up to 0.6 T.

Paleomagnetism of the Bonanza King Formation

For most sites the NRM directions clustered around the present axial dipole field direction (e.g., site LP, Figure 2) before correcting for the dip of bedding. Thermal demagnetization was necessary to remove magnetic overprints and to isolate the characteristic magnetization. Most specimens were thermally demagnetized in 10-12 steps to 600°C.

Upon demagnetization to 400°C, samples from 12 sites revealed a south or southeasterly, nearly horizontal characteristic direction (e.g., site LP, Figure 2). At most sites there were a number of samples that were strongly magnetized with only a single, randomly oriented component of magnetization, which is typical of samples that have been remagnetized by

lightning. Commonly, a group of adjacent samples all appear to have been lightning-struck (for instance, samples 15-17 on Figure 2). At two of the more exposed sites (MR and MW), where an older southerly component was evident, scatter apparently due to lightning strikes made it impossible to determine the remanent direction accurately (±20°). At two other sites (EC, SM) the direction of the characteristic component could not be determined accurately because most of the samples were heavily overprinted. Even at the most protected sites, well away from ridges, typically 10-20%, and in one case 70%, of the specimens have been remagnetized, presumably by lightning strikes and weathering. Such clearly remagnetized samples were not used in calculating the mean direction of the characteristic magnetization.

At the remaining five sites (BT, PC, QS, BL, GV), thermal demagnetization failed to reveal a consistent magnetization direction. At two of these sites (QS and BL), samples were drilled from blocks of a suspected cave breccia in the lower Bonanza King Formation [Gillett, 1982]. For these sites the magnetization directions were scattered, as would be expected if the magnetization predated the brecciation [Gillett, 1982]. At the other three sites where the characteristic magnetization could not be isolated, it is probable that weathering and lightning strikes have obliterated the ancient magnetization.

Specimens from the eight sites where the effects of lightning strikes could be minimized had quite similar thermal demagnetization paths. Three components of magnetization were present: (1) a very soft, viscous component aligned with the present earth field and removed by heating to 200°C, (2) an intermediate component, which is removed by demagnetization to 350°C, oriented north or northwest with a moderate (≈60°) inclination, and (3) the characteristic magnetization left after heating to 350°C,

which has a south to southeasterly declination and a shallow, negative inclination. A modified Zijderveld diagram [Roy and Park, 1974; Zijderveld, 1967] of a representative sample (Figure 3) shows these three components clearly. As the specimen was demagnetized and the north-northeast modern field component was removed, the magnetization shifted westward. As the north-northwesterly intermediate component was removed, the magnetization became more southerly and shallow until only the southerly, nearly horizontal characteristic component remained. To determine accurately the direction of these different components (Table 1), we used a least squares fit program [Kirschvink, 1980]. The intermediate component represents the magnetization removed between 200° and 350°C, and the characteristic component was removed between 350° and 500°C.

Bingham statistics [Onstott, 1980] were used to calculate the mean and 95% error ellipse for both components of magnetization at each site. At several sites the magnetization directions were not distributed according to a Fisherian distribution [Fisher, 1953], possibly because thermal demagnetization did not completely remove a present-day or Tertiary overprint in some samples. The uncertainty quoted for the declination of a component equals half the total range in declination of the Bingham error oval. As Demarest [1983] pointed out for a Fisherian distribution, this will over-estimate the uncertainty in declination by ≈25%.

The characteristic magnetization of these rocks is carried in magnetite. Heating the rocks to 600°C (just above the Curie temperature of magnetite) destroys more that 95% of the natural remanent magnetization (NRM), making it impossible to measure the remaining remanent field accurately. Studies of isothermal remanent magnetization (IRM) acquisition for four representative samples showed the rapid acquisition

of IRM typical of magnetite-bearing rocks. Gillett and Van Alstine [1982], on the basis of alternating-field demagnetization behavior, bulk susceptibility measurements, and petrographic evidence, concluded that magnetite is the carrier of both the characteristic and the intermediate components of magnetization in the Bonanza King Formation of the Desert Range.

Paleomagnetism of Other Formations in the Las Vegas Range

Samples from the Permo-Pennsylvanian Bird Spring Formation were collected at two sites in the Las Vegas Range, EW and EP, 12 and 45 km north of the shear zone, respectively, to determine whether these limestones had an ancient magnetization that could be used as a structural marker. These samples were very weakly magnetized (NRMs with intensities of $\approx 5 \times 10^{-8}$ emu/g) in the direction of the present axial dipole field. After thermal demagnetization to 400°C the specimens' magnetization was of the order of the noise level of the magnetometer ($\approx 10^{-9}$ emu/g). Because of these unpromising results, no further sampling was done in the Bird Spring Formation.

The Miocene Horse Spring Formation, deposited while the LVVSZ was active, is exposed near the north and south ends of the Las Vegas Range. Lacustrine limestones in the Horse Spring Formation were sampled at 3 sites, south of Fossil Ridge, near site LO, 12 km from the shear zone (Figure 4). The magnetization was aligned with the present earth field and apparently resided in goethite because it was destroyed upon heating to 100°C. There was no evidence of an ancient magnetization.

East of Mormon Pass and site CM, near the north end of the Las Vegas Range (Figure 4), rhyolitic tuff beds up to 3 m thick occur in thick deposits of fanglomerate made up of Paleozoic limestone clasts. Guth [1980] identified these beds as Horse Spring Formation. The tuffs were

sampled at two sites 35 km north of the shear zone. Samples of a coarse-grained tuff (≈1-mm grain size) at the first site yielded randomly oriented magnetization directions and had very erratic demagnetization paths. At the second site, fifteen samples from four beds of finer-grained (≈0.3-mm grain size) reworked tuff were collected. These had NRM directions aligned with the present field. Upon demagnetization to 400°C all four samples from one of the tuff beds revealed a southerly magnetization direction with an inclination of about -60° after a tilt correction. After demagnetization at 400°C and a structural correction for the 25° dip of bedding, the magnetization directions for the remaining 11 samples grouped around a Tertiary pole of normal polarity. These tuffs probably record a primary magnetization imposed before the beds were tilted. The paleomagnetic evidence implies that these rocks have not been rotated more than 20°. Unfortunately, these tuffs are not exposed farther south.

INTERPRETATION

The characteristic magnetization of the Bonanza King Formation in the Las Vegas Range is similar to that measured by Gillett and Van Alstine [1982] for the Desert Range. At their northernmost site (V, see Figure 1), 52 km from the shear zone, the rocks of the Bonanza King Formation have a characteristic magnetization (after tilt correction) of D = 121°, I = -18°, and α_{95} = 2°, for 42 samples. At their southernmost site (U, see Figure 1), 28 km north of the shear zone, they found a characteristic magnetization of D = 165°, I = -22°, and α_{95} = 4°, for 47 samples. The characteristic magnetization measured in the Las Vegas Range (after tilt correction) varied from D = 133°, I = -10.2° for site UP to I = 196°, D = -6.8° for site LO. This magnetization was presumably acquired as a

viscous partial thermoremanent magnetization when the rocks were uplifted and cooled during Late Permian time [Gillett and Van Alstine, 1982]. The Late Permian paleopole for cratonic North America is 49° N, 121° E [Irving and Irving, 1982]. Because the field was reversed throughout most of the Permian [Irving, 1966], the field direction for the Desert and Las Vegas Ranges would have been about D = 148°, I = -15.8° (Figure 5a).

At the three northernmost sites, NM, CM, and UP, both the intermediate and the characteristic magnetization directions are quite consistent (±8°), indicating that there has been little rotation between these sites. The mean characteristic magnetization direction (D = 139°, I = -10°, after tilt correction) is very close to the Permian field direction for cratonic North America (Figure 5a). The slightly shallower inclination may be explained if the strata were tilted gently (<10°) to the west before they were remagnetized in the late Paleozoic. The regional stratigraphy indicates that this was likely [Gillett and Van Alstine, 1982]. If all of the shallow present-day dip (5°-10° to the west) was acquired by the late Paleozoic, then the mean in situ direction (D = 140°, I = -15.8°) would be a more accurate measure of the field direction when the rocks were remagnetized. Regardless, correcting for this minor amount of regional tilting does not significantly change the declination of the characteristic magnetization. An equal angle plot of the field direction for the Las Vegas Range since the late Paleozoic (Figure 5a) shows clearly that this magnetization must have been acquired before early Jurassic time, after which the field inclination was much steeper than that of the characteristic magnetization (with or without correcting for the dip of bedding).

At the remaining sites the inclination of the characteristic magnetization varies with the dip of the beds, indicating that the

magnetization was acquired before the beds were tilted to their present attitude. If the acquisition of magnetization preceded tilting, then the variance of the mean inclination for all eight sites should decrease after the tilt correction is made. Indeed, the characteristic component passes this inclination-only fold test at the 99% confidence level (Table 2) [McFadden and Reid, 1982; McElhinny, 1964].

The changes in the declination of the characteristic component between sites in the Las Vegas Range are primarily due to rotations related to motion on the Las Vegas Valley Shear Zone. Gillett and Van Alstine [1982] saw a similar discrepancy in declination between their sites and the expected field direction and attributed it to vertical axis rotations related to motion on the LVVSZ south of the Desert Range and the Pahranagat Shear Zone to the north.

The intermediate component of magnetization, as measured at the three least rotated, northernmost sites, NM, CM, and UP (D = 326°, I = 53°, before tilt correction), is within 5° of the late Mesozoic magnetic field direction for the Las Vegas Range (Figure 5a). In contrast to the characteristic component, the intermediate component does not pass the inclination-only fold test at the 95% confidence level (Table 2), indicating that it was imposed either while the beds were being tilted or afterwards. This component appears to have been acquired during uplift associated with movement on the Gass Peak Thrust.

TECTONIC IMPLICATIONS

The paleomagnetic evidence shows that parts of the Las Vegas Range have undergone over 60° of relative tectonic rotation around a vertical or near-vertical axis. The declination of the characteristic magnetization increases more than 60° from site UP, 24.4 km north of the axis of the Las

Vegas Valley, to site LO, 12.8 km north of it. Likewise, the declination of the intermediate component increases 50.8° ± 4.8° over the same 11.6 km interval (Table 1, Figure 4).

At the northernmost sites (UP, NM, CM) the intermediate component can be very accurately measured and indicates that there has been very little rotation between these three sites since the Sevier orogeny. Hence, we measure all rotations due to the LVVSZ with respect to these relatively fixed sites. In contrast to the intermediate magnetization direction the declination of the characteristic magnetization increases 13.7° ± 3.6° in the 15.5 km from site UP to NM. This is probably due to minor, local faulting and folding which occurred after the acquisition of the characteristic magnetization but before the acquisition of the intermediate magnetization. Similarly, local structures are probably also responsible for the 17.1° ± 9.8° difference in the declination of the characteristic magnetization between sites YF and LP, which are less than 2 km apart. Apparently there are ±10° variations in the declination of the characteristic magnetization due to smaller-scale structures superimposed upon the much larger systematic rotation of both components of magnetization due to movement on the LVVSZ.

Since the characteristic magnetization was acquired, the rocks of the Las Vegas Range have undergone two significant rotations: a tilt around a roughly north-south, horizontal axis due to Sevier age thrusting, followed by a near-vertical axis rotation due to movement on the LVVSZ. In contrast, the intermediate component has only been affected by the vertical axis rotation. To use the characteristic component as a structural marker to determine the amount of vertical axis rotation, the effects of the horizontal axis rotation must be removed using a simple tilt correction. When this is done, the inclinations of the

characteristic magnetization are between 3° and -14°, but the declinations range from 133° and 204°. The difference in declination between the three northern, unrotated sites and the other sites reflects the amount of rotation due to movement on the LVVSZ.

When this vertical axis rotation is subtracted from the in situ directions for both the characteristic and intermediate component, both components cluster nicely. The intermediate component directions cluster around a Cretaceous or early Tertiary field direction, while the characteristic magnetization directions move toward a late Paleozoic field direction (Figure 5b). When a tilt correction is applied to restore bedding to horizontal, the intermediate component directions scatter, while the characteristic magnetization directions cluster further (Figure 5c), reaffirming our inference that the characteristic direction predates tilting while the intermediate direction was acquired after tilting.

In contrast, Gillett and Van Alstine [1982] concluded that the intermediate component of magnetization they measured in the Desert Range predated tilting. This is explained by the differing deformational histories of the Las Vegas Range and the Desert Range. In the Desert Range, bedding dips steeply (40-60°) as a result of listric normal faulting during Basin and Range extension in the late Tertiary, well after the intermediate magnetization was acquired. About 100% extension occurred in the Sheep and Desert ranges, while the Las Vegas Range was almost unaffected [Guth, 1980]. The gentler dips of bedding in the Las Vegas Range were acquired as a result of thrusting along the Gass Peak Thrust during the Sevier Orogeny, before the intermediate magnetization was acquired. The Desert Range did not undergo significant tilting during the Sevier orogeny [Guth, 1980].

MECHANISMS OF OROFLEXURAL BENDING

Several studies have used paleomagnetism to document tectonic rotations, but few have attempted to explain how these rotations occur. Most workers ascribe the rotations to the movement of rigid blocks without documenting the sizes of the blocks, the nature of their boundaries, or even whether the blocks are indeed rigid. There are a variety of possible mechanisms for deformation in and near shear zones, including those proposed by Ron et al. [1984], McKenzie and Jackson [1983], and England et al. [1985]. We will consider a number of these to see if they apply in the Las Vegas Range.

The first and simplest mechanism accommodates displacement on a shear zone along a series of faults parallel to the main shear zone (Figure 6b) and is similar to that proposed by Geissman et al. [1984] for shear across the Walker Lane in west central Nevada. Such a mechanism could explain the outcrop pattern seen in the Las Vegas Range. However, the blocks between the faults would not be rotated, and thus such a mechanism cannot explain the paleomagnetic data from the Las Vegas Range.

Another possible mechanism for deformation near shear zones is that of pervasive simple shear (Figure 6c). In such a case, shearing would be accommodated by recrystallization and deformation of individual grains in the rock, and the paleomagnetic samples themselves would have been deformed. During Miocene time the rocks of the Las Vegas Range were not deeply buried and were not heated enough to reset the characteristic magnetization, which was acquired when the rocks were at ≈250°C in late Paleozoic time [Gillett and Van Alstine, 1982]. Recrystallization certainly occurs at the pressures and temperatures reached at mid-crustal depths but is unlikely to have affected these rocks. There is no macroscopic textural evidence in the samples for pervasive deformation,

but there is abundant field evidence of brittle faulting. In general, the sites sampled were located in apparently rigid blocks well away from zones of faulting and folding.

In a third model, offset across a shear zone is accommodated by slip along mappable, strike-slip, bounding faults and by rotation of rigid blocks within the shear zone (Figure 6d). Ron et al. [1984, 1986] and Luyendyk et al. [1980, 1985] have invoked such a mechanism to explain discordant paleomagnetic declinations in northern Israel, southern Nevada, and southern California. This type of mechanism cannot explain the paleomagnetic data from the Las Vegas Range, because the amount of rotation increases smoothly toward the LVVSZ, indicating that if there are rotating rigid blocks, they do not span the entire shear zone. In addition, this model cannot explain the gradual change in the structural trend from north-south to nearly east-west near the LVVSZ.

McKenzie and Jackson [1983] considered the case where the fault-bounded blocks are much smaller than the width of the deforming zone and rotate in response to continuous deformation in the ductile material beneath them (Figure 6e). They showed that for a rigid block surrounded by faults and deforming zones and floating on a continuum the rotation rate of the block will be $\underline{\omega}/2$, where $\underline{\omega}$ is the vorticity in the ductile substrate. In such a case the continuous, ductile deformation at middle and lower crustal levels controls the movement of the brittle rock near the surface. In the Las Vegas Range it appears that more than just the upper crust is involved in the deformation, since the rotation of magnetization directions (and hence of the upper crust) up to 20 km from the LVVSZ indicates that a comparable thickness of crust is involved in the deformation.

The paleomagnetic data indicate that this last mechanism is applicable, since the rocks of the Las Vegas Range are broken into a number of small

blocks, each one rotated by a different amount. The paleomagnetic declination changes significantly over a range of less than 5 km (for example, between sites LP, YF, and CK). Since the geologic mapping of the Las Vegas Range [Guth, 1980; Ebanks, 1965] does not show any crosscutting faults with enough offset to accommodate the 10°-20° of rotation between sites, it seems likely that the Las Vegas Range is actually broken into many blocks ranging in size from a few kilometers to a few meters in length, separated by small faults and fractures. Such small-scale structures would be too small to appear on any but the most detailed geologic maps and yet can account for much of the deformation in a given area. In a detailed study of a particularly well-exposed part of the Sierra Nevada, Lockwood and Moore [1979] found that microfaults accommodated ≈2.3% extension in an area previously thought to be undeformed due to the lack of large mappable structures. Similarly, Riedel et al. [1984] measured discordant paleomagnetic declinations in the Pomona flow of the Columbia Plateau Basalt Group that indicated rotations which could not be explained by mapped geologic structures. They concluded that movement along much smaller scale fractures and faults was responsible for the rotations.

Thus, because the block size is smaller than the width of the deformed zone, we would expect the amount of rotation to equal half the vorticity $\underline{\omega}$ of the underlying ductile layer. The key question then is to determine how deformation will occur in a continuous ductile solid cut by a strike-slip fault.

THIN VISCOUS PLATE MODEL

England et al. [1985] and Sonder et al. [1986] have done numerical experiments using a thin viscous plate model to examine the length scales

of deformation along a strike-slip fault. In contrast to McKenzie and Jackson [1983], who calculated rotations in a shear zone given the total offset and width of the shear zone, Sonder et al. [1986] calculate both the amount of rotation and how it decreases away from the shear zone for a given fault offset, fault length, and plate rheology.

England et al. [1985] and Sonder et al. [1986] consider a thin viscous plate with a fault parallel to the x axis. The components u and v of the velocity are taken to be parallel to the x and y axes, respectively (Figure 7). A tangential velocity boundary condition

$$u(x,0) = U_0 \sin(2\pi x/\lambda) \tag{1}$$

is imposed on the x axis between $x = 0$ and $x = \lambda/2$, where $\lambda/2$ is the length of the fault. On the boundaries $x = 0$ and $x = \lambda/2$ a reflecting boundary condition is imposed. England et al. [1985] first assumed a Newtonian viscosity and derived exact solutions for both plane strain deformation and for deformation of a thin viscous sheet in a gravity field normal to the sheet.

For the case of plane strain deformation,

$$u = U_0 \sin(2\pi x/\lambda)\ e^{-2\pi y/\lambda}(1 - 2\pi y/\lambda) \tag{2a}$$

$$v = -U_0 \cos(2\pi x/\lambda)\ e^{-2\pi y/\lambda}(2\pi y/\lambda) \tag{2b}$$

For the case of a thin viscous sheet,

$$u = U_0 \sin(2\pi x/\lambda)\ e^{-2\pi y/\lambda}[1 - \tfrac{3}{5}(2\pi y/\lambda)] \tag{3a}$$

$$v = -U_0 \cos(2\pi x/\lambda)\ e^{-2\pi y/\lambda}[\tfrac{3}{5}(2\pi y/\lambda)] \tag{3b}$$

Now, the instantaneous angular velocity of a small, horizontal rigid block is

$$\underline{\Omega} = \underline{\omega}/2 = \tfrac{1}{2}\,\underline{\nabla} \times \underline{v}$$

$$= \tfrac{1}{2}(\partial v/\partial x - \partial u/\partial y)\hat{\underline{z}} \tag{4}$$

From this we can calculate the rotations for points near the line $x = \lambda/4$ for comparison with the rotations measured in the Las Vegas Range.

For points near $x = \lambda/4$, $u >> v$ and $\partial u/\partial x$ will be small. Thus for a given point, $\underline{v}$ and $\underline{\Omega}$ will remain almost constant through time even though the point will move with respect to the line $x = \lambda/4$ during deformation. So if t is the duration of deformation, the amount of rotation

$$\begin{aligned} R &\approx |\underline{\Omega}|t = -t/2\ \partial u/\partial y \\ &= U_0 t \sin(2\pi x/\lambda)\ e^{-2\pi y/\lambda}(2\pi/\lambda) \\ &\approx U_0 t\ e^{-2\pi y/\lambda}(2\pi/\lambda) \end{aligned} \tag{5}$$

for plane strain and

$$\begin{aligned} R &\approx |\underline{\Omega}|t = -t/2\ \partial u/\partial y \\ &\approx \tfrac{4}{5} U_0 t \sin(2\pi x/\lambda)\ e^{-2\pi y/\lambda}(2\pi/\lambda) \\ &\approx \tfrac{4}{5} U_0 t\ e^{-2\pi y/\lambda}(2\pi/\lambda) \end{aligned} \tag{6}$$

for a viscous plate.

England et al. [1985] noted that these two cases will bound all plausible Newtonian models. Note that the predicted rotations differ by only 25%. For a left-lateral fault the rotations will be counter-clockwise; for a right-lateral fault like the LVVSZ the rotations will be clockwise.

We can compare the rotations observed in the Las Vegas Range with these expressions. The Las Vegas Range trends roughly perpendicular to the LVVSZ and is located near the midpoint of the fault, where displacement appears to be greatest. To the west-northwest, displacement decreases until in the Specter Range 55 km to the west there is no surface evidence for displacement [Burchfiel, 1965]. Fifty-five kilometers to the east the LVVSZ is cut off by the Lake Mead Shear Zone [Bohannon, 1979]. So the minimum length of the shear zone is ≈110 km (and thus $\lambda \approx 220$ km).

Just how the displacement varies along the shear zone is not known, but let us assume the simple distribution of slip (Figure 7) used by England et al. [1985]. We do know that the Gass Peak Thrust in the Las Vegas

Range has been offset at least 43 km westward to Indian Ridge, so we can make a minimum estimate for the displacement. Because the model is for just one side of the shear zone, we halve the minimum displacement to 22 km. Near the center of the model fault (where $x \approx \lambda/4$) the tangential velocity

$$u(x,0) = U_0 \sin(2\pi x/\lambda)\ e^{-2\pi y/\lambda} \approx U_0 \qquad (7)$$

So the total displacement $D \approx U_0 t$, for $D \ll \lambda$.

Comparison With Paleomagnetic Data

In Figure 8a the relative rotation of the characteristic component of magnetization directions is plotted as a function of distance from the Las Vegas Valley Shear Zone. The rotations are taken relative to 139°, which is approximately the average declination measured at the northern three, least deformed sites and is close to the predicted declination for the Las Vegas Range when these rocks were remagnetized in late Paleozoic time. The uncertainty in declination equals half the range in declination of the Bingham 95% error ellipse at each site. These rotations are compared with (6) for a range of values of maximum displacement ($\approx U_0 t$). For plane strain the rotations would be 25% greater than those plotted (compare (5)). For values appropriate for the LVVSZ, England et al.'s Newtonian viscosity models fail to predict rotations of the magnitude documented in the Las Vegas Range. Furthermore, the calculated values decrease more slowly with distance from the shear zone than do the measured differences in declination.

England et al. [1985] also examined numerically the deformation of non-Newtonian viscous plates. For points near the line $x = \lambda/4$ they found that

$$u \approx U_0\ \sin(2\pi x/\lambda)\ e^{-4\sqrt{n}\pi y/\lambda} \qquad (8)$$

where n is the stress exponent.

Thus, since $\partial v/\partial x \ll \partial u/\partial y$ for $x \approx \lambda/4$,

$$R \approx -t/2\ \partial u/\partial y$$
$$\approx (2U_0 t\pi\sqrt{n}/\lambda)\ \sin(2\pi x/\lambda)\ e^{-4\sqrt{n}\pi y/\lambda} \qquad (9)$$

This expression is plotted in Figures 8b and 8c for different values of the U_0t ($\approx$ displacement) for both n = 3 and n = 10. In addition, the amount of rotation inferred from the declination of the characteristic magnetization is plotted. The amount of rotation inferred from the declination of the intermediate magnetization is plotted in Figure 8d along with model curves for different values of λ to show how the amount of rotation predicted varies with fault length (= $\lambda/2$). It is clear that much better agreement is obtained for n = 3 to 10 than for n = 1. Although the calculated curves do not exactly match the actual data, they do predict both the maximum amount of rotation and the length scale of deformation, especially for the larger values of offset U_0t.

There are a number of possible reasons why the paleomagnetic data do not match the theoretical curves more closely. The most important is that the crustal "blocks" sampled will not perfectly reflect the continuous deformation occurring at depth (see Figure 6e). The blocks have a finite extent and cannot perfectly mirror the continuous changes in the vorticity of the continuum beneath them.

At some sites (e.g., NM and UP) there is a large ($\geq$10°) discrepancy between the amount of rotation inferred from the intermediate component of magnetization and the characteristic component (Table 3). As discussed above, this could be due to small rotations that occurred between the acquisition of the two components. In addition, the error in isolating an intermediate component of magnetization is greater than that in determining the direction of a characteristic magnetization. While the

characteristic component of magnetization is more easily isolated, it has been affected by more tectonic events than the younger intermediate component. Another possible explanation for the discrepancy between the two components is that movement along the LVVSZ caused rotations around slightly nonvertical axes. Because the intermediate direction plunges steeply, a small change (≈5°) in the axis of rotation would significantly alter the change in declination for a given amount of rotation. In contrast, the nearly horizontal characteristic component is much less sensitive to such a perturbation of the axis of rotation. The discrepancy in the amount of rotation inferred from the two components of magnetization is greater than the uncertainty in the declination of the individual components (ΔD in Table 1) and provides a conservative estimate of the uncertainty in the inferred rotation.

Comparison With Structural Data

The near-horizontal characteristic magnetization direction provides an invaluable marker for determining the amount of rotation in the Las Vegas Range because geologic mapping alone cannot definitively determine the amount of rotation. The amounts of clockwise rotation of the characteristic component of magnetization do not equal the differences in the strike of bedding between sample sites (Table 3). This is particularly clear at the three northern sites where the beds are subhorizontal. At most sites the strike varied up to 20° because a small change in the orientation of a subhorizontal bed can cause a large change in strike. Thus the strike of bedding does not provide an adequate marker for determining vertical axis rotations in the Las Vegas Range.

However, other structural data can be used to test the deformation mechanism inferred from paleomagnetic data in the Las Vegas Range.

Geologic mapping by Longwell [1965], Guth [1980], and Ebanks [1965] showed that the Gass Peak Thrust, the associated folds which parallel it, and the contacts between units all trend nearly north-south in the northern Las Vegas Range but become increasingly east-west closer to the LVVSZ (Figure 4). These structures were formed by east-directed thrust faulting during the Sevier orogeny and consistently trend approximately N 10° E in southern Nevada. Everywhere the Gass Peak Thrust is exposed in the Las Vegas Range it places Cambrian Stirling Quartzite over Permo-Pennsylvanian Bird Spring Formation. Since the thrust is ramping upsection in the Las Vegas Range, this consistent juxtaposition indicates that erosion has exposed the same structural level everywhere. Thus the trend of the Gass Peak Thrust defines the structural trend particularly well. If we assume that the Gass Peak Thrust ramp originally trended N 10° E, paralleling other Sevier age thrusts well removed from the LVVSZ, we can use the trace of the fault to determine the change in structural trend due to the Miocene motion on the LVVSZ.

The structural trend, as defined by the trace of the Gass Peak Thrust, initially ran nearly perpendicular to the LVVSZ. The general trend of a passive marker initially perpendicular to a shear zone where $v = 0$ will rotate with an angular velocity of magnitude

$$\dot{\theta} = \tan^{-1}(\partial u/\partial y) \tag{10}$$

(For a more general expression, refer to McKenzie and Jackson [1983, equation 18].) Using the non-Newtonian viscous plate model of England et al. [1985] we can find the rotation of this marker:

$$\theta \approx \dot{\theta} t$$

$$\approx \tan^{-1}[(4U_0 t\pi\sqrt{n}/\lambda)e^{-4\sqrt{n}\pi y/\lambda} \sin(2\pi x/\lambda)] \tag{11}$$

$$\approx \tan^{-1}[(4U_0 t\pi\sqrt{n}/\lambda)e^{-4\sqrt{n}\pi y/\lambda}] \tag{12}$$

This result is plotted (Figure 9) with the inferred rotation of the trace

of the Gass Peak Thrust in the Las Vegas Range as a function of distance from the LVVSZ. Because the Gass Peak Thrust was surely not perfectly linear and because it bifurcates and varies locally in orientation, making it difficult to accurately determine the general trend of structure, this estimate was assigned a rather large uncertainty (±15°). For appropriate values of fault length and displacement, England et al.'s [1985] expression predicts both the observed maximum rotation and the observed decrease in rotation with distance away from the shear zone.

SUMMARY

Thermal demagnetization of samples of the Cambrian Bonanza King Formation in the Las Vegas Range has revealed two components of magnetization: a steeply-dipping, northerly intermediate direction due to a late Mesozoic remagnetization and a more stable, shallow, south to southeasterly direction due to a late Paleozoic remagnetization. We have used these magnetization directions as structural markers to conclude that the rocks of the Las Vegas Range were tilted during Sevier age thrusting, prior to the acquisition of the intermediate component, and then rotated around a vertical axis due to Miocene movement on the LVVSZ. The amount of rotation systematically increases from 0° at sites more than 24 km from the LVVSZ to >50° at sites 10-13 km from the shear zone. By using both ancient components of magnetization we have documented both the amount of rotation between sites and the near-vertical orientation of the rotation axis.

Rotations in the Las Vegas Range due to displacement on the LVVSZ can be explained by the independent rotations of small (<5 km in length) rigid blocks rotating in response to the deformation of a viscous continuum below [McKenzie and Jackson, 1983; Sonder et al., 1986]. Despite the

uncertainties of the paleomagnetic data and the simplicity of the models, our results do support the use of non-Newtonian viscous plate models to describe large-scale deformation of the crust. One such model has been used successfully to explain rotations associated with deformation along the >1000-km-long San Andreas Fault system [Sonder et al., 1986]. Our results from the Las Vegas Range indicate that this model is also applicable at smaller length scales (≈100 km), like that of the LVVSZ.

How small (<1 km) faults and fractures accommodate distributed shear has not been considered in many paleomagnetic studies of rotated terranes. Several workers [e.g., Luyendyk et al., 1980; Ron et al., 1984] have used rigid block models to explain their paleomagnetic results. Evidence for rotation of paleomagnetic directions from one site is used to infer that all of a large fault-bounded block containing the site has been similarly rotated. Such an assumption cannot be applied in the Las Vegas Range because it has not behaved as a single rigid block. The observed rotations in the Las Vegas Range are due to deformation up to tens of kilometers away from the mappable faults that bound it. Rigid block rotations have occurred, but the blocks must be much smaller than those often postulated. The complexity of such deformation could easily go unrecognized in an area where the outcrop is less continuous or the geologic structure less well known.

Acknowledgments. We are grateful to P. Molnar who got us going (and kept us going) on this problem. We thank J. Kirschvink, who generously gave us advice and encouragement as well as use of his rock drills, lab, and software. We thank D. Van Alstine, P. England, and B. Burchfiel for useful discussions, E. Shoemaker for use of his rock drills, and B. Yoder and B. Zeller of the U. S. National Wildlife Service for their assistance in the field. S. Gillett, J. Geissman, W. Power, and an anonymous reviewer provided invaluable suggestions for improving the original manuscript. This study was funded in part by the Carnegie Institute of Washington and the Student Research Fund of the MIT Department of Earth, Planetary, and Atmospheric Sciences. M. Nelson was supported by an NSF graduate fellowship.

REFERENCES

Albers, J. P., Belt of sigmoidal bending and right-lateral faulting in the western Great Basin, Geol. Soc. Am. Bull., 78, 143-156, 1967.

Anderson, R. E., Large-scale magnitude late Tertiary strike-slip faulting north of Lake Mead, Nevada, U. S. Geol. Surv. Prof. Pap., 794, 1-18, 1973.

Bohannon, R. G., Strike-slip faults of the Lake Mead region of southern Nevada, in Cenozoic Paleogeography of the Western United States, Pac. Coast Paleogeogr. Symp. 3, edited by J. M. Armentrout et al., pp. 129-139, Society of Economic Paleontologists and Mineralogists, Pacific Section, Los Angeles, Calif., 1979.

Burchfiel, B. C., Structural geology of the Specter Range quadrangle, Nevada, and its regional significance, Geol. Soc. Am. Bull., 76, 175-192, 1965.

Burchfiel, B. C., R. J. Fleck, D. T. Secor, R. R. Vincelette, and G. A. Davis, Geology of the Spring Mountains, Nevada, Geol. Soc. Am. Bull., 85, 1013-1022, 1974.

Channell, J. E. T., W. Lowrie, F. Medizza, and W. Alvarez, Paleomagnetism and tectonics in Umbria, Italy, Earth Planet. Sci. Lett., 39, 199-210, 1978.

Davis, G. A., and B. C. Burchfiel, Garlock Fault: An intracontinental transform structure, southern California, Geol. Soc. Am. Bull., 84, 1407-1422, 1973.

Demarest, H. H., Error analysis for the determination of tectonic rotation from paleomagnetic data, J. Geophys. Res., 88, 4321-4328, 1983.

Ebanks, W. J., Structural geology of the Gass Peak area, Las Vegas Range, Nevada, M.S. thesis, 56 pp., Rice University, Houston, Texas, 1965.

Ekren, E. B., C. L. Rogers, R. Ernest Anderson, and P. P. Orkild, Age of Basin and Range normal faults in Nevada Test Site and Nellis Air Force Range, Nevada, in The Nevada Test Site, edited by E. B. Eckel, Geol. Soc. Am. Mem., 110, 247-250, 1968.

England, P., G. Houseman, and L. Sonder, Length scales for continental deformation in convergent, divergent, and strike-slip environments: Analytical and approximate solutions for a thin viscous sheet model, J. Geophys. Res., 90, 3551-3557, 1985.

Fisher, R. A., Dispersion on a sphere, Proc. R. Soc. London Ser. A, 217, 295-305, 1953.

Geissman, J. W., J. T. Callian, J. S. Oldow, and S. E. Humphries, Paleomagnetic assessment of oroflexural deformation in west-central Nevada and significance for emplacement of allochthonous assemblages, Tectonics, 3, 179-200, 1984.

Gillett, S. L., A probable cave breccia in middle Cambrian limestone, southern Nevada: Petrography and paleomagnetic constraints on the time of formation, J. Sediment. Petrol. 53, 221-229, 1982.

Gillett, S. L., and D. R. Van Alstine, Paleomagnetism of Lower and Middle Cambrian sedimentary rocks from the Desert Range, Nevada, J. Geophys. Res., 84, 4475-4489, 1979.

Gillett, S. L., and D. R. Van Alstine, Remagnetization and tectonic rotation of Upper Precambrian and lower Paleozoic strata from the Desert Range, southern Nevada, J. Geophys. Res., 87, 10929-10953, 1982.

Grubbs, K. L., and R. Van der Voo, Structural deformation of the Idaho-Wyoming overthrust belt, as determined by Triassic paleomagnetism, Tectonophysics, 33, 321-336, 1976.

Guth, P. L., Geology of the Sheep Range, Clark County, Nevada, Ph.D. thesis, 189 pp., Mass. Inst. of Technol., Cambridge, Mass., 1980.

Guth, P. L., Tertiary extension north of the Las Vegas Valley shear zone, Sheep and Desert Ranges, Clark County, Nevada, Geol. Soc. Am. Bull., part I, 92, 763-771, 1981.

Irving, E., Paleomagnetism of some Carboniferous rocks from New South Wales and its relation to geological events, J. Geophys. Res., 71, 6025-6051, 1966.

Irving, E., and G. A. Irving, Apparent polar wander paths--Carboniferous through Cenozoic and the assembly of Gondwana, Geophys. Surv., 5, 141-188, 1982.

Kirschvink, J. L., The least-square line and plane and the analysis of paleomagnetic data, Geophys. J. R. Astron. Soc., 62, 699-718, 1980.

Lockwood, J. P., and J. G. Moore, Regional deformation of the Sierra Nevada, California, on conjugate microfault sets, J. Geophys. Res., 84, 6041-6049, 1979.

Longwell, C. R., Measure and date of movement on Las Vegas Valley Shear Zone, Clark County, Nevada, Geol. Soc. Am. Bull., 85, 985-990, 1974.

Longwell, C. R., E. H. Pampeyan, B. Bowyer, and R. J. Roberts, Nev. Bur. Mines Bull., 62, 1-218, 1965.

Luyendyk, B. P., M. J. Kamerling, and R. Terres, Geometric model for Neogene crustal rotations in southern California, Geol. Soc. Am. Bull., part I, 91, 211-217, 1980.

Luyendyk, B. P., M. J. Kamerling, R. R. Terres, and J. S. Hornafius, Simple shear of southern California during Neogene time suggested by paleomagnetic declinations, J. Geophys. Res., 90, 12454-12466, 1985.

McElhinny, M. W., Statistical significance of the fold test in paleomagnetism, Geophys. J. R. Astron. Soc., 8, 338-340, 1964.

McFadden, P. L., and A. B. Reid, Analysis of paleomagnetic inclination data, Geophys. J. R. Astron. Soc., 69, 307-319, 1982.

McKenzie, D. P., and J. A. Jackson, The relationship between strain rates, crustal thickening, paleomagnetism, finite strain, and fault movement within a deforming zone, Earth Planet. Sci. Lett., 65, 184-202, 1983.

Onstott, T. C., Application of the Bingham distribution function in paleomagnetic studies, J. Geophys. Res., 85, 1500-1510, 1980.

Reidel, S. P., G. R. Scott, D. R. Bazard, R. W. Cross, and B. Dick, Post-12 million year clockwise rotation in the Central Columbia Plateau, Washington, Tectonics, 3, 251-274, 1984.

Ron, H., A. Aydin, and A. Nur, The role of strike-slip faulting in the deformation of Basin and Range provinces (abstract), Eos, 67, 358, 1986.

Ron, H., R. Freund, Z. Garfunkel, and A. Nur, Block rotation by strike-slip faulting: Structural and paleomagnetic evidence, J. Geophys. Res., 89, 6256-6270, 1984.

Roy, J. L., and J. K. Park, The magnetization process of certain red beds: Vector analysis of chemical and thermal results, Can. J. Earth Sci., 11, 437-471, 1974.

Sonder, L. J., P. C. England, and G. A. Houseman, Continuum calculations of continental deformation in transcurrent environments, J. Geophys. Res., 91, 4797-4810, 1986.

Stewart, J. H., J. P. Albers, and F. G. Poole, Summary of regional evidence for right-lateral displacement in the western Great Basin, Geol. Soc. Am. Bull., 79, 1407-1414, 1968.

Van Alstine, D. R., and S. L. Gillett, Paleomagnetism of Upper Precambrian sedimentary rocks from the Desert Range, Nevada, J. Geophys. Res., 84, 4490-4500, 1979.

Wernicke, B., J. E. Spencer, B. C. Burchfiel, and P. L. Guth, Magnitude of crustal extension in the southern Great Basin, Geology, 10, 499-502, 1982.

Zijderveld, J. D. A., A. C. demagnetization of rocks: analysis of results, in Methods in Paleomagnetism, edited by D. W. Collinson, K. M. Creer, and S. K. Runcorn, pp. 254-286, Elsevier, New York, 1967.

TABLE 1. Summary of Bingham Statistics for Paleomagnetic Sites

Site		Declination	Inclination	K_1	K_2	95% angles		N/N_o
				Intermediate Component				
NM	in situ	327.7°	53.1°	-515.73	- 76.55	1.3°	3.3°	12/13
NM	tilt-corrected	322.3°	45.0°	-455.77	- 81.88	1.3°	3.2°	12/13
CM	in situ	325.5°	57.4°	-119.04	- 42.64	2.0°	3.4°	21/23
CM	tilt-corrected	320.8°	52.0°	- 97.07	- 50.10	2.2°	3.1°	21/23
UP	in situ	326.0°	49.7°	-349.20	-194.80	1.2°	1.6°	19/21
UP	tilt-corrected	319.9°	48.8°	-233.35	-203.88	1.5°	1.6°	19/21
LP	in situ	349.0°	47.7°	-137.25	- 12.19	2.5°	8.6°	12/18
LP	tilt-corrected	344.7°	40.6°	-114.08	- 16.87	2.7°	7.2°	12/18
YF	in situ	354.4°	47.2°	-429.23	-142.14	1.8°	3.2°	7/21
YF	tilt-corrected	1.8°	53.9°	-426.20	-142.50	1.8°	3.2°	7/21
CK	in situ	13.6°	59.4°	- 24.71	- 10.60	5.1°	7.9°	17/22
CK	tilt-corrected	350.6°	9.9°	- 24.01	- 10.01	5.2°	8.1°	17/22
LO	in situ	16.8°	64.8°	-317.88	-108.64	1.6°	2.8°	12/20
LO	tilt-corrected	353.7°	37.6°	-319.47	-108.73	1.6°	2.8°	12/20
IR	in situ	15.4°	69.5°	- 17.81	- 5.40	8.6°	16.4°	9/13
IR	tilt-corrected	348.9°	35.8°	- 19.31	- 4.92	8.3°	17.4°	9/13
				Characteristic Component				
NM	in situ	147.6°	-18.5°	-253.23	- 77.38	1.8°	3.3°	12/13
NM	tilt-corrected	146.3°	-10.5°	-161.56	- 73.26	2.3°	3.4°	12/13
CM	in situ	139.3°	-16.8°	- 46.55	- 26.46	3.2°	4.3°	21/23
CM	tilt-corrected	138.5°	-11.2°	- 43.30	- 25.92	3.4°	4.4°	21/23
UP	in situ	133.6°	-12.1°	-409.27	-222.42	1.1°	1.5°	19/21
UP	tilt-corrected	132.6°	-10.2°	-485.36	-197.61	1.0°	1.6°	19/21
LP	in situ	156.6°	-21.7°	- 84.88	- 13.99	3.2°	8.0°	12/18
LP	tilt-corrected	156.4°	-13.6°	- 61.76	- 12.31	3.8°	8.6°	12/18
YF	in situ	139.3°	0.5°	- 25.09	- 18.66	7.8°	9.0°	7/21
YF	tilt-corrected	139.3°	- 8.4°	- 25.02	- 18.67	7.8°	9.0°	7/21
CK	in situ	211.2°	-40.7°	- 27.43	- 9.41	4.8°	8.4°	17/22
CK	tilt-corrected	191.6°	- 4.0°	- 24.33	- 8.62	5.2°	8.9°	17/22
LO	in situ	204.0°	-28.1°	- 47.25	- 14.40	4.3°	7.9°	12/20
LO	tilt-corrected	196.2°	- 6.8°	- 47.28	- 14.41	4.3°	7.9°	12/20
IR	in situ	208.7°	-18.4°	-135.27	- 28.50	2.9°	6.3°	9/13
IR	tilt-corrected	204.4°	3.3°	- 77.19	- 38.07	3.8°	5.4°	9/13

TABLE 2. Inclination-Only Fold Test

Without Structural Correction		With Structural Correction		
Mean Inclination	k_1, Estimate of the Parameter k	Mean Inclination	k_2, Estimate of the Parameter k	k_2/k_1
		For the Intermediate Component		
56.9°	48.76	42.0°	16.91	0.347
		For the Characteristic Component		
- 19.8°	23.35	- 7.7°	116.81	5.00

TABLE 3a. Amount of Relative Rotation of the Characteristic Component (Tilt-Corrected)

Site	Distance From the Axis of the Las Vegas Valley	D, Declination of the Characteristic Component	Uncertainty ΔD	Rotation Relative to 139°	Local Attitude of Bedding	Structural Trend
NM	39.9 km	146.3°	3.3°	7.3°	N 26 E 10 W	N 05 E
CM	35.9 km	138.5°	4.4°	-0.5°	N 21 E 7 W	N 05 E
UP	24.4 km	132.6°	1.5°	-6.4°	N 26 W 5 W	N 10 E
LP	20.7 km	156.4°	5.8°	17.4°	N 66 E 9 N	N 25 E
YF	18.8 km	139.3°	7.9°	0.3°	N 46 E 9 S	N 25 E
CK	14.5 km	191.6°	6.4°	52.6°	N 60 E 56 N	N 60 E
LO	12.8 km	196.2°	4.3°	57.2°	N 61 E 32 N	N 70 E
IR	10.6 km	204.4°	4.3°	65.4°	N 61 E 32 N	N 50 E

TABLE 3b. Amount of Relative Rotation of the Intermediate Component (in Situ)

Site	Distance From the Axis of the Las Vegas Valley	D, Declination of the Intermediate Component	Uncertainty ΔD	Rotation Relative to 326°	Local Attitude of Bedding	Structural Trend
NM	39.9 km	327.7°	5.5°	1.7°	N 26 E 10 W	N 05 E
CM	35.9 km	325.5°	6.3°	-0.5°	N 21 E 7 W	N 05 E
UP	24.4 km	326.0°	2.1°	0	N 26 W 5 W	N 10 E
LP	20.7 km	349.0°	8.3°	23.0°	N 66 E 9 N	N 25 E
YF	18.8 km	354.4°	2.7°	28.4°	N 46 E 9 S	N 25 E
CK	14.5 km	13.6°	15.3°	47.6°	N 60 E 56 N	N 60 E
LO	12.8 km	16.8°	4.3°	50.8°	N 61 E 32 N	N 70 E
IR	10.6 km	15.4°	41.1°	49.4°	N 61 E 32 N	N 50 E

FIGURE CAPTIONS

Fig. 1. Index map of southern Nevada. Mountain ranges shown are: ACR, Arrow Canyon Range; DR, Desert Range; FM, Frenchman Mountain; LVR, Las Vegas Range; MM, Muddy Mountains; MoM, Mormon Mountains; PR, Pintwater Range; SM, Spring Mountains; ShR, Sheep Range; SdR, Spotted Range; and SpR, Specter Range. Faults indicated are the Wheeler Pass Thrust (WPT), Gass Peak Thrust (GPT), Las Vegas Valley Shear Zone (LVVSZ), and the Lake Mead Shear Zone (LMSZ). Solid circle marks sample site at Indian Ridge (IR). Stars mark sample sites U and V of Gillett and Van Alstine [1982].

Fig. 2. Equal area plots of the magnetization directions for samples from site LP, before and after demagnetization to 425°C. Open circles plot on the upper hemisphere, x plot on the lower hemisphere. Samples 15-17 have been remagnetized by lightning strikes. Only data from the 12 samples plotting in the south eastern quadrant after demagnetization were used to determine the mean direction of the characteristic component.

Fig. 3. Thermal demagnetization path for a representative sample from site LP on both an equal area plot and a modified Zijderveld plot using in situ coordinates. On the equal area plot the solid squares lie on the lower hemisphere, and the open squares lie on the upper hemisphere. On the modified Zijderveld plot the solid symbols represent successive positions of the end point of the magnetization vector during stepwise thermal demagnetization projected onto the horizontal (north, east) plane. The open symbols represent a plot of the horizontal and vertical components of the magnetization direction at each demagnetization step.

Fig. 4. Summary diagram of the declination of both the intermediate and the characteristic magnetization direction for the seven (lettered) sites in the Las Vegas Range. The angle subtended by the darkened wedge indicates the 95% uncertainty in the declination of the characteristic component, the uncolored wedge subtends an angle equal to the 95% uncertainty in the declination of the intermediate component. The stippling indicates Paleozoic bedrock outcrop. The striped region indicates outcrop of Cambrian Bonanza King Formation. The Las Vegas Valley Shear Zone (LVVSZ), the Gass Peak Thrust (GPT), and the Mormon Pass Fault (MPF) are also shown. An eighth sample site at Indian Ridge lies south of the LVVSZ, 8 km west of the west edge of the map. Open circles indicate sample sites where a consistent magnetization direction could not be determined. Geology from Guth [1980], Ebanks [1965], and Longwell et al. [1965].

Fig. 5. (a) Equal angle plot showing the predicted magnetic field direction for the Las Vegas Range since the late Paleozoic derived from the mean APW path for North America of Irving and Irving [1982]. Stippled band represents the 3°-4° uncertainty in the APW path. Geologic period abbreviations: P, Pennsylvanian; P, Permian; Tr, Triassic; J, Jurassic; K, Cretaceous; and T, Tertiary. Also plotted are 95% Bingham error ellipses for the components of magnetization measured at the eight sample sites in present-day coordinates. Means plot as dots on the lower hemisphere, open circles on the upper hemisphere. Stars mark the mean tilt-corrected directions for the three northernmost, unrotated sites. (b) Equal angle plot showing the 95% Bingham error ellipses for the intermediate and characteristic magnetization directions after removing

the vertical axis rotation due to movement on the LVVSZ. Note the clustering of the intermediate directions around the mean direction for the three northernmost sites (star). This mean direction corresponds to the middle Cretaceous magnetic field direction for the Las Vegas Range. (c) Equal angle plot showing error ellipses for the intermediate and characteristic magnetization directions after correcting for both the vertical axis rotation due to the LVVSZ and tilting due to Sevier thrusting along the Gass Peak Thrust. The intermediate magnetization directions scatter, indicating that the intermediate magnetization post-dates tilting. The characteristic magnetization directions, however, cluster around the late Paleozoic magnetic field direction for the Las Vegas Range, indicating that it predates both the tilting and the vertical axis rotation.

Fig. 6. Possible mechanisms of deformation in a shear zone. (a) An undeformed region prior to development of a shear zone. The stippled zone represents a marker which defines the structural trend of the region. Arrows represent the direction of an ancient magnetization direction. Dashed line shows the unrotated magnetization direction. (b) Shearing along faults parallel to the main shear zone. There is no rotation and hence no change in the direction of the ancient magnetization direction. (c) Pervasive, continuous simple shear. The paleomagnetic samples themselves are deformed and the magnetization direction altered; how much depends upon the mechanism of deformation operating at the microscopic scale. This may be occurring at depth beneath the Las Vegas Range. (d) The large block model of Ron et al. [1984]. Displacement across a shear zone is accommodated by the two bounding strike-slip faults and blocks rotating between them. The amount of rotation inferred from paleomagnetic data is the same everywhere in the shear zone.

(e) The small block model. The brittle upper crust is broken into small blocks which rotate independently in response to the continuous, ductile deformation at greater depth. The blocks rotate with an angular velocity equal to half the vorticity of the deforming continuum beneath them. The rigid blocks shown are separated by faults and smaller rigid blocks. Note that the amount of block rotation will be greater than the change in general structural trend. In particular, some blocks may rotate more than 90°, while the change in general structural trend will only approach 90°.

Fig. 7. Summary of the thin viscous plate model of England et al. [1985]. A strike-slip fault follows the x axis. Positive values of velocity component u correspond to left-lateral slip on the fault. The velocity boundary condition shown is imposed upon the fault. Reflecting boundary conditions are imposed on $x = 0$ and $x = \lambda/2$.

Fig. 8. (a) Plot of the rotation of the characteristic magnetization direction versus distance from the LVVSZ. The uncertainty in amount of rotation equals half the range in declination of the 95% Bingham error ellipse. The 2-km uncertainty in distance from the shear zone is due to the alluvium of the Las Vegas Valley, which conceals the shear zone. The curves show the amount of rotation predicted by the viscous plate model of England et al. [1985] for $n = 1$ (i.e., a Newtonian rheology) and $\lambda = 220$ km with three values of U_0t ($\approx D$, the maximum displacement on the fault). (b) Same as Fig. 8a with $n = 3$. (c) Same as Fig. 8a with $n = 10$. (d) Plot of the rotation of the intermediate magnetization direction versus distance from the LVVSZ. The curves show the predicted rotations for a viscous plate model for $n = 3$ and $U_0t = 35$ km with three values of λ (= twice the fault length).

Fig. 9. (a) Plot of the inferred rotation of the structural trend as defined by the Gass Peak Thrust and associated folds versus distance from the LVVSZ. The curves show the change in orientation of a marker originally perpendicular to the LVVSZ predicted by a viscous plate model with n = 3 and λ = 220 km with three values of U_0t. (b) Same as Fig. 9a with n = 10.

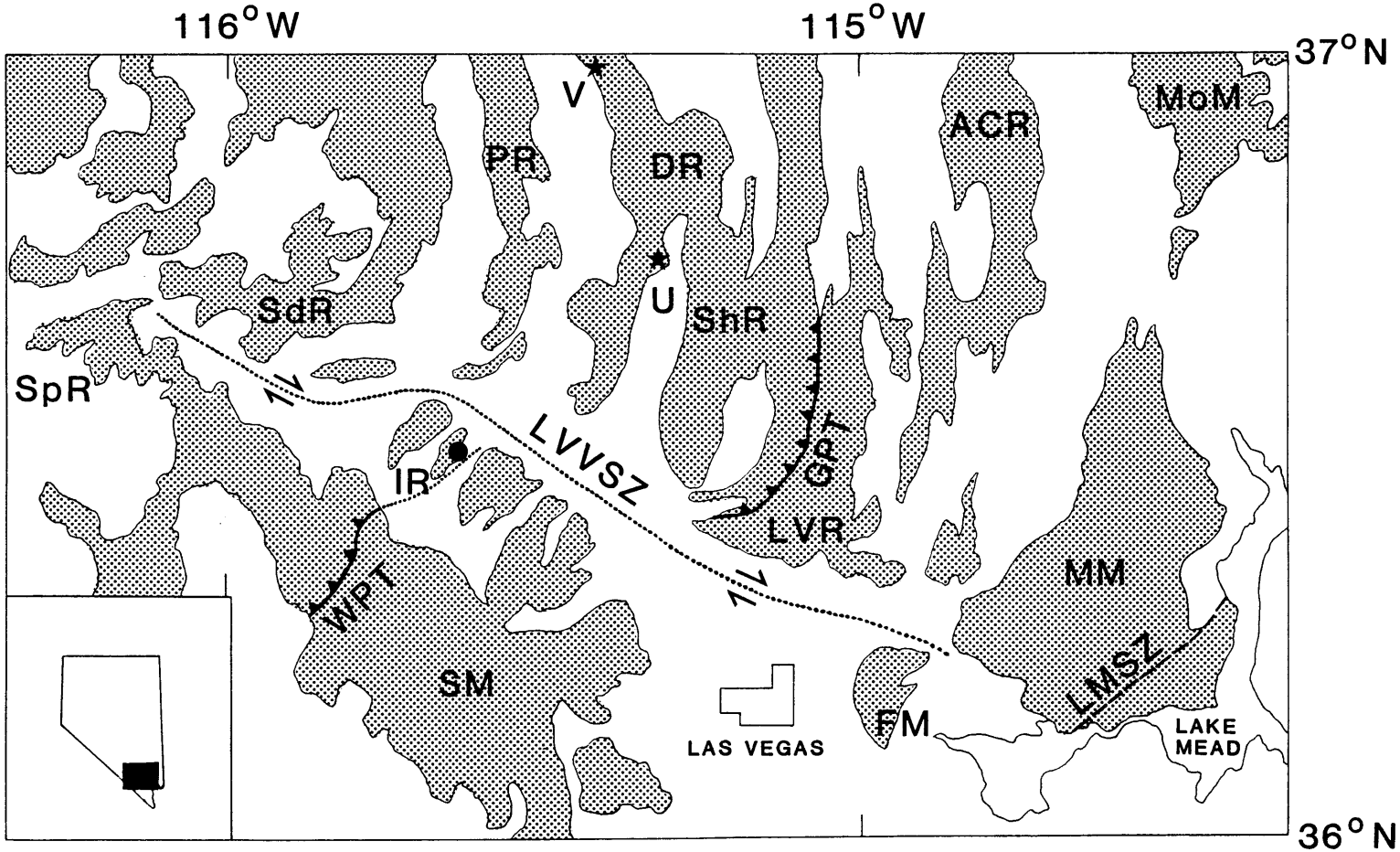
116°W
115°W
37°N
36°N
V
U
PR
DR
ACR
MoM
SdR
ShR
SpR
LVVSZ
GPT
IR
LVR
WPT
MM
SM
LMSZ
FM
LAS VEGAS
LAKE
MEAD

Figure 1

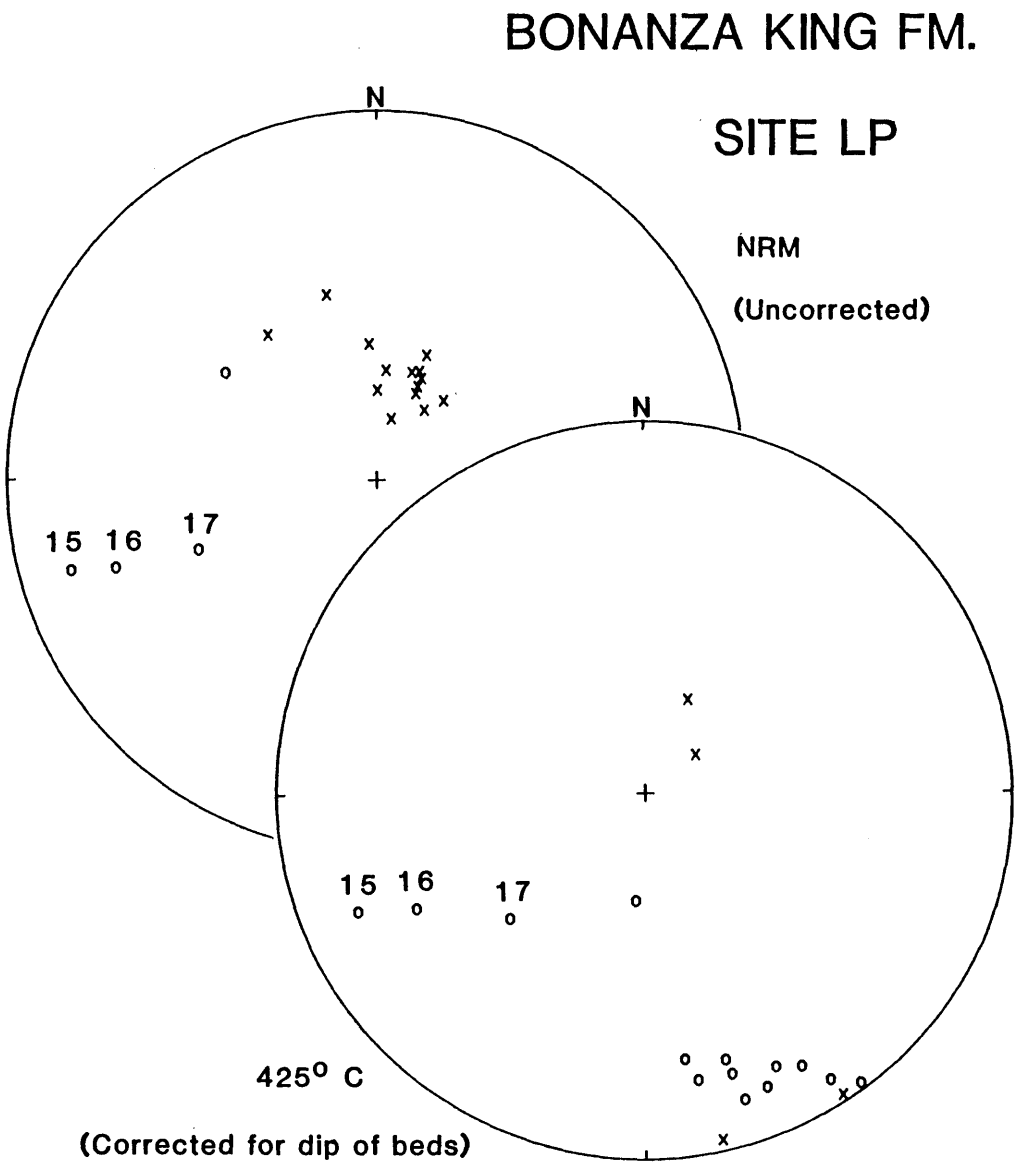
BONANZA KING FM.
SITE LP
NRM
(Uncorrected)
N
15 16 17
N
15 16 17
425° C
(Corrected for dip of beds)

Figure 2

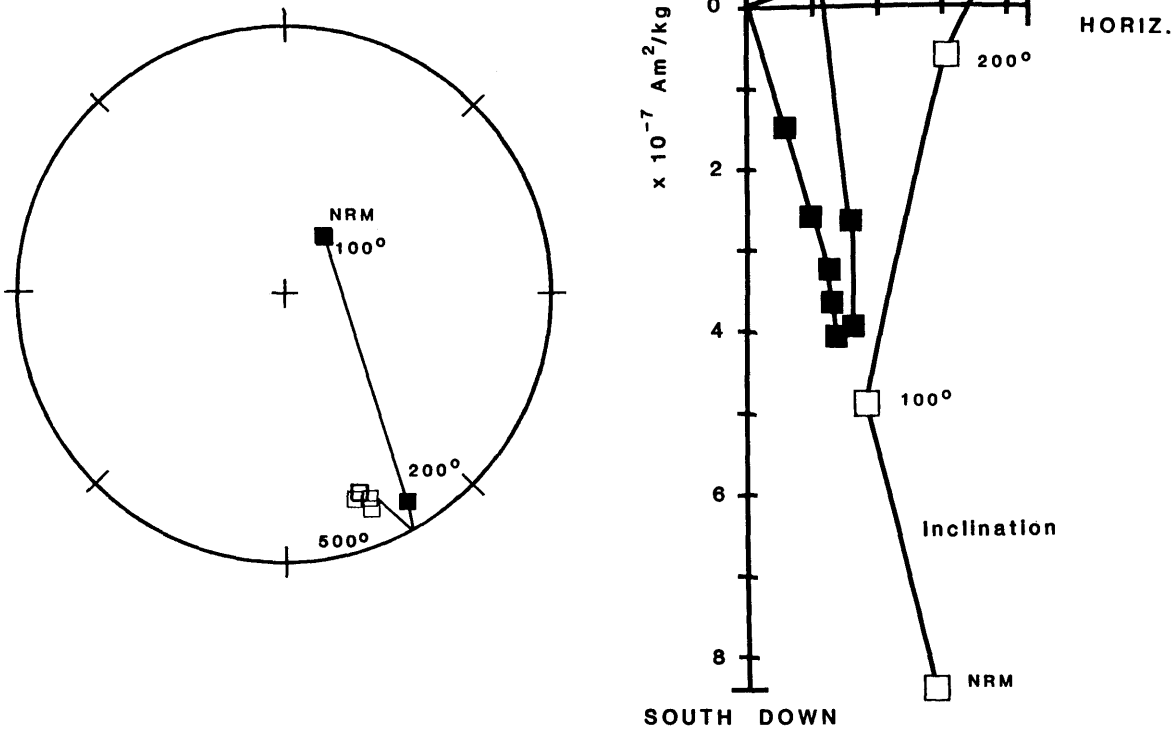
NRM
100°
200°
500°
NORTH UP
Declination
400°
425°
350°
450°
300°
500°
EAST
HORIZ.
200°
x 10⁻⁷ Am²/kg
2
0
2
4
6
8
100°
Inclination
NRM
SOUTH DOWN

Figure 3

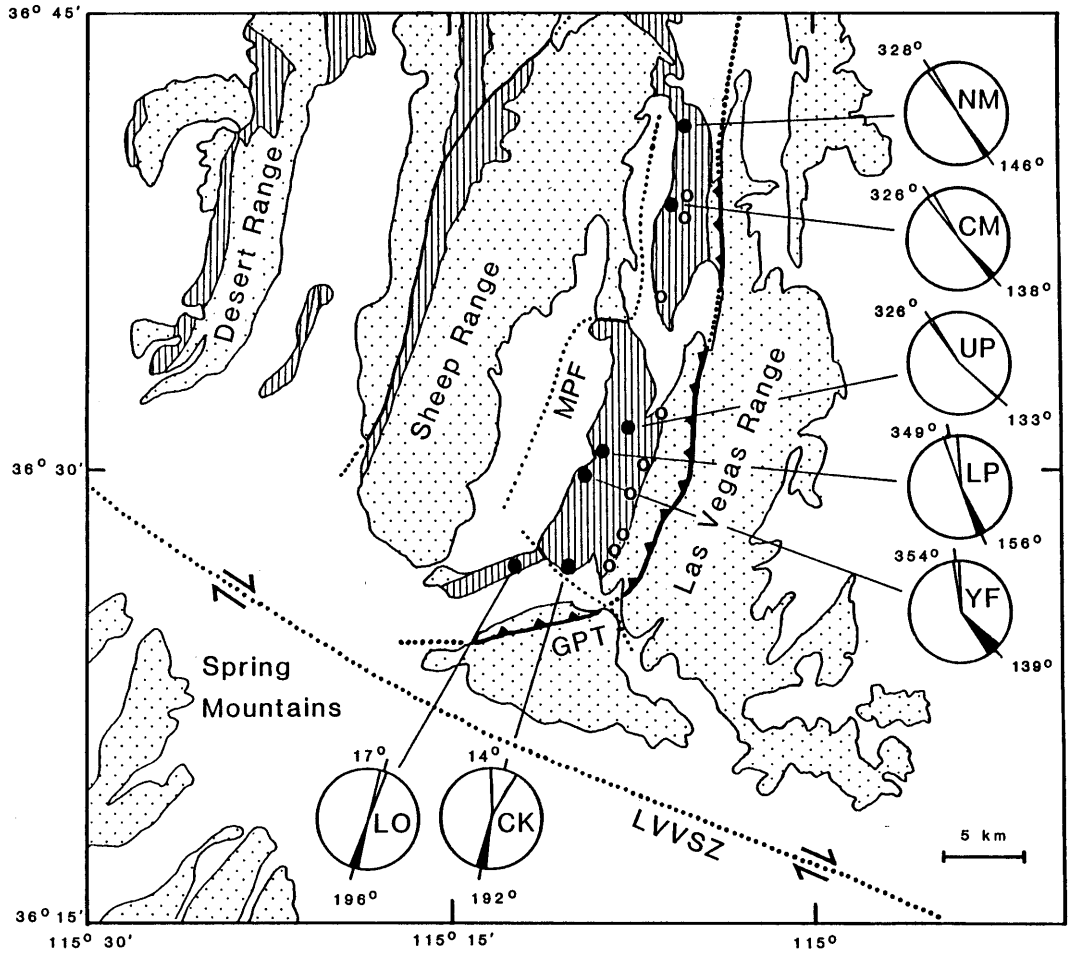
36° 45'
36° 30'
36° 15'
115° 30'
115° 15'
115°
Desert Range
Sheep Range
MPF
Las Vegas Range
GPT
LVVSZ
Spring
Mountains
NM
328°
146°
CM
326°
138°
UP
326°
133°
LP
349°
156°
YF
354°
139°
LO
17°
196°
CK
14°
192°
5 km

Figure 4

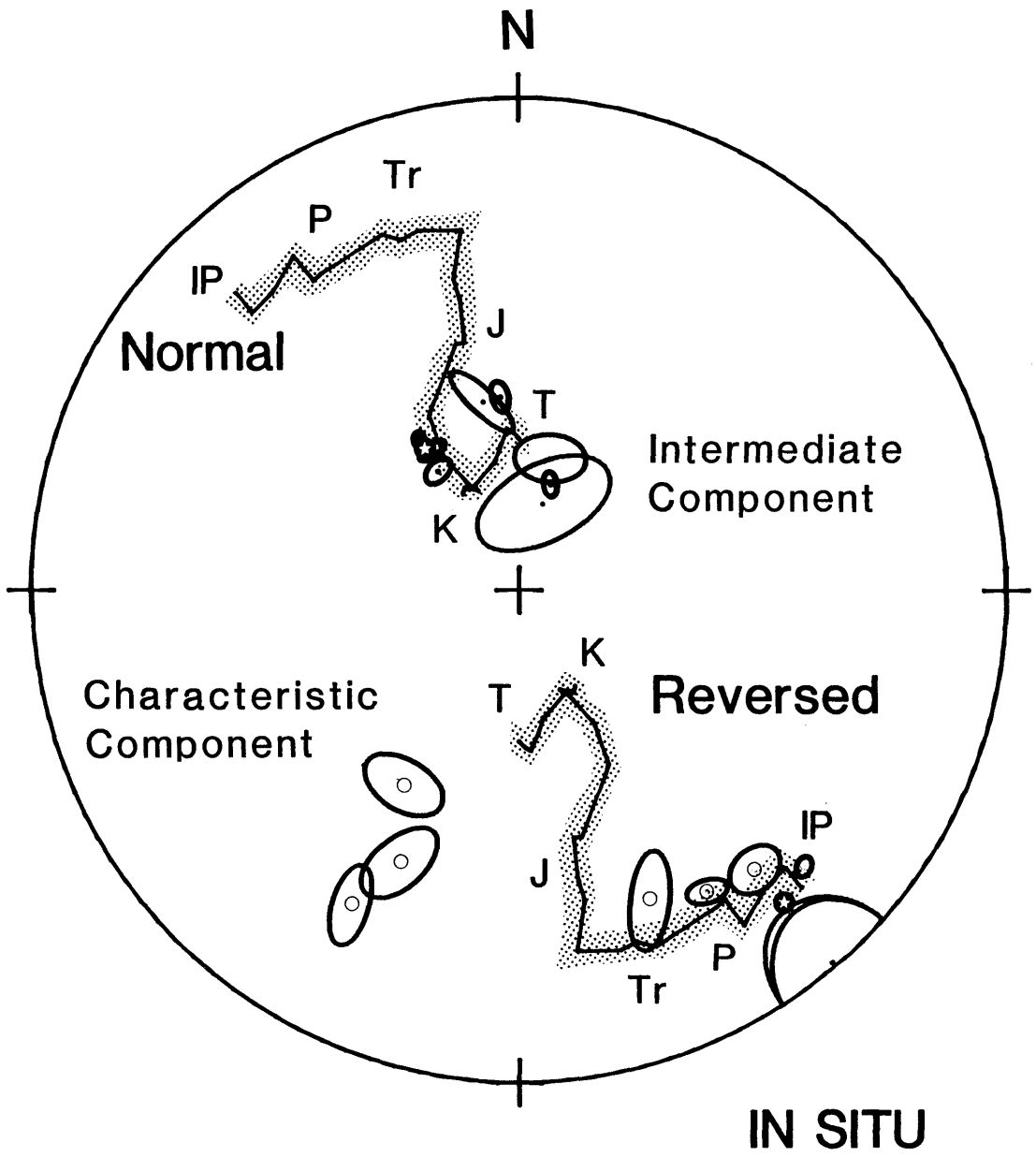
N
Tr
P
IP
Normal
J
T
Intermediate
Component
K
Characteristic
Component
K
T
Reversed
IP
J
P
Tr
IN SITU

Figure 5a

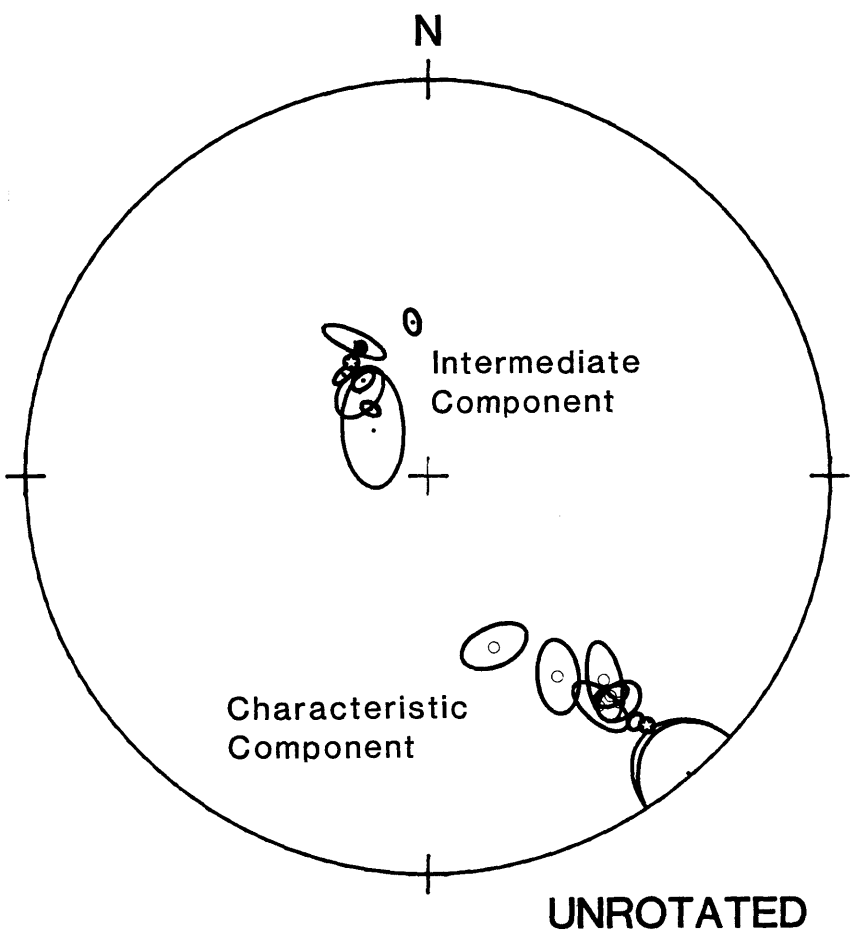

Figure 5b

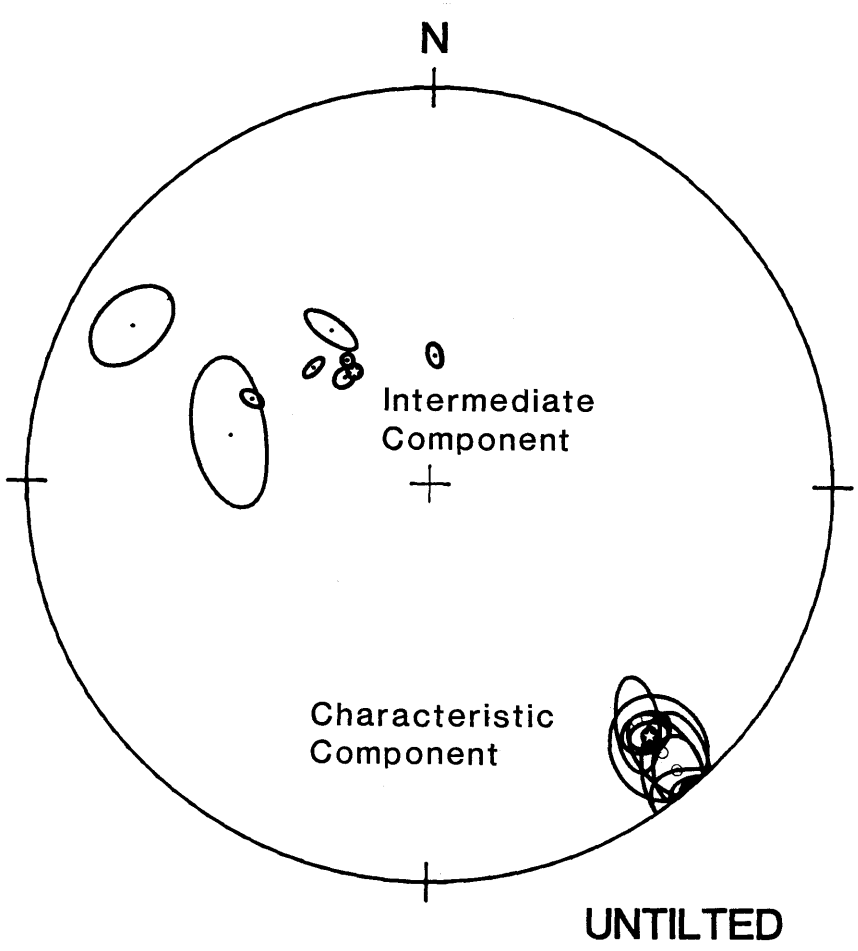

Figure 5c

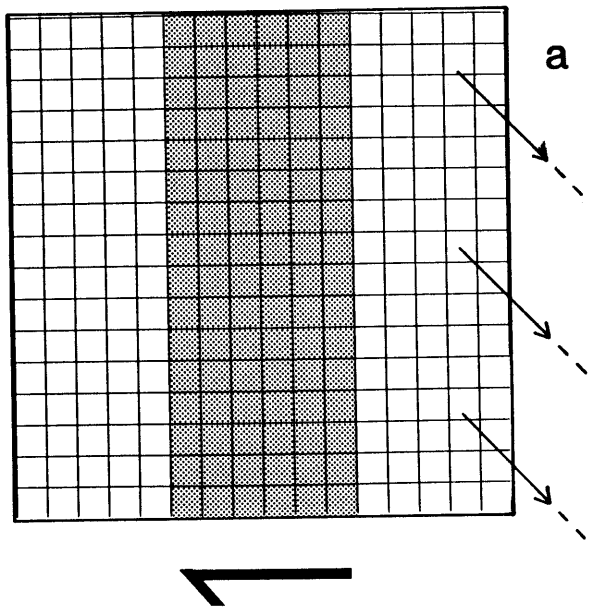

Figure 6a

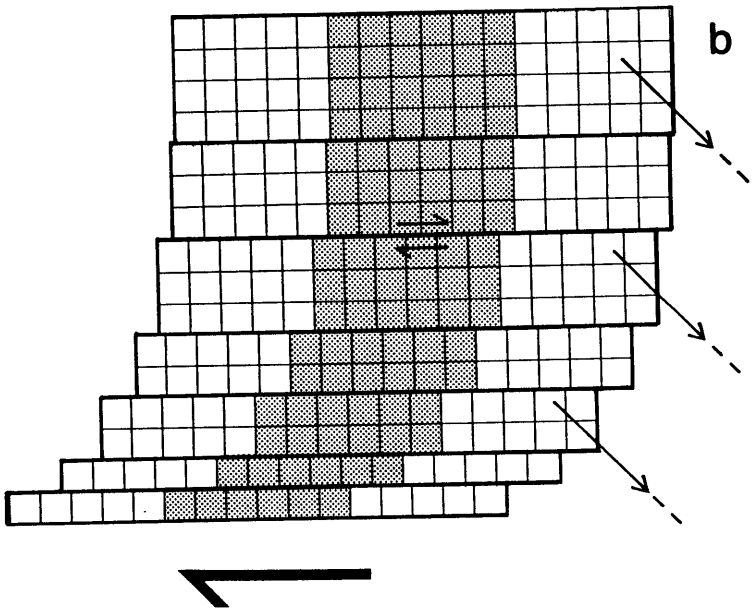

Figure 6b

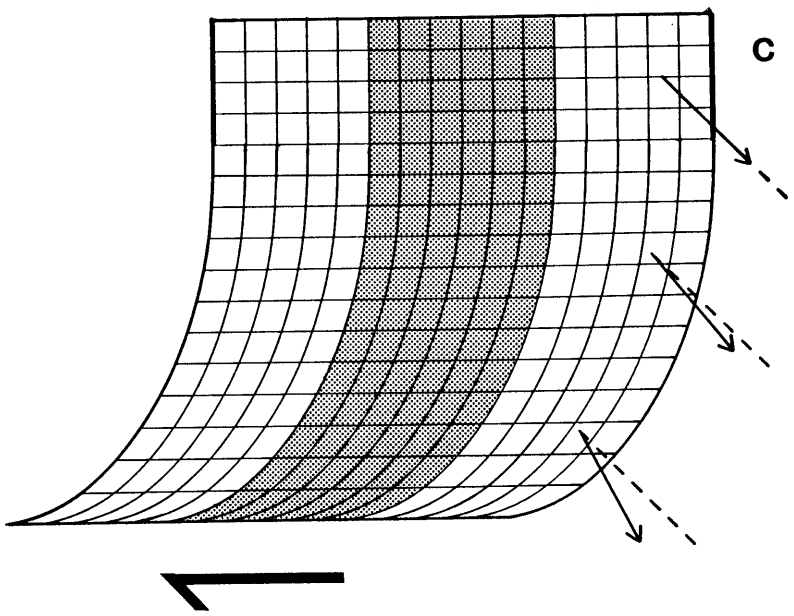

Figure 6c

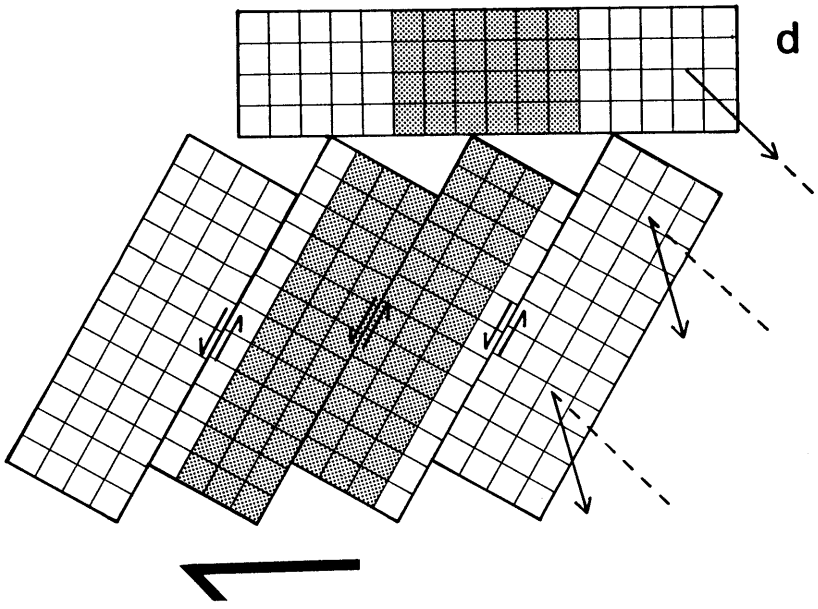

Figure 6d

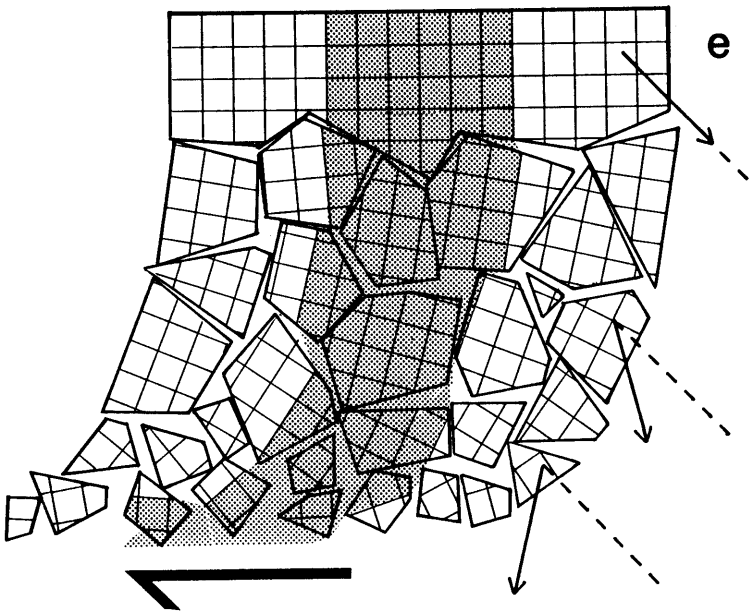

Figure 6e

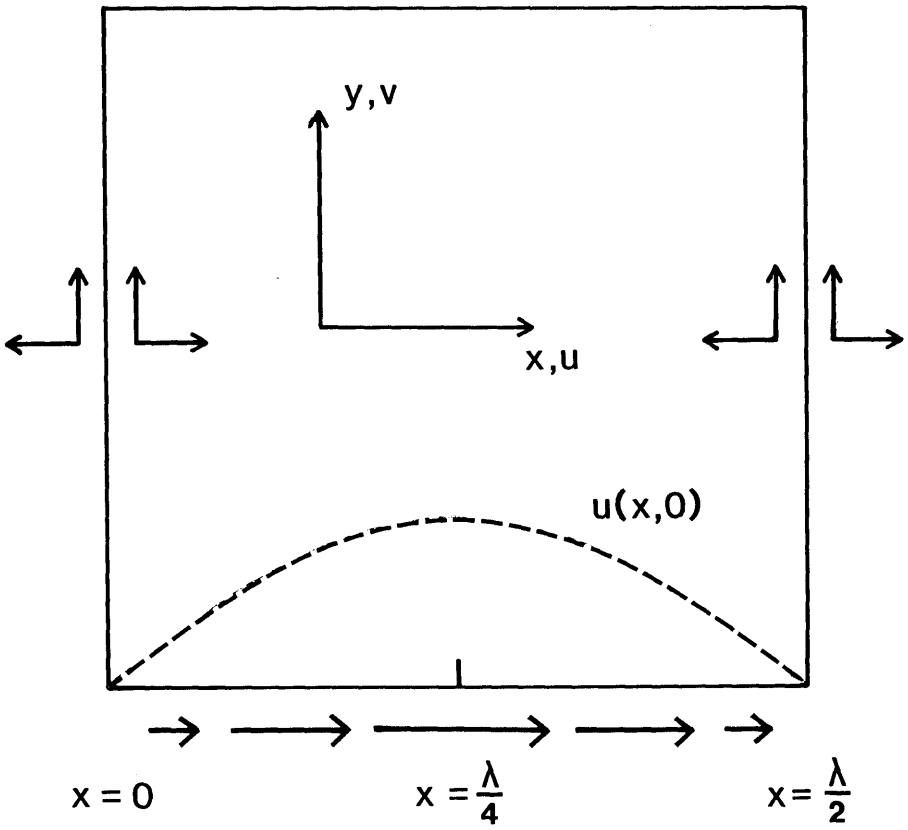

$$u(x,0) = U_0 \sin \frac{2\pi x}{\lambda}$$

$$v(x,0) = 0$$

Figure 7

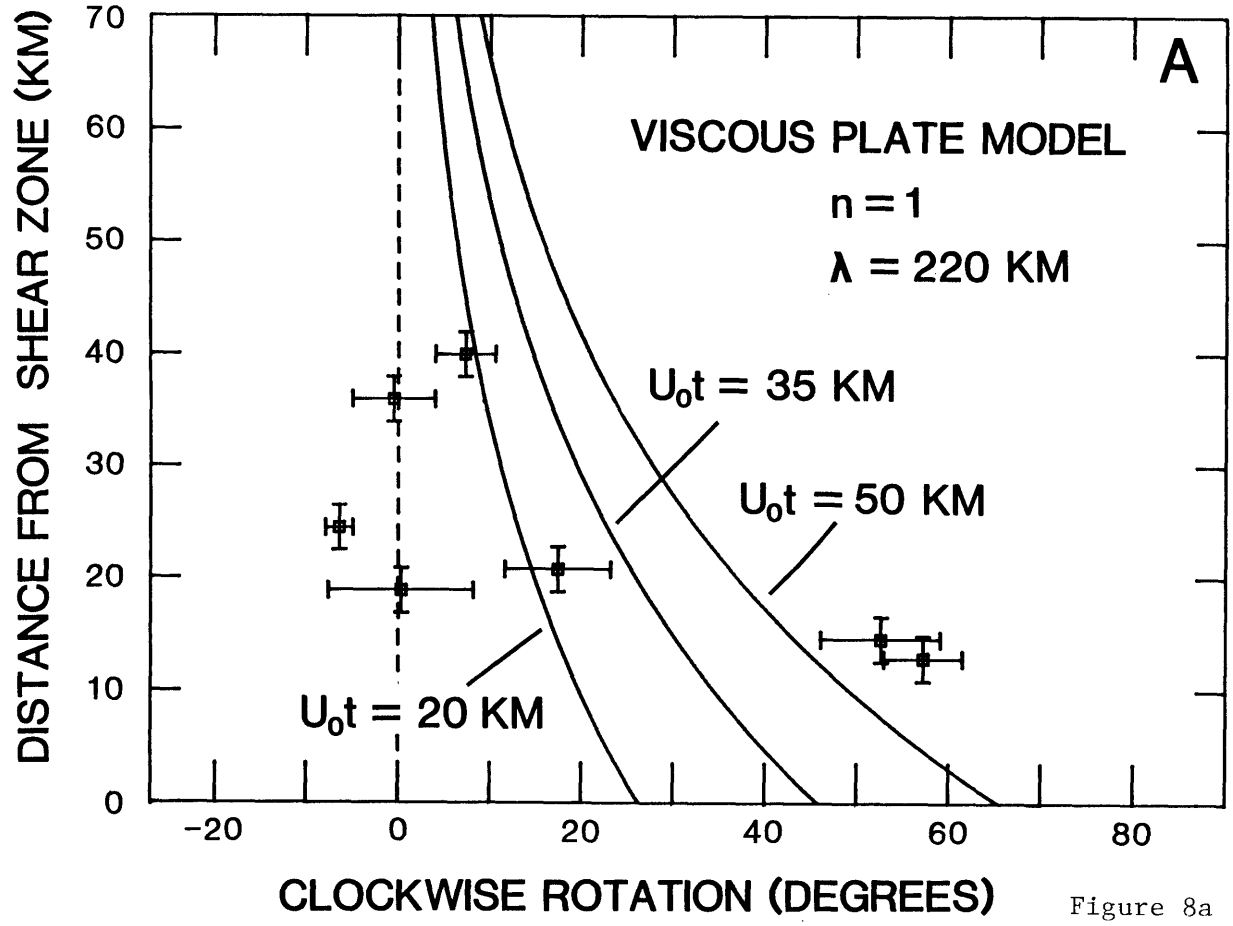

Figure 8a

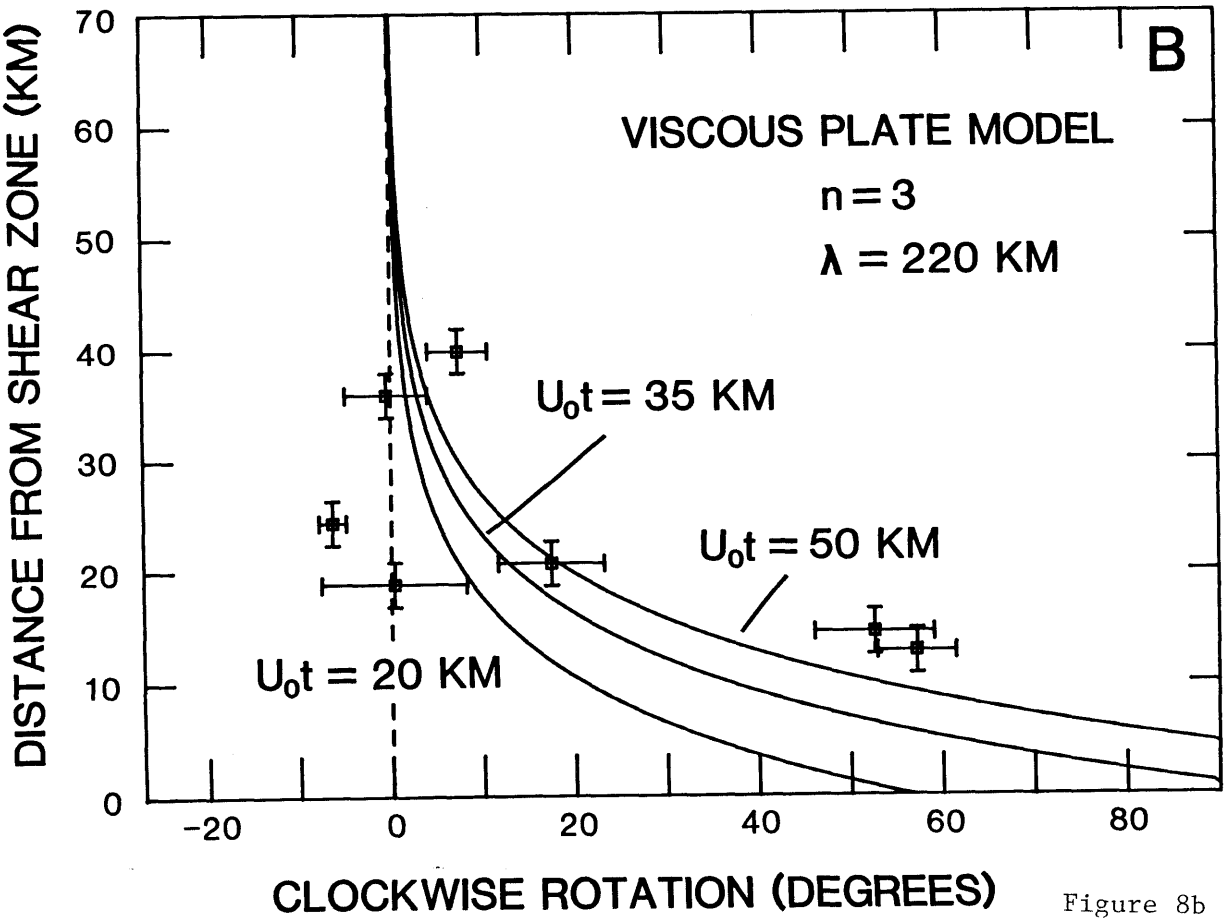

Figure 8b

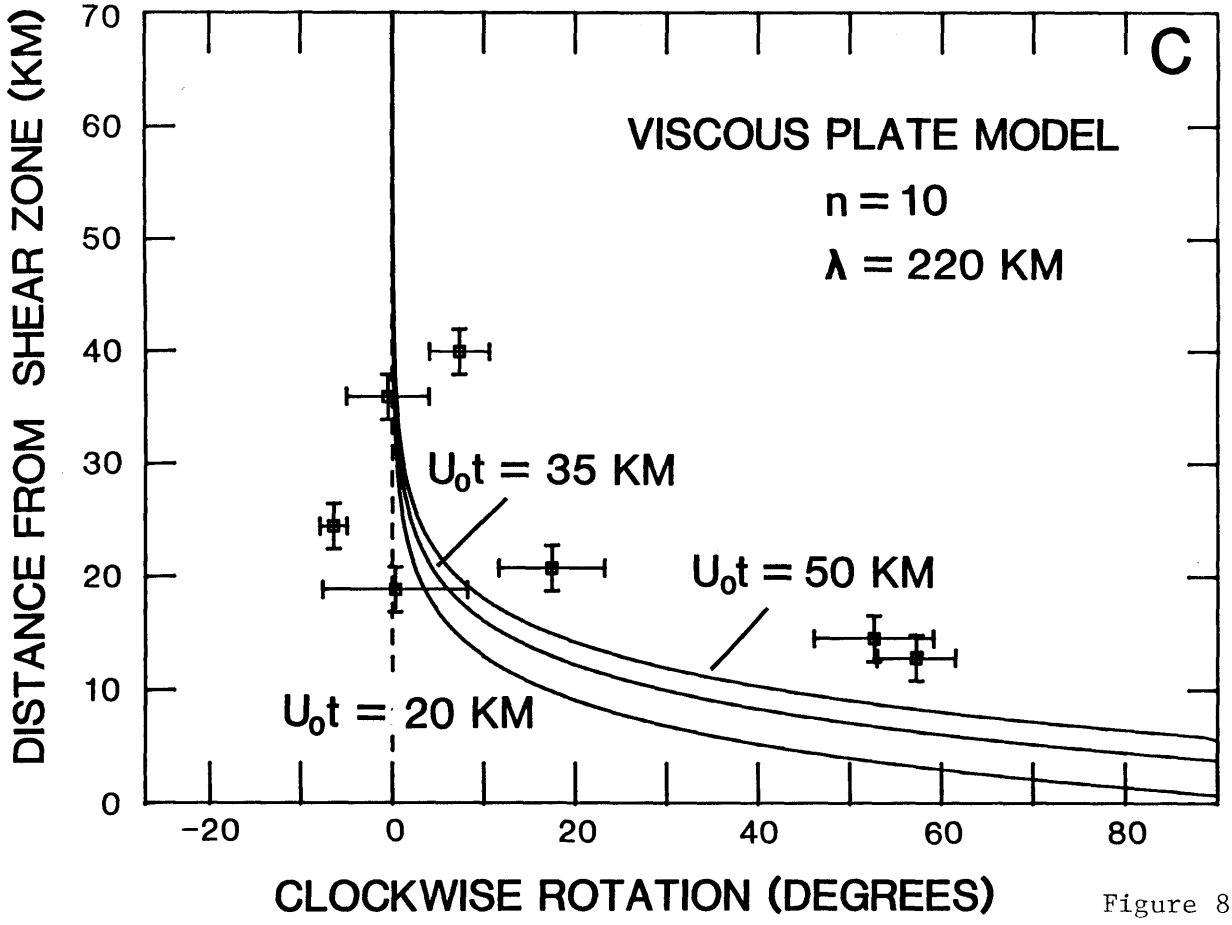

Figure 8c

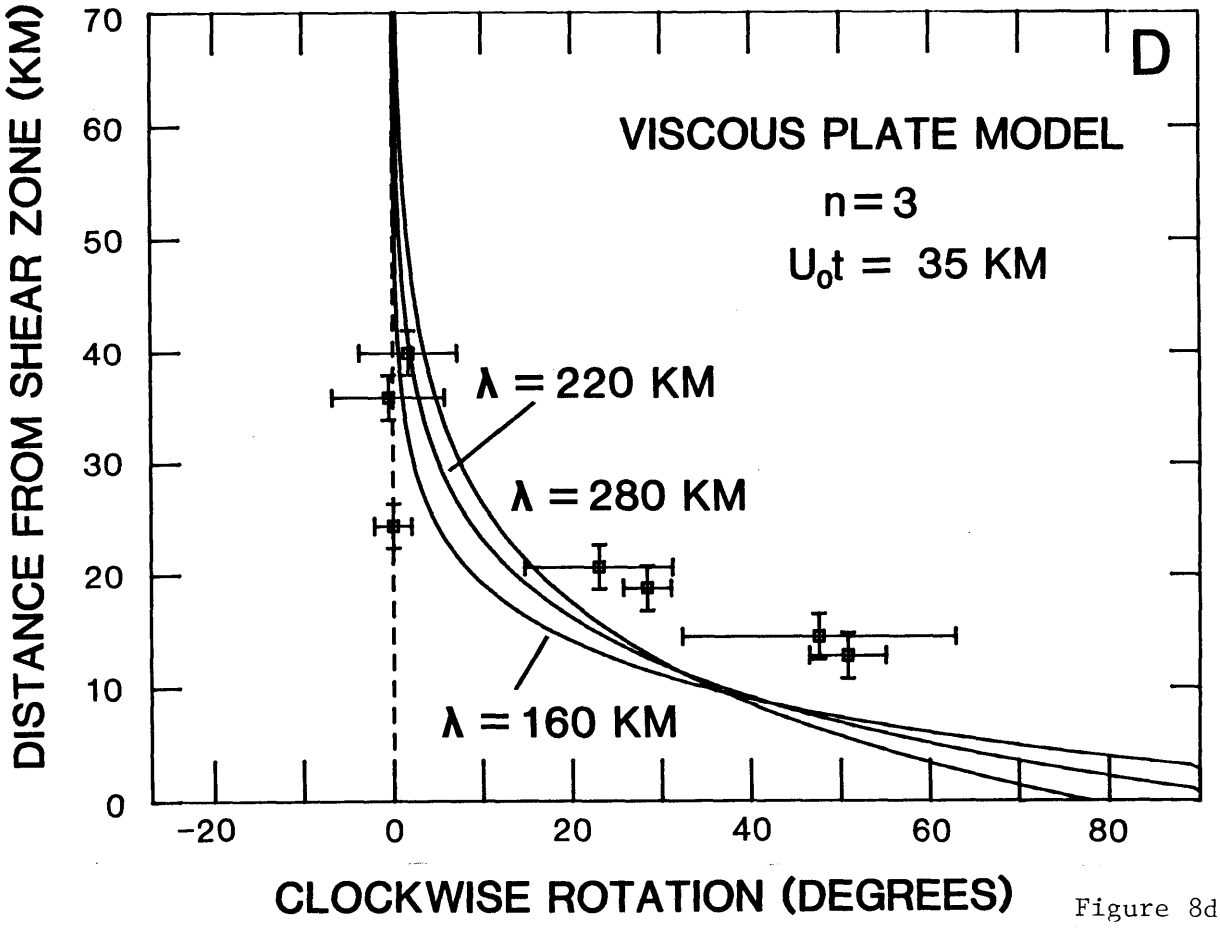

Figure 8d

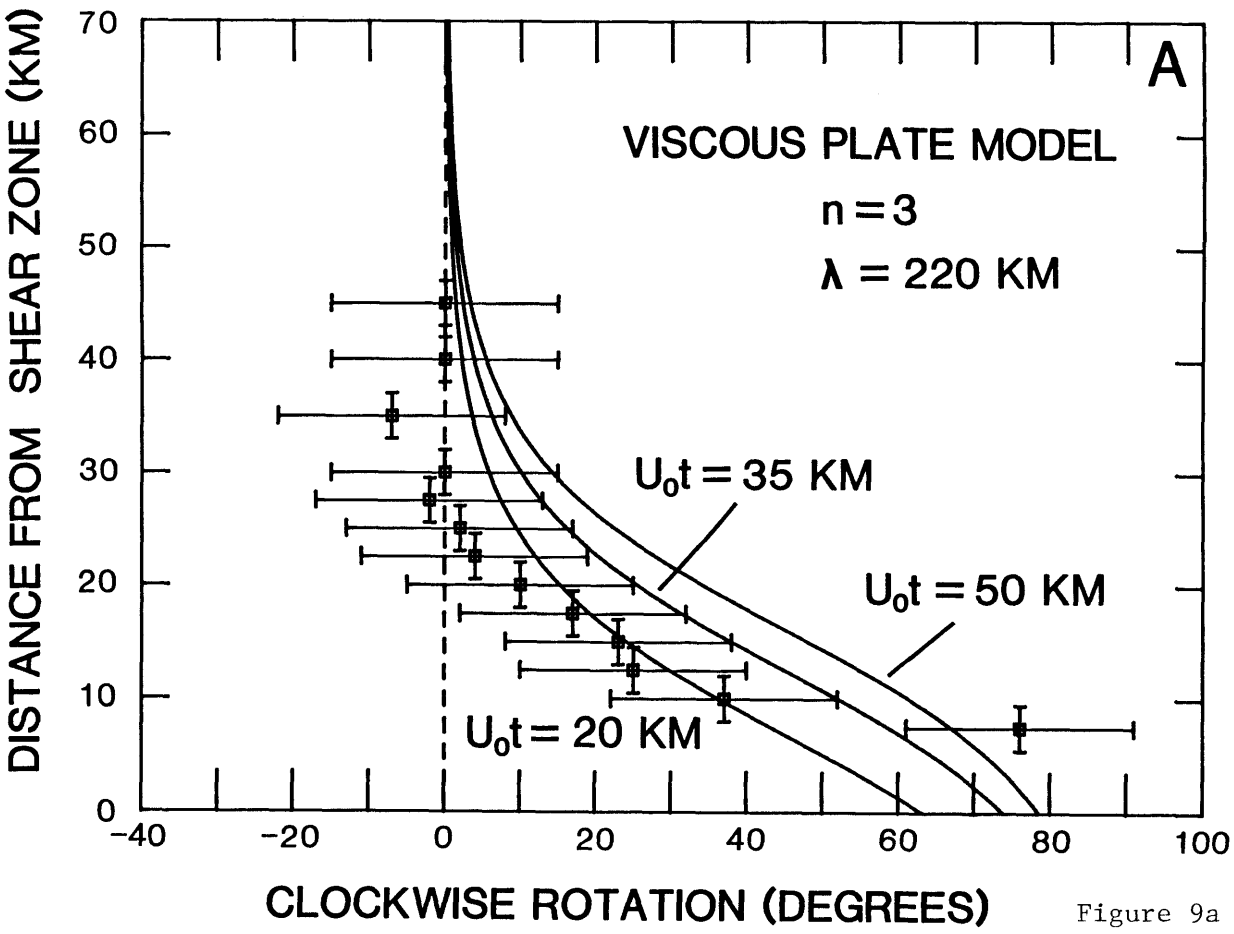

Figure 9a

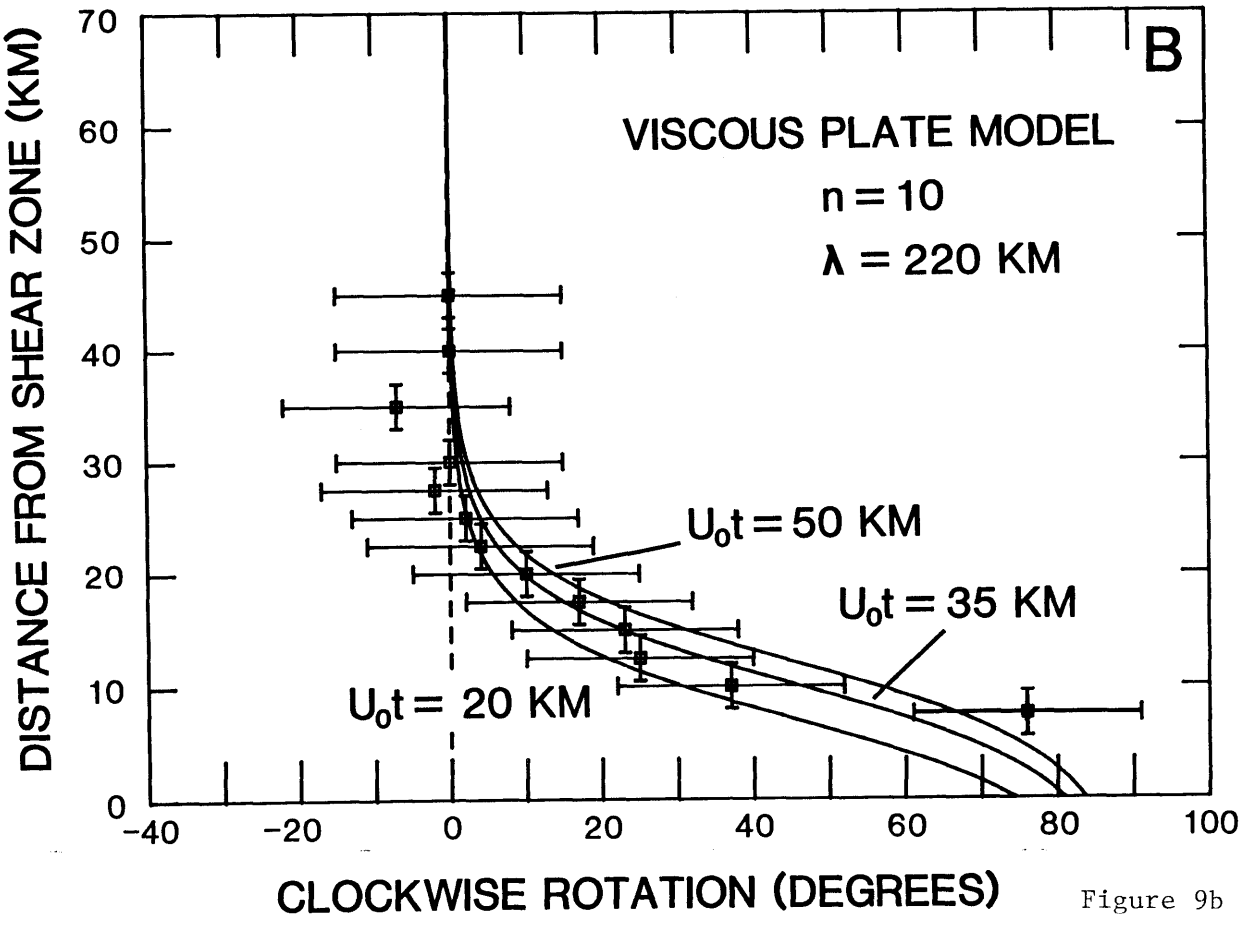

Figure 9b

CHAPTER 2

SOURCE PARAMETERS FOR 11 EARTHQUAKES IN THE TIEN SHAN, CENTRAL ASIA, DETERMINED BY P AND SH WAVEFORM INVERSION

Michael R. Nelson, Robert McCaffrey, and Peter Molnar
Department of Earth, Atmospheric, and Planetary Sciences,
Massachusetts Institute of Technology, Cambridge, MA

ABSTRACT

The Tien Shan mountain belt of central Asia was formed in late Paleozoic time and reactivated in Tertiary time following the collision of India with Eurasia, more than 1500 km to the south. To study the style and distribution of faulting occurring today in the Tien Shan, we digitized long-period World-Wide Standard Seismograph Network P and SH waveforms of 11 of the largest Tien Shan earthquakes between 1965 and 1982 and then used a least squares inversion routine to constrain their fault plane solutions and depths. Four of the earthquakes occurred near the southern edge of the Tien Shan, and two occurred in the intermontane Fergana Basin. These earthquakes occurred at depths of 10-20 km and are associated with thrust faulting on east-west to southwest-northeast striking fault planes that dip moderately (35°-55°). The other five earthquakes, in the northern Tien Shan, were mostly deeper (15-44 km), and the fault plane solutions of four of them are similar to the events farther south. The exception, an event on June 2, 1973, probably occurred on a gently northward dipping, east-west striking fault plane. All events occur within the basement at depths of 10 km or greater. Waveforms for

earthquakes near the edges of the Dzungarian, Fergana, and Kucha basins are fit best using velocity structures with thick sediment layers, implying that sediments from these basins have been and are being underthrust beneath the neighboring mountains. We examined only the relatively small (m_b = 5.5-6.2) events after 1965 and did not study any of the largest events (M_s > 8) that occurred in the Tien Shan earlier in this century. Still, we can conclude that north-south shortening is presently occurring in the Tien Shan, with the formation of basement uplifts flanked by moderately dipping thrust faults. The present-day tectonics of the Tien Shan seem to be analogous to those of the Rocky Mountains in Colorado, Wyoming, and Utah during the Laramide orogeny in Late Cretaceous and Early Tertiary time.

INTRODUCTION

The Tien Shan in northwestern China and Soviet central Asia is one of the world's most rapidly deforming intracontinental regions. The mountain belt stretches east-west more than 2000 km, and in places elevations exceed 7000 m with many ranges higher than 5000 m (Figure 1). The present belt overlaps part of a Paleozoic orogenic belt that was reactivated in Tertiary time following the collision of India with Eurasia more than 1500 km to the south. The region is seismically quite active, producing several earthquakes with M_s > 8 since 1900. Since 1965 there have been more than a dozen earthquakes with body wave magnitudes $\approx$ 6. Here we examine these later events in order to understand better how intracontinental deformation is occurring in the Tien Shan.

Crustal deformation in the interior of continents is generally more complex and diffuse than that occurring at plate margins. At mid-ocean ridges and in subduction zones, seismicity and active deformation are confined to rather narrow zones. In contrast, intracontinental

deformation like that in the Tien Shan, in the Atlas Mountains of north Africa, in the Basin and Range Province, or in Turkey is diffuse, and the related seismicity is much more complex. Typically, the level of seismicity and the style of deformation vary markedly over distances of tens of kilometers.

Most continental regions with significant seismic activity are near active or recently active plate boundaries (e.g., the Himalaya, California, or the East African Rift Zone). In contrast, seismicity in the Tien Shan occurs more than 1500 km north of the nearest recent plate boundary, the Indus-Tsangpo Suture Zone just north of the Himalaya. The Tertiary shortening in the Tien Shan has been entirely within what was the Eurasian plate before its collision with India; there are no known Tertiary ophiolites or pelagic sediments to indicate the subduction of oceanic crust near the Tien Shan in Tertiary time. The Tien Shan can be compared to other regions where intracontinental shortening has occurred in the past, like the Rocky Mountains.

TECTONIC SETTING

The Tien Shan consists mainly of Paleozoic sedimentary rocks folded and faulted during the Carboniferous and Permian periods [Burtman, 1975] when slip on gently dipping, east-west striking thrust faults accommodated north-south shortening. In addition, a number of northwest-southeast trending right-lateral faults (e.g., the Talasso-Fergana fault) apparently were active. Since the collision of India and Eurasia in Tertiary time many of these strike-slip faults have been reactivated [Burtman, 1980; Leith, 1986; Suvorov, 1963; Trifonov, 1978; Wallace, 1976], and north-south shortening is again being accommodated along east-west trending thrust faults, producing the east-west trending block uplifts seen today. Geologic mapping and Landsat imagery indicate that many of these uplifts

are flanked on both their north and south sides by thrust faults that dip beneath the mountains [Tapponnier and Molnar, 1979].

The actively deforming Tien Shan is flanked by the relatively aseismic Siberian Shield and Dzungarian Basin on the north and the stable Tarim Basin on the south (Figure 1). The low levels of seismicity, little relief, and low elevations (<1000 m) in the Tarim Basin were attributed by Molnar and Tapponnier [1981] to the presence beneath the Tarim Basin of cold, strong Precambrian shield that has been relatively unaffected by the deformation occurring both in the Tien Shan to the north and the Tibetan Plateau to the south.

Little geologic mapping or geophysical work from the Tien Shan has been published. In the early part of this century a number of expeditions in the Tien Shan made geologic traverses across parts of the region, collecting stratigraphic and paleontological data [Dmitriyev et al., 1935; Gröber, 1914; Norin, 1937, 1941]. Because of the inaccessibility of the region, much of the more recent work done on the Tien Shan has relied upon Landsat imagery and seismograms recorded at stations of the World-Wide Standard Seismograph Network (WWSSN) [Molnar et al., 1973; Ni, 1978; Tapponnier and Molnar, 1979; Vilkas, 1982]. First-motion fault plane solutions using WWSSN seismograms indicate that thrust faulting predominates in the Tien Shan but the strikes of the nodal planes are poorly constrained. Vilkas [1982] analyzed long-period teleseismic P waveforms for six earthquakes in the Tien Shan and found that all six events are characterized by thrust or oblique thrust faulting. Unfortunately, the P waveforms alone do not tightly constrain the strike of the nodal planes. Vilkas also confirmed that in the Tien Shan, faulting occurs down to depths of 45 km or greater [Chen and Molnar, 1977]. In the western Tien Shan, Soviet workers have operated about 20

regionally distributed seismic stations that provide data that have been used to locate earthquakes, to determine their first-motion fault plane solutions, and to make preliminary seismic velocity models for the region [Vinnik and Saipbekova, 1984; Wesson et al., 1975]. Unfortunately, most of the data from these stations are unavailable to us.

METHODOLOGY

In order to learn more about the tectonics of the Tien Shan we matched synthetic seismograms to WWSSN long-period P and SH waveforms to constrain both the depths and the fault plane solutions of all 11 earthquakes in the Tien Shan that were well-recorded by the WWSSN between 1965 and 1983. Three other earthquakes with $m_b \approx 6$ (0952, March 23, 1971; July 26, 1971; and March 24, 1978) could not be studied because they occurred shortly after larger earthquakes elsewhere. The remaining earthquakes in the Tien Shan were too small to be analyzed using this technique. We estimated the strike and dip of the nodal planes and the rake for these 11 earthquakes with uncertainties of 5°-15° (see the appendix). In contrast, published first-motion fault plane solutions for the same earthquakes in the Tien Shan often disagree by as much as 45° in strike and rake angles because of the lack of data from local stations (compare Ni [1978] and Tapponnier and Molnar [1979]). Waveforms allow the centroid depths to be determined with uncertainties of only 3-7 km. Our results show that for these earthquakes the depths determined by the International Seismological Centre (ISC), using reported P wave arrival times and pP-P times, are often inaccurate by more than 30 km.

We digitized WWSSN long-period P and SH waveforms recorded at epicentral distances of 30°-86° for P waves and 30°-72° for SH waves. For these distance ranges the effects of upper mantle triplications and core phases are avoided; the long-period waveforms are most strongly influenced

by the source mechanism and depth of the earthquake and the source and receiver velocity structures [Langston and Helmberger, 1975]. An inversion routine similar to that of Nabelek [1984, 1985] was used to determine the best fitting double-couple fault plane solution, far-field source time function, and centroid depth. The fault plane solution is specified by the strike and dip of one of the two nodal planes and the rake on that plane, following the convention Aki and Richards [1980, Figure 4.13]. We estimate typical uncertainties to be dip, ±5°; strike, ±10°; rake, ±15°; and centroid depth, 3 km plus 10% of the depth. In the appendix we discuss the assumptions made in modeling the seismograms and the uncertainties that result from those assumptions. In addition, we present waveforms for a range of source parameters for one deep (depth ≈ 40 km) and one shallow (depth ≈ 12 km) representative earthquake, so that readers can judge for themselves the uncertainties in the solutions.

SEISMIC VELOCITY STRUCTURE IN THE SOURCE REGION

The seismic velocity structure of the Tien Shan is poorly constrained due to the lack of appropriate seismic refraction studies. For each earthquake the inversion routine was first run using a crustal half-space in the source region (v_p = 6.0-6.2 km/s, $v_s = v_p/\sqrt{3}$, density = 27002800 kg/m^3 with the larger values of v_p and density used for the deeper earthquakes). For four of the earthquakes (A, F, I, and K) there were clear phases on the observed seismograms which could not be explained using a half-space. To explain these phases and to study the dependence of the synthetic seismograms on the source velocity structure, we calculated seismograms for a variety of such structures. It is not possible to determine uniquely the source velocity structure using long-period seismograms. However, it is possible to recognize and discard inappropriate source velocity structures and thus decrease the mismatch

between the synthetic and observed seismograms due to an unrealistic velocity structure. This in turn decreases the uncertainty in the inferred focal parameters.

For earthquake K shown in Figure 2 the amplitude and timing of the direct P and reflected phases could be matched using a crustal half-space, but an additional reflected phase is seen consistently before the pP phase. This phase is clearest at the European stations (AQU, NUR, and KBS) shown in Figure 2 where it causes a sharp dip after the small, nearly nodal direct P arrival (the upward phase starting at the tick mark). At NUR this phase and the pP phase that follows it form a W-shaped trough. We interpret this first negative polarity phase as a reflection from a boundary below the free surface. By adding a 4.5-km-thick layer (v_p = 3.0 km/s, v_s = 1.73 km/s, density = 2400 kg/m^3) the additional phase is matched well as a reflection from the base of this layer. Note that this chang in velocity structure changed the inferred strike, dip, and rake of the fault plane solution by less than 1°, while the inferred depth decreased from 20.7 to 19.6 km.

The presence of sediments also affects the amplitude of the reflected phases. The Ürümqi earthquake of November 13, 1965 (event A), is deep enough that the reflected phases are clearly separated from the direct phases on the seismograms (Figures 3 and 6). For a crustal half-space (v_p = 6.2 km/s) the timing of the reflected phases is matched well, but their amplitudes relative to the direct P are not. As shown in the first row of seismograms in Figure 3, the mismatch is particularly large for sP, the sharp downward pulse that starts about 20 s after the direct P arrival. A 12-km-thick lower-velocity (v_p = 4.2 km/s) sedimentary layer over the half-space decreases the amplitude of the reflected phases and decreases the variance by about 10%.

Besides finding evidence for the presence of a thick section of sediments above the hypocenter, we can also test the possibility that this earthquake is in the mantle, by placing it in a half-space with v_p = 8.0 km/s, density = 3300 kg/m^3, beneath the sedimentary layer and a 30-km-thick crustal layer. The resulting increase in takeoff angles causes several of the stations (e.g., SNG, KOD, NUR, KEV) to fall closer to the nodal planes (Figure 3). At those stations the amplitude of the direct P phase for the best fit solution is too small. The increased misfit between seismograms caused by putting the source in the mantle suggests that the centroid is in the lower crust.

The P wave first motion recorded at SHL (Δ = 18.6°) is dilatational and apparently contradicts the evidence just presented (Figure 3). Specifically, SHL falls in the dilatational quadrant if a mantle source is assumed but in the compressional quadrant if a crustal source is assumed. However, in this distance range the actual takeoff angle of the first-arriving ray has a large uncertainty (5°-10°) because its turning point is in the uppermost mantle where the velocity structure is poorly known. Because of this uncertainty, we think that the waveforms provide more convincing evidence and conclude that the source was in the lower crust. As shown in Figure 3, the change in the assumed velocity structure does not significantly affect the best fit double-couple orientation. However, when a mantle source is assumed, the depth increases by 0.5 km and the seismic moment increases by 60%.

A systematic mismatch between some observed waveforms and their corresponding synthetic seismograms generated using a plane-layered source structure indicates that the source velocity structure varies with azimuth. For example, a close look at the synthetic and the recorded seismograms for the November 13, 1965, earthquake (Figure 4) reveals that

the interval between the P and pP phases is consistently about 2 s less at southern Asian and African stations than at European stations (Figure 4). The epicenter for this event is near Ürümqi, near the southern edge of the Dzungarian Basin, which reputedly contains up to 11 km of sediments [Terman et al., 1967]. For a focal depth of 44 km the bounce points for pP and sP are between 20 and 30 km from the epicenter. Consequently, pP and sP ray paths to Europe will pass through some of these sediments, while ray paths to southern Asia and Africa will travel through the basement rock exposed in the Tien Shan range, as illustrated in Figure 5. The observed 2.0- to 2.5-s delay of the pP phase at European stations could be explained if it traversed 13-16 km of sedimentary rock with an average v_p = 4.2 km/s instead of crystalline rock (assumed v_p = 6.2 km/s). Synthetic seismograms in Figures 4 and 6 were generated using a crustal half-space overlain by a 12-km-thick low-velocity layer.

Although the real source velocity structure is different from the assumed plane-layered velocity structure, and these differences will lead to some mismatch between the synthetic and the observed seismograms, it is the orientation of the nodal planes and the centroid depth that have the largest effect on the waveforms. Consequently, the best fit fault plane solution varies little if the source velocity structure is changed (Figures 2 and 3).

RESULTS

Earthquakes in the northern Tien Shan. Five of the earthquakes studied occurred at or north of the northern edge of the Tien Shan (earthquakes A, C, E, G, J; Figure 1). All five are characterized by thrust or oblique thrust mechanisms with north-northeast to north-northwest trending P axes. For all but one earthquake the nodal planes dip between 40° and 55°

(Figures 6-10). The source durations are short (<5 s), and the centroid depths range from 15 to 44 km.

The deepest and largest earthquake studied occurred ≈50 km northeast of Ürümqi in the Chinese Tien Shan on November 13, 1965 (earthquake A, Figures 1 and 6, Table 1). The ISC epicenter and the Chinese isoseismal maps [State Seismology Bureau of China, 1979] indicate that this earthquake occurred under the western end of the Bogda Ula range (Figure 5). The P and SH waveforms indicate nearly pure thrust faulting with moderately dipping nodal planes striking just north of east (Figure 6). The strikes of the nodal planes roughly parallel both the northern edge of the range and the long axis of the elliptical zone of maximum intensity (Modified Mercali 8) (Figure 5). Which of the nodal planes is the fault plane could not be determined from the waveforms. The centroid depth of 44 ± 7 km and short source time function (<3 s) indicate that faulting did not extend into the upper crust, and we are not aware of any reports of surface rupture. It is thus difficult to link the earthquake to any particular fault, although we suspect that the earthquake occurred on the downward continuation of one of the south dipping thrust faults that runs along the north side of the range.

This earthquake is notable because it is surprisingly deep for a crustal intracontinental earthquake. Both Chen and Molnar [1977] and Vilkas [1982] noted that the focal depth of this event was >40 km. There are no published refraction profiles from the Chinese Tien Shan and little gravity data, so the crustal thickness beneath the Bogda Ula is not constrained well. Zhang et al. [1984] published a map of crustal thickness for China showing the Moho at a depth of 46-50 km in the Ürümqi area. The average elevation in the source region of ≈3 km would imply a Moho depth of ≈50 km if the region is isostatically compensated. Hence

the centroid depth of 44 ± 7 km places the earthquake in the lower crust, although it may have extended into the mantle. As discussed above, waveforms are matched best for a crustal velocity in the source region.

Earthquake J, on September 25, 1979, was also unusually deep (40 ± 7 km) and indicates oblique thrust faulting well north of the main part of the Tien Shan (Figures 7 and 19). A Soviet seismic refraction profile, east of the epicenter, was interpreted as showing a 48-km-thick crust consisting of an 11-km-thick layer (v_p = 5.5 km/s) overlying a higher-velocity (v_p = 6.3 km/s) layer [Gamburtsev et al., 1955; Vol'vovskii and Vol'vovskii, 1975]. We approximated the crust with a half-space (v_p = 6.2 km/s), but the quoted uncertainty in the centroid depth reflects the range of plausible velocity structures (average v_p = 5.6-6.8 km/s). This ±10% range in average seismic velocity for the Tien Shan leads to a ±10% uncertainty in the depth in addition to the ±3 km uncertainty demonstrated in the appendix. Again the centroid depth indicates that faulting occurred in the lower crust.

The centroid depths of the remaining three earthquakes along the northern edge of the Tien Shan (earthquakes C, E, and G) are midcrustal (15-26 km). All three events reflect thrust or oblique thrust faulting with north-northwest and north-northeast trending P axes (Figures 1 and 8-10).

Earthquakes in the Fergana Basin. Earthquakes H and K occurred beneath the southern edge of the Fergana Basin, which lies in the western Tien Shan between the Chatkal range on the north and the Alay range on the south (Figure 1). The elevations in the basin are ≈1000 m, but peaks of the ranges flanking it reach over 4500 m. East-west striking thrust faults bound the basin, which in places contains more than 9 km of sediments [Krestnikov, 1962; Terman et al., 1967; Vol'vovskii and

Vol'vovskii, 1975]. Both events are characterized by nearly pure thrust mechanisms with moderately dipping nodal planes (35°-55°) and north-northwest trending P axes. Presumably, the nodal planes that dip south beneath the mountains are the fault planes.

The epicenter published by the ISC for event K is at the foot of the mountains south of the basin. The Soviet seismological network, with stations in the Fergana Basin, located the earthquake approximately 25 km farther to the north and beneath the basin at a depth of 20 km. We found the centroid depth to be 20 ± 5 km. The waveforms for this earthquake could not be matched well using a half-space, particularly for stations to the northwest where a phase prior to pP is clearly visible (Figures 2 and 11). Using a 4.5-km-thick low-velocity sedimentary layer over a half-space produced synthetic seismograms that matched this feature better (Table 2). We thus infer that there are several kilometers of sediments within a few tens of kilometers of the thrust faults along the southern edge of the Fergana Basin. This requires that the crystalline rocks of the Tien Shan have been uplifted several kilometers along the range-bounding thrust faults and juxtaposed against the thick sediments of the basin.

A second, shallower earthquake (H) occurred approximately 60 km west of event K, along the northern edge of the Alay range south of the Fergana Basin. The waveforms were matched (Figure 12) using a half-space (Table 2), and the centroid depth was found to be 12 ± 4 km. Because the earthquake was rather shallow, the depth phases interfere, and a reflection from the base of a sediment layer, if present, would be difficult to see. Presumably, both of these earthquakes occurred along south dipping thrust faults on which the mountains to the south are thrust northward over the sediments of the basin.

Earthquakes along the southern edge of the Tien Shan. Four of the earthquakes studied occurred along the southern edge of the Chinese Tien Shan (Figure 1). All four occurred at depths of less than 15 km on moderately dipping (40°-50°) thrust faults. The P axes indicate roughly north-south shortening. Along the southern edge of the Tien Shan the bedrock of the mountains is thrust southward over the alluvium of the Tarim Basin, so that the nodal planes dipping north beneath the mountains are probably the fault planes.

Earthquakes F and I both are characterized by pure thrust faulting with north trending P axes. Both events are relatively small (m_b = 5.8) with sharp, uncomplicated waveforms and shallow centroid depths (13 ± 4 km). In neither case could the waveforms be matched well using a half-space. On records from European stations (e.g., ATU and AQU), there is a small phase after the direct P but before the large sP phase (Figures 13 and 14). This phase causes the inflection seen in the downswing following the sharp up of the P arrival. It is too early to be the pP phase; the waveforms are not matched well using only a half-space. A two-layered structure with a 7.0-km-thick lower-velocity layer over a half-space (see Table 2) can produce such a phase with the correct timing and amplitude. The earthquakes occurred along the northern edge of the Kucha Basin, which reputedly contains as much as 9 km of sediments, although only 3 km of sediments are shown beneath the epicentral region by Terman et al. [1967]. However, in this area, their map is based upon sparse data, and apparently, they assumed that the sediments do not extend beneath the thrust faults of the Tien Shan. The waveforms suggest that there are several kilometers of sediments in the region, which may indicate the underthrusting of Tarim Basin sediments.

The remaining two earthquakes (B and D) are among the largest in a swarm of earthquakes along the southern edge of the Chinese Tien Shan near

the border between China and the Soviet Union. A third large event occurred in the same region, also on March 23, 1971, but could not be studied due to an earlier, large earthquake elsewhere. The events studied were similar in magnitude (m_b = 5.8), and the similar fault plane solutions indicate thrusting to the south-southeast on moderately dipping (39°-54°) fault planes (Figures 15 and 16).

CONCLUSIONS

The focal mechanisms of all 11 earthquakes studied include large thrust components and indicate north-northwest to north-northeast shortening. With one exception (earthquake G) the nodal planes are moderately dipping (35°-55°) to the north and south. These events appear to have occurred on range-bounding faults that dip beneath the mountains, with the basement being thrust over the sediments of the basins flanking the ranges. For four earthquakes (A, F, I, and K) the waveforms contain phases that cannot be explained by a simple half-space velocity model but that can be explained as reflections from the base of a thick sediment layer above the earthquake. Thus they suggest that there may be several kilometers of sediments thrust beneath the mountains that bound the Dzungarian, Fergana, and Kucha basins.

The centroid depths of these events range from 26-44 km for the three northernmost earthquakes to 10-13 km for those along the southern edge of the Tien Shan. These depths require that basement be involved in the shortening occurring in the Tien Shan. Two of the earthquakes (A and J) are unusually deep (≥40 km) for intracontinental earthquakes and probably occurred in the lowermost crust.

It is instructive to compare the Tien Shan to other zones of intercontinental deformation far from plate margins. Are there other regions where shortening has occurred along moderately dipping thrust

faults that involve basement and extend to depths of ≥40 km? One analog is in the Rocky Mountains of Colorado, Wyoming, and Utah where shortening in the late Cretaceous was accommodated by thrusting along faults like the Wind River Thrust, which dips 35°-45° and extends from the surface to depths of at least 30 km [Smithson et al., 1980]. During the Laramide orogeny, crustal shortening produced block uplifts similar to those in the Tien Shan.

The style of deformation in the Tien Shan and in the Rockies is not the only similarity. In both regions, crustal shortening has occurred thousands of kilometers from the plate margin. The consistent, north-south directions of the P axes suggest that the shortening seen in the Tien Shan is probably due to the collision of India with Eurasia ≈1500 km to the south [Tapponnier and Molnar, 1979]. The trends of the P axes for these earthquakes have been determined to within 10° (Figure 17 and Table 3) and are in accord with the orientations of maximum compressive stress predicted both by Tapponnier and Molnar's [1976] application of slip-line field theory to describe the deformation of Asia and by England and Houseman's [1985, 1986] calculations for a thin viscous sheet.

The east-west shortening in the Laramide Rockies is thought to be driven by subduction of the Farallon plate beneath the western edge of North America. To link the uplift of the Rockies with the subduction going on more than 1000 km to the west, some workers [e.g. Bird, 1984; Burchfiel and Davis, 1975; Dickinson and Snyder, 1978; Engebretson et al., 1984] have suggested that the subducting Farallon plate did not sink into the asthenosphere under California but instead moved horizontally under western North America, finally sinking into the asthenosphere beneath the Rockies (Figure 18). The shortening occurring today in the Tien Shan seems to be due to the collision of India with Eurasia, yet there appears

to be no horizontal slab linking the two. If a slab were moving horizontally beneath Tibet and the Tarim Basin, we would expect to see Tertiary volcanism and numerous intermediate depth earthquakes there. However, there are very few outcrops of Tertiary volcanic rocks and very little seismicity in the Tarim Basin. Apparently, subduction of a horizontal slab is not required to cause the uplift of the Tien Shan. Although this analogy cannot prove that the Rockies are not related to horizontal subduction, it does show that it is not necessary to explain the Laramide shortening that occurred there.

APPENDIX: UNCERTAINTIES IN STRIKE, DIP, AND RAKE ANGLES OF FAULT PLANE SOLUTIONS

Several approximations to the real earth must be made in generating the synthetic seismograms, and each contributes to a misfit of the observed and synthetic seismograms that translates into an uncertainty in the parameters being estimated. Here we discuss these approximations and attempt to evaluate their effect on the solution.

Assumptions required to generate the synthetic seismograms include the instrument response, the attenuation operator, and the source and receiver velocity structure. With the exception of the source velocity structure, which is discussed above, these fixed parameters are known fairly well, and regardless, the synthetic waveforms change little if they are varied within physically reasonable limits. The instrument response for WWSSN seismographs is known well, and the instruments are calibrated often. We use the causal attenuation operator of Futterman [1962] with a t^* of 1 s for P waves and 4 s for SH waves ($t^* = t/Q$, where t is the travel time and Q is the averaged attenuation along the ray path). These values are within 10% of those estimated for the mantle [e.g., Dziewonski and

Anderson, 1981]. Experiments in which t* was varied by a factor of 2 showed that the fault plane solution and the centroid depth were not sensitive to the attenuation operator because the inversion routine simply compensates by changing the source duration and the seismic moment. The assumed receiver structure, a half-space with v_p = 6.0 km/s, v_s = 3.4 km/s, density = 2700 kg/m^3, is an approximation to the average velocity structure beneath the various stations. Because the inversion routine is sensitive only to coherent signals in the waveforms, we expect that receiver structure will not bias the solution as it is unlikely that all receivers have a similar velocity structure.

The seismic source is approximated by a point double-couple, which appears to be valid for the relatively short durations of the earthquakes studied. Nabelek [1984] showed that when using WWSSN long-period data, a point source is a good approximation for earthquakes with fault dimensions of 25 by 11 km^2 and a source duration of 9 s. The earthquakes studied here have much shorter source durations (all but two are less than 5 s) and probably have fault rupture areas of less than 100 km^2.

Two additional parameters that must be determined are the P and SH arrival times. These were initially picked using the ISC location and the Jeffreys-Bullen (J-B) travel time tables. The arrival times were later adjusted by cross-correlating the observed seismogram with the synthetic waveform. The adjusted arrival time and the time predicted by the J-B tables rarely disagreed by more than 3 s for P waves and more than 9 s for SH waves.

Due to background noise on the seismogram, the distribution of stations, and unmodeled contributions to the observed seismograms, there typically is an adequate fit between the synthetic and recorded seismograms for a range of source parameters. To examine the resulting

uncertainties, each source parameter was fixed at values bracketing its best fit value, the inversion routine was rerun while allowing the other parameters to change, and the new best fit synthetic waveforms were compared to the observed seismograms (see Figures 19 and 20). In this way we estimated the uncertainties to be ±5° in dip, ±10° in strike, ±15° in rake, and 3 km in centroid depth. These uncertainties include the effects of trade-offs among the parameters since all the parameters but one were left free to change during these tests.

Earthquake J of September 25, 1979, is representative of the deeper thrust events studied (e.g., A, G, J, and K). It has simple waveforms indicative of a simple source time function (Figure 19a). For each row in Figure 19a the depth was held fixed and the fault plane solution and source time function were allowed to vary. The timing of the reflected phases is not matched for values of focal depth 6 km above and below the best fit depth. Even for depths of 37 and 43 km, there is a consistent mismatch between the synthetic and the observed seismograms (Figure 19a), which is confirmed by the increase in variance. Note that the fault plane solution is stable despite the variation in depth and source time function.

The centroid depth is constrained largely by the P waveforms (Figure 19a), while the SH waveforms are more sensitive to the strike, dip, and rake angles (Figures 19b-19d). In general, the stations nearest the P and SH nodal surfaces are most sensitive to changes in the orientation of the nodal planes. For instance, in Figure 19b, synthetic SH waveforms for station IST change markedly as the strike changes from 200° to 220°, but for strikes of 220°-240° the rays to this station are far from the SH nodal surface and the waveforms change very little and so are not shown. The JER and HLW seismograms, however, constrain the strike to be less than

about 230°. Thus the strike is constrained to be between 210° and 230°. The pairs of stations ATU and IST and JER and HLW plot at almost identical points on the focal sphere so that the difference in waveforms at these pairs of stations reveal to some degree the character of the "noise" present in the data. The waveforms shown in Figure 19c show how the dip angle is constrained to be 47°-57°, primarily by the amplitude of the first-arriving P and SH waves at stations near the nodal surfaces. The slip is likewise constrained to be between 50° and 80° (Figure 19d).

A similar set of plots is shown for earthquake H of January 31, 1977, a relatively shallow event with a simple time function, typical of many of the earthquakes studied (Figure 20). Here, too, the timing of the reflected P phases constrains the centroid depth. Even for a 1-s source duration, at a depth of 17.5 km the synthetic waveforms are too broad due to the late arriving reflected phases. The P/SH amplitude ratio also constrains the depth. For shallow events with this type of mechanism the P and pP phases interfere destructively, while the S and sS waves interfere constructively, so that the P/SH amplitude ratio decreases with decreasing focal depth. The best fitting solution with the depth fixed at 5.5 km produces P wave amplitudes that are too small relative to the SH wave amplitudes. This shows the importance of using the amplitudes, and not just the shape, of the waveforms in the inversion. The remaining plots show that the SH waveforms are particularly useful in constraining the orientation of the fault plane solution. For thrust earthquakes like this one, the P waveforms are rather insensitive to changes in the orientation of the nodal planes (compare synthetic waveforms for JER in Figure 20b). In contrast, many of the stations fall near the SH nodal surfaces.

For each earthquake many more solutions were generated than are presented here. These experiments lead us to quote uncertainties of ±5° in dip, ±10° in strike, ±15° in rake and 3 km in centroid depth for these thrust earthquakes. In addition, as explained above, uncertainties in the velocity structure contribute an additional ±10% uncertainty in the centroid depth.

Acknowledgments. We wish to thank John Nabelek and Geoff Abers for helping with the development of the computer software used in this study. Geoff Abers and Craig Jones made helpful suggestions, and Brian Evans provided useful computer hardware and software. James Ni, Terry Wallace, and Douglas Wiens suggested several useful improvements to the original manuscript. This work was supported in part by National Science Foundation grant 8500810-EAR and NASA grant NAG4-795.

REFERENCES

Aki, K., and P. G. Richards, Quantitative Seismology - Theory and Methods, 932 pp., W. H. Freeman, San Francisco, Calif., 1980.

Bird, P., Laramide crustal thickening event in the Rocky Mountain foreland and Great Plains, Tectonics, 3, 741-758, 1984.

Burchfiel, B. C., and G. A. Davis, Nature and controls of Cordilleran orogenesis, western United States: Extension of an earlier synthesis, Am. J. Sci., 272, 97-118, 1975.

Burtman, V. S., Structural geology of the Variscan Tien Shan, Am. J. Sci., 275A, 157-186, 1975.

Burtman, V. S., Faults of Middle Asia, Am. J. Sci., 280, 725-744, 1980.

Chen, W.-P., and P. Molnar, Seismic moments of major earthquakes and the average rate of slip in central Asia, J. Geophys. Res., 82, 2945-2969, 1977.

Dickinson, W. R., and W. J. Snyder, Plate tectonics of the Laramide orogeny, Mem. Geol. Soc. Am., 151, 355-366, 1978.

Dmitriyev, M. I., M. A. Demtchenko, and I.I Lando, The Central Tien Shan, Report of the Ukrainian Scientific Expedition to the Central Tien Shan (in Ukrainian), 551 pp., Radianska Shkola, Kharkov, 1935.

Dziewonski, A. M., and D. L. Anderson, Preliminary reference Earth model, Phys. Earth Planet. Inter., 25, 297-356, 1981.

Engebretson, D. C., A. Cox, and G. A. Thompson, Correlation of plate motions with continental tectonics: Laramide to Basin-Range, Tectonics, 3, 115-119, 1984.

England, P., and G. Houseman, The role of lithospheric strength heterogeneities in the tectonics of Tibet and neighboring regions, Nature, 315, 297-301, 1985.

England, P., and G. Houseman, Finite strain calculations of continental deformation, 2, Comparison with the India-Asia collision zone, J. Geophys. Res., 91, 3664-3676, 1986.

Futterman, W. I., Dispersive body waves, J. Geophys. Res., 67, 5279-5291, 1962.

Gamburtsev, G. A., P. S. Veitsman, and Yu. V. Tulina, Structure of the crust in the northern Tien Shan according to data from deep seismic sounding, Dokl. Akad. Nauk SSSR, 105, 83-86, 1955.

Gröber, P., Der Südliche Tiën-Schan, 110 pp., B. G. Teubner, Leipzig, 1914.

Krestnikov, V. N., History of oscillatory movements in the Pamirs and adjacent regions of Asia, 199 pp., Akademii Nauk SSSR Press, Moscow, 1962.

Langston, C. A., and D. V. Helmberger, A procedure for modelling shallow dislocation sources, Geophys. J. R. Astron. Soc., 42, 117-130, 1975.

Leith, W., and A. Teremetsky, Trenching and geomorphological studies of the Talas-Fergana fault, Soviet Central Asia, Eos Trans. AGU, 67, 375, 1986.

Molnar, P., and P. Tapponnier, A possible dependence of tectonic strength on the age of the crust in Asia, Earth Planet. Sci. Lett., 52, 107-114, 1981.

Molnar, P., T. J. Fitch, and F. T. Wu, Fault plane solutions of shallow earthquakes and contemporary tectonics in Asia, Earth Planet. Sci. Lett., 19, 101-112, 1973.

Nabelek, J., Determination of earthquake source parameters from inversion of body waves, Ph.D. thesis, 361 pp., Mass. Inst. of Technol., Cambridge, 1984.

Nabelek, J., Geometry and mechanism of faulting of the 1980 El Asnam, Algeria, earthquake from inversion of teleseismic body waves and comparison with field observations, J. Geophys. Res., 91, 12,713-12,728, 1985.

Ni, J., Contemporary tectonics in the Tien Shan Region, Earth Planet. Sci. Lett., 41, 347-354, 1978.

Norin, E., Geology of Western Quruq Tagh, E. Tien Shan, 194 pp., Tryckeri Aktiebolaget Thule, Stockholm, 1937.

Norin, E., Geologic Reconnaissances in the Chinese Tien Shan, 229 pp., Tryckeri Aktiebolaget Thule, Stockholm, 1941.

Smithson, S. B., J. A. Brewer, S. Kaufman, J. Oliver, and C. Hurich, Structure of the Laramide Wind River uplift, Wyoming, from COCORP deep reflection data and gravity data, Geology, 6, 648-652, 1980.

State Seismological Bureau of China, Isoseismal maps of earthquakes in China, 107 pp., Seismology Publishing House, Beijing, 1979.

Suvorov, V. P., Main faults of Kazakhstan and Central Asia, Faults and Horizontal Movements of the Earth's Crust, Tr. Geol. Inst. Akad. Nauk SSSR, 80, 173-237, 1963.

Tapponnier, P., and P. Molnar, Slip-line field theory and large scale continental tectonics, Nature, 264, 319-324, 1976.

Tapponnier, P., and P. Molnar, Active faulting and Cenozoic tectonics of the Tien Shan, Mongolia, and Baykal regions, J. Geophys. Res., 84, 3425-3459, 1979.

Terman, M. J., C. C. Woo, D. C. Alverson, D. P. Cox, and A. J. Woloshin, Atlas of Asia and Eastern Europe - To support detection of underground nuclear testing, vol. 2, Tectonics, U.S. Geological Survey, Reston, Va., 1967.

Trifonov, V. G., Late Quaternary tectonic movements of western and central Asia, Geol. Soc. Am. Bull., 89, 1059-1072, 1978.

Vilkas, A., Sismicité et tectonique du Tien Shan: Etude de quelques séismes par la méthode des sismogrammes synthétiques, M. S. thesis, 172 pp., Univ. of Paris, Paris, 1982.

Vinnik, L. P., and A. M. Saipbekova, Structure of the lithosphere and the asthenosphere of the Tien Shan, Ann. Geophys., 2, 621-626, 1984.

Vol'vovskii, I. S., and B. S. Vol'vovskii, Cross-Sections of the Earth's Crust in the Territory of the USSR, Plotted From Deep Seismic Soundings, 268 pp., Sovetskoe Radio, Moscow, 1975.

Wallace, R. E., The Talas-Fergana fault, Kirghiz and Kazakh, USSR, Earthquake Info. Bull., 8, 4-13, 1976.

Wesson, R. L., I. L. Nersesov, and F. G. Fischer, Seismicity and focal mechanism study in Peter the First Range, Tadzhik SSR, Eos Trans. AGU, 56, 1025, 1975.

Zhang, Zh. M., J. G. Liou, and R. G. Coleman, An outline of the plate tectonics of China, Geol. Soc. Am. Bull., 95, 295-312, 1984.

TABLE 1. Focal Mechanisms for 11 Tien Shan Earthquakes

	Date	Origin Time (UT)	Epicenter (ISC)		Focal Mechanism			Moment, 10^{17} N m	Source Duration, seconds	Centroid Depth, km
			Latitude	Longitude	Strike	Dip	Slip			
A	Nov. 13, 1965	0433:50.6	43.87° N	87.74° E	72°	43°	81°	37	2.4	44
					264°	48°	98°			
B	Feb. 11, 1969	2208:51.0	41.42° N	79.24° E	65°	41°	83°	20	6.9	10
					253°	49°	96°			
C	June 5, 1970	0453:07.4	42.48° N	78.71° E	69°	41°	68°	31	3.8	17
					277°	53°	108°			
D	March 23, 1971	2047:16.0	41.42° N	79.20° E	73°	46°	93°	5.9	7.0	11
					248°	44°	87°			
E	May 10, 1971	1451:45.0	42.85° N	71.29° E	37°	48°	57°	1.3	1.3	15
					262°	51°	122°			
F	April 9, 1972	0410:48.9	42.09° N	84.58° E	100°	49°	90°	1.3	1.0	13
					279°	41°	90°			
G	June 2, 1973	2357:02.4	44.14° N	83.60° E	148°	28°	133°	2.1	0.8	26
					282°	70°	70°			
H	Jan. 31, 1977	1426:15.1	40.11° N	70.86° E	81°	40°	100°	5.2	1.0	12
					249°	51°	82°			
I	March 29, 1979	0201:32.1	41.95° N	83.38° E	71°	53°	86°	2.3	1.3	13
					258°	38°	96°			
J	Sept. 25, 1979	1305:54.5	45.09° N	76.96° E	77°	44°	119°	1.7	2.0	40
					220°	52°	65°			
K	May 6, 1982	1542:22.2	40.15° N	71.54° E	70°	36°	95°	2.0	3.6	20
					244°	54°	86°			

Estimated uncertainties: strike ±10°, dip ± 5°, rake ±15°, and depth ± 3-7 km.

TABLE 2. Source Velocity Structures Used to Generate Synthetic Waveforms

	Event	Layer Thickness, km	Seismic Velocity, km/s v_p	Seismic Velocity, km/s v_s	Density, kg/m^3
A	Nov. 13, 1965	12	4.20	2.40	2500
		half-space	6.20	3.60	2800
B	Feb. 11, 1969	half-space	6.00	3.46	2700
C	June 5, 1970	half-space	6.10	3.50	2800
D	March 23, 1971	half-space	6.00	3.46	2700
E	May 10, 1971	half-space	6.00	3.46	2800
F	April 9, 1972	7	4.00	2.30	2500
		half-space	6.20	3.60	2800
G	June 2, 1973	half-space	6.10	3.50	2800
H	Jan. 31, 1977	half-space	6.00	3.50	2700
I	March 29, 1979	7	4.00	2.30	2500
		half-space	6.00	3.46	2700
J	Sept. 25, 1979	half-space	6.05	3.50	2800
K	May 6, 1982	4.5	3.00	1.73	2400
		half-space	6.10	3.50	2800

TABLE 3. Orientations of P and T Axes

	Date	P Axis		T Axis	
		Trend	Plunge	Trend	Plunge
A	Nov. 13, 1965	348.5°	2.5°	235.0°	83.6°
B	Feb. 11, 1969	339.0°	4.2°	205.0°	84.0°
C	June 5, 1970	354.2°	6.0°	242.0°	74.4°
D	March 23, 1971	160.2°	1.1°	44.2°	87.4°
E	May 10, 1971	330.4°	1.6°	237.0°	65.6°
F	April 9, 1972	190.0°	4.0°	12.3°	86.0°
G	June 2, 1973	27.0°	22.2°	162.4°	60.2°
H	Jan. 31, 1977	344.4°	5.6°	116.3°	81.6°
I	March 29, 1979	163.9°	7.6°	318.0°	81.5°
J	Sept. 25, 1979	327.3°	4.5°	69.8°	70.0°
K	May 6, 1982	337.0°	9.2°	138.7°	80.4°

FIGURE CAPTIONS

Fig. 1. Summary map of the Tien Shan showing the ISC epicenters and fault plane solutions of the 11 earthquakes studied. The fault plane solutions show thrust and oblique thrust faulting occurring primarily on east-west trending range-bounding faults. The dashed line marks the USSR-China border. The 1000-m contour is dotted. Regions with elevations >2000 m are stippled, and regions above 4000 m are shaded. For each fault plane solution (Table 1) the lower hemisphere equal-area projection of the focal sphere is shown with the compressional quadrants shaded. Next to each focal mechanism are an identifying letter and the centroid depth in kilometers. Also shown are ISC epicenters for earthquakes occurring between 1971 and 1981 with $m_b > 5.0$. Symbols plotted indicate focal depths, h, reported by the ISC: square, $h < 33$ km; diamond, 33 km $< h <$ 70 km; plus, 70 km $< h <$ 100 km; cross, $h > 100$ km.

Fig. 2. Long-period P waveforms for earthquake K (May 6, 1982) recorded at eight WWSSN stations (top row) with synthetic seismograms illustrating the effects of varying the source velocity structure. The synthetic seismograms were generated using a crustal half-space overlain by a lower-velocity sediment layer (see Table 2). The waveforms for the half-space model (second row) do not match the sharp downturn following the direct P arrival. We explain this downturn as a reflection from the bottom of a sediment layer. The waveforms are fit best using a 4.5-km-thick sediment layer. The reflections from the base of the sediments and the free surface can be seen best at near-nodal stations (e.g., NUR and KBS) where the reflections from the sediment layer and the free surface appear as distinct downward pulses, producing a W-shaped trough. Also shown are the best fitting far-field source time function, centroid depth, and the lower

hemisphere projection of the fault plane solution for each of the six velocity structures. The solid triangles mark the P axes; the open triangles mark the T axes. Note that changing the assumed velocity structure at the source has little effect on the inferred fault plane solution but the centroid depth decreases as the sediment layer is thickened.

Fig. 3. Recorded waveforms (solid line) and synthetic (dashed line) seismograms for the earthquake A (November 13, 1965) for three assumed source velocity structures. The top row of seismograms shows the best fit solution using a half-space with v_p = 6.2 km/s. The second row shows the improved fit when a 12-km-thick low-velocity (v_p = 4.2 km/s) layer is included above the half-space. The third row shows the effect of putting the source in a mantle velocity layer (v_p = 8.0 km/s) beneath the sediment and crustal layers. On the lower hemisphere projection, lower case letters mark the stations for a mantle source, upper case letters mark the stations for a crustal source. When a mantle source velocity is used, the direct P (first upward pulse) amplitude is too small at those stations that fall close to the nodal planes (SNG, KOD, NUR, KEV) relative to that at stations far from the nodal planes (e.g., BUL and IST). Regional stations (Δ = 16°-21°) QUE (H), LAH (J), and NDI (G) recorded compressional first motions while SHL (I) recorded a dilatational first motion.

Fig. 4. Effects of azimuthal variations in the source velocity structure surrounding earthquake A (November 13, 1965). Solid lines represent the recorded waveform, and the dashed lines represent the best fitting synthetic seismograms. The reflected P waves which bounce off the sediment-basement contact (sed.) and the free surface (pP) are marked, as

is the SV wave reflected from the free surface (sP). At the European stations to the northwest the reflected phases pP and sP arrive about 1 s late relative to those predicted by the synthetic seismograms. For Asian and African stations to the south of the epicenter the reflected phases arrive about 1 s early. We attribute this 2-s difference to the thick (>10 km) sediments of the Dzungarian Basin north of the epicenter.

Fig. 5. Epicentral region earthquake A of November 13, 1965. The unshaded regions are basins. Isopachs of Mesozoic and Tertiary sediment thickness in the Dzungarian Basin are marked in kilometers [Terman et al., 1967]. Paleozoic sediment is indicated by vertical lines, and crystalline basement is cross-hatched. Star marks the ISC epicenter. The hatched oval northeast of Ürümqi is the area of maximum intensity (Modified Mercali 8) according to the State Seismology Bureau of China [1979]. The circle represents the locus of bounce points for pP. Arrows show the directions of ray-paths to European, African, and Asian stations shown in Figure 4. The reflected phases at the European stations are delayed 2.0-2.5 s, with respect to those of the Asian stations, probably by transmission through the thick sediments of the Dzungarian Basin.

Fig. 6. Fault plane solution and waveforms for earthquake A (November 13, 1965). Recorded (solid) and synthetic (dashed) seismograms are shown with tick marks enclosing the part of the seismogram used in the inversion. The lower hemisphere plots show the locations of the stations and the nodal surfaces on the focal sphere (P on the left, SH on the right). Solid triangle marks the P axis, and open triangle marks the T axis. The normalized source time function is shown on the time scale axis. Seismograms are scaled to a common epicentral distance ($\Delta = 40°$) and instrument magnification (3000×). The amplitude scale corresponds to

waveforms that would be observed on such an instrument at such a distance. The source velocity structure is given in Table 2. Depth phases indicate a centroid depth of 44 ± 7 km.

Fig. 7. Fault plane solution and waveforms for earthquake J (September 25, 1979). Format as in Figure 6. The centroid depth is 40 ± 7 km.

Fig. 8. Fault plane solution and waveforms for earthquake C (June 5, 1970). Format as in Figure 6.

Fig. 9. Fault plane solution and waveforms for earthquake E (May 10, 1971). Format as in Figure 6.

Fig. 10. Fault plane solution and waveforms for earthquake G (June 2, 1973). Format as in Figure 6.

Fig. 11. Fault plane solution and waveforms for earthquake K (May 6, 1982). Format as in Figure 6.

Fig. 12. Fault plane solution and waveforms for earthquake H (January 31, 1977). Format as in Figure 6.

Fig. 13. Fault plane solution and waveforms for earthquake F (April 9, 1972). Format as in Figure 6.

Fig. 14. Fault plane solution and waveforms for earthquake I (March 29, 1979). Format as in Figure 6.

Fig. 15. Fault plane solution and waveforms for earthquake B (February 11, 1969). Format as in Figure 6.

Fig. 16. Fault plane solution and waveforms for earthquake D (March 23, 1971). Format as in Figure 6. The seismograms for CHG ($\Delta = 28°$) were not used in the inversion.

Fig. 17. Lower hemisphere equal-area projection of the P axes (squares) and T axes (triangles) of the earthquakes studied.

Fig. 18. Cartoon illustrating the similarities of tectonic setting and styles of deformation between the intracontinental thrusting in the Tien Shan and the Laramide thrusting in Wyoming, Utah, and Colorado during the Cretaceous period. In both cases shortening has occurred more than 1000 km from the plate margin where subduction occurred. Several workers have suggested that the Laramide thrusting was linked to the subduction of the Farallon plate beneath California by horizontal subduction. However, shortening is occurring in the Tien Shan today even farther from a plate margin, and there is no evidence of a horizontal slab beneath Tibet and the Tarim Basin.

Fig. 19. Waveforms illustrating the uncertainties in parameters for the best fitting focal mechanism for earthquake J of September 25, 1979. (a) Best fitting solutions computed for each of five centroid depths. Observed (solid) and synthetic (dashed) waveforms from only diagnostic stations are shown (Figure 7 shows all waveforms used in the inversion). The time scale and source time function are shown on the right. The nodal surfaces and the positions of the stations are shown on a lower hemisphere projections of the focal sphere (P on left, SH on right). The best fit solution at a centroid depth at 40.4 km is shown by the middle row of seismograms. When the centroid depth is fixed above or below the best fitting depth, the reflected phases are not matched and the normalized variance increases. For a given source velocity structure, the centroid depth can be constrained in this way to within 3 km. Note that the focal mechanism changes very little as the depth is varied. (b) Similar

diagrams in which the strike of the northwest dipping nodal plane is varied. Note that the middle two rows of seismograms are for the best fit solution with a strike of 220°. The SH waveforms in particular constrain the strike within 10°. (c) Similar diagrams showing how the dip can be constrained within 5°. Again the middle row(s) are for the best fit solution. (SH nodal surfaces are only shown for the best-fit solution.) (d) Similar diagrams showing how the slip can be constrained within 15°.

Fig. 20. Diagrams illustrating the uncertainty in inversion parameters for the best-fitting focal mechanism for earthquake H of January 31, 1977. Format as in Figure 19. (a) depth, (b) strike, (c) dip, (d) slip.

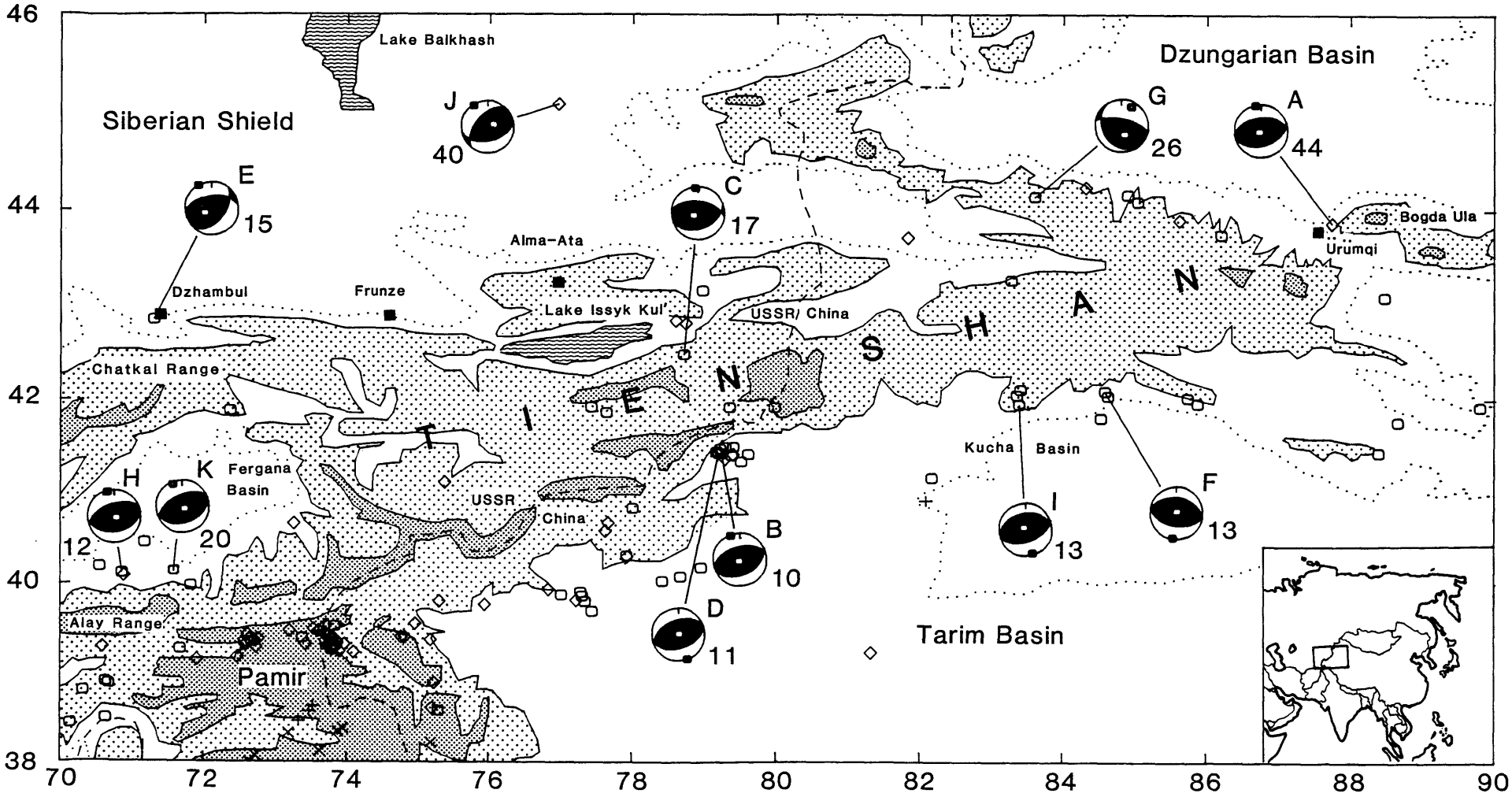
Lake Balkhash
Dzungarian Basin
Siberian Shield
J
40
G
26
A
44
E
15
C
17
Bogda Ula
Urumqi
Alma-Ata
Dzhambul
Frunze
Lake Issyk Kul'
USSR/ China
T I E N S H A N
Chatkal Range
Kucha Basin
H
12
K
20
Fergana Basin
USSR
China
B
10
I
13
F
13
D
11
Alay Range
Pamir
Tarim Basin
46
44
42
40
38
70
72
74
76
78
80
82
84
86
88
90

Figure 1

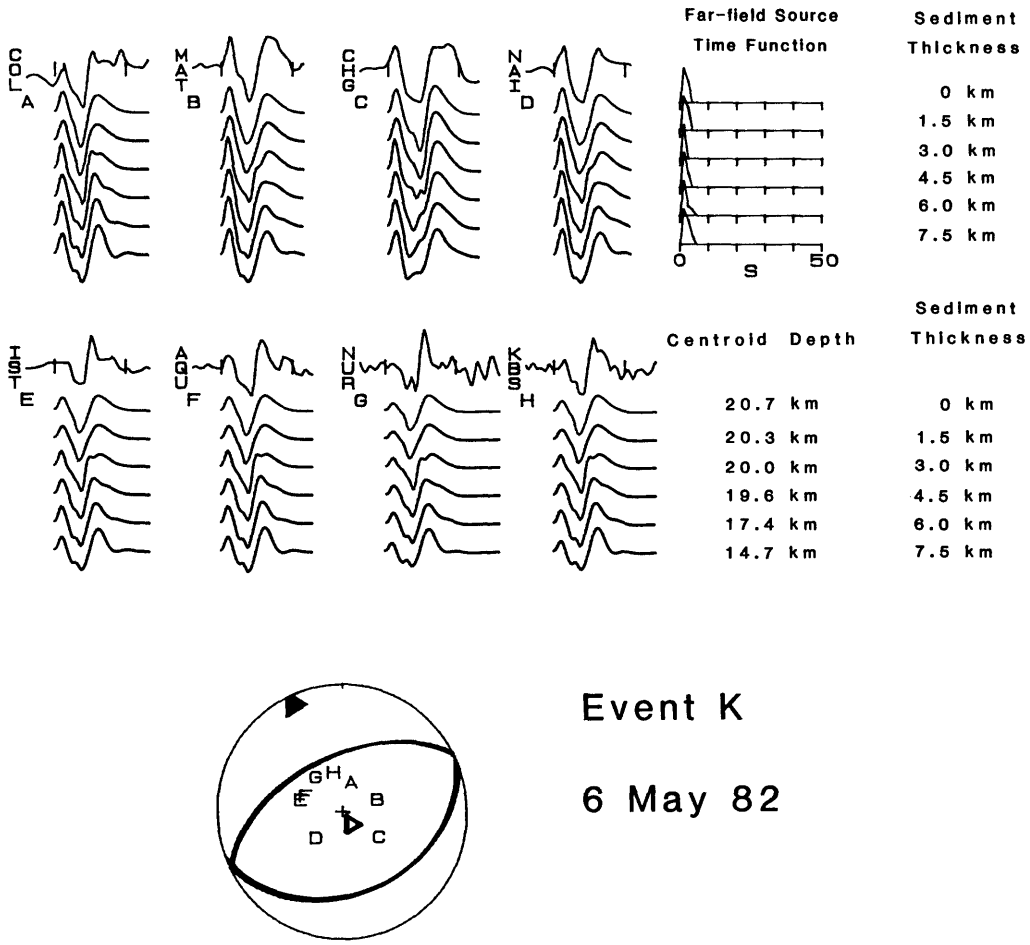

Event K

6 May 82

Figure 2

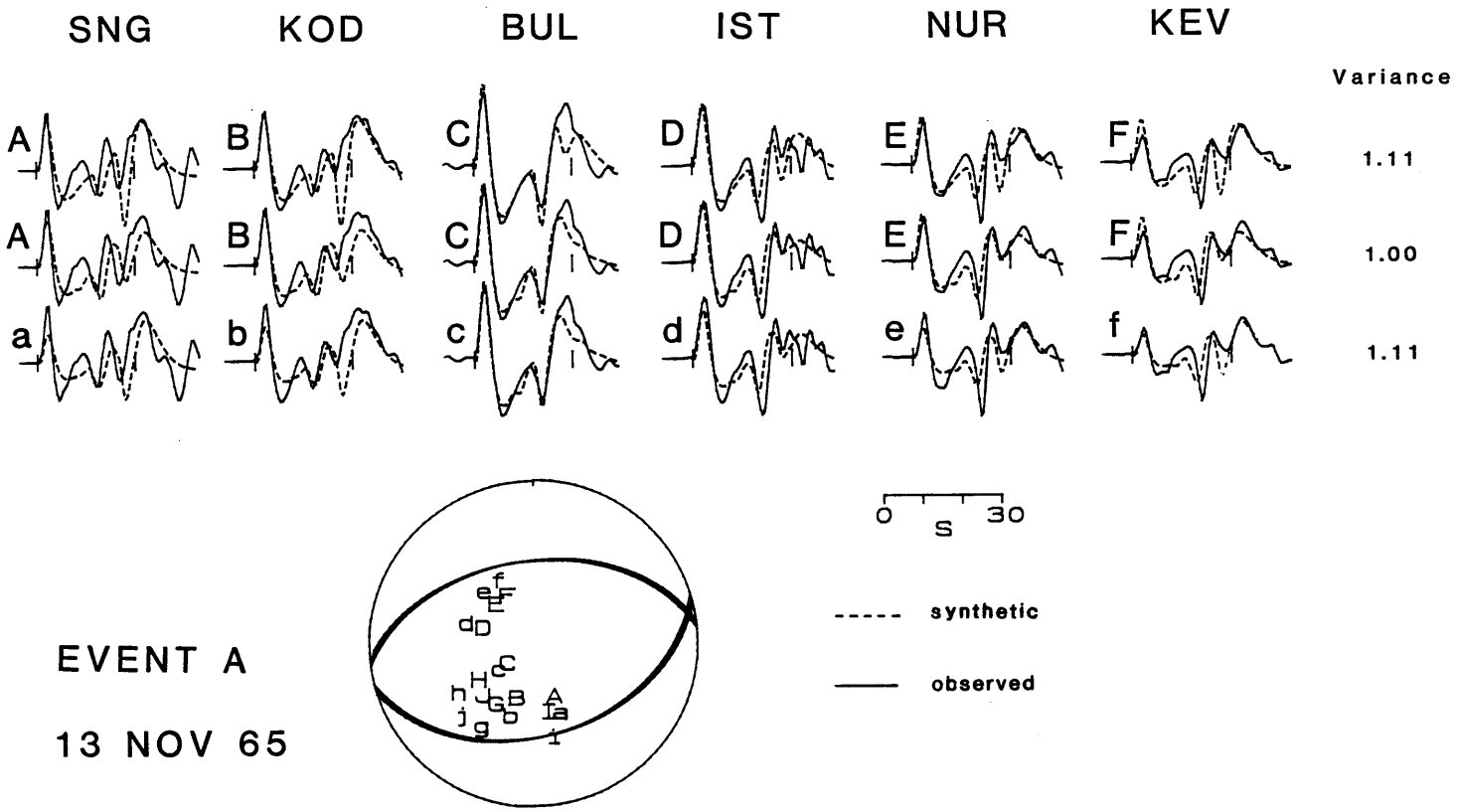
SNG
KOD
BUL
IST
NUR
KEV
Variance
A
B
C
D
E
F
1.11
A
B
C
D
E
F
1.00
a
b
c
d
e
f
1.11
0
S
30
synthetic
observed
EVENT A
13 NOV 65

Figure 3

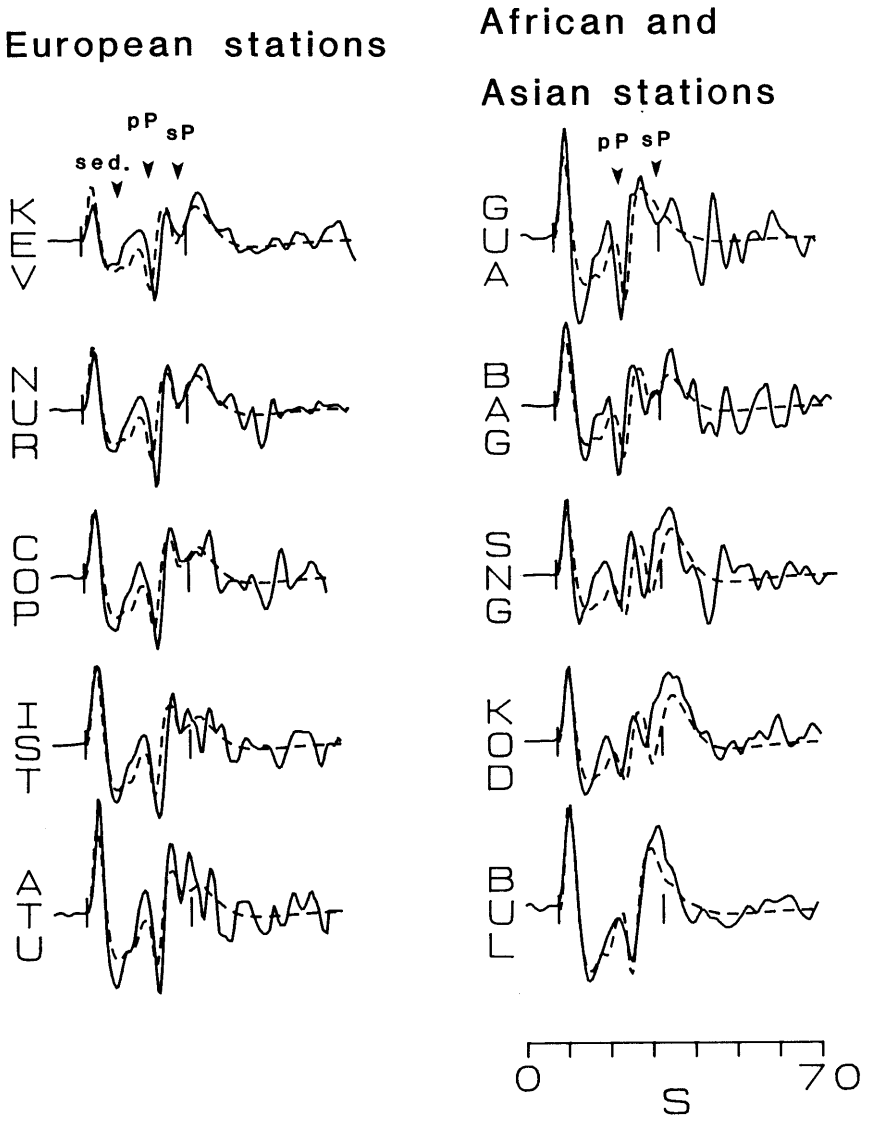
European stations
African and
Asian stations
pP
sP
sed.
KEV
NUR
COP
IST
ATU
pP sP
GUA
BAG
SNG
KOD
BUL
0
70
S

Figure 4

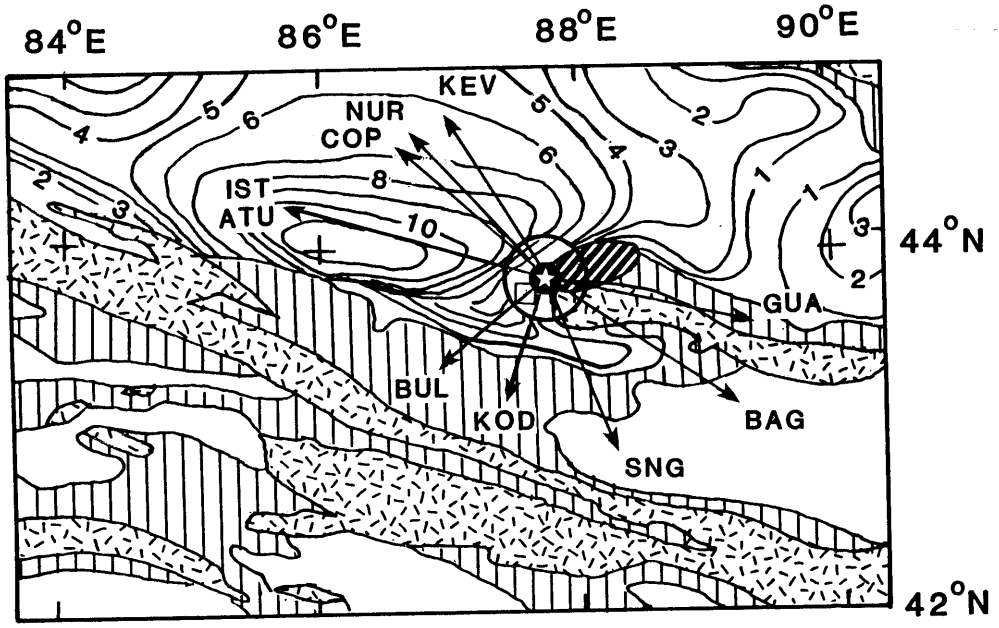

Figure 5

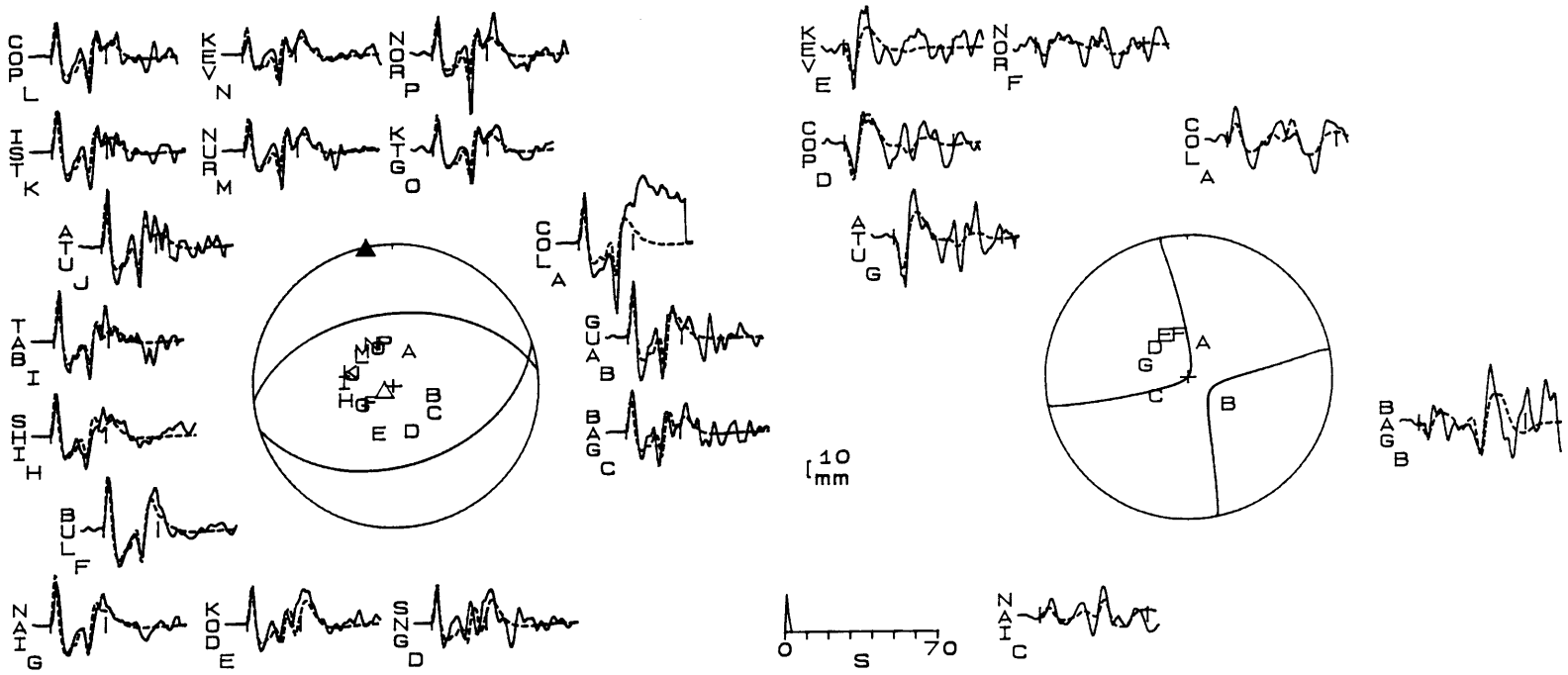
A. 13 NOV 65
COP L
KEV N
NOR P
HST K
NCR M
KTG O
ATU J
TAB I
SHH H
BUL F
NAH G
KOD E
SNG D
COL A
GUA B
BAG C
KEV E
NOR F
COP D
ATU G
COL A
10 mm
0
S
70
NAH C
BAG B

Figure 6

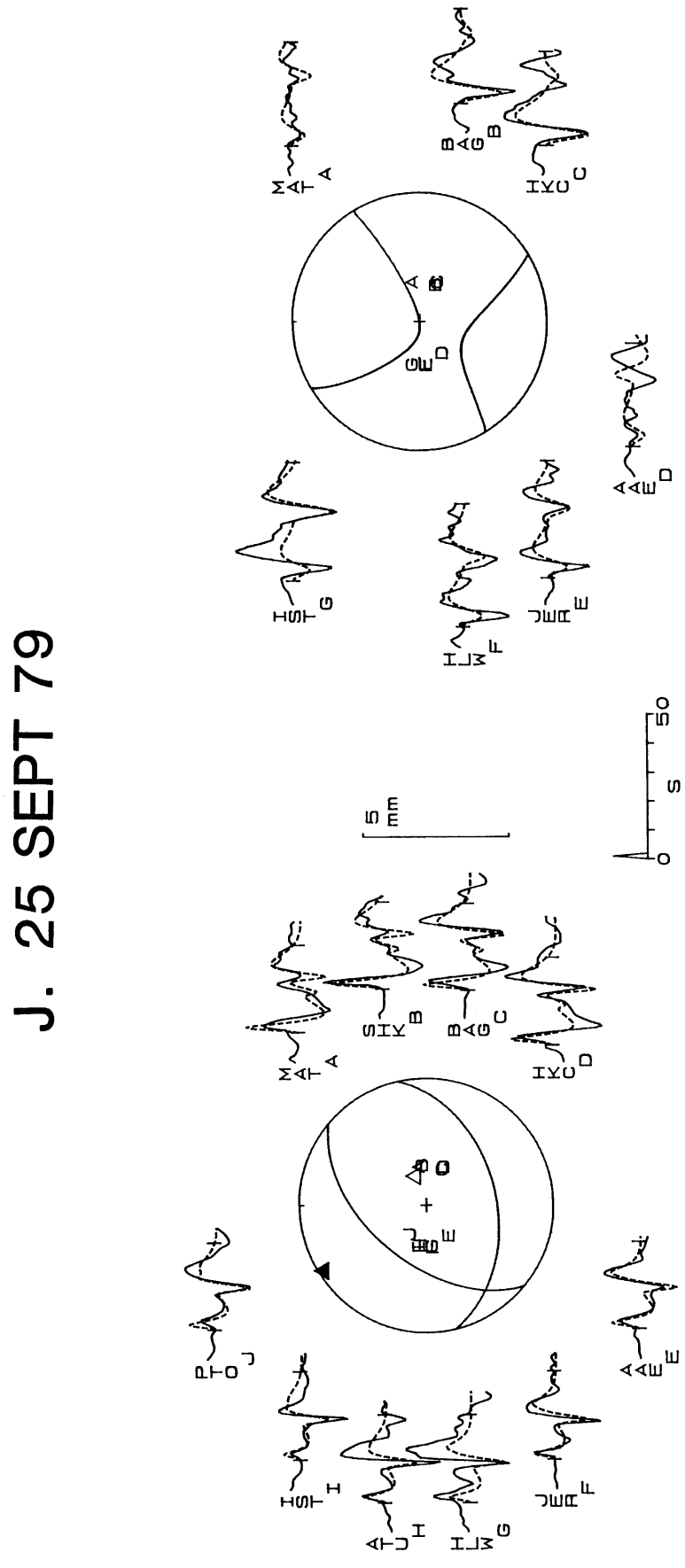

Figure 7

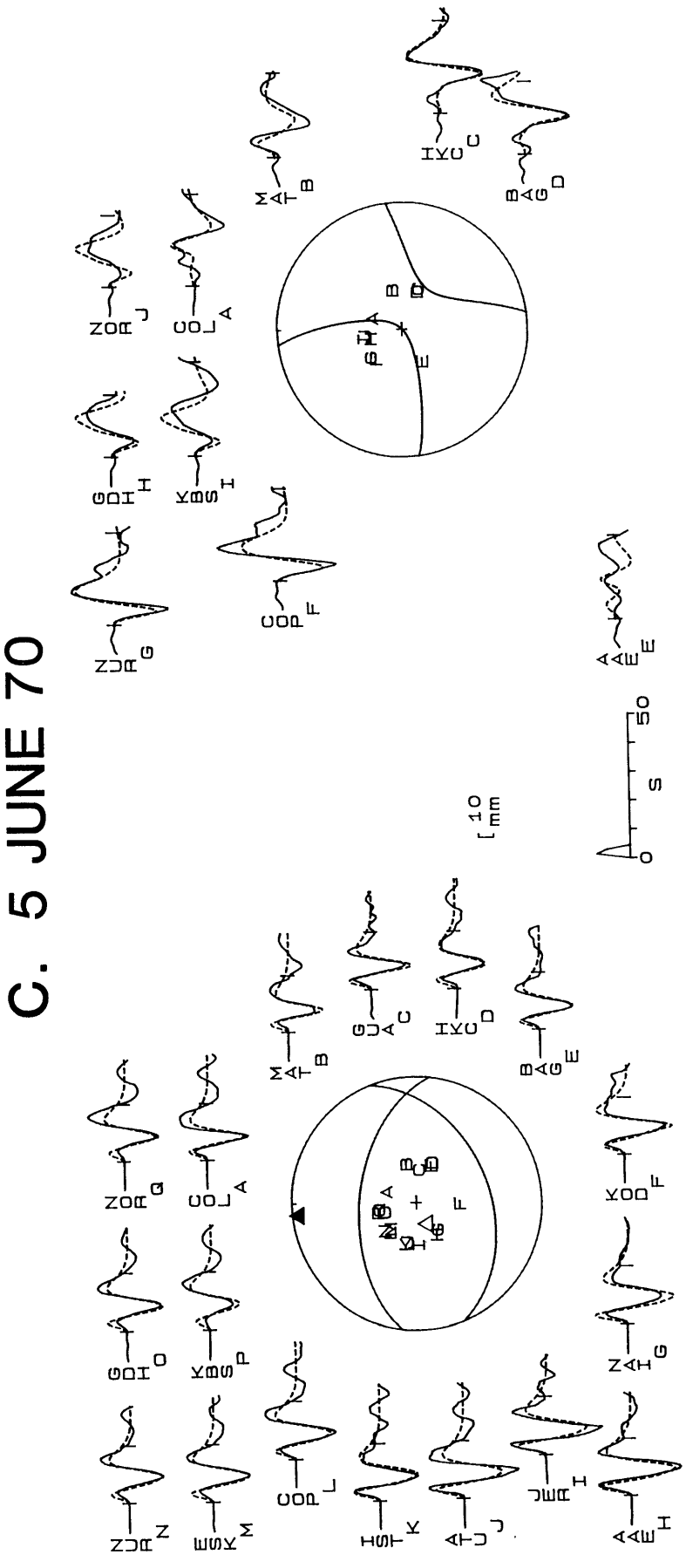

Figure 8

E. 10 MAY 71

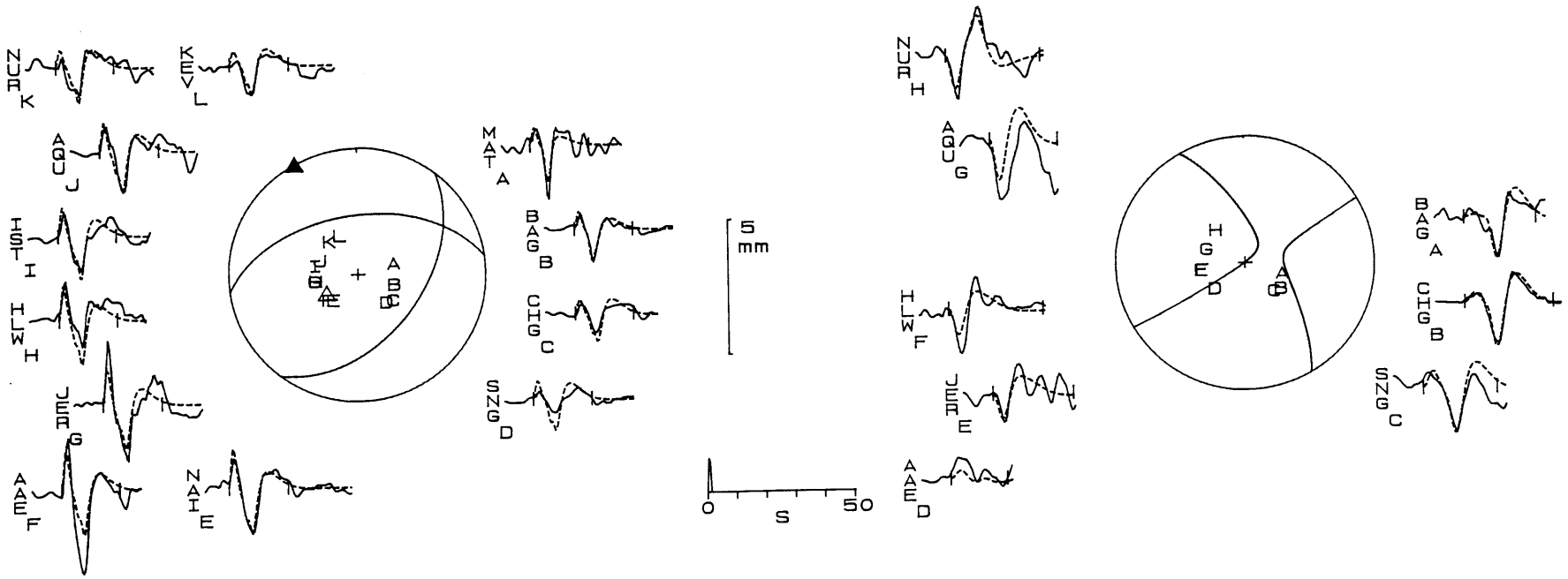

Figure 9

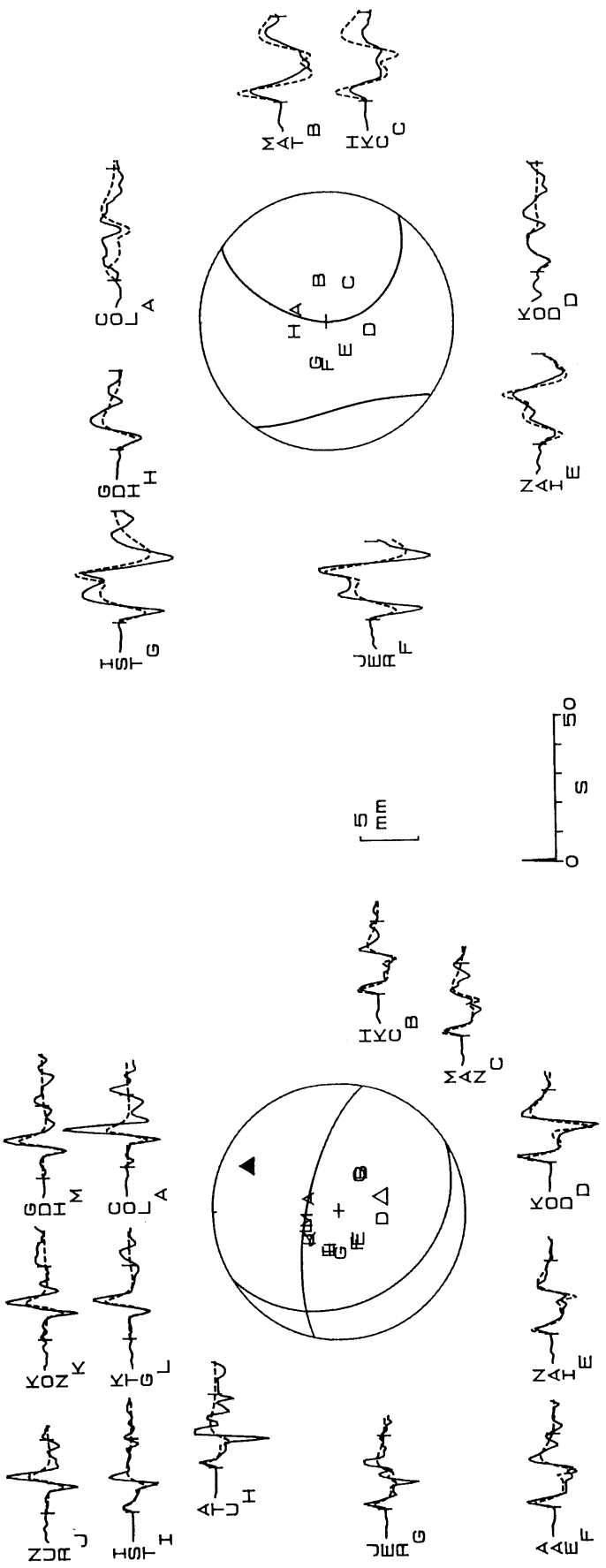

Figure 10

K. 6 MAY 82

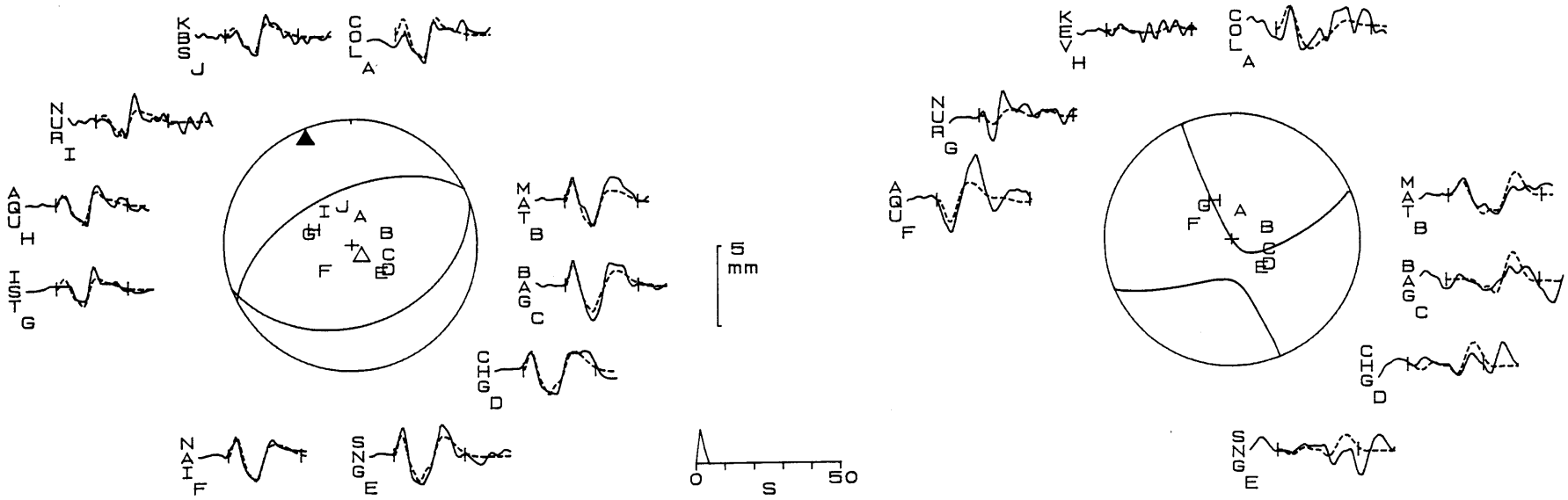

Figure 11

H. 31 JAN 77

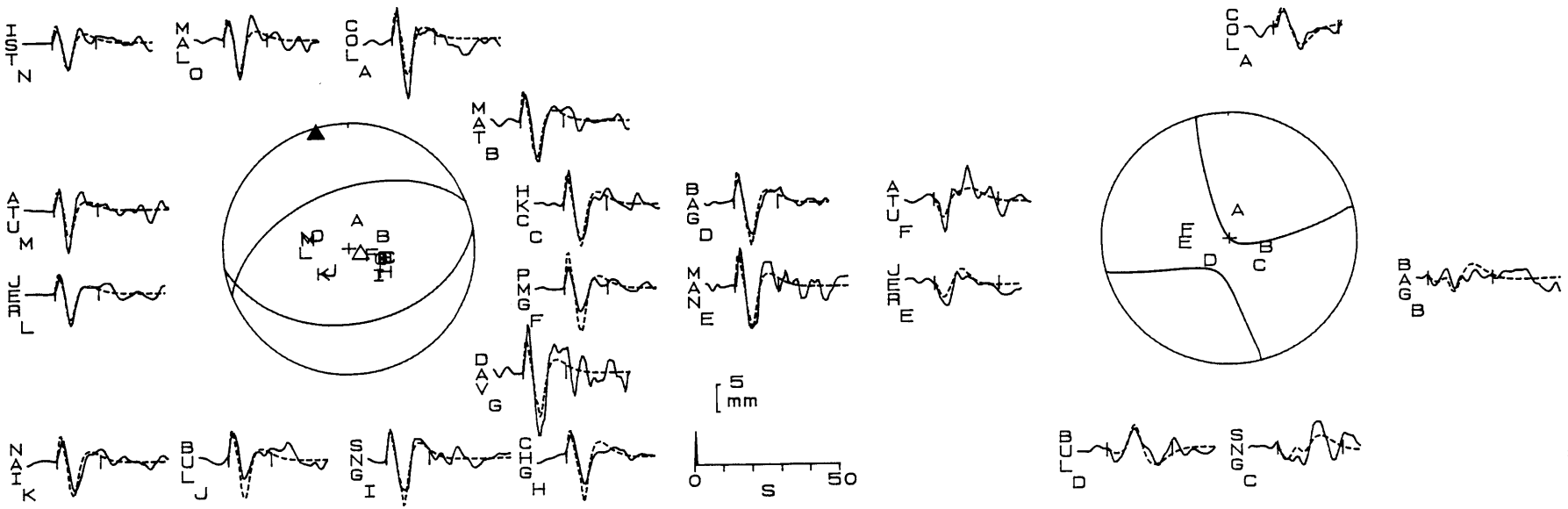

Figure 12

F. 9 APR 72

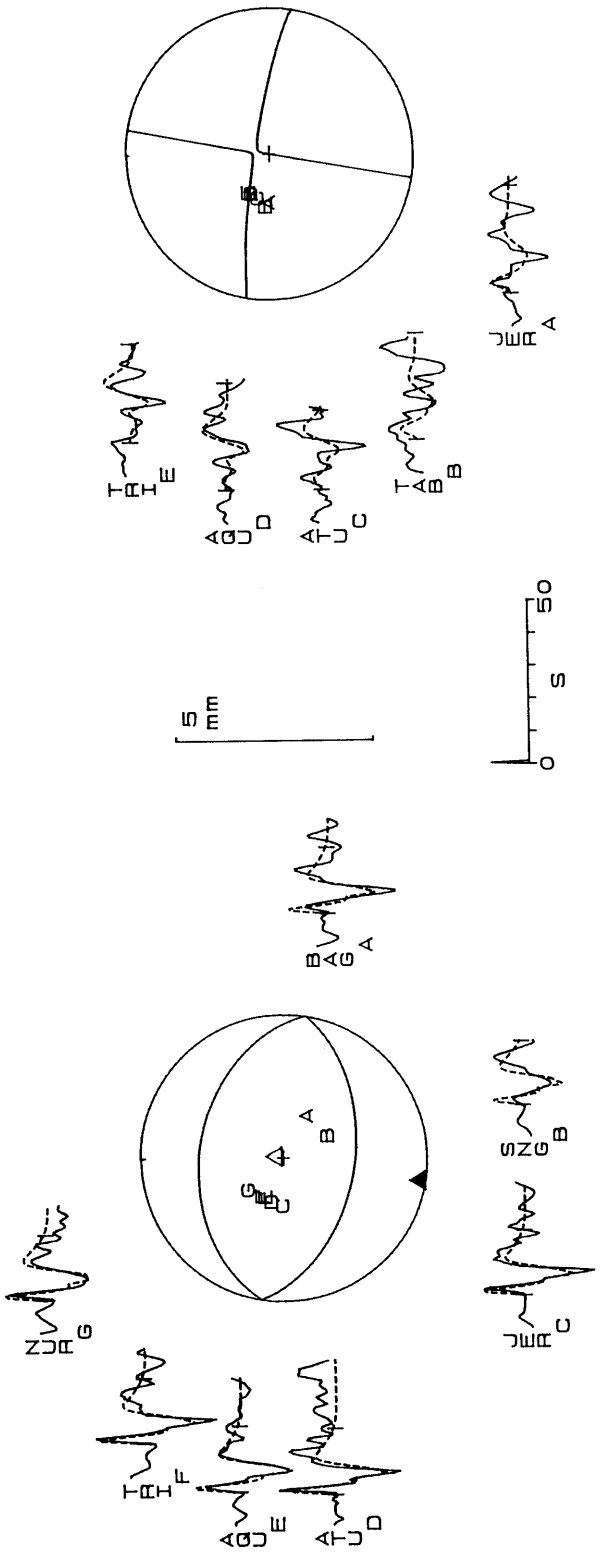

Figure 13

I. 29 MAR 79

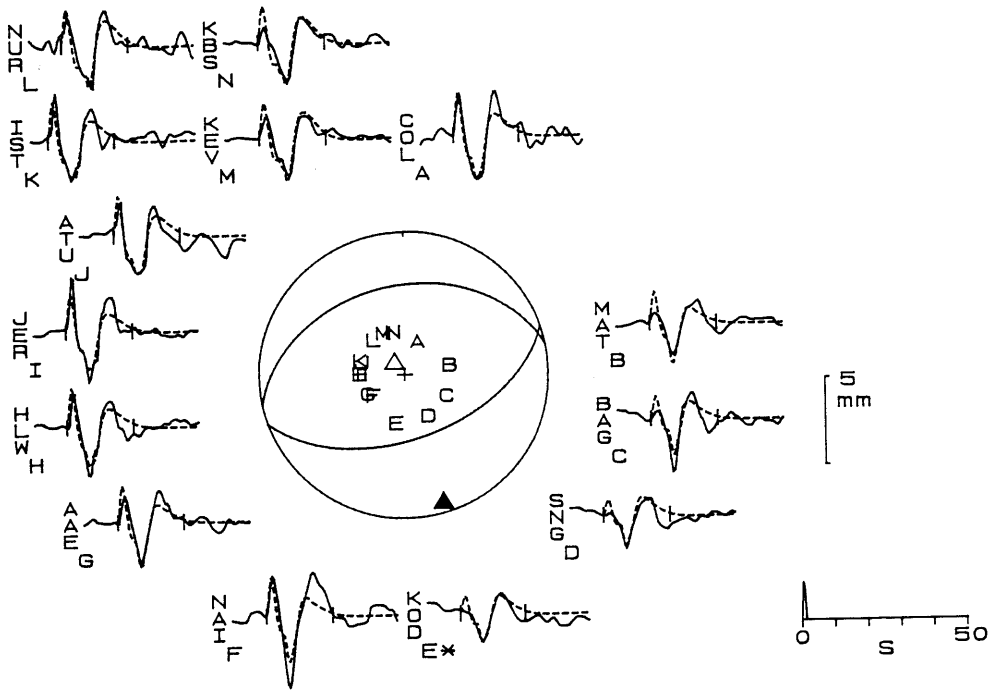

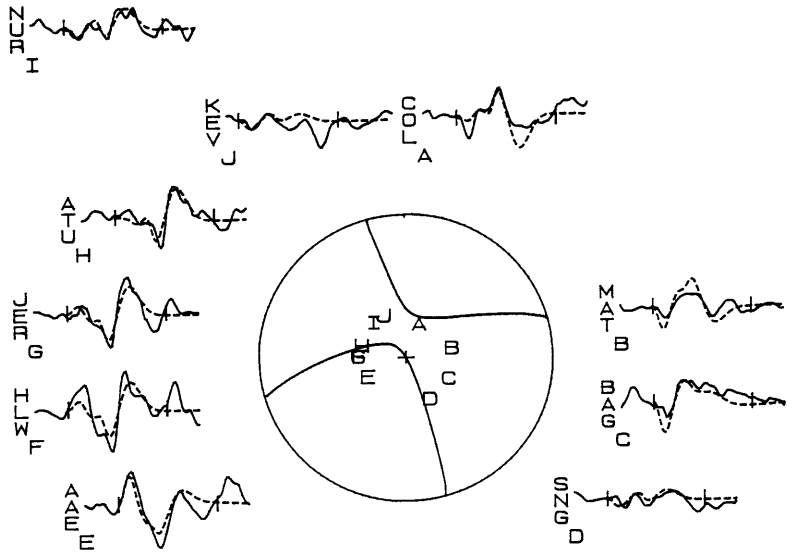

Figure 14

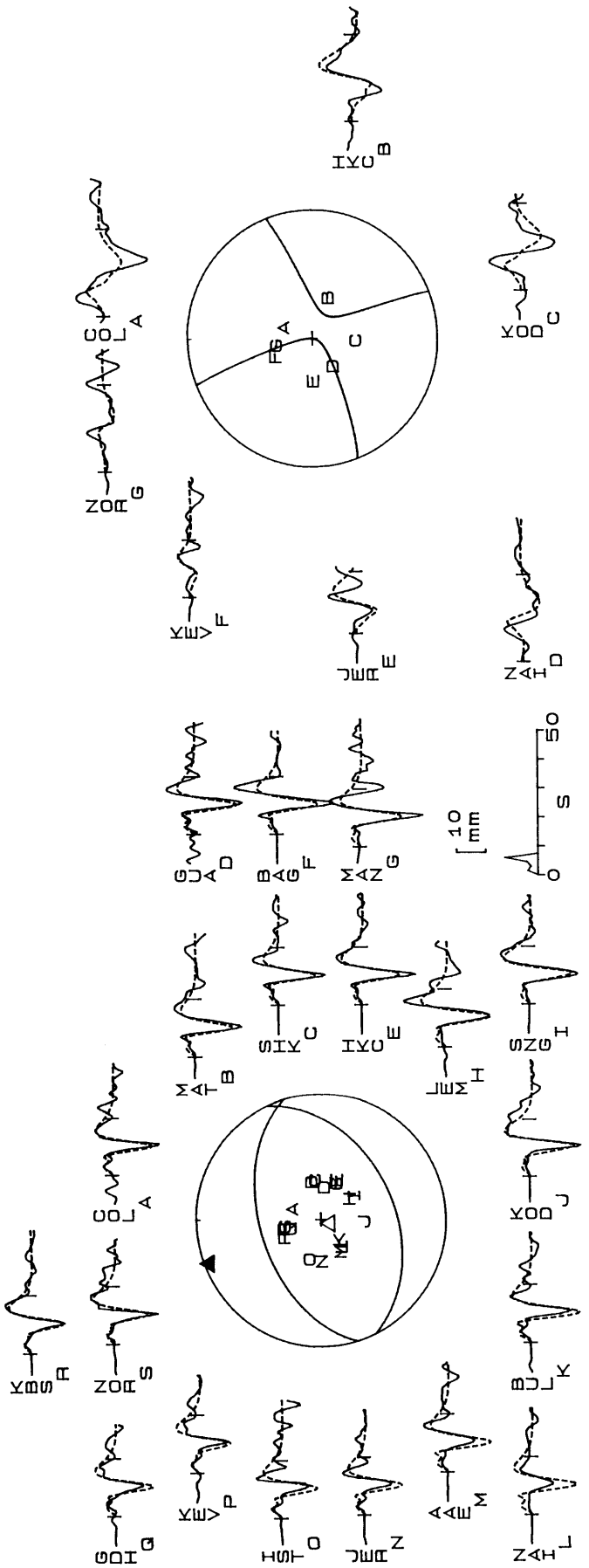

Figure 15

D. 23 MAR 71

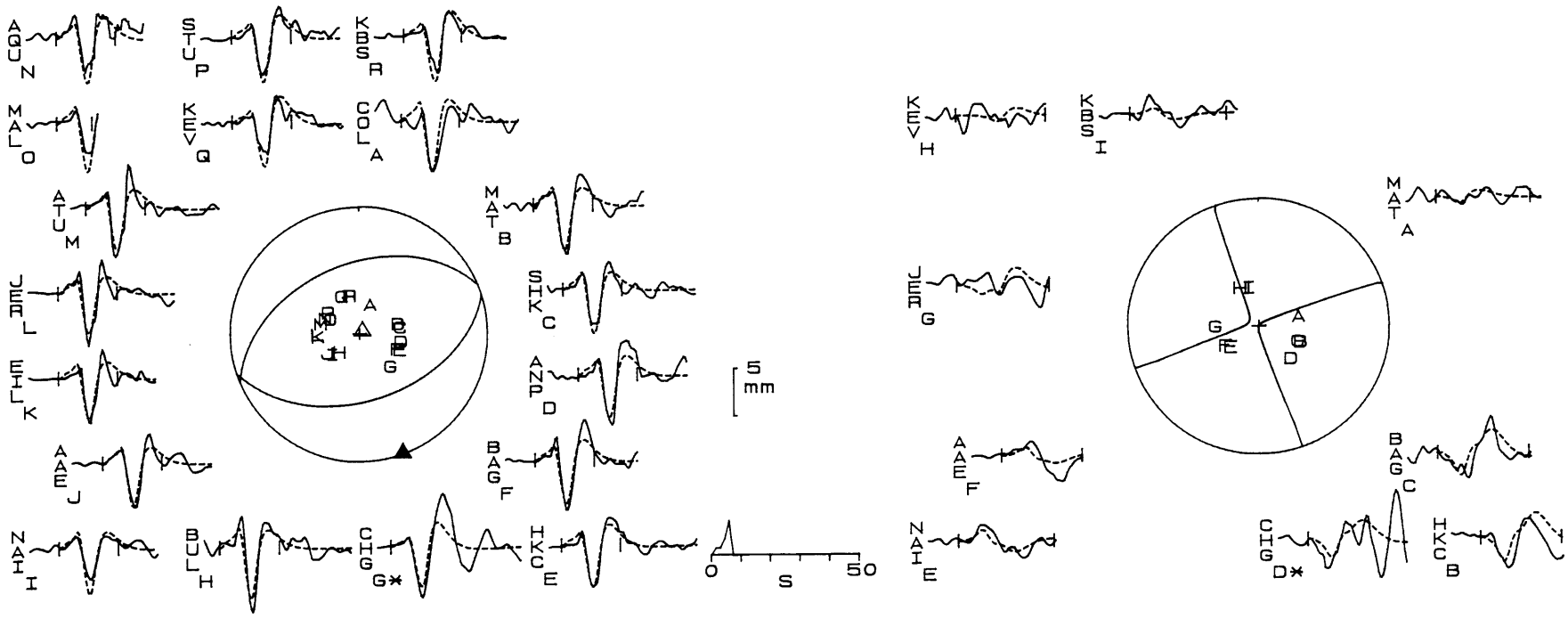

Figure 16

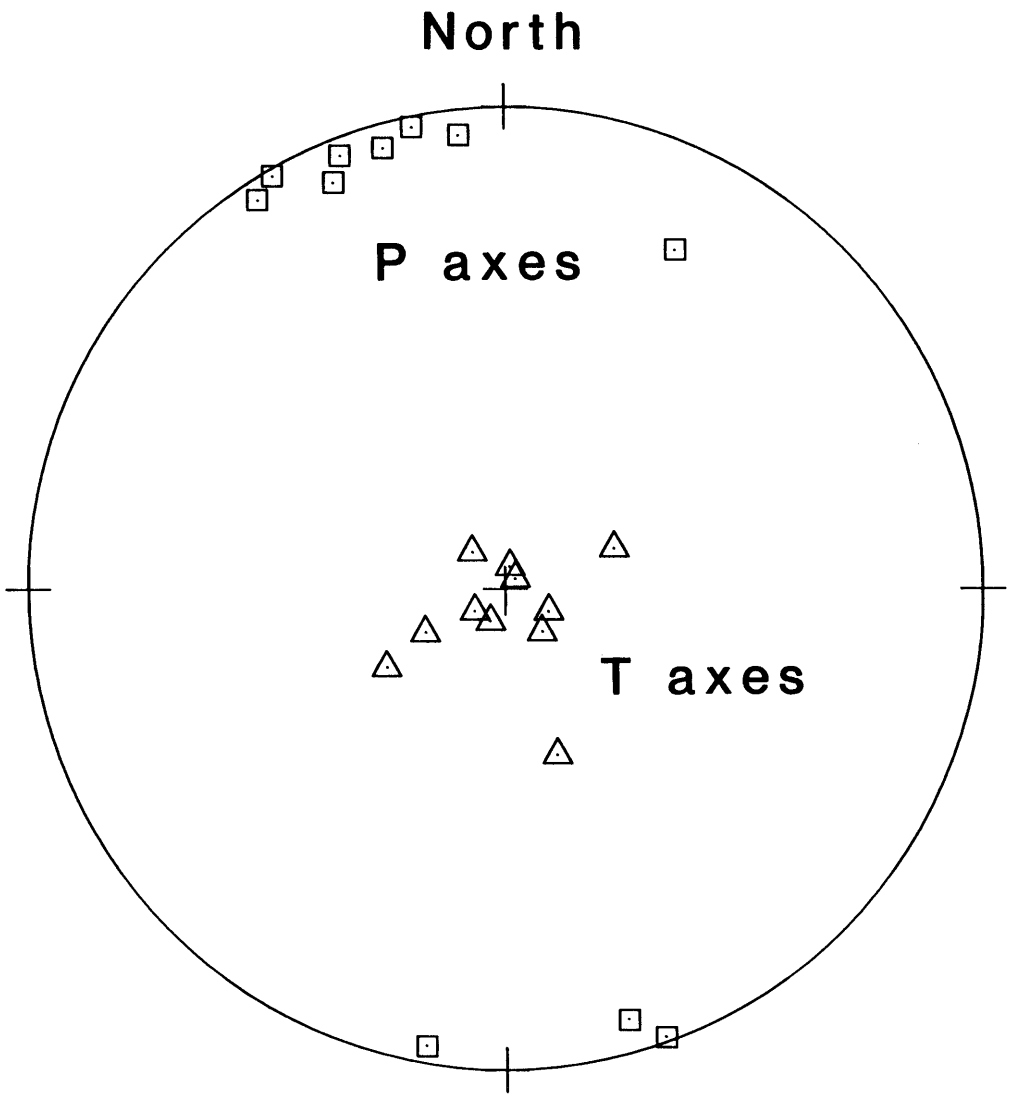

Figure 17

P AND T AXES
EQUAL AREA PROJECTION

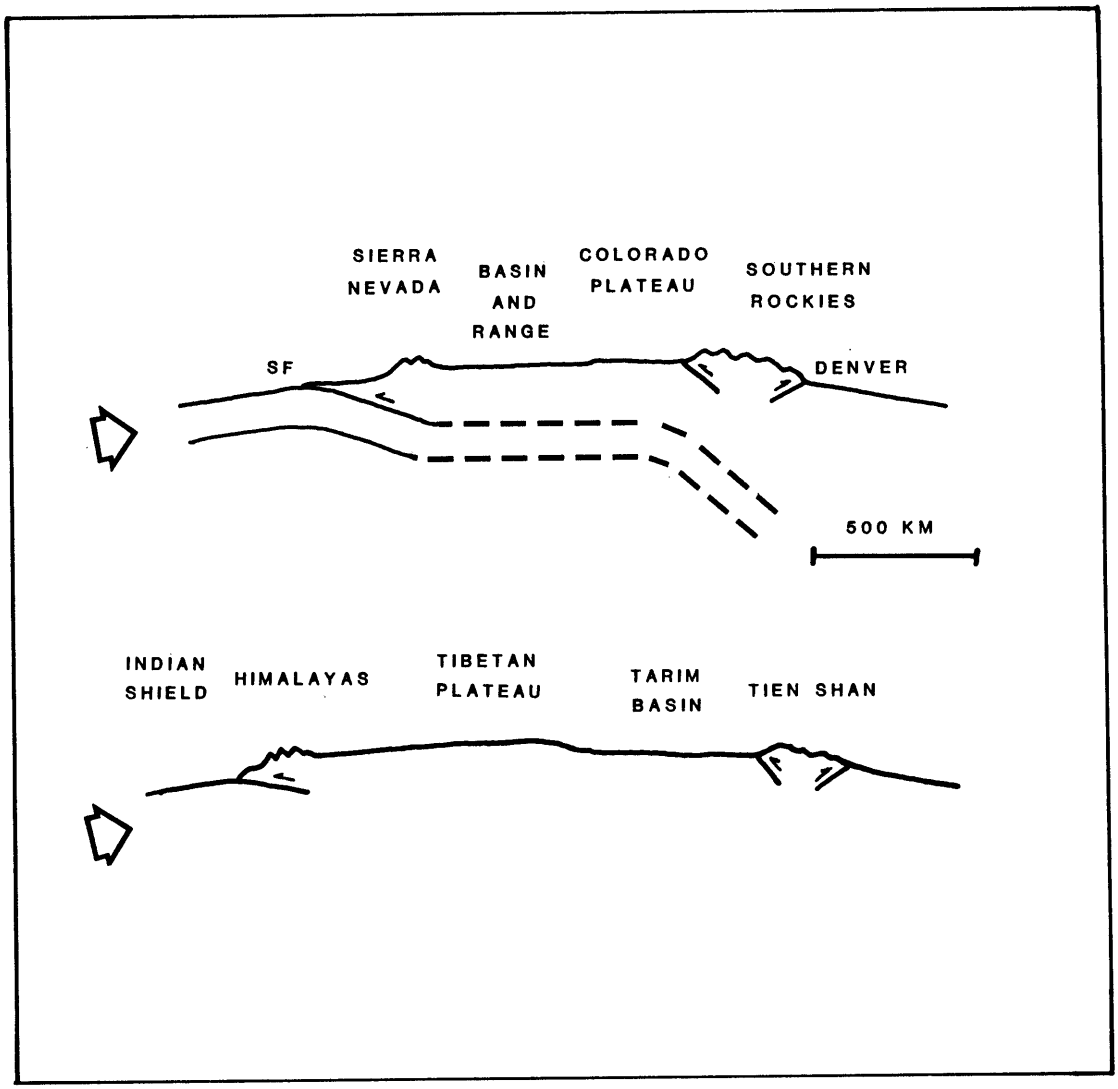
SIERRA NEVADA
BASIN AND RANGE
COLORADO PLATEAU
SOUTHERN ROCKIES
SF
DENVER
500 KM
INDIAN SHIELD
HIMALAYAS
TIBETAN PLATEAU
TARIM BASIN
TIEN SHAN

Figure 18

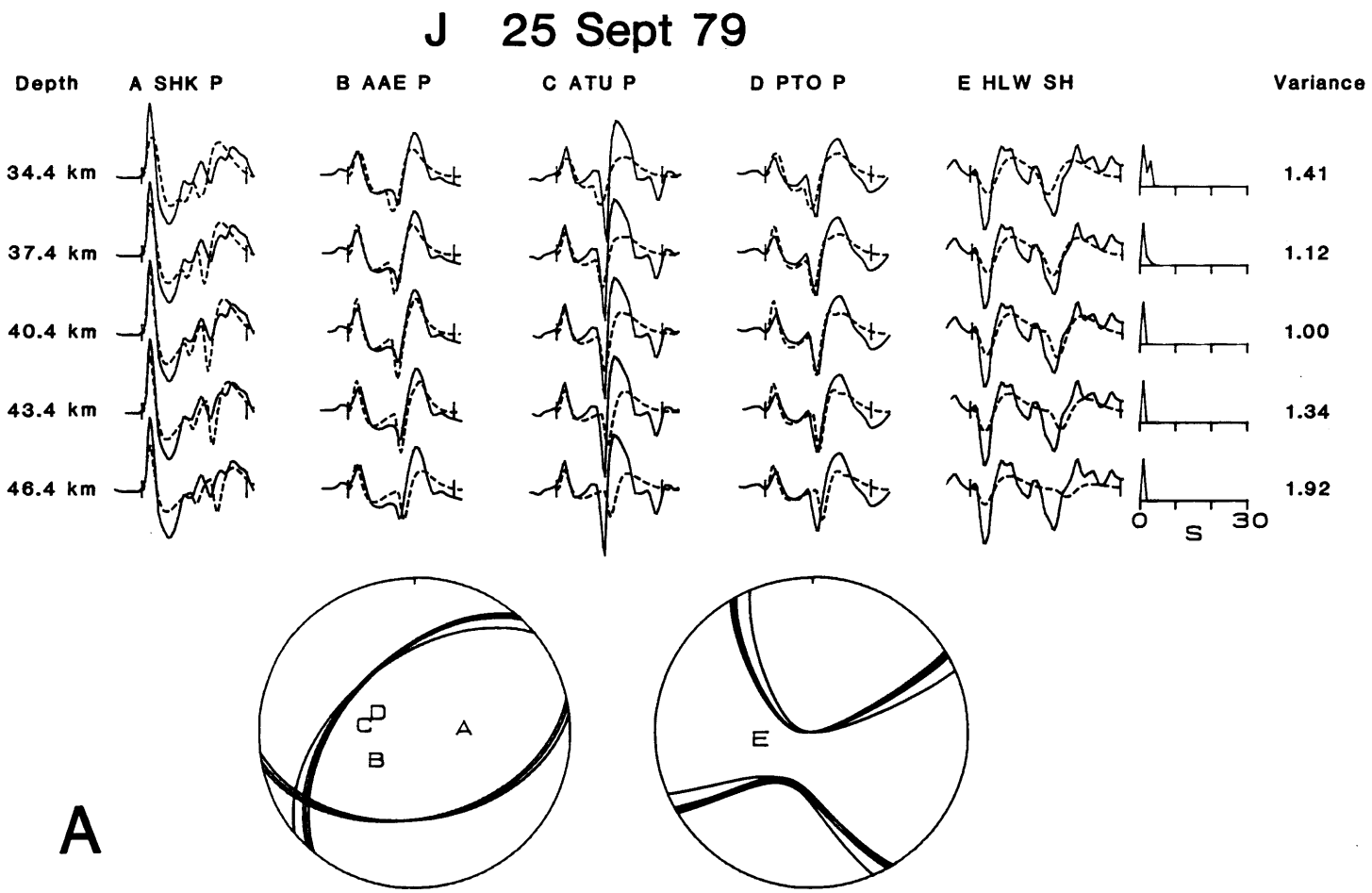
J 25 Sept 79
Depth
A SHK P
B AAE P
C ATU P
D PTO P
E HLW SH
Variance
34.4 km
37.4 km
40.4 km
43.4 km
46.4 km
1.41
1.12
1.00
1.34
1.92
0
S
30
A
B
C
D
E

Figure 19a

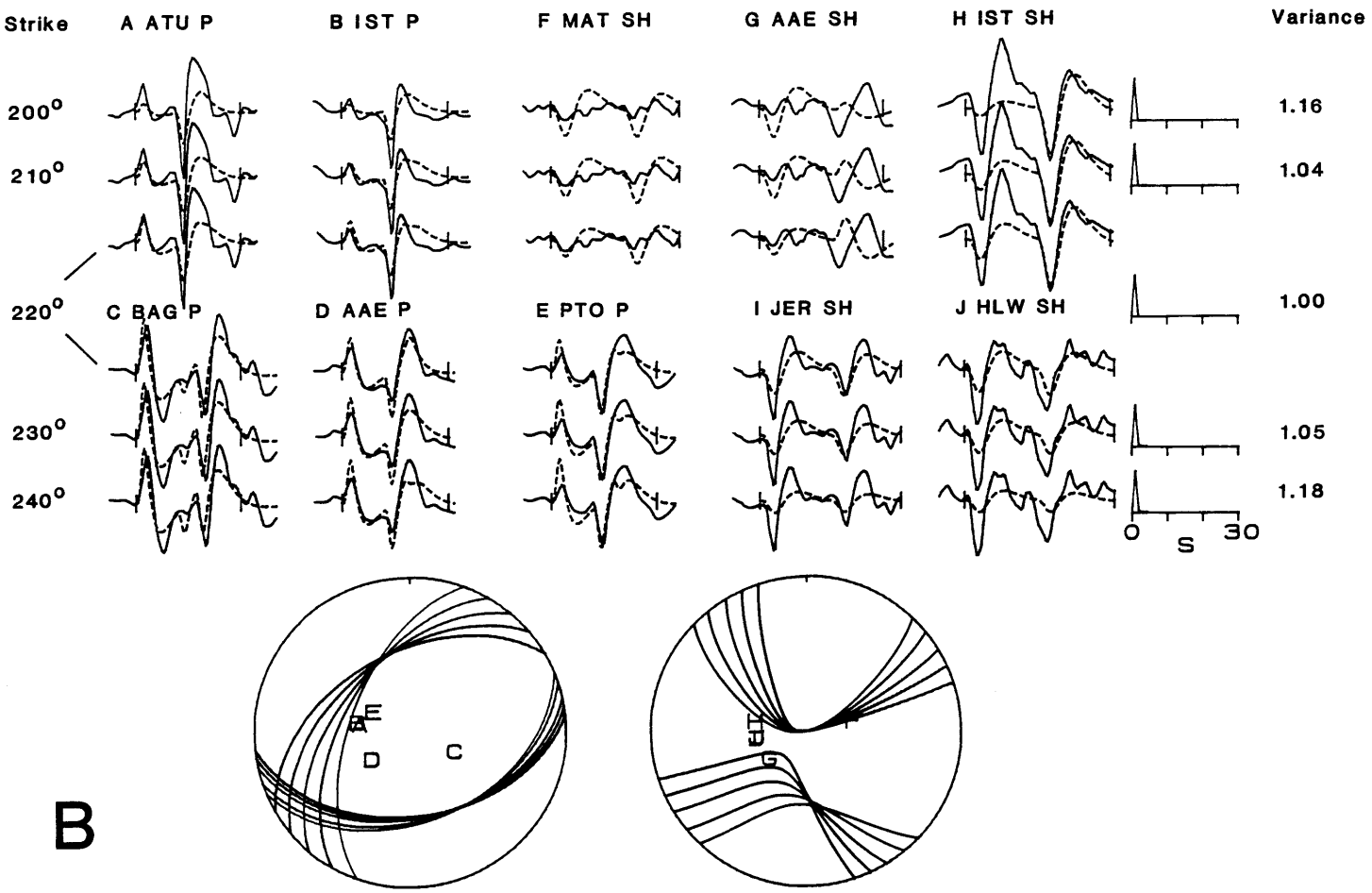
J 25 Sept 79
Strike
A ATU P
B IST P
F MAT SH
G AAE SH
H IST SH
Variance
200°
210°
220°
230°
240°
C BAG P
D AAE P
E PTO P
I JER SH
J HLW SH
1.16
1.04
1.00
1.05
1.18
0
S
30
B
A
E
D
C
H
G

Figure 19b

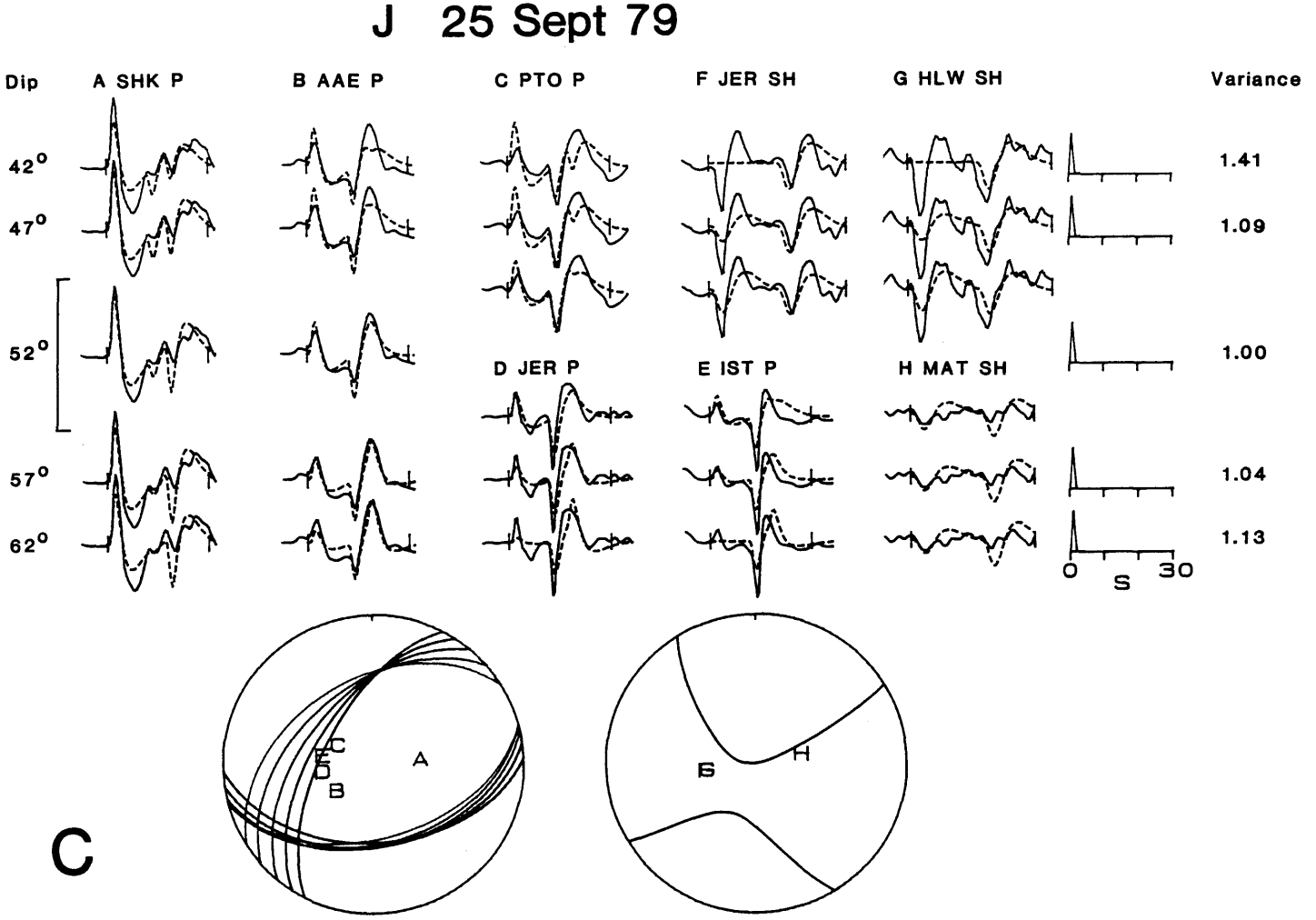
J 25 Sept 79
Dip
A SHK P
B AAE P
C PTO P
F JER SH
G HLW SH
Variance
42°
47°
52°
57°
62°
D JER P
E IST P
H MAT SH
1.41
1.09
1.00
1.04
1.13
0
S
30
C
A
B
C
D
E
F
G
H

Figure 19c

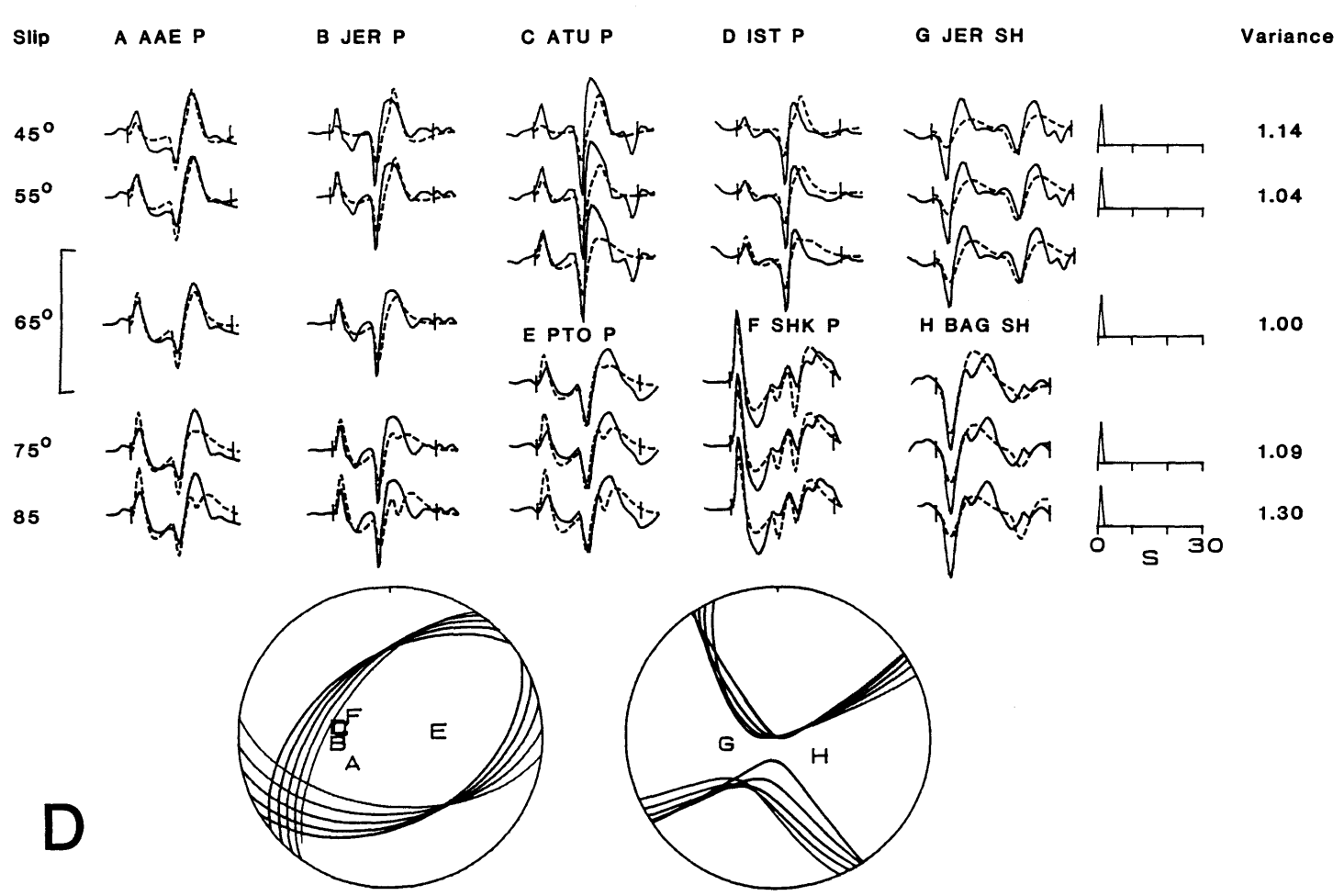
J 25 Sept 79
Slip
A AAE P
B JER P
C ATU P
D IST P
G JER SH
Variance
45°
55°
65°
75°
85
E PTO P
F SHK P
H BAG SH
1.14
1.04
1.00
1.09
1.30
0
S
30
D
A
B
C
E
F
G
H

Figure 19d

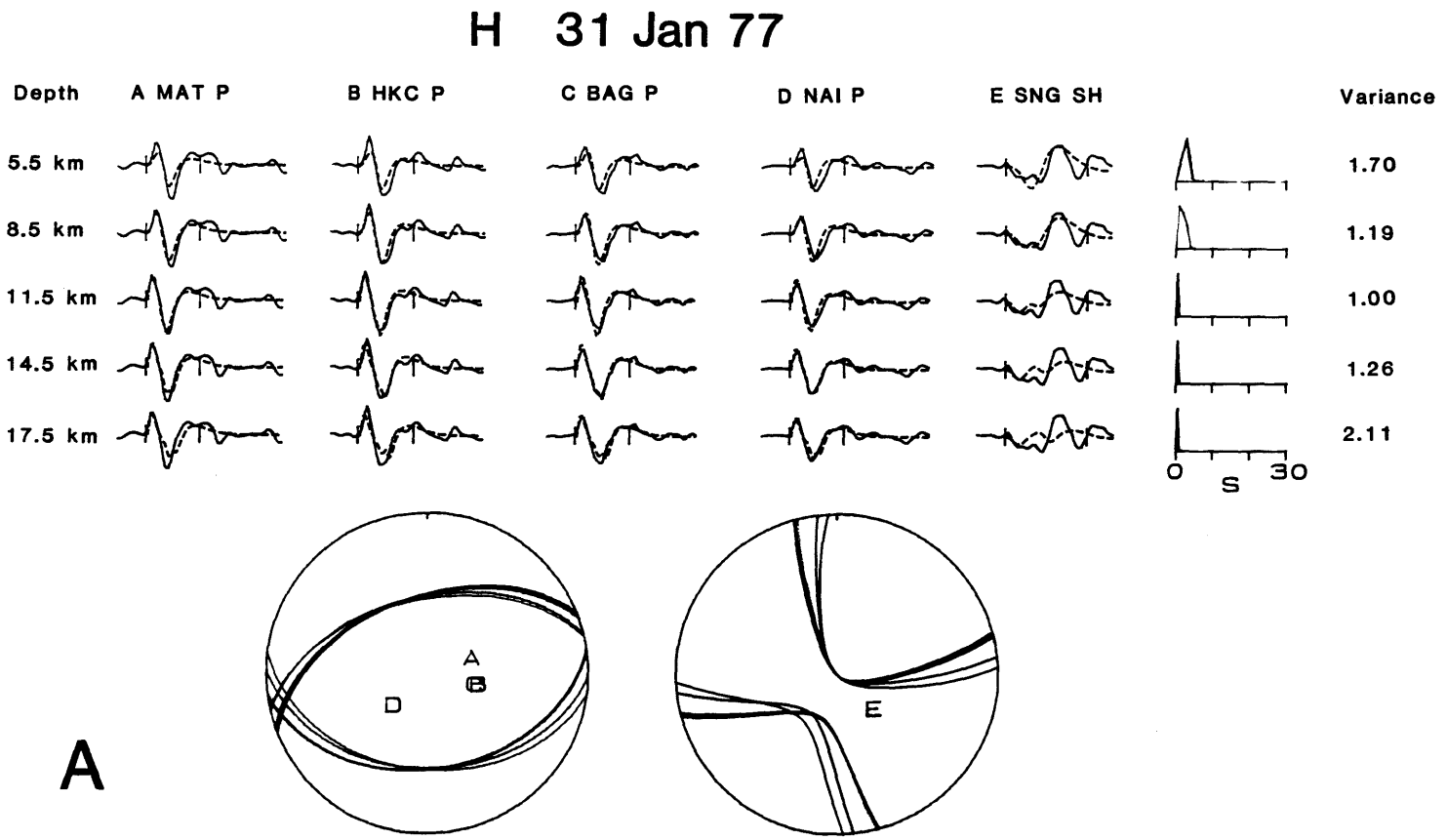
H 31 Jan 77
Depth
A MAT P
B HKC P
C BAG P
D NAI P
E SNG SH
Variance
5.5 km
8.5 km
11.5 km
14.5 km
17.5 km
1.70
1.19
1.00
1.26
2.11
0
S
30
A
B
D
E
A

Figure 20a

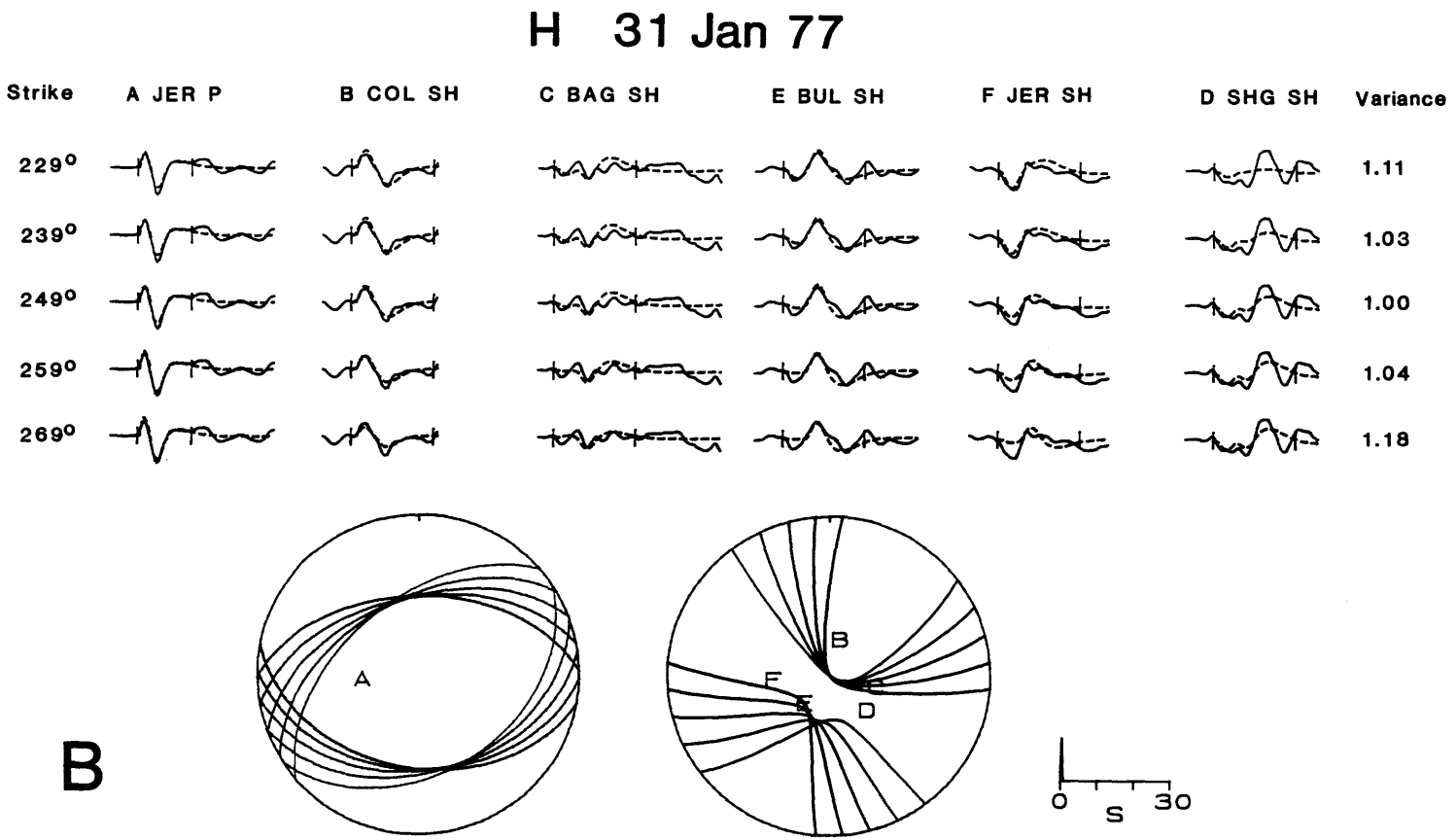
H 31 Jan 77
Strike
A JER P
B COL SH
C BAG SH
E BUL SH
F JER SH
D SHG SH
Variance
229°
239°
249°
259°
269°
1.11
1.03
1.00
1.04
1.18
B
A
B
F
E
D
0
S
30

Figure 20b

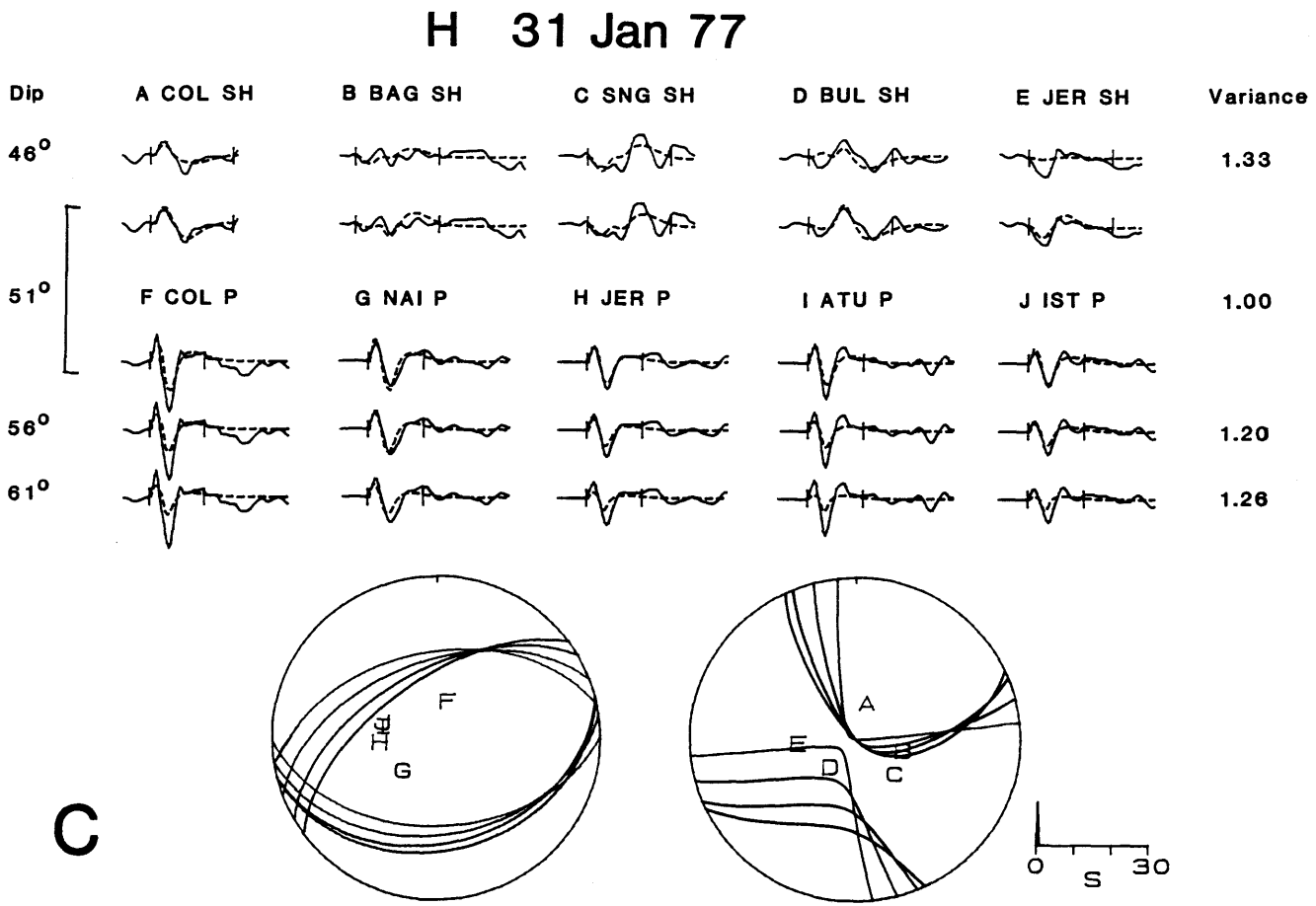
H 31 Jan 77
Dip
A COL SH
B BAG SH
C SNG SH
D BUL SH
E JER SH
Variance
46°
1.33
51°
F COL P
G NAI P
H JER P
I ATU P
J IST P
1.00
56°
1.20
61°
1.26
C
F
H
G
A
E
D
C
0
S
30

Figure 20c

H 31 Jan 77

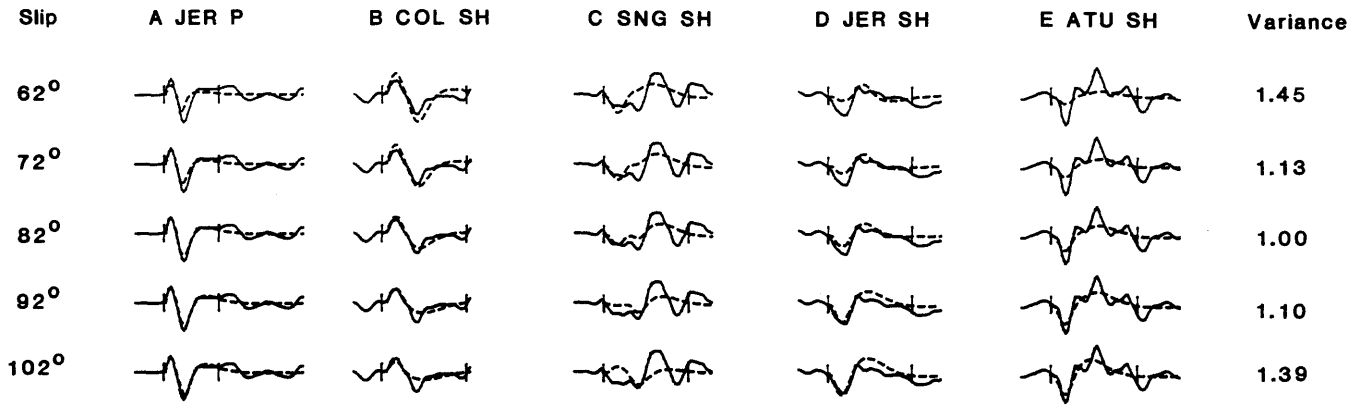

D

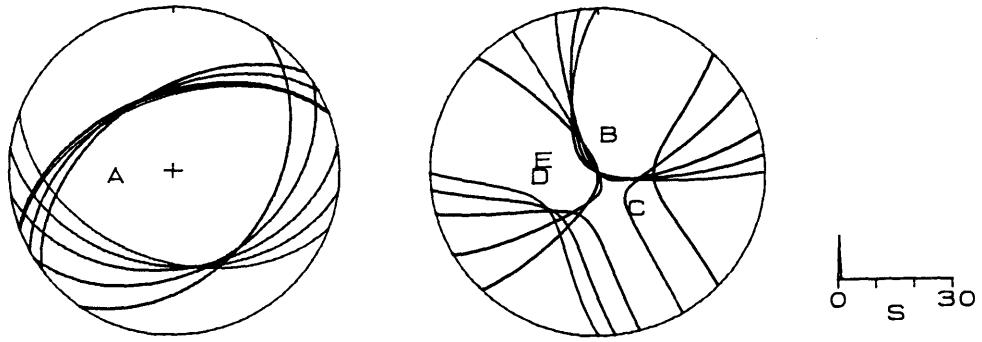

Figure 20d

CONSTRAINTS ON THE SEISMIC VELOCITY STRUCTURE OF THE CRUST AND UPPER MANTLE BENEATH THE EASTERN TIEN SHAN, CENTRAL ASIA

Michael R. Nelson

Department of Earth, Atmospheric, and Planetary Sciences,
Massachusetts Institute of Technology, Cambridge, MA

ABSTRACT

Uplift in the Tien Shan mountain belt of Central Asia began in Oligocene time, following the collision of India with Eurasia more than 1000 km to the south. Since then there has been more than 100 km of north-south shortening across the belt, resulting in elevations of over 7 km and east-west trending thrust faults. The relatively simple, linear geometry and Tertiary history of the eastern Tien Shan make it an excellent place to study the effects of crustal shortening on the upper mantle.

In this study a number of seismological techniques are used to determine whether shortening in the eastern Tien Shan has resulted in the thickening of the mantle lithosphere and the formation of a "lithospheric root" beneath the mountain belt. Thickening the mantle lithosphere will reduce the geothermal gradient, resulting in lower temperatures, and thus higher seismic velocities, in the upper mantle.

Previous studies of P wave and S wave station corrections have found larger delays in the eastern Tien Shan than in the Siberian Shield to the north. Soviet refraction profiles indicate that P_n velocities in the eastern Tien Shan are neither exceptionally high nor exceptionally low.

These observations, along with heat flow measurements, indicate that the upper mantle beneath the Tien Shan is warmer than the upper mantle beneath the shield regions that flank it.

By matching synthetic seismograms to long-period World-Wide Standard Seismograph Network (WWSSN) seismograms, I measured P and S arrival times at teleseismic distances for eleven earthquakes in the Tien Shan. By using synthetic seismograms for both P and SH waves, it is possible to alleviate many of the problems with travel-time residual studies caused by hypocenter mislocations and the misidentification of S arrivals. The P and S arrival times were used to calculate "S-P residuals", which are less affected by mislocation errors than P wave or S wave residuals alone. To correct for variations in the seismic velocity structure beneath the WWSSN stations, the P wave station corrections of Dziewonski and Anderson [1983] were used along with S wave station corrections equal to 3 times the P wave corrections. These corrections significantly reduce the scatter in the S-P residuals. For the Tien Shan, mean S-P residuals for individual earthquakes fall between -0.2 and -1.8 s, slightly less negative than mean S-P residuals measured in shield regions.

In order to estimate P wave velocities in the uppermost mantle, seven travel-time plots for raypaths from earthquakes in the Tien Shan to stations in the Tien Shan were constructed, using arrival times measured from seismograms from the Toktogul Reservior seismic network and arrival times reported to the International Seismological Centre (ISC) by Soviet and Chinese seismograph stations. For epicentral distances of 300-1700 km, the first-arriving P wave is the P_n phase, which travels in the uppermost mantle. The travel-time plots yielded P_n velocities of between 8.12 and 8.30 km/s (with typical 1 σ uncertainties of 0.1 km/s). Such velocities are lower than those measured for the Indian, Canadian, and

Siberian shields and higher than those measured in regions of crustal extension, like the Basin and Range of western North America or the East African Rift.

Both the S-P residuals and the P_n velocities indicate that the upper mantle beneath the Tien Shan is warmer and the lithosphere thinner than beneath the shields that flank it. It is possible that the lithosphere beneath the Tien Shan was originally thicker, but that crustal shortening created a lithospheric root that dropped off, driving convection that heated the upper mantle beneath the range. Alternatively, the upper mantle beneath the Tien Shan may have been warmer than the upper mantle beneath the surrounding regions when shortening began, and has simply remained that way.

INTRODUCTION

The collision of India with Eurasia dominates the tectonics of much of Central Asia, affecting a region more than a thousand kilometers wide and two thousand kilometers long [Molnar and Tapponnier, 1975]. Active faulting in the Himalaya, on the Tibetan Plateau, in the Pamir, and in the Tien Shan all seem to be due to the northward penetration of India into Eurasia. The underthrusting of India beneath the Himalaya has built the world's highest mountain range, and crustal shortening in Tibet has doubled the thickness of the crust, resulting in an average elevation of about 5 kilometers (Figure 1). Likewise, in the Tien Shan, north of Tibet, active thrust faulting has produced elevations of up to 7 km, with the heights of many mountain ranges reaching 5 km. These high elevations and active faulting are the most obvious results of crustal shortening in Central Asia. What is less obvious is the effect of this shortening on the underlying mantle. This study focuses on shortening in the eastern Tien Shan and how it might have affected the upper mantle structure of that region.

When crustal shortening like that in the Tien Shan occurs, the crust will thicken and the mantle directly below the crust will be displaced downward (Figure 2), depressing the isotherms in the thickened crust and uppermost mantle and reducing the geothermal gradient. The resulting cool, dense "lithospheric root" of mantle material is likely to be gravitationally unstable, and it should eventually either drop off or warm up to the temperature of the surrounding mantle. Houseman et al. [1981] showed that the if the thickness of the lithosphere is doubled it would take >100 m.y. for the geotherm to return to its pre-shortening value if convection did not occur. Both Houseman et al. [1981] and Buck and Toksöz [1983] used two-dimensional convection models of the upper mantle to examine the stability of the thickened lithosphere that results from crustal shortening. Houseman et al. [1981] studied convection in a medium with constant viscosity and found that for a range of Rayleigh numbers appropriate for the upper mantle and for a variety of initial and boundary conditions, a thickened boundary layer would typically be removed in less than 10 m.y., a time much less than the duration of crustal shortening in typical collision zones (usually 30-50 m.y.). This relatively rapid removal of a lithospheric root would lead to heating of the lower part of the thickened crust, thereby explaining the high grade metamorphism and post-tectonic granites observed in many orogenic belts. Using simple viscous models of the lithosphere, Fleitout and Froidevaux [1982] showed that once a lithospheric root starts to form, the resulting density contrast would cause it to continue to grow until the root dropped off. In this way the formation of a lithospheric root could actually lead to additional crustal shortening. In contrast, Buck and Toksöz [1983] considered convection in fluids with viscosity dependent on

temperature and inferred that thickened lithosphere should be relatively stable for >100 m.y. after thickening occurs. These differing results highlight our lack of understanding about the properties and rheological behavior of the upper mantle and how they affect the dynamics of collision zones.

The relatively simple geometry and history of the eastern Tien Shan make it a particularly good place to study the deep structure and evolution of an intracontinental mountain belt. The eastern Tien Shan is one of the world's largest and most seismically active intracontinental mountain belts. North-south shortening due to the collision of India with Eurasia has produced this linear, east-west trending mountain belt which stretches more than 2000 km across Soviet Central Asia and northwestern China (Figure 1)[Tapponnier and Molnar, 1979]. This shortening continues today as evidenced by the consistent north-south trending P-axes seen in teleseismically-determined fault plane solutions of earthquakes in the eastern Tien Shan [Nelson et al., 1987]. Stratigraphic studies indicate that the present-day elevation of the Tien Shan is due to uplift starting in late Oligocene time [Krestnikov, 1965] and that prior to that time, in late Mesozoic and early Tertiary time, the region was low-lying with little relief.

The Tien Shan is part of an ancient orogenic belt that was active in late Paleozoic time [Burtman, 1975]. It lies between the Siberian Shield and the Tarim Basin, both relatively stable and low-lying regions thought to be underlain by Precambrian basement [Terman et al., 1967; Molnar and Tapponnier, 1981]. A map showing the seismicity for 1971-1984 (Figure 1) reveals that there have been far fewer large earthquakes under the Siberian Shield and the Tarim Basin than in either the Tien Shan or the Tibetan Plateau. In both stable regions, elevations are generally less

than 1500 m. Molnar and Tapponnier [1981] suggested that seismicity and deformation seem to be concentrated in the Tien Shan because the lithosphere of the Tien Shan is warmer, and thus weaker, than that of the adjoining Siberian Shield and Tarim Basin. England and Houseman [1985], using a thin, non-linearly viscous sheet as a model of the lithosphere, examined how heterogeneities in the strength of the lithosphere could have influenced the tectonics of Asia. They found that the lack of deformation, low elevation, and relatively thin crust of the Tarim Basin could be explained if the average strength of the lithosphere underlying the Tarim Basin is 3 or more times greater than that underlying Tibet and the Tien Shan. A difference in strength of this amount could be achieved if the temperature at the Moho was just a few tens of °C cooler under the shield than elsewhere. This difference could also be due to a difference in crustal thickness, because at Moho temperatures and pressures the olivine-rich rock of the upper mantle is much stronger than the more silicic rock of the crust. So an increase in crustal thickness results in relatively strong mantle material being replaced by much weaker crustal rock, causing the average strength of the lithosphere to decrease markedly [Molnar and Tapponnier, 1981]. In this study, I put constraints on the crustal and upper mantle structure beneath the Tien Shan in order to determine the extent to which it differs from the structure underlying the Siberian Shield and the Tarim Basin.

In particular, I consider whether crustal shortening in the eastern Tien Shan has led to the formation of a lithospheric root. The presence of such a root beneath a mountain range can be detected using a number of different geophysical techniques. Because the root is cooler and thus denser than the mantle around it, it might be possible to use gravity measurements to put constraints on the extent of any such root. If the

geothermal gradient in the lithospheric root is decreased, the amount of heat flowing into the crust will be decreased, and this might be reflected in borehole heat flow measurements. Seismic methods also provide constraints on the thermal structure of the upper mantle. If a lithospheric root exists, seismic waves will travel faster in the cooler, denser root than in the warmer mantle around it.

There have been very few studies showing evidence for lithospheric roots beneath actively deforming mountain ranges. From Rayleigh wave dispersion curves for raypaths crossing the Alps, Panza and Mueller [1978] and Mueller [1982b] inferred the presence of a lithospheric root consisting of material with S wave velocities up to 10% greater than those in the surrounding asthenosphere and extending to depths of greater than 200 km. Unfortunately, because of the difficulties in interpreting surface wave dispersion curves for regions with complicated structure, it is hard to evaluate the uncertainties in this inferred velocity structure. Mueller [1982a] presented additional evidence from seismic refraction profiles that indicate that P wave velocities in the uppermost mantle beneath the Alps are unusually high. Baer [1980] found that travel-time residuals at seismic stations in the Alps were similar to those at stations in the northern Alpine foreland, despite the greater crustal thickness under the Alps. Apparently, delays caused by the greater thickness of lower-velocity crustal material beneath the stations in the Alps are compensated by above-average upper mantle seismic velocities, which were inferred to extend to a depth of at least 220 km [Baer, 1980].

In this study I use a number of techniques to examine the velocity structure of the upper mantle of the eastern Tien Shan in order to examine how shortening in the crust has affected the structure of the

underlying mantle. If crustal shortening does lead to the formation of a lithospheric root (Figure 2), we would expect to find one under the eastern Tien Shan. In the last 30 m.y. there has been over 100 km of crustal shortening that must be accommodated by deformation of the upper mantle. Determining how this deformation has occurred is made much easier by the linear geometry of the eastern Tien Shan and its relatively uncomplicated Tertiary history. Most mountain belts have much more complicated geometries and have undergone numerous orogenic episodes. The relative simplicity of the eastern Tien Shan makes it an excellent laboratory in which to study crustal shortening and the effects it has on the structure of the upper mantle.

PREVIOUS WORK

The study of the structure of the crust and upper mantle beneath the eastern Tien Shan and surrounding regions has been hampered by both geography and geopolitics. The rugged, roadless terrain makes access to much of the region very difficult and the Chinese-Soviet border which divides the eastern Tien Shan is another major hurdle to any integrated study of the region.

Very little work has been published on the deep structure of the Chinese Tien Shan. I am not aware of any seismic refraction profiles for the region, although the Chinese have shot thousands of kilometers of reflection profiles in the Tarim Basin and the Dzungarian Basin as part of their petroleum exploration effort [Yuan et al., 1986]. Similarly, there have been very few published studies of seismicity and seismic velocity structure of the Chinese Tien Shan, primarily because of the lack of local seismic stations. Until the early 1980's there were only two seismograph stations operating in the Chinese Tien Shan, one at Ürümqi and one at Kashgar (Figure 1). For this reason, Wang and Li

[1984] relied on first-motion polarities reported by the International Seismological Centre (ISC) in their study of fault plane solutions for earthquakes in northwestern China. The opening of several new seismological stations in the region in the last few years, including some with digital seismometers, should result in a major improvement in both the quantity and quality of seismic data available from the Chinese Tien Shan.

Western geophysical studies. Foreign researchers studying the structure of the eastern Tien Shan have also been hindered by the lack of available data. Although Chinese and Soviet scientists have made thousands of gravity measurements in the region, these data are classified and unavailable. Likewise, seismic data are very difficult to obtain. Most published geological maps are published only at a very small-scale and often lack geographical coordinates or even a scale.

In one of the few Western studies of the crustal structure of the Tien Shan region, Patton et al. [1985] used seismographs from explosions at the Soviet Central Asian nuclear test site at Semipalatinsk (Figure 1) recorded at the Chinese seismograph station at Ürümqi to study surface wave dispersion for paths crossing the Dzungarian Basin. They determined dispersion curves for surface waves with periods 4-20 seconds and found evidence for several kilometers of low-velocity sediment in the Dzungarian Basin. Shear wave velocities for depths greater than 15 km were not significantly different from those found in continental regions underlain by Precambrian or Paleozoic basement.

In their study of the Tarim Basin, Lyon-Caen and Molnar [1984] used pendulum gravity measurements made on the 1929-1933 Sino-Swedish Expedition across the Tarim Basin to show that the western part of the Tarim Basin is not in isostatic equilibrium. They found that the gravity

data could be explained if a strong plate underlying the Tarim Basin were thrust under the adjoining Kunlun Mountains at least 80 km, thus supporting part of the topography of that part of the Tibetan Plateau. The Tarim plate is apparently quite strong, with a flexural rigidity of about 5×10^{23} N m (corresponding to an equivalent elastic plate thickness of about 40 km). Such a value is somewhat less than those inferred for shields but significantly greater than those typical of orogenic regions. For example, Lyon-Caen and Molnar [1983], using the same approach, found the Indian Shield to have a flexural rigidity of about 7×10^{24} N m where it is bent down beneath the Ganga Basin and the Lesser Himalaya.

McNutt and Kogan [1987] used Soviet gravity admittance data from the eastern Tien Shan to determine that the region was not locally isostatically compensated. They found evidence that the Tien Shan is partially supported by the underthrusting of the Tarim Basin from the south. Their value for the flexural rigidity of the Tarim Basin plate was slightly larger (corresponding to an equivalent elastic plate thickness of $\approx$50 km) than that found by Lyon-Caen and Molnar [1984] in the southwestern Tarim Basin. Nevertheless, both results imply that the Tarim Basin is underlain by relatively cold, strong lithosphere.

Soviet refraction profiles. The vast majority of geophysical research done in the eastern Tien Shan has been done by Soviet researchers working in the western part of the region. Over the past thirty years, Soviet scientists have conducted more than 200 deep seismic sounding (DSS) experiments [Belyaevsky et al., 1973; Vol'vovskii and Vol'vovskii, 1975]. Unfortunately, only a few profiles have been made in the eastern Tien Shan, mostly along the western and northern margins (see Figure 3). Gamburtsev and Veitsman [1956] and Gamburtsev et al. [1955] constructed

cross-sections of the crust and upper mantle from the results of gravity measurements and two refraction profiles between Lake Issyk-Kul and Lake Balkhash (profiles 4 and 5 on figure 3). These sections show the crust, consisting of a "granitic" layer over a "basaltic" layer, increasing in thickness from 40 km in the center of the profile to almost 60 km beneath Issyk-Kul. They inferred a P wave velocity of 8.1 km/s for the uppermost mantle beneath the center of the profile. On their seismic section from a DSS profile running east-west across the northern foothills of the Tien Shan near Frunze (profile 3 in Figure 3), Vol'vovskii and Vol'vovskii [1975; see their Figure 85] indicate that the depth to the Moho is ≈46 km at the east end of the profile, increases to ≈50 km in the center, and then decreases to ≈ 40 km near the west end of the profile. A P wave velocity of 8.1 km/s is shown for the uppermost mantle beneath the center of the profile. The longer of two DSS profiles in the intermontane Fergana Basin (profile 1 in Figure 3) showed the depth to the Moho increasing from ≈42 km at the west end of the profile to ≈54 km in the center of the basin and then decreasing to ≈51 km at the east end of the profile [Godin et al., 1960; Vol'vovskii and Vol'vovskii, 1975, Figures 92 and 93]. A P wave velocity of 8.3 km/s was inferred for the uppermost mantle beneath the center of the basin. The cross-profile (profile 2 in Figure 3) revealed a crustal thickness of 52 km and an upper mantle velocity of 8.2 km/s beneath the center of the valley, with the crustal thickness decreasing to ≈47 km near the edges of the basin. Unfortunately almost none of the seismograms from these DSS profiles have been published, making it very difficult to assess these interpretations. Still, it is clear that the crust of the Soviet Tien Shan is significantly thicker than average continental crust. Maps of crustal thickness for Central Asia based on the results of DSS profiles and

topographic and gravity data [e.g. Belyaevski et al., 1973; Kosminskaya et al., 1969; Yudakhin, 1983] differ in detail, but all show crustal thicknesses of 40-50 km for the Siberian Shield north of the Tien Shan, an average crustal thickness of 50-55 km in the Tien Shan, and thicknesses of up to 65 km under the highest part of the eastern Tien Shan.

Travel time residuals. Much of the Soviet seismological work in Central Asia has been motivated by the need to quantify the seismic risk for the several large and growing cities in the area (e.g. Alma-Ata and Frunze)[Galperin et al., 1986]. The first seismograph stations in Central Asia were established in Tashkent and Alma-Ata in the first decade of this century and by 1950, more than ten seismic stations were operational [Kirnos et al., 1962]. Today, there are more than 40 stations in the Tien Shan.

Vinnik and Saipbekova [1984] used arrival times for teleseisms recorded at these stations to calculate P wave travel-time residuals for the eastern Tien Shan between 70° E and 80° E. For each station they determined average travel-time residuals for those back-azimuth windows (each 20° wide) that contained data. A correction for crustal thickness was made based on the crustal thickness map of Yudakhin [1983]. Unfortunately, Vinnik and Saipbekova [1984] did not publish the teleseismic residuals for each station, but instead smoothed the data, constructed a two-dimensional model of average upper mantle velocities, and published a contour map of P wave residuals calculated for their model. Figure 4 is a redrafted version of their contour map [Figure 27 of Saipbekova, 1986]. The most obvious feature of the map is that residuals are slightly positive (0-0.5 seconds) in the Tien Shan around Issyk-Kul in the eastern part of the study area, while in the western part of the study area, residuals tend to be negative, reaching values of

less than -1.0 second near the western edge of the map. The residuals change most rapidly across a northwest-trending zone roughly corresponding to the Talas-Fergana Fault, a Paleozoic strike-slip fault re-activated in Tertiary time and active today [Burtman, 1980; Leith et al., 1986]. The map also shows quite negative residuals (and thus relatively high seismic velocities) for the Siberian Shield north of the Tien Shan. Unfortunately, this region is near the edge of the study area, where there are few seismic stations. In addition, it appears that no correction was made for the thick accumulation of sedimentary rock beneath stations in the Fergana and Issyk-Kul basins that may account in part for the lower seismic velocities reported for the Tien Shan. Although it is hard to evaluate their work without knowing the values of the residuals for each station, it appears that Vinnik and Saipbekova [1984] have found evidence for somewhat lower seismic velocities beneath the eastern Tien Shan than beneath either the Siberian Shield or the rest of the Soviet Tien Shan.

In their global studies of station corrections, Poupinet [1977; 1979] and Dziewonski and Anderson [1983] used teleseismic arrival times reported to the ISC by Soviet seismological stations. Dziewonski and Anderson [1983] determined P wave station corrections for eleven stations in the Tien Shan (Figure 3; Table 1). Poupinet [1977], using a smaller set of ISC arrival times, determined both P wave and S wave station corrections for several of the same stations. Both studies found that P wave station corrections were generally positive in the Tien Shan indicating that average seismic velocities beneath the stations are somewhat lower than the global average. Stations in the eastern Tien Shan (AAA, AAB, FRU, NRN, PRZ, and TLG) tended to have more positive corrections than those in the rest of the Tien Shan. Poupinet's [1977] S

wave station corrections range from 2.46 to 3.48 seconds for those stations in the eastern Tien Shan. In contrast to the generally positive P wave and S wave station corrections in the Tien Shan, station corrections for the Siberian Shield, north of the Tien Shan, are consistently negative (Table 1). According to Dzeiwonski and Anderson [1983], the average P wave station correction for the Tien Shan is about one second greater than that for stations on the Siberian Shield. Likewise, Poupinet [1977] found negative P wave and S wave station corrections for stations on the Siberian Shield. In the Lake Baikal region northeast of the Tien Shan, both studies found values lying between those in the Tien Shan and those on the Siberian Shield.

Part of the statistically significant difference in average station correction between the stations in the Tien Shan and those on the Siberian Shield can be explained by the greater crustal thickness beneath the Tien Shan. Dziewonski and Anderson [1983] used arrival times for events with epicentral distances of 30° to 90°. At these distances, assuming P wave velocities of 6.4 km/s for the lower crust and 8.2 km/s for the upper mantle, the P wave arrival time will be delayed 0.038 ± 0.002 s/km of increase in crustal thickness. If the average crustal thickness beneath the stations in the Tien Shan were 15 km greater than that beneath the three stations on the Siberian Shield, this would explain more than half (0.57 ± .03 s) of the observed one-second difference in station correction. The average elevation of stations in the Tien Shan is about 1 km greater than that of stations on the Siberian Shield. For an upper crustal velocity of 6.0 km/s, this corresponds to an additional 0.17 to 0.20 seconds delay. Nonetheless, even after accounting for delays due to crustal thickness and elevation, station corrections in the Tien Shan are on average 0.4 seconds larger than those

for stations on the Siberian Shield. This difference, which is even larger for stations in the eastern Tien Shan, may be indicative of lower P wave velocities in the upper mantle beneath the Tien Shan and would seem to support the conclusions of Vinnik and Saipbekova [1984].

Other Soviet studies. Vinnik and Saipbekova [1984] also constructed travel-time curves using industrial explosions recorded at seismograph stations in the Tien Shan. They found relatively low average P wave velocities (< 8.0 km/s) for the upper mantle in the eastern Tien Shan east of the Talas-Fergana Fault and inferred the presence of a low-velocity zone directly beneath the crust, a deduction confirmed by Ryaboi and Nikitina [1986] using similar data. In contrast, for raypaths in the Tien Shan west of the Talas-Fergana Fault, for distances of 350 to 500 km, Vinnik and Saipbekova [1984] found arrival times to be more than 2 seconds earlier than those east of the fault. This led them to conclude that there is no low-velocity zone beneath the western Tien Shan and that upper mantle P wave velocities there increase from ≈8.0 km/s directly beneath the Moho to ≈8.4 km/s at a depth of ≈90 km.

Vinnik and Saipbekova [1984] correlated this difference in upper mantle velocity structure with differences in the gravity field on either side of the Talas-Fergana Fault. Artem'yev and Golland [1983] reported that the lithosphere of the eastern Tien Shan is in almost perfect isostatic equilibrium, but that in the western Tien Shan there are large isostatic gravity anomalies. Unfortunately, the gravity data upon which they base their conclusion are unavailable.

Surface wave studies in the Tien Shan also reveal significant differences in velocity structure across the northwest-trending Talas-Fergana Fault. Sabitova and Yanovskaya [1986] inverted group velocity dispersion curves for Rayleigh waves with periods from 5 to 12 s for 51

paths in the Soviet Tien Shan and northeastern Tarim Basin and constructed smoothed group velocity maps for various periods of Rayleigh waves. The most prominent feature of these maps is the consistently low Rayleigh wave group velocities in the Tarim Basin due to the thick accumulation of sediments there. According to Bally et al. [1986], in places in the northwestern Tarim Basin there are more than 10 km of Mesozoic and Cenozoic sedimentary rock. At longer periods (9-12 s) Sabitova and Yanovskaya [1986] found evidence for a marked decrease in group velocity in the vicinity of the Talas-Fergana Fault, which they associated with a similar decrease in upper mantle P wave velocity observed by other workers. Arkhangelskaya and Sadykov [1973] calculated Rayleigh wave phase and group velocity dispersion curves for paths between seismic stations in the Soviet Tien Shan and found abnormally low group and phase velocities for paths across the Fergana Basin, presumably due to the presence of several (8-10) km of sedimentary rocks. Unfortunately, both these studies utilized only short period (2-13 s) surface waves and thus do not place constraints on the velocity structure of the upper mantle beneath the Tien Shan.

At least 100 heat flow measurements have been made in the Soviet Tien Shan [Lyubimova et al., 1986]. More than twenty borehole measurements have been made in the southern Tien Shan southeast of Samarkand and most fall in the range 50-75 mW/m^2. Another 35 measurements have been made in and around the Fergana Basin, where values range from 30 to 107 mW/m^2 with a mean value of $\approx$70 mW/m^2. Lyubimova et al. [1986] reported three measurements from the northern foothills of the eastern Tien Shan around Frunze and Alma-Ata, ranging from 46 to 50 mW/m^2. More than thirty measurements have been made in and around Issyk-Kul, with most of them made on the lake bottom using an electron thermogradiograph [Lyubimova et

al., 1986]. The resulting values show a very large scatter (29 to 134 mW/m^2) over distances of < 10 km, making them hard to interpret. The bulk of Soviet heat flow measurements for the eastern Tien Shan are somewhat greater than the worldwide average, but typical of Tertiary orogenic regions. They fall between values measured on platforms and shields, like the central United States and Canadian Shield (where heat flow, q, is typically 30-50 mW/m^2) and values measured in regions of active crustal extension like the Rio Grande Rift and Basin and Range of the western United States, where q is typically 60-100 mW/m^2 [Lachenbruch and Sass, 1977; Morgan and Sass, 1984]. Because of the scatter in the heat flow measurements in the Tien Shan and the difficulty in evaluating the effects of uplift and erosion on heat flow measurements in orogenic belts [e.g. England and Richardson, 1980], the Soviet heat flow data do little to constrain the thermal structure of the crust and upper mantle of the eastern Tien Shan.

The available geophysical data for the eastern Tien Shan do not put tight constraints on the structure of the mantle beneath the region. Travel time residual studies using Soviet seismic stations indicate that seismic velocities in the upper mantle beneath the Soviet Tien Shan may be somewhat lower than average. Unfortunately, there are no such data for the Chinese Tien Shan. Refraction profiles in the Soviet Tien Shan west of the ≈74° E indicate rather high P wave velocities (8.2-8.3 km/s) in the uppermost mantle. In contrast, refraction profiles in the eastern Tien Shan have been interpreted as showing a low-velocity zone in the upper mantle with P wave velocities of <8.0 km/s. Gravity measurements in the eastern Tien Shan have been used by one group of workers to infer that the region is locally isostatically compensated and by another group to infer that the Tien Shan is supported in part by the underthrusting of

the Tarim Basin beneath the mountain range. Since the raw gravity measurements are unavailable, it is difficult to evaluate these two opposing conclusions. Heat flow measurements from the eastern Tien Shan show a large amount of scatter around a mean value typical of Tertiary orogenic belts.

TELESEISMIC S-P TRAVEL TIME RESIDUALS

In order to determine whether the crustal shortening in eastern Tien Shan has led to the formation of a lithospheric root, I have studied S wave and P wave travel time residuals from well-located earthquakes in the Tien Shan. If crustal shortening in the Tien Shan were associated with a lithospheric root beneath it, we would expect to find evidence for relatively high seismic velocities in the upper mantle beneath the Tien Shan. The magnitude of such velocity anomalies should depend upon how much shortening has occurred, upon the velocity structure of the region before shortening began, and upon how quickly the cool lithospheric root is heated by the surrounding mantle.

The amount of Tertiary shortening in the eastern Tien Shan cannot be accurately determined without much more detailed geological mapping, but it is possible to make rough estimates from the topography and the few available measurements of crustal thickness. As shown on north-south topographic profiles across Tibet and the Tien Shan (Figure 5), the eastern Tien Shan lies between the 40° N and 45° N, a region about 550 km wide with an average elevation of about 2 km. According to Vinnik and Saipbekova [1984] the eastern Tien Shan is in almost perfect isostatic equilibrium. If this is the case, then the average depth to the Moho under the Tien Shan is given by:

$$H_1 = \frac{(\rho_m - \rho_c)H_0 + \rho_c h}{\rho_m - \rho_c} = H_0 + \frac{\rho_c h}{\rho_m - \rho_c} \quad (1)$$

Where, H_0 is the thickness of the crust prior to shortening, h is the average elevation of the Tien Shan, and ρ_c and ρ_m are the average density of the crust and mantle, respectively. For ρ_c equal to 2800 kg/m3, ρ_m equal to 3300 kg/m3, and h equal to 2 km, and assuming an original crustal thickness of 35 km, H_1 will be ≈46 km and the average crustal thickness (H_1 + h) will be 48 km. We can calculate how much north-south shortening would be required to increase the average crustal thickness from 35 km to 48 km in the Tien Shan. Assuming that there has been little transport of material east or west (out of the plane of the sections in Figure 6) the cross-sectional areas must be equal, so

$$H_0W_0 = (H_1 + h)W_1 \quad (2)$$

where W_0 is the original width of the shortened region (750 km) and W_1 is the present width of the shortened region (550 km). This implies that there has been ≈200 km of crustal shortening in the shortened region.

Yudakhin's [1983] map of crustal thickness for the Soviet Tien Shan shows the crustal thickness increasing from 40-45 km under the Siberian Shield to nearly 65 km under the Issyk-Kul region. His map, based upon a few refraction profiles and numerous gravity measurements in the region, indicates that the average crustal thickness in the Soviet Tien Shan is 50-55 km. Thickening 40-km thick crust to 50 km implies ≈140 km of shortening spread over 550 km. Because of the assumptions involved and because erosion has been neglected, these estimates of the amount of shortening across the Tien Shan are quite uncertain and the actual amount of shortening in the region probably could be anywhere from 100 to 350 km, corresponding to 18%-63% crustal thickening.

This crustal shortening will result in deformation of the upper mantle. One possibility is that the crust and the mantle directly beneath it will

be thickened by the same amount (37% in the cross-sections in Figure 6). In the cartoons in Figure 6, it has been assumed that in Cretaceous time, prior to the formation of the present-day Tien Shan, the crustal thickness and thermal structure of the Tarim Basin, the Tien Shan orogenic belt, and the Siberian Shield were all the same. Typically for a shield the temperature at the Moho, T_M will be relatively low (≈400° C) and the geothermal gradient, dT/dz, will be on the order of 5° C/km. For these values, the 1000° C isotherm, the base of the mechanical lithosphere, would be at a depth of ≈155 km. Then ≈200 km of shortening of a region originally 750 km wide would depress the isotherms below the Tien Shan and thicken the mechanical lithsphere by ≈37% (or ≈55 km).

In these cartoons it has been assumed that the effects of conduction and convection in the mantle are small. If this were the case and there were a stable, lithospheric root beneath the Tien Shan, the root should be revealed by seismic travel times, because seismic waves would travel faster in the colder material of the lithospheric root than in the surrounding mantle at the same depth. It is possible to estimate the magnitude of these differences in travel times, even though the geotherm and physical properties of the mantle are not well-constrained. This requires first estimating the difference in temperature between the lithospheric root and the surrounding mantle.

The temperature of the mantle outside the lithospheric root, assuming a constant geothermal gradient, dT/dz, for the undisturbed mantle, will be

$$T(z) = T_M + (z - H_0)\frac{dT}{dz} \qquad (3)$$

where T_M is the temperature at the Moho and z is depth.

For the purpose of this calculation it is assumed that the lithospheric root has not been heated since it was formed. Thus, the

temperature at the depth of the Moho, H_1, beneath the Tien Shan will be the same as it was before shortening began, namely, T_M. The geotherm in the lithospheric root will be decreased by γ, where

$$\gamma = H_0/(H_1 + h) \tag{4}$$

So the temperature in the lithospheric root at depth z will be

$$T(z) = T_M + \gamma(z - H_1)\frac{dT}{dz} \tag{5}$$

and the difference in temperature between the lithospheric root and the surrounding mantle will be

$$\begin{aligned}\Delta T(z) &= [T_M + (z-H_0)\frac{dT}{dz}] - [T_M + \gamma(z - H_1)\frac{dT}{dz}] \\ &= [z - H_0 - (z-H_1)/\gamma]\frac{dT}{dz}\end{aligned} \tag{6}$$

Then the difference in temperature between the lithospheric root and the surrounding mantle averaged between the Moho at depth H_1 and the 1000° C isotherm beneath the shortened region (Z_L) will be

$$\overline{\Delta T} = \frac{1}{2}[H_1 + Z_L - 2H_0 - (Z_L - H_1)/\gamma]\frac{dT}{dz} \tag{7}$$

If we know how seismic velocity in the mantle varies with temperature we can estimate the average difference in seismic velocity,

$$\overline{\Delta v} = \frac{1}{2}[H_1 + Z_L - 2H_0 - (Z_L - H_1)/\gamma]\frac{dT}{dz}\frac{dv}{dT} \tag{8}$$

Laboratory measurements for olivine indicate that dV/dT varies little over for the temperatures and pressures in the upper mantle. Birch [1969] has measured and calculated the temperature dependence of P wave velocity in olivine and has found that for mantle temperatures and pressures $d(\log V_p)/dT$ ranged from -70×10^{-6}/° C at 727° C to -83×10^{-6}/° C at 1227° C. For a value of -75×10^{-6}, with $V_p = 8.1$ km/s, $dv_p/dT \approx 6.1 \times 10^{-4}$ km/s/° C. Using this value and a value of γ appropriate for the Tien Shan (0.73), we find that between the Moho and the 1000° C at a depth of 210 km, the average difference in P wave velocity between the lithospheric root and the surrounding mantle,

$$\overline{\Delta v_p} \approx .10 \text{ km/s} \tag{9}$$

For S waves, $d(\log v_S)/dT$ ranges from $-79 \times 10^{-6}/^\circ$ C at 727° C to -89×10^{-6} at 1227° C [Birch, 1969]. For

$$d(\log v_S)/dT = -84 \times 10^{-6}/^\circ \text{ C and } v_S = 4.7 \text{ km/s}$$

$$dv_S/dT \approx 3.9 \times 10^{-4} \text{ km/s}/^\circ \text{ C}$$

and so,

$$\overline{\Delta v_S} \approx .07 \text{ km/s} \tag{10}$$

Now we can estimate the travel times for seismic waves propagating vertically downward from two crustal earthquakes, both at a depth of H_0, one in the Tien Shan and one in the undisturbed shield (Figure 6b). Seismic waves from earthquake B will reach a depth of Z_L in time

$$t_B = \int_{H_0}^{Z_L} \frac{dz}{v(z)}$$

$$\approx (Z_L - H_0)/\overline{v_m} \tag{11}$$

Where $\overline{v_m}$ is the mean seismic velocity in the undisturbed mantle between the Moho and a depth of Z_L (210 km in this case). Seismic waves from earthquake A will reach the same depth in time

$$t_A = (H_1 - H_0)/v_c + \int_{H_1}^{Z_L} \frac{dz}{v(z) + \Delta v(z)}$$

$$\approx (H_1 - H_0)/v_c + (Z_L - H_1)/(\overline{v_m} + \overline{\Delta v}) \tag{12}$$

because $v(z)$ does not vary much with depth and $\overline{\Delta v} \ll \overline{v_m}$. The difference in travel time,

$$t_A - t_B = (H_1 - H_0)/v_c + (Z_L - H_1)/(\overline{v_m} + \overline{\Delta v}) - (Z_L - H_0)/\overline{v_m}$$

$$\approx (H_1 - H_0)/v_c - (H_1 - H_0)/\overline{v_m} + (Z_L - H_1)\overline{\Delta v}/\overline{v_m}^2 \tag{13}$$

because $\overline{\Delta v} \ll \overline{v_m}$.

The first two terms represent the delay caused by the greater thickness of crust beneath the epicenter of earthquake A. With an 11-km crustal root, $H_1 - H_0 = 11$ km. For P waves, with $v_c = 6.4$ km/s and $\overline{v_m} = 8.1$ km/s, this delay will be about 0.36 s. For S waves, with

v_c = 3.7 km/s and $\overline{v_m}$ = 4.7 km/s, this delay will be about 0.63 s. These delays will be partially offset by the higher seismic velocities in the lithospheric root than in the surrounding mantle. Substituting the values from equations (9) and (10) into equations (11) and (12) yields

$t_A \approx 21.0$ s and $t_B \approx 20.8$ s for P waves.

If a correction for the travel time delay caused by the greater crustal thickness beneath earthquake A is subtracted from t_A, we get

$t_A' = t_A - 0.36$ s = 20.6 s

Thus, for the velocity structure shown in Figure 6, the lithospheric root should cause a 0.2 s difference in travel time for vertically-travelling P waves from the two earthquakes. For S waves,

$t_A = 37.4$ s and $t_B = 37.2$ s

Adding a crustal thickness correction yields

$t_A' = t_A - 0.63$ s = 36.8 s,

so that the lithospheric root could cause a 0.4 s delay of S waves from earthquake B relative to those from earthquake A. For rays travelling to stations at epicentral distances of 30°-40°, take-off angles in the mantle will be about 45° (as shown in Figure 6 with 5× vertical exaggeration). For these rays travel time delays should be be greater by $1/\sin(45°) \approx 1.41$.

These rough estimates are lower bounds on the travel time anomalies that would arise from the temperature structure shown in Figure 6. Only the differences in seismic velocity above the 1000° C isotherm at 210 km were considered. If the lithospheric root were to extend to greater depths, the differences in travel time would increase accordingly. The actual thermal dependence of seismic velocities in the mantle are probably greater than those measured for olivine in the laboratory. In his study of slab earthquakes, Sleep [1973] empirically derived a value

of $dv_p/dT \approx 50\%$ greater than that used here. If this value had been used the P wave delays calculated above would have been 50% greater. Moreover, the values of dv_p/dT and dv_s/dT measured for pure, solid olivine in the laboratory may not be applicable if there is partial melt present in the upper mantle. Even a small percentage of partial melt could dramatically change the S wave velocity and increase the value of dv_s/dT.

So it appears that travel time residuals of at least 0.5 s and possibly 1-2 s could arise from a well-developed lithospheric root beneath the Tien Shan. By measuring P and S wave residuals for teleseismically recorded earthquakes we can obtain evidence to constrain the extent of such a lithospheric root. As illustrated below, travel time residuals at a single station can be measured with uncertainties of less than 0.5 s and, although the scatter between stations can be quite large, it is possible to achieve an uncertainty in the average residual for a given earthquake of <0.5 s.

Technique

In an earlier study [Nelson et al., 1987] the focal mechanisms and focal depths for eleven of the largest earthquakes in the Tien Shan between 1965 and 1982 were determined, using a waveform inversion routine [Nabelek, 1984]. For that study, long-period P and S waveforms from World-Wide Standardized Seismograph Network (WWSSN) seismograms were digitized, the S wave components were rotated to isolate the SH component, and then the P and SH waveforms were matched to synthetic seismograms [Langston and Helmberger, 1975]. These digitized records and the synthetic seismograms generated by the waveform inversion routine have been used in this study to determine reliable P wave and S wave arrival times at teleseismic distances for these earthquakes.

The waveforms were hand digitized with a digitizing interval of about 1 s. Peak, troughs, and inflection points were digitized and a cubic spline was used to interpolate the data at 0.2 s intervals [Wiggins, 1976]. Digitizing the same seismogram repeatedly revealed that the seismograms could be digitized with an accuracy of about ±0.2 seconds. Using the source parameters determined previously [Nelson et al., 1987], synthetic seismograms were generated and cross-correlated with the interpolated data to determine the P wave and S wave the arrival times. For each event studied between 6 and 12 P and S arrivals were determined. In all but one case (9 Apr 72), where S arrivals were obscured by a later earthquake, there is coverage for at least three quadrants of the focal sphere.

Figures 7-9 show the seismograms used for the earthquake of 2 June 1973. This earthquake was relatively small (m_b = 5.7) and so most of the waveforms had peak-to-peak amplitudes of less than 10 mm. For such relatively small events the signal-to-noise ratio on short-period WWSSN seismograms is quite small at teleseismic distances, making it difficult to determine the P arrival time from the short-period records.

Figure 8 illustrates how the long-period WWSSN seismograms were used to determine the P arrival times. In the middle row the arrival time was adjusted so that the mismatch between the synthetic seismograms (dashed lines) and the WWSSN waveform (solid lines) was minimized. In the top and bottom rows the synthetic seismograms have been shifted one second to the left and right, respectively. For stations with relatively strong P wave first arrivals, like HKC, IST, and ATU, the seismograms were aligned using only the first 3 s of the waveforms, which includes only the first peak. The variance was calculated for a range of arrival times (Figure 8b), and the quality of the correlation at each station was

graded according to the estimated uncertainty: A for ±0.2 s; B for ±0.5 s; C for ±1.0 s; and D for stations where P could not be reliably picked. For HKC, the first arrival is large and distinct, the variance plot has a sharp minimum, and the arrival time can be determined with an uncertainty of ±0.2 s. For stations like IST and ATU, the first arrival is smaller than later arrivals, but there is still an obvious minimum on the variance plot (Figure 8b). An apparent error in the instrument magnification reported for ATU increases the mismatch between the seismograms for that station. Nevertheless, changing the arrival time by ±1 s causes an unacceptable mismatch between the waveform and the synthetic seismogram (Figure 8a). At both COL and GDH, the P phase is nearly nodal and thus its arrival time is not clear. For such stations the first 15 s of the waveforms were cross-correlated with the synthetic seismograms generated using the fault plane solution and focal depth estimated from waveforms recorded at other stations. By matching both the direct P and the larger reflected phases pP and sP, the P arrival time could be estimated with an uncertainty of ±1.0 s even though P is nodal. Fortunately, most of the earthquakes studied occurred on thrust faults with moderately-dipping (35°-55°) nodal planes, so that stations at teleseismic distances, which plot near the bottom of the focal sphere, do not fall near the P wave nodal planes.

In contrast, SH is nearly nodal at many stations, complicating the already difficult task of picking S arrival times. Unlike the direct P phase, S must be distinguished from earlier phases, which tend to obscure it. In particular, the Sp conversion at the base of the crust beneath the receiver can make it difficult to measure the S arrival. I avoid the problems posed by S to P converted phases by working with SH waves. Still, when SH is nearly nodal, noise from earlier P phases obscures the

S arrival. For each earthquake, I used the previously determined fault plane solutions to determine the stations where SH should be nearly nodal and ignored them, rather than risk misidentifying some other phase as S. Most of the waveforms shown in Figures 7 and 9 are for stations that plot well away from the SH nodal surfaces, and accordingly the SH waveforms are large, making it easy to estimate the S wave arrival time by matching the first 15 s of the SH waveforms with the corresponding synthetic seismograms. For the stations COL and KOD, however, SH is nearly nodal and indistinct. At KOD, the S arrival could not be reliably identified without having the synthetic seismogram to provide the polarity and shape of the SH waveform. At COL, SH is nodal and is indistinguishable from the noise. The first clear phase is sS, which is predicted to arrive ≈15 s after the small direct phase. Having a good estimate of the fault plane solution allows one to recognize near-nodal seismograms, such as that at COL, and cull them from the data set used to calculate the mean S-P residual.

In addition, inverting the waveforms for the far-field source time function of the earthquake enables us to identify those earthquakes that are comprised of several subevents. Such earthquakes are more difficult to use for residual studies and also more likely to be mislocated. Nine of the eleven earthquakes studied had simple, short (<5 s) source time functions making them well-suited for this kind of study. The two exceptions (11 February 1969 and 23 March 1971) appear to consist of two subevents, with the second, much larger one occurring about five seconds after the first [Nelson et al., 1987]. For these two events, the first-arriving P waves are emergent, making it more difficult to determine accurate P wave arrival times.

Another source of uncertainty in most S wave residual studies stems from the lack of depth control for the earthquake [see Chen and Molnar,

1981]. For instance, if the assumed focal depth is overestimated by 10 km then the calculated origin time will be ≈1.5 s early and the predicted S wave travel time for stations at teleseismic distances will be in error by 2.5 s, increasing the S wave residual by 1 s. For the earthquakes studied, the centroid depths are known with an uncertainty of 4 to 7 kilometers and often differ from the focal depths published by the ISC by more than 15 km (Figure 10). By using the depths determined by waveform inversion, this error in residuals is lessened.

For each earthquake, P and S arrival times were determined as described above. Clock corrections were applied assuming linear drift. These amounted to less than 0.1 s for 80% of the arrivals picked. Only four clock corrections were larger than 1.0 s.

Predicted arrival times were calculated using the epicenters determined by the ISC and the J-B travel time tables [Jeffreys and Bullen, 1967]. The focal depths determined for these events by Nelson et al. [1987] were used and the ISC origin times were adjusted accordingly, using an appropriate value of dT/dh (according to the J-B tables for Δ = 40°-50°, dT/dh = 4.9 s/33 km ≈ .148 s/km).

Interpretation

The P and S waves recorded at distances of 30° to 85° spend more of their time in the lower mantle than in upper mantle and crust beneath the source and receiver. Nevertheless, because the lower mantle is much less heterogeneous than the crust and upper mantle [e.g. Dziewonski and Anderson, 1981] travel time residuals primarily reflect lateral variations in the seismic velocity structure beneath the source and the receiver. By averaging residuals from a number of stations and by applying station corrections, the effects of receiver structure can be minimized, allowing us to isolate the delay due to the velocity structure beneath the source.

The average P wave residuals alone do not tell us much about the seismic velocity structure beneath the source because of the uncertainty in the origin time. Because there are few local stations in the Tien Shan, the origin time is constrained primarily by arrival times at stations at teleseismic distances and the ISC location routine will simply adjust the origin time so that the average P wave residuals at these stations is zero. An error in the origin time will cause a corresponding error in the P wave residual,

$$\Delta t_p = t_p - t_0 - t_p^{JB}$$

where t_p is the P wave arrival time, t_0 is the origin time determined by the ISC, and t_p^{JB} is the P wave travel time predicted from the Jeffrey-Bullen travel-time tables. Subtracting the P wave travel-time residual from the S wave travel-time residual,

$$\Delta t_s = t_s - t_0 - t_s^{JB}$$

where t_s is the S wave arrival time, t_s^{JB} is the S wave travel time predicted from the Jeffrey-Bullen travel-time tables yields the "S-P residual",

$$\Delta t_{S-P} = \Delta t_s - \Delta t_p$$

$$= t_s - t_p - (t_s^{JB} - t_p^{JB})$$

Because the S-P residual is independent of the origin time, it provides a better measure of the S wave delay due to the velocity structure along the raypath than does the S wave residual itself. If the origin time were known precisely, the S-P residual would be approximately equal to 60% of the S wave residual because S wave residuals tend to be equal to 2-3 times the corresponding P wave residuals [e.g. Hales and Doyle, 1967].

For nine of the earthquakes studied, the average S-P residuals fall between -1.4 and 0.9 s. The remaining two events (11 February 1969 and 23 March 1971) have very different average S-P residuals (1.6 and 6.0

s, respectively), even though their computed epicenters are within 10 km of each other. The scatter in S-P residuals is larger for these two events than for any of the other nine earthquakes (Figure 11). As mentioned above, these two events were the only ones that were not characterized by simple, short source time functions. Both earthquakes consisted of a small subevent followed about 5 s later by a larger subevent. At more distant or particularly noisy stations, arrivals from the first event could easily have been overlooked so that the arrival times reported would be for the second, larger subevent. Presumably, this led to errors in the ISC locations of these events, which in turn caused the large scatter in the residuals (Table 2). Such location errors can be detected by plotting the residuals as a function of azimuth (Figures 11a-k). If the epicenter were mislocated 0.5° (≈56 km) too far south, at a station south of the epicenter at a distance of 40°, the P wave residual would be 4.1 s too large and at a station a similar distance north of the epicenter, it would be 4.1 s too small. In the same manner, the S wave residuals will be in error by 7.45 s, leading to errors in the S-P residuals of as much as 3.35 s. This may be the cause of the large scatter in the residuals for the earthquake of 11 February 1969. Figure 11b shows how for this event, S-P residuals for stations to the south are larger than average, and for stations to the north they are smaller than average. A similar problem seems to affect the residuals for the 23 March 1971 event (Figure 11d). Because there are no stations in the quadrant between 345° and 75° for this event, errors in the S-P residuals at southern stations could lead to a large error in the average S-P residual. The disparate mean S-P residuals and the large scatter for these two earthquakes imply that both are mislocated by >20 km.

Accordingly, I have used only the remaining nine, well-located earthquakes to constrain the velocity structure beneath the Tien Shan.

Variations in the seismic velocity structure beneath the receiver also contribute to the scatter in the data. For several stations, most notably the East African stations NAI and AAE, the S-P residuals are larger than average, a phenomenon also observed by Molnar and Chen [1984] (Figure 11). At other stations they are consistently small.

In order to correct for the effects of receiver structure, I use two different sets of P wave station corrections, those of Poupinet [1977] and those of Dziewonski and Anderson [1983]. There are far fewer sets of S wave station corrections [Sengupta, 1975; Poupinet, 1977]. Sengupta [1975] analyzed S wave travel times at only 14 deep-focus earthquakes, most of which occurred around the margins of the Pacific Ocean. Thus, his results are not strictly applicable to raypaths from shallow events in Central Asia. Poupinet's [1977] results are based upon routine S picks reported to the ISC, which are often unreliable due to the problems of picking S arrivals outlined above. Nevertheless, when the P wave and S wave station corrections of Poupinet [1977] were used, the standard deviation of the mean S-P residuals decreased for eight of the eleven earthquakes (Table 2), and the standard deviation of the mean S-P residual for all nine well-located events decreased by ≈25%, indicating that his station corrections are useful.

As an alternative to using Poupinet's station corrections, I used Dziewonski and Anderson [1983] P wave station corrections both to correct the P arrival times and to derive S wave station corrections. Dziewonski and Anderson [1983] used a much larger and more recent subset of ISC arrival times than did Poupinet [1977] and also studied azimuthal variation of travel-time anomalies at those stations for which they had enough data.

I have used only the azimuth-independent term of their station corrections because the azimuthal terms usually account for less than 10% of the total station correction. Dziewonski and Anderson [1983] determined only P wave station corrections, but P wave and S wave station corrections are likely to be correlated because differences in density and shear modulus that affect P wave velocities will also affect S wave velocities. Several studies of P wave and S wave station corrections have found that the ratio of S wave to P wave station corrections is significantly larger than the expected value of $\sqrt{3} \approx 1.73$ (for a Poisson's ratio of 0.25) and instead tends to fall in the range of 2.5 to 3.5 [Hales and Doyle, 1967; Souriau and Woodhouse, 1985; Romanowicz and Cara, 1980; K. Toy, personal communication, 1987]. Dziewonski and Anderson's [1983] P wave station corrections were multiplied by five different ratios of S wave to P wave station correction (1.73, 2.0, 2.5, 3.0, 3.5) to produce five sets of station corrections for S waves, which were then applied to the S arrival times. Varying the value of this ratio changed the mean S-P residual for a few earthquakes by more than 1 s, but the mean S-P residual for all nine well-located events changed by less than 0.7 s (see Table 3). This is rather insignificant because S-P residuals have been observed to vary by as much as 10 s from one tectonic region to another [e.g. Duschenes and Solomon, 1977; Molnar and Chen, 1984]. A value of 3.0 was used to derive the S wave station corrections for the S-P residuals listed in Table 2. By using Dziewonski and Anderson's [1983] station corrections in this way the standard deviation of the S-P residuals was reduced for eight of the eleven earthquakes and the standard deviation of the mean for all nine well-located earthquakes was reduced by ≈20%. The mean corrected S-P residuals for the nine well-located earthquakes fall in the range of -1.3 to 0.3 s (Table 2).

As explained above, it is necessary to make a correction for the thicker crust of the Tien Shan in order to isolate the effect of the upper mantle velocity structure. For epicentral distances of 30°-80° and typical values of P and S wave velocities for the lower crust and mantle, the S-P residuals should be increased by 0.025 ± .002 s per additional km of crust [Molnar and Chen, 1984]. Maps of the depth to the Moho for the Tien Shan indicate that the crust is ≈65 km thick under the highest part of the Tien Shan and 50-55 km thick beneath the northern and southern edges of the range where most of the earthquakes studied occurred [Zhang et al., 1984; Kosminskaya et al., 1969; Terman et al., 1967; Yudakhin, 1983]. Unfortunately, the crustal thickness is not well-constrained and different maps can vary by more than 5 km for the same location. If the globally averaged crustal thickness is 33 km, then the crust beneath these earthquakes is on average 20 km thicker, and a correction of 0.5 s should be subtracted from the S-P residuals calculated here. Thus, the range of values, after applying station corrections based on Dziewonski and Anderson's [1983] values and correcting for crustal thickness, is -1.8 to -0.2 s (Figure 12).

These values indicate that the average S wave velocity for the crust and upper mantle beneath the Tien Shan is slightly higher than the world-wide average, somewhat lower than that beneath shield regions, and higher than that beneath regions like the Basin and Range or the East African Rift. The S-P residuals do not provide evidence for a thick lithospheric root. As explained above, if there were a thick root beneath the eastern Tien Shan, we would expect to find S-P residuals even more negative (by 0.5 to 2.0 s) than those observed beneath shield regions like those flanking the Tien Shan.

Molnar and Chen [1984] measured S-P residuals for earthquakes in the Himalaya similar in value to those in the Tien Shan. After applying a crustal thickness correction but not station corrections, they found mean S-P residuals between -1.0 and 0.6 s for the Himalaya, which is underlain by the cold Indian Shield [Lyon-Caen and Molnar, 1983]. Chen and Molnar found much larger, positive values for Tibet (all but one value greater than 1.0 s). The largest values (4.5 and 4.9 s) were found for the north central Tibetan Plateau where extensive partial melting of the lower crust has presumably occurred [Barazangi and Ni, 1982]. Pettersen and Doornbos [1987] also found large, positive S-P residuals (4.6 and 4.8 s with respect to the J-B tables) for northern Tibet.

Azimuthal variation of travel-time residuals

The P and SH-wave travel time residuals measured in this study can also be used to study azimuthal variations in the velocity structure beneath the Tien Shan. Most of the earthquakes studied occurred near the edges of the Tien Shan, so that if there were a well-developed lithospheric root of higher-velocity mantle beneath the Tien Shan, seismic waves from these earthquakes would travel more rapidly beneath the Tien Shan than beneath the adjoining shield regions. For instance, for earthquakes B, D, F, and I along the southern edge of the Tien Shan, we would expect to see more negative P wave and S wave travel-time residuals at stations north of the epicenter than at stations to the south (Figure 12).

A close examination of the plots of S-P residuals versus azimuth (figures 11a-l) fails to reveal any such pattern. There does appear to be an azimuthal variation of S-P residuals for earthquakes B and D, with larger S-P residuals for stations southwest of the epicenter, but as explained above, this is probably due, not to near-source velocity

variations, but to location errors resulting from the complex source time functions of these earthquakes. For the other seven earthquakes along the edges of the Tien Shan there is no obvious pattern of azimuthal variation indicative of higher-velocity mantle beneath the Tien Shan. Such variations, however, could be masked by errors in locating the earthquakes.

Unfortunately, without local stations to constrain the epicenter, we are forced to use the same teleseismic P arrivals both to locate the earthquake and to measure variations in the velocity structure beneath the earthquake. Higher-velocity material to one side of the epicenter will result in the hypocenter being mislocated in the direction of the higher-velocity material, because the epicenter location routine assumes that travel time varies only with distance and adjusts the hypocenter location so that the average P wave residual is zero. This mislocation will likewise reduce any variation in the S wave residuals. Thus, although the S-P residuals provide no evidence for large azimuthal variations in the upper mantle velocity structure beneath these earthquakes, epicenter mislocations, the limited number of measurements, and the scatter in the S-P residuals make it difficult to rule out such variations.

Residual spheres

In another attempt to find evidence of seismic velocity anomalies in the upper mantle beneath the Tien Shan, residuals were plotted on the focal sphere using ISC arrival times for 14 earthquakes in the Tien Shan (Table 4), employing the technique Creager and Jordan [1984; 1986] used to analyze travel times from dozens of intermediate and deep-focus earthquakes in subducting slabs around the Pacific. For each earthquake the ISC P wave arrival times were used to compute residuals relative to a

spherically symmetric velocity model of the earth [Herrin et al., 1968]. These residuals were then corrected using the ellipticity correction of Dziewonski and Gilbert [1976], the lower mantle velocity model L02.56 of Dziewonski [1984], and the receiver station corrections of Dziewonski and Anderson [1983]. These corrected residuals were then used to relocate the earthquakes and to determine new travel-time residuals. These new residuals were plotted on the lower half of the focal sphere and smoothed to average the effects of small-scale heterogeneities far from the source.

This residual sphere technique has been used extensively to document near-source velocity anomalies due to the subduction of cold, higher-velocity slabs into the mantle. After smoothing, Creager and Jordan [1984] found variations in travel time residuals of as much as 2 s between different regions of the focal sphere for slab earthquakes. As might be expected, residuals are negative for raypaths in the cold slab and positive for raypaths that exit the slab near the source.

Residual spheres were plotted and smoothed for 14 earthquakes in the Tien Shan (Table 4). For ten of these events, focal mechanisms and focal depths were well-constrained by earlier studies [Nelson et al., 1986; Nelson et al., 1987]. When these events were relocated, their focal depths were fixed at the values determined in these earlier studies. For the remaining earthquakes, the ISC focal depth was assumed. The choice of focal depth affects only the take-off angle for stations plotted on the focal sphere and does not otherwise alter the pattern of residuals on either the raw or smoothed residual sphere.

The residual spheres for 12 of the 14 earthquakes showed little or no evidence for velocity heterogeneities in the upper mantle beneath these earthquakes. The raw data (Figures 13) show no significant, consistent

pattern that might indicate near-source velocity anomalies beneath the Tien Shan. When the residual spheres were smoothed, the total variation in the residuals shrank to less than 0.5 s, and no consistent pattern was seen, even for tightly-clustered earthquakes (cf. earthquakes 7-10).

For two earthquakes, events 1 and 2, both on March 23, 1971, the smoothed residual spheres did show significant (>1 s) variations in travel-time residuals. Both the unsmoothed and smoothed residual spheres for these two earthquakes showed positive residuals (late arrivals) to the northeast and southwest and negative residuals (early arrivals) to the northwest and southeast. However, a third event, earthquake 4, in the same region three months later, did not reveal any significant variation in residual across the focal sphere. This discrepancy is probably due to inaccurately reported arrival times for earthquakes 1 and 2. Earthquake 1 occurred just 26 minutes after an earthquake in the Jan Mayen region (m_b = 5.9). Later phases from this earlier, larger earthquake made it impossible to use the WWSSN waveforms of the Tien Shan event to determine the focal mechanism and focal depth [Nelson et al., 1987] and apparently also made it difficult to accurately determine P wave arrival times at stations reporting to the ISC. Determining the P wave arrival times for earthquake 2 was made difficult by its complex source time function. As explained above, because the event consisted of one event followed by a much larger one ≈5 s later, it is likely that at some stations the first event was detected while at other, more distant or more noisy stations, only the second subevent was detected. For both earthquakes 1 and 2 the residuals at African stations in the southwestern quadrant of the focal sphere and Alaskan and Canadian stations in the northeastern quadrant were on average 1-2 s later than those at stations in Europe, southern Asia, and Australia. This most likely reflects

differences in ambient noise level or instrument magnification at these stations and does not reflect near-source velocity structure.

Thus, neither the S-P residuals nor the P wave residual spheres provide any evidence of azimuthal variation in the velocity structure of the upper mantle beneath the Tien Shan. This may be in part due to the lack of local seismic stations in much of the Tien Shan, which increases the uncertainty in the epicenter, and thus the residuals, for the earthquakes studied. Nonetheless, if there is a well-developed, well-defined lithospheric root beneath the Tien Shan, either of these two approaches would most likely have found evidence of it.

Pn TRAVEL TIMES CURVES

The S-P residuals indicate that the average S wave velocity in the upper mantle beneath the Tien Shan is higher than the worldwide average, but they do not provide information on how seismic velocity varies with depth. Are the small S-P residuals due to higher-than-average seismic velocities in the uppermost mantle or to the absence of a low-velocity zone deeper in the mantle? How deep do these seismic variations extend?

The velocity structure of the Tien Shan, especially the Chinese Tien Shan, is very poorly constrained. I am aware of no published refraction profiles for the Chinese Tien Shan and only a few for the Soviet Tien Shan (figure 3) [Vol'vovskii and Vol'vovskii, 1975]. So, I have constructed refraction profiles using arrival times from stations in the Tien Shan for a number of earthquakes with well-determined epicenters and origin times.

This study will focus on the first-arriving P wave at epicentral distance of 300-1700 km, which I will refer to as P_n. P_n travels in the uppermost mantle with a phase velocity of 7.8 to 8.5 km/s. It was first recognized in 1909 by Mohorovicic, who interpreted it as a head wave

traveling along the crust-mantle boundary [Richter, 1958, p. 282]. More recently, Menke and Richards [1980] have viewed P_n as the sum of whispering gallery waves propagating within a high-velocity zone between the Moho and the upper mantle low-velocity zone. Langston [1982] showed how the character of P_n can vary with the upper mantle velocity structure. He found that in the western United States, P_n was a head wave, but in the eastern United States, it consists primarily of waves that bottom 10-70 km beneath the Moho.

Herrin and Taggart [1962] documented P_n velocity variations in the United States using travel times from both explosions and earthquakes. Apparent P_n velocities ranges from 8.5 km/s in the south central United States to 7.5 km/s in the central Basin and Range. Low P_n velocities were found to be associated with large P wave travel time residuals and high heat flow. Using refraction profiles in North America, Black and Braile [1982] showed that P_n velocity is correlated with heat flow and the temperature at the Moho, suggesting that P_n velocity increases with crustal age. It appears that P_n velocity increases as the continental lithosphere cools after a thermo-tectonic event.

I have determined P_n velocities for the Tien Shan to test the hypothesis that the upper mantle of the Tien Shan is warmer than the upper mantle beneath the shields that it adjoins. If the Tien Shan region is underlain by a cool thermal structure like that beneath a shield, we would expect to see relatively high P_n velocities (8.3-8.5 km/s) like those seen beneath shield regions. Because v_p increases with pressure and thus depth, shortening might actually lead to an increase in P_n velocity. On the other hand, lower P_n velocities (8.0-8.2 km/s) would indicate that the mantle beneath the Tien Shan region is warmer than the surrounding shields.

Refraction profiles east of the Toktogul seismograph network

There are relatively few seismograms available from stations in the Tien Shan. I have used seismograms recorded by the joint US-USSR seismograph network established in 1978 around the Toktogul reservior in the Soviet Tien Shan to monitor induced seismicity [Simpson et al., 1981]. Although this network of short-period seismometers was installed to study local seismicity, it is possible to use it to determine travel times for P waves from earthquakes in the Tien Shan, the Pamir, and the Tibetan Plateau.

The Tien Shan and the region adjoining it are seismically very active; between 1979 and 1985, the years for which seismograms are available, more than 200 regional earthquakes with $m_b > 5.0$ were recorded at Toktogul. For those events northeast, east, and southeast of Toktogul, arrival times were read from the paper records of seismograms. The data from all stations in the network are recorded on analog tape with paper copies of seismograms made for two or three of the ten stations in the network. More than 600 arrival times were measured for 276 events. Arrival times were graded according to estimated uncertainty (A, ±0.2 s; B, ±0.5 s; C, ±1.0 s; D, worse than ±1.0 s and thus not used). Clock corrections were made assuming linear drift. The timing was checked daily and was rarely in error by more than 0.1 s. An integral for the distance between two points on a spheroidal earth was evaluated numerically [Pearson, 1984; equation 3.3.13] to determine the distance between the epicenter and the station, using the ISC epicentral coordinates. To correct for the varying elevations (1000-3200 m) of the stations, a correction equal to the elevation divided by 3.5 km/s was subtracted from each travel time. In addition, the raypaths for each event were back-projected through the focus to the surface in order that

the results of this study could be compared with those of ordinary refraction profiles. For each earthquake the angle of incidence at the focus was determined using the value of the ray parameter for a surface focus event from the J-B tables, assuming a crustal velocity of 6.1 km/s. The ray path could then be extended to the surface and a correction made to the travel time and the epicentral distance.

The major source of error in determining travel times lies not in measuring the arrival time, but in the origin time, epicenter, and focal depth determined by the ISC. As discussed above, a 0.5° error in epicenter can lead to a 4.1 s error in P wave travel time. For those events recorded by more than 100 stations the formal uncertainties in the ISC location is $\leq$ 0.04° in latitude and longitude. Of course, these errors are calculated assuming a radially symmetrical earth, and lateral variations in P wave velocity could lead to location errors that are much larger. But even an error of 0.40° (44 km) would lead to only a 3.3 s error in travel time. In the study area most earthquakes occur above a depth of 50 km [Chen and Molnar, 1977; Nelson et al., 1987] and only those events with ISC focal depths of less than 60 km were used. Because of the trade-off between focal depth and origin time, an error in focal depth is not as important as an error in epicentral location. An error in focal depth of 40 km would result in an error in travel time of only 2 s.

Interpretation

Reduced travel time plots were made for earthquakes in the Tien Shan (azimuth 60°-90° from Toktogul) and for earthquakes in the Tarim Basin and northeastern Tibet (azimuth 90°-135° from Toktogul) (Figure 15). The scatter on the plots of all events recorded at more than 30 stations is very large (>10 s), indicating that many of these earthquakes are too poorly located to be useful in this study (Figures 16a-b). For many of

the events reported by fewer than 100 stations the ISC reports location errors of 0.05° to 0.10°. By using only those 96 earthquakes recorded by more than 100 ISC stations, the scatter could be reduced considerably (Figures 16c-d). A linear regression on arrival times with Δ = 300-1700 km yields values for the velocity of P_n (Table 5). To examine how the P_n velocity varies with epicentral distance, linear regressions were done for smaller ranges of epicentral distances (e.g. Δ = 1000-1700 km) (Table 6). Unfortunately, the uncertainties in the P_n velocity for these subsets of the data are so large that it is not possible to constrain how P_n velocity varies with epicentral distance.

There appears to be no statistical difference in the P_n velocity for paths beneath the Tien Shan and for paths beneath the Tarim Basin and Tibet. The value for the Tien Shan is actually somewhat larger (8.22 ± 0.06 (1σ) km/s) than that for paths beneath the Tarim Basin and Tibet (8.11 ± 0.04 km/s), but the large uncertainties make them indistinguishable at a 95% confidence level. Unfortunately, without earthquakes in the Tarim Basin, it is not possible to constrain the P_n velocity for paths limited to the Tarim Basin.

One difficulty with these refraction profiles is that they are unreversed. A dip in the Moho could result in errors in the P_n velocity. According to maps of the crustal thickness for the northwestern China [Zhang et al., 1984], the depth to the Moho varies from ≈45 km in the center of the Tarim Basin to up to 65 km under the highest part of the Tien Shan. Such a difference in depth to Moho over a 400 km profile would result in an average dip on the Moho of 3° which could lead to an error of as much as ≈3% (or 0.25 km/s) [Telford, 1976; equation 4.54b]. Thus a dipping Moho could explain much of the scatter in the data, because raypaths from a range of azimuths were used for each profile.

Refraction profiles to Soviet seismograph stations

Fortunately, there is another source of travel times available for the Tien Shan, the arrival times reported to the ISC by Soviet and Chinese stations in Central Asia (Figure 17). Arrival times for Central Asian events between 1971 and 1984 were processed in the same way as the travel time data from Toktogul. It is clear that some of these travel times are suspect and were not used; a few were obviously in error by exactly one minute. Because some of these stations have been in operation since before 1971, much more data are available. Figure 18 shows the distribution of earthquakes used for the refraction profile east of the seismic station TAS (see Figure 19). Note that there are earthquakes along the entire length of the Tien Shan and the raypaths were entirely within the Tien Shan.

For paths along the Tien Shan P_n velocities range from 8.10 to 8.34 km/s for paths westward to Soviet stations (Figures 19 and 20a-d; Table 5). Paths to the one Chinese station in the Tien Shan, WMQ, (Figures 21 and 22) indicate a P_n velocity of 8.26 $\pm$ 0.06 km/s, providing a reversed profile for paths to the Soviet stations. These results seem to corroborate the results from Toktogul, which indicate a P_n velocity of 8.22 $\pm$ 0.06 km/s for paths along the Tien Shan.

Refraction profiles east from Gazli

Since April, 1976, three earthquakes with body-wave magnitudes of 6 or greater and more than a dozen large ($m_b > 5.0$) aftershocks have occurred in the the Gazli region, about 500 km west of the eastern Tien Shan. All of these events have been reported to the ISC by more than 100 stations. These large, well-located events (Table 7) are ideally located to serve as sources for a refraction profile along the axis of the eastern Tien Shan, utilizing the Soviet and Chinese seismograph stations in the Tien

Shan (Figure 23). The number of these earthquakes recorded at each station varied; there were 14 at TAS, 13 at FRU and ANR, 12 at NRN and PRZ, 9 at TLG, 6 at WMQ, 3 at URT, and only one at FRG. The travel times and epicentral distances were calculated according to the procedures explained above, and plotted (Figure 24). A least-square fit to the data for epicentral distances 400-1400 km yields a P_n velocity of 8.23 ± 0.06 km/s, which is consistent with both the profiles from earthquakes in the Chinese Tien Shan to Soviet seismograph stations and also with the profile west of the Chinese station at Ürümqi (see Table 5).

Interpretation

I infer that the uppermost mantle beneath the Tien Shan is warmer than that beneath old shields; arrival times from both the Toktogul network and the ISC yield P_n velocities in the range 8.10 to 8.34 km/s. Unfortunately, it is not possible to infer how P wave velocity varies with depth from a travel time curve for P_n, but it is possible to estimate a regional average of the highest P velocity in the upper 50-100 km of the mantle. For example, if a reversed refraction profile reveals an apparent P_n velocity of v_a, then there must be a layer in the mantle at some depth h with an average velocity of

$$v_p = v_a(r_e - h)/r_e$$

where r_e is the radius of the earth (≈6371 km). Unfortunately, we cannot determine the depth of that layer from P_n travel times alone.

Instead of trying to infer how the P wave velocity varies with depth in the upper mantle beneath the Tien Shan, I have compared the P_n velocities measured in the Tien Shan with similar measurements made elsewhere. Black and Braile [1982] studied refraction profiles in North America and found that P_n velocity varied from 7.79 ± .03 km/s beneath the Basin and Range to 8.20 ± .04 km/s beneath the Atlantic Coastal

Plain. They correlated P_n velocity with estimated temperature at the Moho, finding that P_n velocity decreased ≈0.073 km/s for each 100° C increase in estimated Moho temperature. This result is consistent with laboratory measurements for olivine indicating that a 100° C increase in temperature causes v_p to decrease ≈ 0.061 km/s [Birch, 1969].

Black and Braile's [1982] results are based primarily upon P_n velocities determined from refraction profiles <500 km long and thus should not be used to infer a Moho temperature from P_n velocities measured in the Tien Shan for distances of 300-1700 km. For most plausible upper mantle velocity structures, P_n will penetrate deeper into the mantle as epicentral distance increases. For Δ = 1500 km, a straight line from the source to the receiver will reach a depth of almost 100 km simply due to the curvature of the earth.

One of the few studies to determine P_n velocities at distances of >500 km is that of Ni and Barazangi [1983] for the Indian Shield, the Himalaya, and the Tibetan Plateau. Using short-period seismograms recorded at Indian and Afghan WWSSN stations, Ni and Barazangi [1983] measured travel times for Central Asian earthquakes at epicentral distances of 4°-20° (450-2200 km). They found relatively high P_n velocities for both the Indian Shield (8.40 ± 0.08 km/s) and the Himalaya (8.45 ± 0.08 km/s), which is thought to be underlain by underthrust Indian Shield [Lyon-Caen and Molnar, 1983].

Similarly high P_n velocities have been observed for the Canadian Shield. Figure 25 shows a travel time curve determined from the Early Rise refraction experiment [Hales, 1972]. This curve was used to derive the ER1 velocity model of Green and Hales [1968] for the crust and upper mantle beneath central United States and the Canadian Shield. In this model the P wave velocity for the uppermost mantle is ≈8.1 km/s. At a

depth of about 60-100 km is a discontinuity that gives rise to the triplication in the travel-time curve at a distance of ≈650 km. Below this discontinuity the velocity is ≈8.35 km/s, which corresponds to an apparent velocity at the surface of ≈8.5 km/s. Thus, for the Canadian Shield the apparent velocity of the first-arriving P wave in the distance range 300-1700 km is on the order of 8.4 km/s.

The relatively high values for P_n velocity measured beneath shield regions are similar to the P_n velocity (8.41 ± 0.10 km/s) (Figure 20e) inferred for ray paths to Semipalatinsk (SEM) a station on the Siberian craton, about 500 km north of the Tien Shan (Figure 17). Because of the lack of large earthquakes in the Siberian Shield, however, most of the earthquakes used for the SEM profile are in the Tien Shan at epicentral distances of 1000-1500 km. The raypaths from these events probably penetrate more deeply than those from more nearby events and thus may reflect the presence of higher velocity material at those depths. So the higher P_n velocity may be due to a bias introduced by the lack of large earthquakes closer than 700 km to the station. The apparent velocity of 8.41 ± 0.10 km/s for the first-arriving P wave at distances of 700-1700 km along the profile from SEM is almost as large as the value of ≈8.5 km/s from the Canadian Shield determined in the Early Rise refraction profile (Figure 25) and indicates that seismic velocities beneath the Siberian Shield are relatively high and that temperatures are relatively low.

In contrast to the relatively high P_n velocities for shield regions, P_n velocities in regions of active crustal extension are often less than 8.0 km/s. The data points in Figure 25 are for explosions at the Nevada Nuclear Test Site recorded in the Basin and Range northeast, east, and southeast of the test site. Note that the scatter in the travel times is

large, even though the epicenter, focal depth, and origin time are known precisely. When a line is fit to the Basin and Range data for distances of 300 to 1700 km, a P_n velocity of 7.92 ± .09 is found, significantly less than that found in the Tien Shan.

Similar low P_n velocities were found by Gumper and Pomeroy [1970] for raypath crossing the East Africa Rift Zone. For epicentral distances of up to 2200 km, they found a P_n velocity of 8.06 km/s.

Thus, the P_n velocities measured in Tien Shan appear to be about average, between the high velocities seen beneath shields and the low velocities seen in extensional terranes like the Basin and Range and the East African Rift Zone.

CONCLUSIONS

Average P and S wave velocities in the upper mantle beneath the eastern Tien Shan are measurably less than those observed in shield areas like the Indian Shield or the Canadian Shield. Station corrections [Poupinet, 1977; Dziewonski and Anderson, 1983] and Soviet P wave travel-time residuals [Vinnik and Saipbekova, 1984] are larger for the Tien Shan than for the Siberian Shield to the north. S-P residuals for the Tien Shan are similar or somewhat less negative than those observed in shields. For the eastern Tien Shan, Soviet travel-time plots indicate that seismic velocities in the mantle beneath the eastern Tien Shan are lower than those in the western Tien Shan and the Siberian Shield [Vinnik and Saipbekova, 1984]. Travel time plots of P_n, constructed using arrival times at stations in the Tien Shan yield P_n velocities of 8.10 to 8.34 km/s, significantly less than is observed for shield regions where P_n velocities are typically $\geq$8.4 km/s for epicentral distances of 300-1700 km.

All these observations are consistent with the conclusion that the upper mantle beneath the Tien Shan is as warm or somewhat warmer than the upper mantle beneath shield regions. The region is clearly not as warm as regions of active crustal extension, like the Basin and Range, or regions with active volcanism, like the north, central Tibetan Plateau. Unfortunately, the nature of the data and our lack of understanding of the thermal properties of the upper mantle make it difficult to put tight constraints on the temperatures in the upper mantle beneath the Tien Shan.

Because the upper mantle in the Tien Shan is warmer than that of the shields adjoining it, it is clear that a lithospheric root like that illustrated in Figure 6 and Figure 26b does not exist beneath the Tien Shan. If such a root existed, the cooler upper mantle temperatures would lead to more negative S-P residuals, higher P_n velocities, and more negative station corrections than are observed in the Tien Shan.

If the lithosphere beneath the Tien Shan has not been thickened, how has the shortening in the crust been accommodated in the mantle? One possibility is that the shortening that has occurred in the crust is displaced from the the shortening in the mantle, perhaps along a decollement extending from the Tien Shan south under the rigid Tarim block (Figure 26c)[B. C. Burchfiel, pers. comm., 1987]. Then, thickened lithosphere would underlie the Tarim Basin and not the Tien Shan, which would be underlain by undisturbed mantle lithosphere. This would be consistent with much of the seismic data, although the P_n velocities and travel-time residuals imply that the upper mantle in the Tien Shan is somethat warmer than that beneath shields.

Another possibility is that the lithospheric root formed by shortening in the Tien Shan has been warmed relatively rapidly by conduction or some

other process (Figure 26d). Then the thermal structure beneath the Tien Shan would be similar to that beneath the surrounding shields.

A fourth possibility is that a lithospheric root formed beneath the Tien Shan but was gravitionally unstable and dropped off into the asthenosphere, driving convection that brought warmer mantle material upward, thereby warming the uppermost mantle (Figure 26e). Houseman et al. [1981] used two-dimensional convection models to show how this could occur for values of Rayleigh number appropriate for the upper mantle.

Another way to explain the higher upper mantle temperatures inferred for the Tien Shan is by assuming that, prior to the initiation of shortening, the Tien Shan region was warmer than the adjoining shield (Figure 27a). If this were the case, then the crustal shortening in the Tien Shan would lead to the thickening of the mantle lithosphere beneath the range. But, depending upon the initial thermal structure, the mantle lithosphere beneath the Tien Shan might still be thinner and warmer that the lithosphere beneath the Siberian Shield and the Tarim Basin. Such a scenerio would explain the seismic data indicating that the Tien Shan upper mantle is somewhat warmer than typical shield regions. It would also explain why deformation has been concentrated in the Tien Shan. If the Tien Shan region were warmer than the surrounding regions, perhaps as a result of late Paleozoic tectonism, the upper mantle would be weaker, and thus more easily deformed [Molnar and Tapponnier, 1981].

The crustal shortening in the Tien Shan must have been accommodated by shortening in the upper mantle. From the available data we cannot determine exactly how this has occurred, but we can eliminate some possibilities. The upper mantle of the Tien Shan appears to be warmer than the upper mantle beneath shields, implying that the mantle lithosphere beneath the Tien Shan is not thicker than that beneath shield

regions. The warmer temperatures might indicate that a lithospheric root formed beneath the Tien Shan but then has dropped off. Or the Tien Shan may have been warmer than the surrounding regions before shortening began. And, of course, it is possible to combine these mechanisms and others illustrated in Figures 26 and 27. For example, the lithospheric root may have been offset from the Tien Shan (Figure 26c) and then dropped off (Figure 26e). Clearly, relating the crustal shortening observed at the surface to the deep structure of intracontinental mountain belts like the Tien Shan is a complicated problem. This study provides constraints on the thickness and thermal structure of the lithosphere beneath Tien Shan, and by doing so, helps us understand better how such mountain belts evolve.

REFERENCES

Arkhangelskaya, V. M., and F. Sadykov, Structure of the upper crust in the Middle Asia by dispersion of surface waves from near earthquakes, Pure and Appl. Geophys., 111, 2223-2235, 1973.

Artem'yev, M. Ye., and V. E. Golland, Isostatic compensation of Tien Shan. Choice of compensation model, Izvestiya, Earth Physics, 19, 30-37, 1983.

Baer, M., Relative travel time residuals for teleseismic events at the new Swiss seismic station network, Annales de Geophysique, 36, 119-126, 1980.

Bally, A. W., I-Ming Chou, R. Clayton, H. P. Eugster, S. Kidwell, L. D. Meckel, R. T. Ryder, A. B. Watts, and A. A. Wilson, Notes on sedimentary basins in China - report of the American sedimentary basins delegation to the People's Republic of China, National Academy of Sciences technical report, 107 pp., 1986.

Barazangi, M., and J. Ni, Velocities and propagation characteristics of P_n and S_n beneath the Himalayan arc and Tibetan plateau: Possible evidence for underthrusting of Indian continental lithosphere beneath Tibet, Geology, 10, 179-185, 1982.

Belyaevsky, N. A., A. A. Borisov, V. V. Fedynsky, E. E. Fotiadi, S. I. Subbotin, and I. S. Volvovsky, Structure of the earth's crust on the territory of the USSR, Tectonophysics, 20, 35-45, 1973.

Birch, F., Density and composition of the upper mantle: First approximation as an olivine layer, in The Earth's Crust and Upper Mantle, P. J. Hart (ed.), Amer. Geophys. Union Geophys. Monogr., 13, 18-36, 1969.

Black, P. R., and L. W. Braile, P_n velocity and cooling of the continental lithosphere, J. Geophys. Res., 87, 10,557-10,568, 1982.

Buck, W. R., and M. N. Toksöz, Thermal effects of continental collisions: Thickening a variable viscosity lithosphere, Tectonophysics, 100, 53-69, 1983.

Burtman, V. S., Structural geology of Variscan Tien Shan, USSR, Amer. J. Sci., 275-A, 157-186, 1975.

Burtman, V. S., Faults of Middle Asia, Amer. J. Sci., 280, 725-744, 1980.

Chen, W.-P., and P. Molnar, Seismic moments of major earthquakes and the average rate of slip in central Asia, J. Geophys. Res., 82, 2945-2969, 1977.

Chen, W.-P., and P. Molnar, Constraints on the seismic wave velocity structure beneath the Tibetan Plateau and their tectonic implications, J. Geophys. Res., 86, 5937-5962, 1981.

Creager, K. C., and T. H. Jordan, Slab penetration into the lower mantle, J. Geophys. Res., 89, 3031-3049, 1984.

Creager, K. C., and T. H. Jordan, Slab penetration into the lower mantle beneath the Mariana and other island arcs of the northwest Pacific, J. Geophys. Res., 91, 3573-3589, 1986.

Duschenes, J. D., and S. C. Solomon, Shear wave travel time residuals from oceanic earthquakes and the evolution of oceanic lithosphere, J. Geophys. Res., 82, 1985-2000, 1977.

Dziewonski, A. M., Mapping the lower mantle: Determination of lateral heterogeneity in P velocity up to degree and order 6, J. Geophys. Res., 89, 5929-5952, 1984.

Dziewonski, A. M., and D. L. Anderson, Preliminary reference earth model, Phys. Earth Planet. Inter., 25, 297-356, 1981.

Dziewonski, A. M., and D. L. Anderson, Travel times and station corrections for P waves at teleseismic distances, J. Geophys. Res., 88, 3295-3314, 1983.

Dziewonski, A. M., and F. Gilbert, The effect of small, aspherical perturbations on travel times and a re-examination of the corrections for ellipticity, Geophys. J. R. astr. Soc., 44, 7-17, 1976.

England, P., and G. Houseman, Role of lithospheric strength heterogeneities in the tectonics of Tibet and neighbouring regions, Nature, 315, 297-301, 1985.

England, P. C., and S. W. Richardson, Erosion and the age dependence of continental heat flow, Geophys. J. Royal astr. Soc., 62, 421-437, 1980.

Fleitout, L., and C. Froidevaux, Tectonics and topography for a lithosphere containing density heterogeneities, Tectonics, 1, 21-56, 1982.

Galperin, E. I., I. L. Nersesov, and R. M. Galperina, Borehole seismology and the study of the seismic regime of large industrial centres (translation of Izuchenie seismocheskogo rezhima krupnykh promyshlennykh tsentrov, Nauka, Moscow, 1978), 316 pp., D. Reidel, Dordrecht, 1986.

Gamburtsev, G. A., and P. S. Veitsman, A comparison of data from deep seismic sounding with seismic and gravity data and the structure of the earth's crust in the northern Tien Shan (in Russian), Izvestiya Akad. Nauk SSSR, 9, 1036-1043, 1956.

Gamburtsev, G. A., P. S. Veitsman, and Yu. V. Tulina, Structure of the crust in the northern Tien Shan according to data from deep seismic sounding (in Russian), Dokl. Akad. Nauk SSSR, 105, 83-86, 1955.

Godin, Yu. N., V. S. Volvovsky, and I. S. Volvovsky, Seismic investigation of the earth's crust in the region of the Fergana intermontane depression, Dokl. Akad. Nauk SSSR, 133, 1398-1401, 1960.

Green, R. W. E., and A. L. Hales, The travel times of P waves to 30° in the central United States and upper mantle structure, Bull. Seismol. Soc. Am., 58, 267-289, 1968.

Gumper, F., and P. W. Pomeroy, Seismic wave velocities and earth structure on the African continent, Bull. Seismol. Soc. Am., 60, 651-668, 1970.

Hales, A. L., The travel times of P seismic waves and their relevance to the upper mantle velocity distribution, in The Upper Mantle, A. R. Ritsema (ed.), Tectonophysics, 13(1-4), 447-482, 1972.

Hales, A. L., and H. A. Doyle, P and S travel time anomalies and their interpretation, Geophys. J. R. astr. Soc., 13, 403-415, 1967.

Herrin, E., and J. Taggart, Regional variations in P_n velocity and their effect on the location of epicenters, Bull. Seismol. Soc. Am., 52, 1037-1046, 1962.

Herrin, E., E. P. Arnold, B. A. Bolt, G. E. Clawson, E. R. Engdahl, H. W. Freedman, D. W. Gordon, A. L. Hales, J. L. Lobdell, O. Nuttli, C. Romney, J. Taggart, and W. Tucker, 1968 seismological tables for P phases, Bull. Seismol. Soc. Am., 58, 1196-1241, 1968.

Houseman, G. A., D. P. McKenzie, and P. Molnar, Convective instability of a thickened boundary layer and its relevance for the thermal evolution of continental convergent belts, J. Geophys. Res., 86, 6115-6132, 1981.

Jeffreys, H., and K. E. Bullen, Seismological Tables, 50 pp., British Assoc. for the Advancement of Science, Gray Milne Trust, London, 1967.

Kirnos, D. P., D. A. Knarin, and N. V. Shebalin, History of development of instrumental seismic observations in the USSR, in Earthquakes of the USSR (a translation by the U.S. Joint Publications Research Service, New York, of Zemletryaseniya v SSSR., E. F. Savarchskii, ed.), U.S. Atomic Energy Comm., pp. 1-69, 1962.

Kosminskaya, I. P., N. A. Belyaevsky, and I. S. Volvovsky, Explosion seismology in the USSR, in The Earth's Crust and Upper Mantle, P. J. Hart (ed.), Amer. Geophys. Union Geophys. Monograph, 13, 195-208, 1969.

Krestnikov, V. N., History of oscillatory movements in the Pamirs and adjacent regions of Asia, (translated from Istoriya razvitiya kolebatel'nykh dvizhenii zemnoi kory Pamira i sopredel'nykh chastei Azii, Izdatel'stvo Akademii Nauk SSSR, Moscow, 1962), S. Monson, Jerusalem, 199 pp., 1965.

Lachenbruch, A. H., and J. H. Sass, Heat flow in the United States and the thermal regime of the crust, in The Earth's Crust - Its Nature and Properties, J. G. Heacock, ed., Amer. Geophys. Union Geophys. Monograph, 20, 626-675, Washington, D.C., 1977.

Langston, C. A., Aspects of P_n and P_g propagation at regional distances, Bull. Seismol. Soc. Am., 72, 457-471, 1982.

Langston, C. A., and D. V. Helmberger, A procedure for modelling shallow dislocation sources, Geophys. J. R. astr. Soc., 42, 117-130, 1975.

Lee, K. Y., Geology of the Tarim Basin with special emphasis on petroleum deposits, Xinjiang Uygar Zizhiqu, Northwest China, U. S. Geol. Surv. Open-File Report, 85-0616, 55 pp., 1985.

Leith, W., M. W. Hamburger, and A. Teremetsky, Trenching and geomorphological studies of the Talas-Fergana Fault, Soviet Central Asia, Eos, 67, 375-376, 1986.

Lyon-Caen, H., and P. Molnar, Constraints on the structure of the Himalaya from the analysis of gravity anomalies and a flexural model of the lithosphere, J. Geophys. Res., 88, 8171-8191, 1983.

Lyon-Caen, H., and P. Molnar, Gravity anomalies and the structure of western Tibet and the southern Tarim Basin, Geophys. Res. Let., 11, 1251-1254, 1984.

Lyubimova, E. A., N. B. Chigarev, and V. S. Firsova, The heat flow and the discontinuity of crustal structure in Central Asia, Izvestiya, Earth Physics, 22, 693-698, 1986.

McNutt, M. K., and M. G. Kogan, Isostasy in the USSR II: Interpretation of admittance data, in Composition, structure, and dynamics of the lithosphere-asthenosphere system, K. Fuchs and C. Froidevaux (ed.), Amer. Geophys. Union Geodynamics Ser., 16, 309-327, 1987.

Menke, W. H., and P. Richards, Crust-mantle whispering gallery phases: A deterministic model of teleseismic P_n wave propagation, J. Geophys. Res., 85, 5416-5422, 1980.

Molnar, P., and W.-P. Chen, S-P wave travel time residuals and lateral inhomogeneity in the mantle beneath Tibet and the Himalaya, J. Geophys. Res., 89, 6911-6917, 1984.

Molnar, P., and P. Tapponnier, Cenozoic tectonics of Asia: Effects of a continental collision, Science, 189, 419-426, 1975.

Molnar, P., and P. Tapponnnier, P., A possible dependence of tectonic strength on the age of the crust in Asia, Earth and Planet. Sci. Let., 52, 107-114, 1981.

Morgan, P., and J. H. Sass, 1984, Thermal regime of the continental lithosphere, Journal of Geodynamics, 1, 143-166, 1984.

Mueller, S., Deep structure and recent dynamics in the Alps, in Mountain Building Processes, K. J. Hsü, ed., pp. 181-200, Academic Press, London, 1982a.

Mueller, S., Geodynamic aspects of the Mediterranean-Alpine region, Rev. de Geofisica, 38, 103-111, 1982b.

Nabelek, J., Determination of earthquake source parameters from inversion of body waves, Ph. D. thesis, Mass. Inst. of Technol., 361 pp., Cambridge, Mass., 1984.

Nelson, M. R., R. McCaffrey, and P. Molnar, Source parameters for 17 earthquakes in the Tien Shan, Central Asia, determined by P and SH waveform inversion, Eos, 67, 305, 1986.

Nelson, M. R., R. McCaffrey, and P. Molnar, Source parameters for 11 earthquakes in the Tien Shan, Central Asia, determined by P and SH waveform inversion, J. Geophys. Res., 92, 12,629-12,648, 1987.

Ni, J., and M. Barazangi, High-frequency seismic wave propagation beneath the Indian Shield, Himalayan Arc, Tibetan Plateau and surrounding regions: high uppermost mantle velocities and efficient S_n propagation beneath Tibet, Geophys. J. R. astr. Soc., 72, 665-690, 1983.

Panza, G. F., and S. Mueller, The plate boundary between Eurasia and Africa in the Alpine area, Memorie di scienze geologiche, 33, 43-50, 1978.

Patton, H. J., S. R. Taylor, D. B. Harris, and J. M. Mills, The utility of regional Chinese seismograms for source and path studies in central Asia, Geophys. J. R. astr. Soc., 81, 469-478, 1985.

Pearson, F., Map Projection Methods, Sigma Scientific, Inc., Blacksburg, Virginia, 292 pp., 1984.

Pettersen, Ø, and D. J. Doornbos, A comparison of source analysis methods as applied to earthquakes in Tibet, Phys. Earth Planet. Inter., 47, 125-136, 1987.

Poupinet, G., Heterogeneites du manteau terrestre deduites de la propagation des ondes de volume - implication geodynamique, Ph.D. thesis, l'Université Scientifique et Médicale de Grenoble, 234 pp., 1977.

Poupinet, G., On the relation between P-wave travel time residuals and the age of continental plates, Earth Planet. Sci. Let., 43, 149-161, 1979.

Richter, C. F., Elementary Seismology, W. H. Freeman and Co., San Francisco, 768 pp., 1958.

Romanowicz, B. A. and M. Cara, Reconsideration of the relations between S and P station anomalies in North America, Geophys. Res. Let., 7, 417-420, 1980.

Ryaboi, V. Z., and L. N. Nikitina, Horizontal nonuniformities of the lower lithosphere of the Tien Shan and adjacent geological structures based on correlation of seismic and other geologic-geophysical data, Izvestiya, Earth Physics, 22, 699-712, 1986.

Sabitova, T. M. and T. B. Yanovskaya, Horizontal inhomogeneities in the earth's crust in the Kirgizian Tien-Shan from the distribution of surface wave group velocities, Izvestiya, Earth Physics, 22, 451-457, 1986.

Saipbekova, A. M., Horizontal seismic velocity heterogeneities in the upper mantle of the Tien Shan and contiguous geostructures (in Russian), in Lithosphere of the Tien Shan, I. E. Gubin (ed.), Nauka, Moscow, pp. 83-88, 1986.

Sengupta, M. K., The structure of the earth's mantle from body-wave observations, Sc. D. thesis, Mass. Inst. of Technol., 578 pp., Cambridge, Mass., 1975.

Simpson, D. W., M. W. Hamburger, V. D. Pavlov, and I. L. Nersesov, Tectonics and seismicity of the Toktogul Reservior region, Kirgizia, USSR, J. Geophys. Res., 86, 345-358, 1981.

Sleep, N. H., Teleseismic P-wave transmission through slabs, Bull. Seismol. Soc. Am., 63, 1349-1373, 1973.

Souriau, A., and J. H. Woodhouse, A worldwide comparison of predicted S-wave delays from a three-dimensional upper mantle model with P-wave station corrections, Physics Earth Planet. Inter., 39, 75-88, 1985.

Tapponnier, P., and P. Molnar, Active faulting and Cenozoic tectonics of the Tien Shan, Mongolia, and Baykal regions, J. Geophys. Res., 84, 3425-3459, 1979.

Telford, W. M., L. P. Geldart, R. E. Sheriff, and D. A. Keys, Applied Geophysics, Cambridge University Press, Cambridge, pp. 860, 1976.

Terman, M. J., C. C. Woo, D. C. Alverson, D. P. Cox, and A. J. Woloshin, Atlas of Asia and Eastern Europe - to support detection of underground nuclear testing, volume 2, tectonics, U. S. Geol. Surv., Washington, D.C., 1967.

Vilotte, J. P., M. Daignieres, R. Madadriaga, and O. C. Zienkiewicz, The role of a heterogeneous inclusion during continental collision, Physics Earth Planet. Inter., 36, 236-259, 1984.

Vinnik, L. P., and A. M. Saipbekova, Structure of the lithosphere and the asthenosphere of the Tien Shan, Annales Geophysicae, 2, 621-626, 1984.

Vol'vovskii, I. S., and B. S. Vol'vovskii, Cross-sections of the earth's crust in the territory of the USSR, plotted from deep seismic soundings (translation by Addis Translations International, Portola Valley, Calif., of Razrezy zemnoy kory territorii SSSR po dannym glubinnogo seysmicheskogo zondirovaniya, Moscow, Sovetskoe Radio, 268 pp., 1975.)

Wang, L. Q., and S. Y. Li, Focal mechanisms and plate tectonic theory in Xinjiang, China, Kexue Tongbao (Science Press), 29(5), 651-655, 1984.

Wiggins, R. A., Interpolation of digitized curves, Bull. Seismol. Soc. Am., 66, 2077-2081, 1976.

Yuan, X., S. Wang, L. Li, and J. Zhu, A geophysical investigation of deep structure in China, in Reflection Seismology: A Global Perspective, M. Barazangi and L. Brown (ed.), Amer. Geophys. Union Geodynamics Series, 13, 151-160, Washington, D.C., 1986.

Yudakhin, F. N., Geophysical fields, deep structure, and seismicity of the Tien Shan (in Russian), Ilim, Frunze, 248 pp., 1983.

Zhang, Zh. M., J. G. Liou, and R. G. Coleman, An outline of the plate tectonics of China, Geol. Soc. Am. Bull., 95, 295-312, 1984.

Table 1. Stations corrections for seismic stations in Soviet Central Asia that report to the ISC

Station	P wave travel time anomaly[1] (sec.) (with number of observations) Dziewonski and Anderson [1983]	Poupinet [1977]	S wave travel time anomaly[1] (with number of observations) Poupinet [1977]	Elev.
In the eastern Tien Shan				
AAA	0.80 ± 0.46 (31)		2.74 ± 0.27 (161)	800 m
AAB	0.40 ± 0.58 (2917)	0.51 ± 0.06 (345)		850 m
ANR	0.79 ± 0.39 (1864)			494 m
DSH	0.74 ± 0.57 (3128)	-0.38 ± 0.05 (402)	1.43 ± 0.21 (301)	847 m
FRU	0.86 ± 0.34 (3422)	0.38 ± 0.04 (421)	2.46 ± 0.19 (257)	655 m
GAR	-0.25 ± 0.55 (2906)	-0.45 ± 0.05 (369)	0.26 ± 0.45 (65)	1300 m
NRN	0.09 ± 0.44 (742)			2849 m
PRZ	0.99 ± 0.46 (1788)	1.05 ± 0.10 (106)	3.48 ± 0.44 (65)	1599 m
SAM	0.49 ± 0.29 (1595)	-0.33 ± 0.09 (115)		704 m
TAS	0.50 ± 0.35 (3277)	0.02 ± 0.04 (529)	2.00 ± 0.17 (394)	470 m
TLG	0.27 ± 0.74 (619)	0.72 ± 0.13 (43)		850 m
Mean	0.52 ± 0.37	0.19 ± 0.56	2.06 ± 1.12	1038 m
On the Siberian Shield				
ELT	-0.62 ± 0.41 (3152)	-1.20 ± 0.08 (140)		≈200 m[2]
NVS	-0.76 ± 0.38 (426)			≈100 m[2]
SEM	-0.21 ± 0.64 (2308)	-0.81 ± 0.05 (392)	-0.68 ± 0.35 (136)	209 m
Mean	-0.53 ± 0.29	-1.00	-0.68	≈170 m
In the Lake Baikal region				
IRK	0.09 ± 0.51 (2664)	-0.40 ± 0.06 (407)	1.78 ± 0.19 (258)	467 m
MOY	0.71 ± 0.59 (2461)	-0.05 ± 0.10 (96)		≈1500 m[2]
ZAK	0.44 ± 0.44 (3173)	-0.35 ± 0.09 (104)		≈1500 m[2]
Mean	0.41 ± 0.31	-0.27 ± 0.19	1.78	≈1150 m

[1] Dziewonski and Anderson [1983] reported the 1 σ standard deviation for one observation while Poupinet [1977] reported the 1 σ standard deviation of the mean station correction. To compare the uncertainties, multiply the standard deviation of the mean reported by Poupinet by the square root of the number of observations.

[2] Actual elevation has not been reported to the International Seismological Centre. Elevation estimated from a topographic map.

Table 2. Summary of mean S-P residuals (using A, B, and C quality picks)

Event	Mean S-P residual (seconds)	Standard Deviation of measurement	Standard Deviation of the mean	N	Corrections
A 13 Nov 65	0.58	2.54	1.04	6	uncorrected
	-1.51	1.88	0.77		A
	0.09	2.43	0.99		B
	-0.41	2.43	0.99		B + C
B 11 Feb 69	1.59	4.00	1.79	5	uncorrected
	-.91	4.18	1.87		A
	-.40	3.06	1.37		B
	-.90	3.06	1.37		B + C
C 5 June 70	0.89	1.60	0.46	12	uncorrected
	-1.48	1.19	0.34		A
	- .14	1.36	0.39		B
	- .64	1.36	0.39		B + C
D 23 Mar 71	6.00	3.26	1.46	5	uncorrected
	3.63	2.56	1.14		A
	3.37	1.93	0.86		B
	2.87	1.93	0.86		B + C
E 10 May 71	0.62	1.55	0.55	8	uncorrected
	-1.04	0.65	0.23		A
	0.33	0.83	0.29		B
	-0.17	0.83	0.29		B + C
F 9 Apr 72	0.79	1.29	0.58	5	uncorrected
	-1.52	0.83	0.37		A
	0.30	0.84	0.38		B
	-0.20	0.84	0.38		B + C
G 2 June 73	0.37	1.19	0.40	9	uncorrected
	-1.77	1.36	0.45		A
	-1.13	1.27	0.42		B
	-1.63	1.27	0.42		B + C
H 31 Jan 77	0.41	1.96	0.88	5	uncorrected
	-1.46	1.33	0.59		A
	0.08	1.19	0.53		B
	-0.42	1.19	0.53		B + C
I 29 Mar 79	-0.53	3.09	0.98	10	uncorrected
	-2.54	2.17	0.69		A
	-1.30	1.87	0.59		B
	-1.80	1.87	0.59		B + C

PAGES (S) MISSING FROM ORIGINAL

Page 166 is missing, but it appears to be just a page numbered error by the author.

Table 3. Mean S-P residuals calculated using Dziewonski and Anderson's P wave station corrections and varying ratios of S wave to P wave station corrections

Event	N	Mean S-P residual		S.D. of the mean	Standard Deviation	$\Delta T_s/\Delta T_p$
13 Nov 65	6	0.402	±	0.998	2.45	1.7
		0.338	±	0.991	2.43	2.0
		0.213	±	0.985	2.41	2.5
		0.092	±	0.993	2.43	3.0
		-0.033	±	1.012	2.48	3.5
11 Feb 69	5	0.862	±	1.602	3.58	1.7
		0.594	±	1.542	3.45	2.0
		0.096	±	1.444	3.23	2.5
		-0.398	±	1.368	3.06	3.0
		-0.896	±	1.318	2.95	3.5
5 June 70	12	0.512	±	0.361	1.25	1.7
		0.377	±	0.344	1.19	2.0
		0.118	±	0.347	1.20	2.5
		-0.137	±	0.394	1.36	3.0
		-0.396	±	0.472	1.63	3.5
23 Mar 71	5	5.038	±	1.183	2.65	1.7
		4.686	±	1.095	2.45	2.0
		4.028	±	0.956	2.14	2.5
		3.374	±	0.862	1.93	3.0
		2.716	±	0.831	1.86	3.5
10 May 71	8	0.514	±	0.437	1.24	1.7
		0.475	±	0.401	1.13	2.0
		0.402	±	0.339	0.96	2.5
		0.328	±	0.293	0.83	3.0
		0.255	±	0.271	0.77	3.5
9 Apr 72	5	0.610	±	0.456	1.02	1.7
		0.544	±	0.423	0.95	2.0
		0.418	±	0.382	0.85	2.5
		0.298	±	0.376	0.84	3.0
		0.172	±	0.409	0.91	3.5
2 June 73	9	-0.174	±	0.339	1.02	1.7
		-0.377	±	0.337	1.01	2.0
		-0.751	±	0.364	1.09	2.5
		-1.126	±	0.422	1.27	3.0
		-1.500	±	0.502	1.50	3.5
31 Jan 77	5	0.286	±	0.724	1.62	1.7
		0.244	±	0.675	1.51	2.0
		0.160	±	0.593	1.33	2.5
		0.080	±	0.534	1.19	3.0
		-0.006	±	0.502	1.12	3.5

29 Mar 79	10	-0.813	±	0.815	2.58	1.7
		-0.914	±	0.760	2.40	2.0
		-1.107	±	0.667	2.11	2.5
		-1.295	±	0.590	1.87	3.0
		-1.488	±	0.538	1.70	3.5
25 Sept 79	6	-0.140	±	0.307	0.75	1.7
		-0.295	±	0.348	0.85	2.0
		-0.590	±	0.442	1.08	2.5
		-0.882	±	0.544	1.33	3.0
		-1.177	±	0.656	1.61	3.5
6 May 82	5	-1.284	±	0.546	1.22	1.7
		-1.240	±	0.552	1.23	2.0
		-1.160	±	0.572	1.28	2.5
		-1.080	±	0.599	1.34	3.0
		-1.000	±	0.635	1.42	3.5
ALL	76	0.391	±	0.255	2.23	1.7
		0.266	±	0.244	2.12	2.0
		0.030	±	0.227	1.98	2.5
		-0.204	±	0.218	1.90	3.0
		-0.440	±	0.218	1.90	3.5
ALL BUT	66	0.003	±	0.201	1.63	1.7
11 Feb 69 AND		0.094	±	0.193	1.57	2.0
23 Mar 71		-0.278	±	0.185	1.50	2.5
		-0.460	±	0.187	1.52	3.0
		-0.644	±	0.198	1.61	3.5

Table 4. Earthquakes used in residual spheres study

	Date	Origin Time (UT)	Epicenter Latitude	Epicenter Longitude	Assumed Focal depth	Body wave Magnitude
1	3/23/71	09:52:12.1 ± 1.02	41.44 ± 0.02	79.17 ± 0.03	29 km[1]	5.7
2	3/23/71	20:47:15.5 ± 1.95	41.42 ± 0.03	79.20 ± 0.03	11 km[2]	5.8
3	5/10/71	14:51:44.8 ± 1.34	42.85 ± 0.02	71.29 ± 0.02	15 km[2]	5.6
4	6/15/71	07:39:35.1 ± 0.96	41.40 ± 0.02	79.38 ± 0.03	17 km[1]	5.4
5	4/09/72	04:10:48.9 ± 0.09	42.09 ± 0.02	84.58 ± 0.02	13 km[2]	5.8
6	6/02/73	23:57:02.4 ± 0.76	44.14 ± 0.01	83.60 ± 0.02	26 km[1]	5.7
7	8/11/74	01:13:55.2 ± 1.28	39.34 ± 0.02	73.76 ± 0.02	4 km[3]	6.2
8	8/11/74	20:05:31.0 ± 0.30	39.44 ± 0.01	73.67 ± 0.02	5 km[3]	5.7
9	8/11/74	21:21:37.1 ± 0.85	39.46 ± 0.02	73.62 ± 0.02	10 km[3]	5.8
10	8/27/74	12:56:01.0 ± 0.92	39.52 ± 0.02	73.82 ± 0.02	3 km[3]	5.7
11	1/31/77	14:26:15.1 ± 0.70	40.11 ± 0.02	70.86 ± 0.02	12 km[2]	6.0
12	3/24/78	21:05:48.5 ± 0.38	42.84 ± 0.02	78.60 ± 0.02	34 km[1]	6.1
13	3/29/79	02:01:32.1 ± 0.07	41.95 ± 0.01	83.38 ± 0.01	13 km[2]	5.8
14	9/25/79	13:05:54.5 ± 0.33	45.09 ± 0.01	76.96 ± 0.01	40 km[2]	5.8

[1] Focal depths as reported by the ISC
[2] Focal depths from Nelson et al., 1987
[3] Focal depths from Nelson et al., 1986

Table 5. Least-square fits to ISC travel times
(for epicentral distances of 300-1700 km)

Station	Azimuth from the station	Slope (km/s)	T-intercept	N
For paths along the Tien Shan				
TOK	60°-90°	8.22 ± 0.06	11.7 ± 0.9 s	35
ANR	60°-90°	8.10 ± 0.07	10.5 ± 1.0 s	32
NRN	60°-90°	8.30 ± 0.11	11.4 ± 1.6 s	19
PRZ	50°-90°	8.12 ± 0.12	10.1 ± 1.7 s	14
SAM	60°-90°	8.16 ± 0.07	10.0 ± 1.0 s	48
TAS	60°-90°	8.34 ± 0.10	11.6 ± 1.5 s	35
WMQ	240°-270°	8.26 ± 0.06	11.6 ± 0.6 s	40
For paths across the Tarim Basin and the Tibetan Plateau				
TOK	90°-135°	8.11 ± 0.04	10.1 ± 0.6 s	34
FOR COMPARISON				
For paths across the Siberian Craton				
SEM	190°-220°	8.41 ± 0.10	14.1 ± 1.7 s	51
For paths east of the Nevada Nuclear Test Site				
Basin and Range [Hales, 1972]	45°-135°	8.08 ± 0.08	10.0 ± 1.5 s	23
From Ni and Barazangi, 1983 (2 σ uncertainties given)				
For paths along the Himalaya (For epicentral distances of 330-2000 km)				
NDI, KBL, SHL		8.45 ± 0.08	10.9 ± 1.3 s	76
For paths across the Tibetan Plateau (For epicentral distances of 670-1900 km)				
NDI, KBL, SHL		8.42 ± 0.10	11.6 ± 1.7 s	78
For paths under the Indian Shield (For epicentral distances of 550-2200 km)				
NDI, SHL, POO		8.40 ± 0.08	10.9 ± 1.3 s	78

Table 6. Least-square fits to ISC travel times

Station	Azimuth from the station	Epicenteral distances (km)	Slope[1] (km/s)	T-intercept[1]	N
For paths along the Tien Shan					
TOK	60°-90°	300-1700	8.22 ± 0.06	11.7 ± 0.9 s	35
		700-1700	8.54 ± 0.16	17.4 ± 2.6 s	21
		300-800	8.98 ± 0.34	16.3 ± 2.2 s	14
		700-1200	8.49 ± 0.36	16.4 ± 5.1 s	12
		1000-1700	8.73 ± 0.24	21.0 ± 4.0 s	16
ANR	60°-90°	300-1700	8.10 ± 0.07	10.5 ± 1.0 s	32
		700-1700	8.03 ± 0.17	9.1 ± 3.2 s	19
		300-800	7.94 ± 0.20	9.3 ± 1.8 s	13
		700-1200	7.80 ± 0.40	5.2 ± 6.8 s	12
		1000-1700	8.09 ± 0.24	10.3 ± 4.7 s	14
NRN	60°-90°	300-1700	8.30 ± 0.11	11.4 ± 1.6 s	19
		700-1700	8.25 ± 0.25	10.4 ± 4.2 s	12
		300-800	8.03 ± 0.11	9.6 ± 1.0 s	9
		700-1200	8.59 ± 0.25	15.0 ± 3.1 s	6
		1000-1700	7.86 ± 0.52	2.3 ±11.0 s	8
PRZ	50°-90°	300-1700	8.12 ± 0.12	10.1 ± 1.7 s	14
		700-1700	8.07 ± 0.26	9.2 ± 4.4 s	8
		300-800	7.83 ± 0.18	8.1 ± 1.8 s	8
		700-1200	8.85 ± 0.43	19.4 ± 5.0 s	6
		1000-1700	7.44 ± 0.36	-5.3 ± 8.4 s	4
SAM	60°-90°	300-1700	8.16 ± 0.07	10.0 ± 1.0 s	48
		700-1700	8.09 ± 0.12	8.7 ± 1.9 s	34
		300-800	8.31 ± 0.09	11.3 ± 0.8 s	22
		700-1200	7.78 ± 0.19	4.6 ± 2.9 s	25
		1000-1700	8.27 ± 0.34	12.8 ± 6.7 s	15
TAS	60°-90°	300-1700	8.34 ± 0.10	11.6 ± 1.5 s	35
		700-1700	8.43 ± 0.19	13.3 ± 2.9 s	34
		300-800	8.41 ± 0.20	12.2 ± 1.8 s	6
		700-1200	8.37 ± 0.24	12.1 ± 3.1 s	21
		1000-1700	7.84 ± 0.34	0.9 ± 7.4 s	15
WMQ	240°-270°	300-1700	8.26 ± 0.06	11.6 ± 0.6 s	40
		700-1700	8.27 ± 0.10	11.9 ± 1.8 s	36
		300-800	7.99 ± 0.16	9.6 ± 1.5 s	6
		700-1200	8.31 ± 0.05	12.7 ± 0.8 s	12
		1000-1700	8.16 ± 0.19	9.7 ± 3.7 s	30

For paths across the Tarim Basin and Tibet

TOK	90°-135°	300-1700	8.11 ± 0.05	10.1 ± 0.8 s	30
		700-1700	8.13 ± 0.13	10.3 ± 2.5 s	19
		300-800	8.07 ± 0.13	9.7 ± 1.0 s	14
		500-1000	8.59 ± 0.12	13.8 ± 1.1 s	6
		700-1200	8.32 ± 0.08	11.9 ± 1.1 s	6
		1000-1700	8.25 ± 0.24	12.8 ± 4.8 s	16

For paths along the Tien Shan east from Gazli

To URT, SAM, FRG, ANR,	300-1700	8.23 ± 0.06	9.5 ± 0.8 s	77
FRU, NRN, TLG, PRZ, WMQ	700-1700	8.24 ± 0.10	9.6 ± 1.5 s	60
	300-800	8.04 ± 0.14	8.0 ± 1.4 s	31
	700-1200	8.67 ± 0.15	14.9 ± 1.9 s	41
	1000-1700	7.71 ± 0.24	-0.4 ± 4.7 s	35

FOR COMPARISON

For paths across the Siberian Craton

SEM	190°-220°	300-1700	8.41 ± 0.10	14.1 ± 1.7 s	51
		700-1700	8.46 ± 0.11	15.0 ± 2.0 s	50
		700-1200	8.29 ± 0.28	12.4 ± 4.1 s	8
		1000-1700	8.68 ± 0.18	19.0 ± 3.2 s	46

For paths in the Basin and Range east of the Nuclear Test Site

Basin and Range	300-1700	8.08 ± 0.08	10.0 ± 1.5 s	23
[Hales, 1972]	700-1700	8.13 ± 0.12	10.9 ± 2.3 s	20
	700-1200	7.68 ± 0.39	3.9 ± 6.9 s	9
	1000-1700	8.32 ± 0.16	15.0 ± 3.2 s	17

[1] The 1 σ uncertainty is given for both the slope and T-intercept.

Table 7. Earthquakes used for refraction profile east of Gazli

	Date	Origin Time (UT)	Epicenter Latitude	Epicenter Longitude	ISC Focal depth	Body wave Magnitude
1	4/08/76	02:40:23.9 ± 0.08	40.31 ± 0.02	63.72 ± 0.01	0 km	6.2
2	4/08/76	12:03:41.3 ± 0.13	40.24 ± 0.02	64.05 ± 0.02	33 km	5.1
3	5/09/76	07:51:15.2 ± 0.16	40.32 ± 0.03	63.95 ± 0.02	0 km	5.1
4	5/17/76	02:58:41.1 ± 0.08	40.35 ± 0.02	63.45 ± 0.01	0 km	6.2
5	6/20/76	23:33:48.1 ± 0.09	40.41 ± 0.02	63.75 ± 0.02	0 km	5.2
6	7/14/77	05:49:08.3 ± 0.11	40.35 ± 0.02	63.71 ± 0.02	0 km	5.5
7	6/04/78	19:30:23.2 ± 0.08	40.40 ± 0.02	63.66 ± 0.01	33 km	5.9
8	2/23/83	14:13:32.5 ± 0.15	40.42 ± 0.03	63.57 ± 0.02	5 km	4.9
9	3/19/84	20:28:38.3 ± 0.06	40.35 ± 0.01	63.36 ± 0.01	15 km	6.4
10	3/20/84	06:28:40.1 ± 0.11	40.28 ± 0.02	63.31 ± 0.02	12 km	5.3
11	7/08/84	23:55:25.0 ± 0.17	40.29 ± 0.03	63.30 ± 0.02	0 km	4.8
12	8/14/84	11:45:48.1 ± 0.09	40.30 ± 0.02	63.26 ± 0.01	11 km	5.3
13	9/27/84	11:33:49.0 ± 0.10	40.32 ± 0.02	63.28 ± 0.02	5 km	4.9
14	11/11/84	09:42:43.6 ± 0.11	40.40 ± 0.02	63.38 ± 0.02	0 km	4.9

CAPTIONS

Fig. 1. Topography and seismicity of Central Asia. Filled circles mark epicenters of earthquakes occurring between 1971 and 1984 recorded by more than 100 stations and with focal depths less than 100 km, as reported by the International Seismological Centre (ISC). Also shown are the 1000 and 3000 m contours, with the region above 3000 m shaded. The triangles mark the Toktogul seismograph network and the Chinese seismograph stations at Ürümqi (WMQ) and Kashgar (KAS). The Soviet nuclear test site at Semipalatinsk is also shown.

Fig. 2. A simple cross section and geotherms to show the effects of crustal thickening [from Houseman et al., 1981]. In cross section the entire lithosphere is thickened by a factor of 2, and the original geotherm is stretched vertically by this amount. Note the difference in temperatures of material at comparable depths in normal and thickened lithosphere.

Fig. 3. Map of Central Asia showing Soviet seismograph stations that report to the ISC and for which P-wave and S-wave station corrections have been published [Dziewonski and Anderson, 1983; Poupinet, 1977]. The locations of five Soviet refraction profiles (labeled 1-5) are also shown. The 3000-m contour line is shown for reference.

Fig. 4. Map of interpolated P-wave travel time residuals based upon arrival times recorded at the numbered seismic stations [redrafted from figure 27 of Saipbekova, 1986]. Caption, translated from Russian, with

corrections and additions in brackets: Map of P wave travel time anomalies in the upper mantle of the Tien Shan. 1) Value of mean travel time anomaly, δt [in seconds]. 2) Contour of δt. 3) Seismological station. 4) Seismological station for which data were used for the first time. Figures in squares: 1. Frunze 2. Naryn 3. Przheval'sk 4. Talgar 5. Fabrichnyy [not shown] 6. Anan'yevo 7. Kadzhi Say 8. Orto-Tokoi 9. Boom 10. Chilik 11. Kurmenty 12. Aral 13. Arslanbob 14. Arkut 15. Manas 16. Kaindy 17. Dzhambul [not shown] 18. Chimkent 19.[20] Osh 20.[21] Sufi-Kurgan 21.[?] Batken 22. Erkin Say 23.[25] Rybach'ye 47. Andizan 48. Alma-Ata. Remaining stations are temporary. 5) Union republic border [6) USSR-China border]

Fig. 5. North-south topographic profiles across Tibet, the Pamir, and the Tien Shan constructed using the National Oceanographic and Atmospheric Administration's ETOPO5 data base of average elevation for each 5 × 5 minute quadrangle worldwide. For each profile the average elevation for the darkened section between 40° and 45° N, roughly the bounds of the Tien Shan, was calculated. The Tien Shan are approximately 5° wide with an average elevation of ≈2 km.

Fig. 6. Cartoon illustrating the effect of localized shortening and thickening of the lithosphere on the geotherm. Before the initiation of shortening, the crustal thickness and thermal structure are assumed to have been the same across the region. Crustal thicknesses and depths to isotherms are for illustrative purposes only. An average elevation of 2 km, if isostatically compensated, requires approximately 13 km of crustal thickening, corresponding to crustal shortening of ≈27%. The

depression of isotherms would lead to a cool lithospheric root with higher seismic velocities than those in the surrounding mantle. This lithospheric root should cause a difference in the travel times for the earthquakes A and B of 0.2-0.4 s for teleseismic P waves and at least 0.4-0.8 s for teleseismic S waves.

Fig. 7. Fault plane solutions for the earthquake of 2 June 1973 and comparison of recorded (solid lines) and synthetic seismograms (dashed lines). The lower hemisphere plots show the locations of stations and nodal surfaces on the focal sphere. The far-field source time function is shown on the time scale axis. Both observed and synthetic seismograms are scaled to a common distance ($\Delta = 40°$) and instrument magnification (3000×). Scale bar indicates ground displacement in microns.

Fig. 8. a) Examples of long-period WWSSN P waveforms (solid lines) and corresponding synthetic seismograms (dashed lines) for the June 2, 1973 earthquake. The synthetic seismograms were calculated using all of the P and SH waveforms aligned as shown in Figure 7. The quality of the match (A,best; D,worst) is given after the station abbrevation. The seismograms in the middle row are properly aligned. The synthetic seismograms in the top row have been advanced 1 s relative to the measured arrival time. Likewise, the synthetic seismograms in the bottom row have been delayed 1 s. For A quality picks, the P arrival time can be determined with an uncertainty of less than 0.5 s. For B quality picks, the uncertainty is about 0.5 s. For C quality picks, the uncertainty approaches 1.0 s because the direct P phase is nearly nodal, and reflected phases, rather than the direct arrival,

must be matched to determine the arrival time. b) Plot showing the root-mean-square variance of the match of the real and the synthetic seismograms as a function of the error in arrival time for the those P waveforms shown in Figure 8a. The variance for each pair of seismograms has been divided by the minimum value of the variance. For A quality picks (like that for HKC) the minimum in the variance for the correct arrival time is particularly pronounced. The minimum is less pronounced for B and C quality picks.

Fig. 9. a) Examples of synthetic and recorded long-period WWSSN SH waveforms for the June 2, 1973 earthquake. Legend is the same as for Figure 8. For A and B quality S picks the uncertainty is ≈0.5 s. At COL, SH is nearly nodal, making it impossible to determine the S wave arrival time accurately. The first identifiable phase is sS. Such D quality picks were not used to determine the S-P residuals. b) Plot showing the normalized variance of the match between the real and synthetic seismograms as a function of the error in arrival time for the SH waveforms shown in Figure 9a.

Fig. 10. A plot of focal depths determined by the ISC versus the centroid depths determined by waveform inversion. The letters refer to the earthquakes listed in Table 2.

Fig. 11 (a-k) Plots of S-P residuals versus azimuth for individual earthquakes. Letters indicate quality of the pick. Estimated uncertainties: A, ±0.2 s; B, ±0.5 s; C, ±1.0 s; D, not used. An upper case letter marks the residual before station corrections are applied. A lower case letter marks the residual calculated using Dzeiwonski and

Anderson's [1983] station corrections for P and an S wave correction equal to three times that for P. Dashed line marks the average for uncorrected residuals and dotted line marks the average of corrected residuals. Points are labelled by station abbreviations. (l and m) Similar plots for all data from all 11 earthquakes studied, with (m) and without (l) station corrections. Dotted line marks the average for all 11 earthquakes, dashed line markes the average for all earthquakes except February 11, 1969, and March 23, 1971.

Fig. 12. Summary map of the Tien Shan showing the epicenters given by the ISC and fault plane solutions of the 11 earthquakes for which S-P residuals were determined. Next to each focal mechanism are an identifying letter (Table 2), the focal depth in kilometers, and the mean S-P residual in seconds (with receiver station corrections and a correction for crustal thickness added). The dashed line marks the USSR-China border. The 1000-m contour is dotted, regions with elevations >2000 m are stippled, and regions above 4000 m are shaded. For each fault plane solution the lower hemisphere equal-area projection of the focal sphere is shown with the compressional quadrants shaded. Also shown are ISC epicenters for earthquakes occurring between 1971 and 1981 with $m_b > 5.0$. Different symbols indicate different focal depths, h, reported by the ISC: square, $h \leq 33$ km; diamond, 33 km $< h \leq 70$ km; plus, 70 km $< h \leq 100$ km; cross, $h > 100$ km.

Fig. 13. Raw (above) and smoothed (below) residual sphere for earthquakes 1-14 of Table 4. Residual spheres are equal-area, lower-hemisphere projections, for take-off angles from 0° to 60° from the

vertical. Circles represent negative residuals, crosses represent positive residuals. Symbol size is proportional to residual magnitude, with 1-second scale shown below the residual sphere. Note the difference in scale between the raw and smoothed residual spheres.

Fig. 14. (a) Diagram of a seismic refraction profile using a single source and many receivers and (b) diagram of a seismic refraction profile using one receiver and many sources (earthquakes).

Fig. 15. Map of Central Asia showing the epicenters (filled circles) of earthquakes for which P_n arrival times were measured to determine P_n velocities for the Tien Shan and the Tarim Basin. An equidistant azimuthal map projection centered on the Toktogul network (filled triangle) was used so that raypaths plot as straight lines from the epicenters to Toktogul. Political boundaries are shown by fine continuous lines. Elevations above 3000 m are shaded.

Fig. 16. (a) Reduced travel time plot (reduction velocity, 8.5 km/s) for raypaths under the Tien Shan from earthquakes located by the ISC using arrival times from more than 30 stations. (b) Reduced travel time plot for raypaths under the Tien Shan using only those earthquakes with more than 100 stations reporting to the ISC. A least-squares fit to the travel times between 300 and 1700 km yields a P_n velocity of 8.22 $\pm$ 0.06 km/s. Also shown for reference are lines for P_n velocities of 8.0 and 8.5 km/s. (c and d) Similar plots for raypaths beneath the Tarim Basin with the least-square fit to the data for earthquakes reported by more than 100 stations indicating a P_n velocity of 8.11 $\pm$ 0.04 km/s. Again, lines for P_n velocities of 8.0 and 8.5 km/s are shown for reference.

Note that the scatter is reduced noticeably by using only those earthquakes reported by more than 100 stations.

Fig. 17. Map of Central Asia showing epicenters of earthquakes (filled circles) used in this study and seismic stations (filled triangles) for which ISC data were used to construct travel-time curves. Also shown are the azimuth ranges sampled by each station. Elevations over 3 km are shaded.

Fig. 18. Map of Central Asia showing the location of the Tashkent (TAS) seismic station and the epicenters of earthquakes (filled circles) used to produce the travel time plot in figure 19. Raypaths from the earthquakes to TAS pass beneath the Tien Shan and are similar to those to Toktogul. The 3000-m contour line shown for reference.

Fig. 19. Reduced travel times (reduction velocity, 8.5 km/s) for paths to TAS running along the Tien Shan. A least-squares fit to the travel times between 300 and 1700 km yields a P_n velocity of 8.34 ± 0.10 km/s.

Fig. 20. Reduced travel times for the remaining ISC stations with least-squares fit shown for the distance range 300-1700 km. For paths along the Tien Shan: (a) For paths to ANR (Andizhan), azimuths 60°-90°, (b) For paths to NRN (Naryn), azimuths, 60°-90°, (c) For paths to PRZ, azimuths 50°-90°, (d) For paths to SAM, azimuths 60°-90°. (e) For raypaths beneath the Siberian Shield to SEM (Semipalatinsk).

Fig. 21. Map of Central Asia showing the location of the Ürümqi (WMQ) seismic station in the Chinese Tien Shan and the epicenters of earthquakes used to produce the travel time plot in figure 22. This

profile essentially reverses the profiles to TAS and Toktogul. The 3000-m contour line shown for reference.

Fig. 22. Reduced travel time plots (reduction velocity, 8.5 km/s) for paths to WMQ running along the Tien Shan (Figure 21). A least-squares fit to the data between 300 and 1700 km yields a P_n velocity of 8.26 ± 0.06 km/s.

Fig. 23. Map showing the epicenters of the 14 Gazli earthquakes used to construct a refraction profile eastward along the axis of the Tien Shan. Arrival times reported to the ISC from the seismic stations shown (filled triangles) were used to construct the travel time plot in Figure 24. The 1500-m and 3000-m contours are shown with elevations above 3000 m shaded. An azimuthal equidistant map projection centered on Gazli was used so that ray paths plot as straight lines from Gazli to the stations.

Fig. 24. Reduced travel times for the earthquakes near Gazli recorded at seismic stations in the Tien Shan.

Fig. 25. Travel time curve determined for the Canadian Shield from the Early Rise refraction experiment [Hales, 1972] and travel times from the western United States for comparison with the results from the Tien Shan. Data points are for explosions at the Nevada Nuclear Test Site (NTS) recorded in the Basin and Range of the western United States east-northeast (triangles), east (circles and squares), and east-southeast (dots) of NTS [Hales, 1972].

Fig. 26. Cartoons illustrating possible effects of crustal shortening in the Tien Shan on the underlying mantle. Assume the crustal thickness and

thermal structure of the Siberian Shield, Tien Shan, and Tarim Basin were the same before crustal shortening began in Oligocene time (Figure 26a). The values shown for the crustal thickness and the depth to the bottom of the mechanical lithosphere are poorly constrained, but are plausible for shield regions. The mantle between the depths of 95 and 155 km has been shaded to illustrate the effects of deformation. Shortening in the crust could be accommodated in a number of possible ways. Thickening of the crust in the Tien Shan could lead to thickening of the mantle lithosphere directly beneath it (Figure 26b and Figure 6). Alternatively, shortening in the Tien Shan could be the result of northward thrusting along a mid- or lower-crustal decollement; the mantle lithosphere south of the Tien Shan would be thickened while the mantle beneath the Tien Shan would be unaffected (Figure 26c). Still another possibility is that conduction or some other mechanism leads to the relatively rapid heating of the lithospheric root (Figure 26d). All three of these possibilities would predict that the geotherm beneath the Tien Shan would be similar to or somewhat cooler than the geotherm beneath shield regions like the Siberian Shield. The lower seismic velocities inferred for the mantle beneath the Tien Shan indicate that upper mantle temperatures are higher there than beneath shield regions. These higher temperatures could be explained if the thickened mantle lithosphere beneath the Tien Shan were so gravitationaly unstable that the thickened lithosphere had dropped off, driving convection that would heat up the uppermost mantle beneath the Tien Shan (Figure 26e).

Fig. 27. The lower seismic velocities beneath the Tien Shan than beneath shields, such as those north and south of the Tien Shan, may indicate

that the thermal structure beneath the Tien Shan was warmer than that beneath the Siberian Shield and the Tarim Basin before shortening began in Oligocene time (Figure 27a). The subsequent crustal shortening in the Tien Shan would depress the isotherms but not enough to compensate for the initial difference in temperature between the Tien Shan region and its surroundings (Figure 27b).

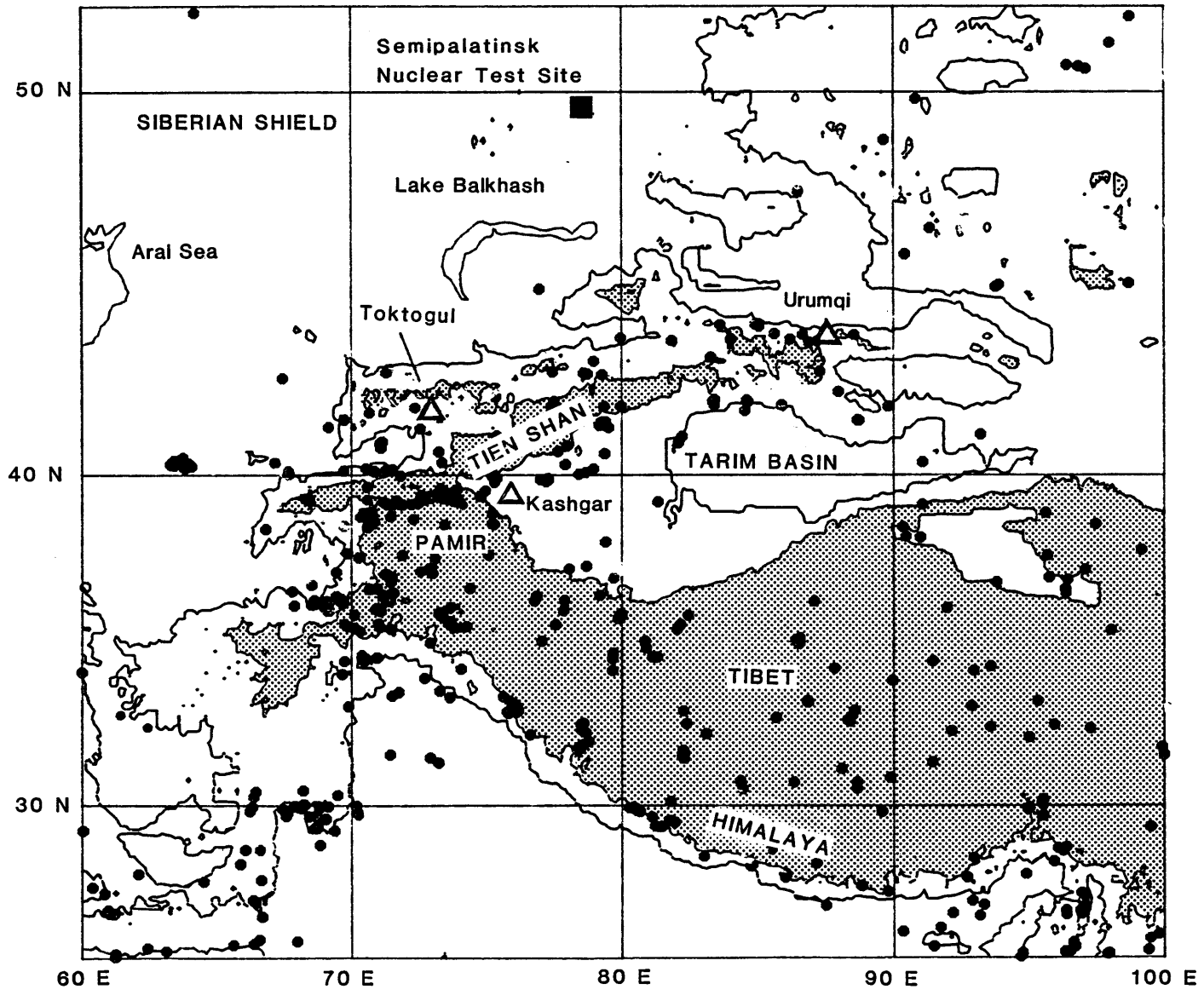
Semipalatinsk
Nuclear Test Site
SIBERIAN SHIELD
Lake Balkhash
Aral Sea
Toktogul
Urumqi
TIEN SHAN
TARIM BASIN
Kashgar
PAMIR
TIBET
HIMALAYA
50 N
40 N
30 N
60 E
70 E
80 E
90 E
100 E

Figure 1

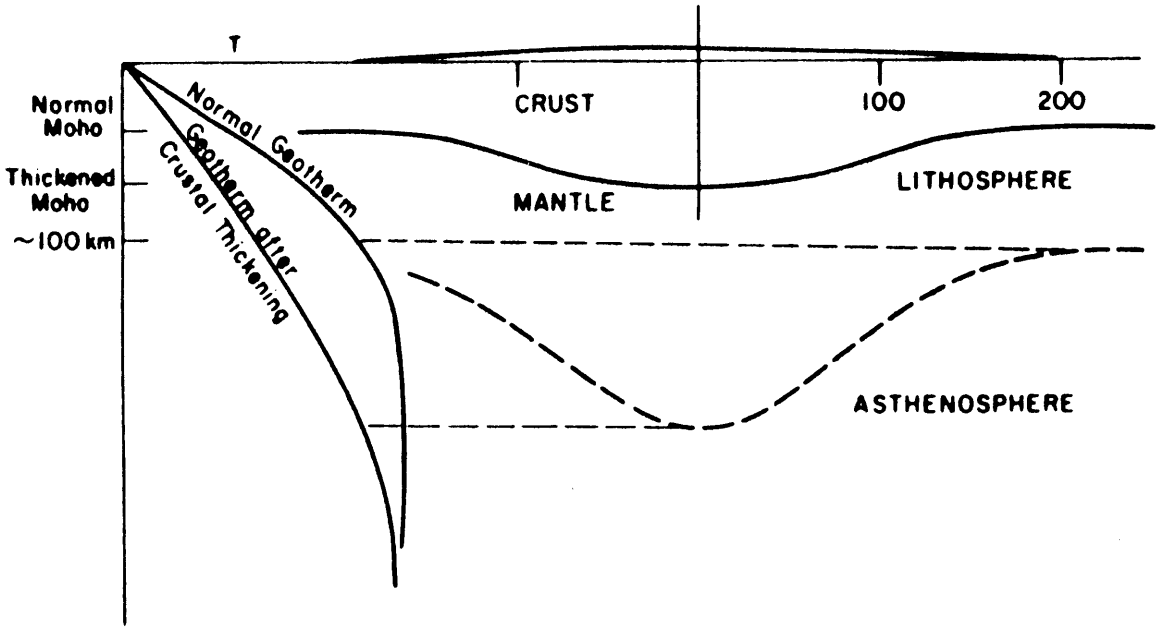
T
Normal Moho
Thickened Moho
~100 km
Normal Geotherm
Geotherm after Crustal Thickening
CRUST
MANTLE
100
200
LITHOSPHERE
ASTHENOSPHERE

Figure 2

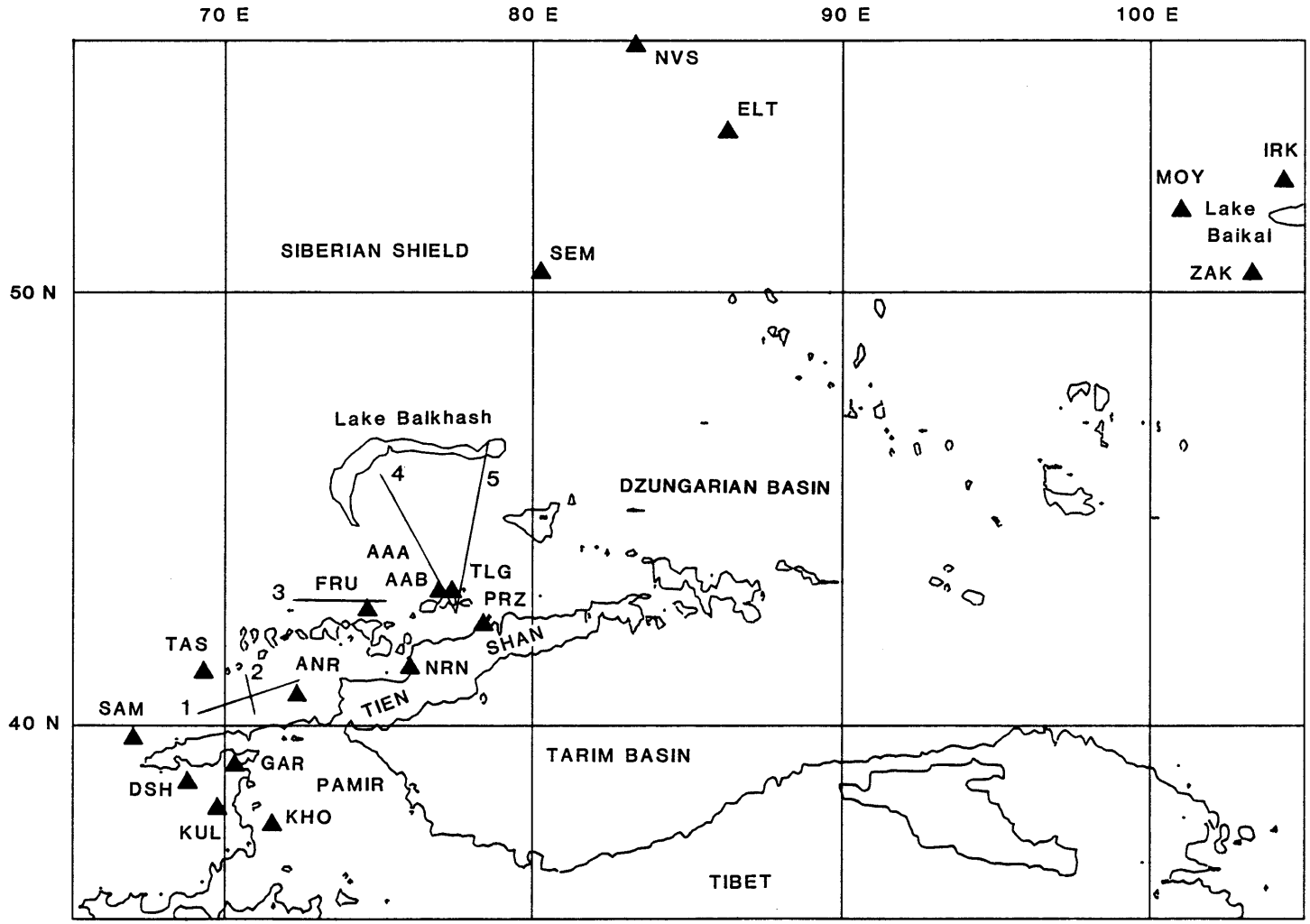
70 E
80 E
90 E
100 E
50 N
40 N
NVS
ELT
IRK
MOY
Lake
Baikal
ZAK
SIBERIAN SHIELD
SEM
Lake Balkhash
4
5
DZUNGARIAN BASIN
AAA
AAB
TLG
3
FRU
PRZ
TAS
SHAN
2
ANR
NRN
SAM
1
TIEN
TARIM BASIN
GAR
DSH
PAMIR
KHO
KUL
TIBET

Figure 3

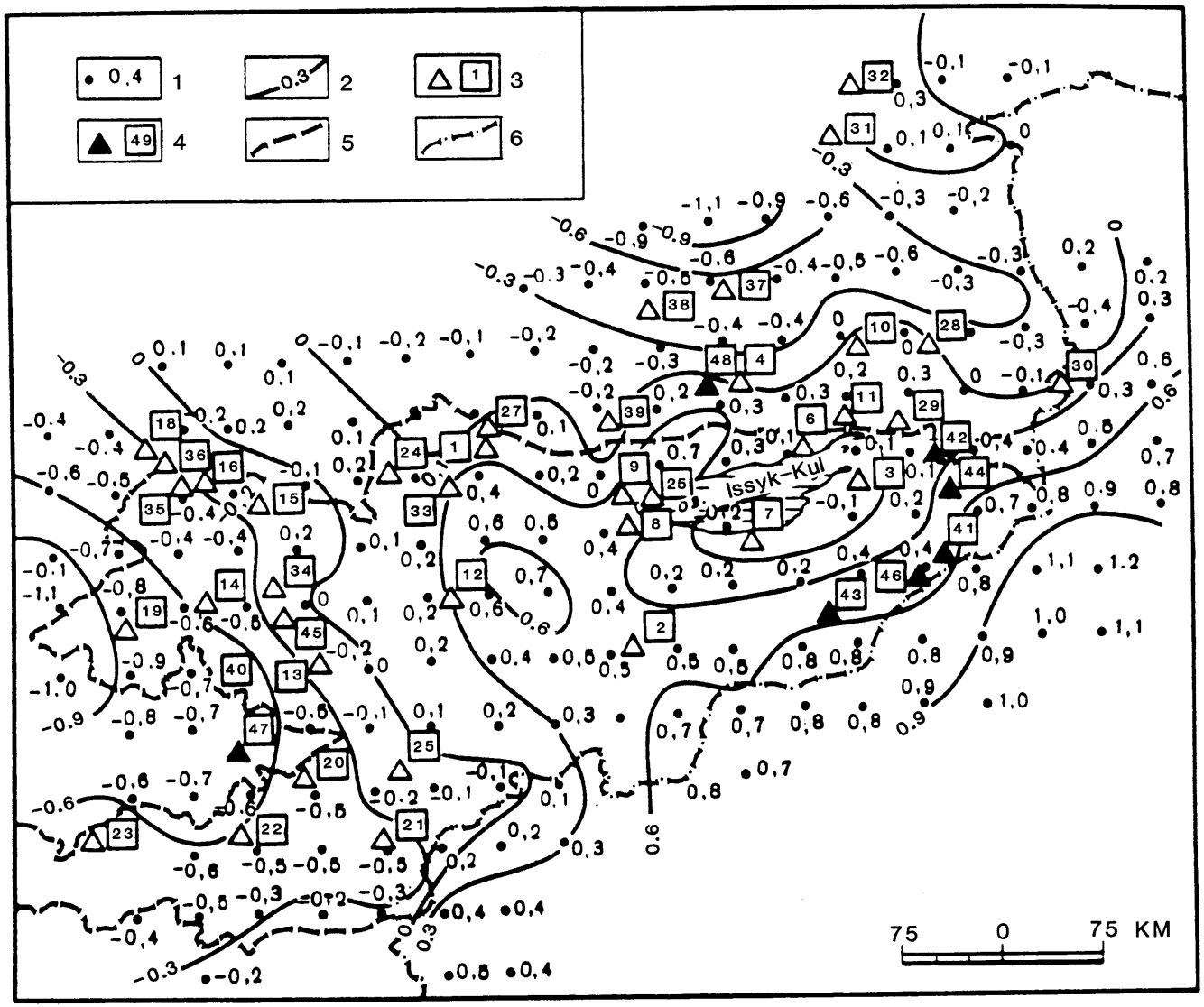

Figure 4

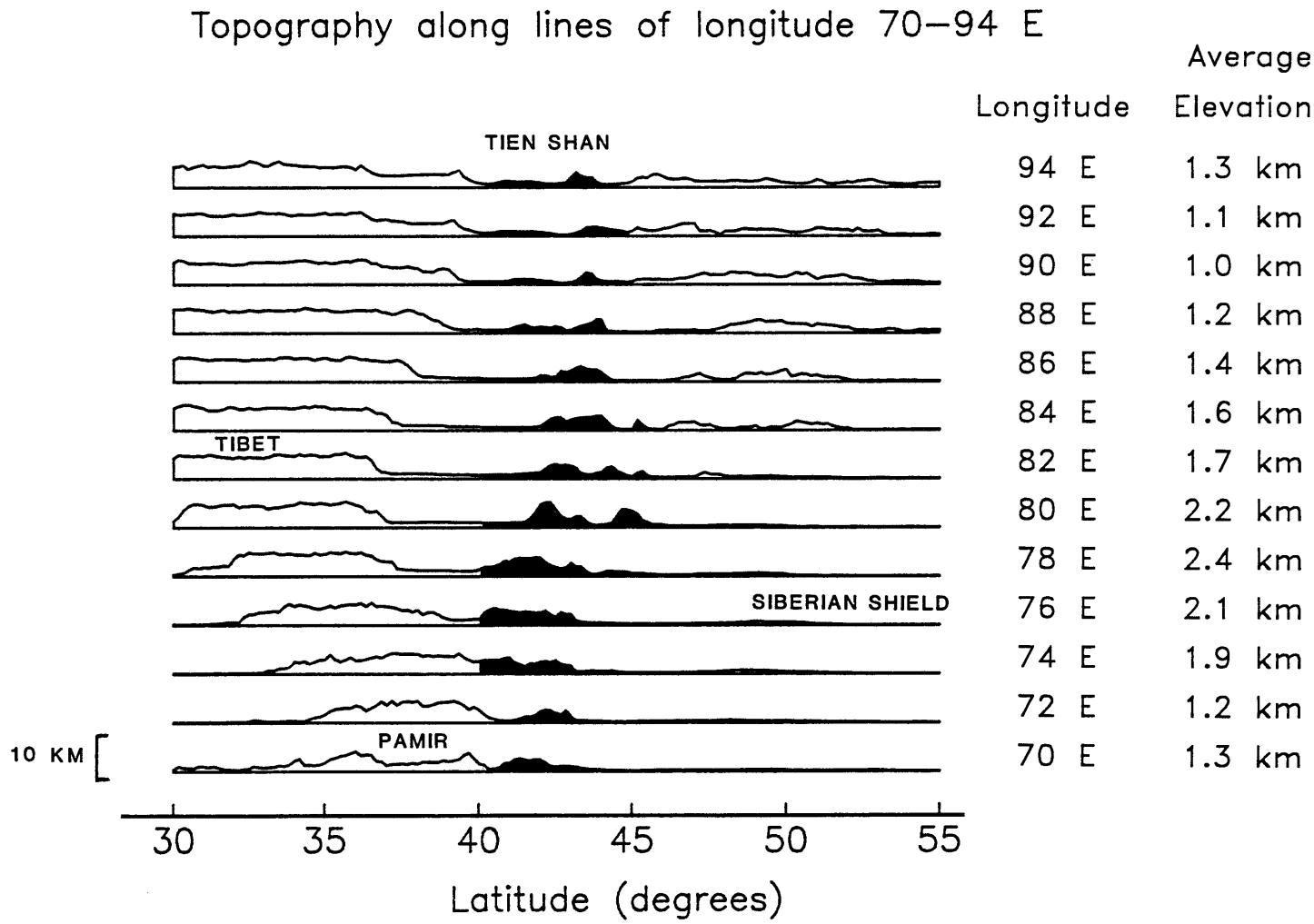
Topography along lines of longitude 70–94 E
Longitude
Average Elevation
TIEN SHAN
94 E 1.3 km
92 E 1.1 km
90 E 1.0 km
88 E 1.2 km
86 E 1.4 km
84 E 1.6 km
TIBET
82 E 1.7 km
80 E 2.2 km
78 E 2.4 km
SIBERIAN SHIELD
76 E 2.1 km
74 E 1.9 km
72 E 1.2 km
PAMIR
70 E 1.3 km
10 KM
30
35
40
45
50
55
Latitude (degrees)

Figure 5

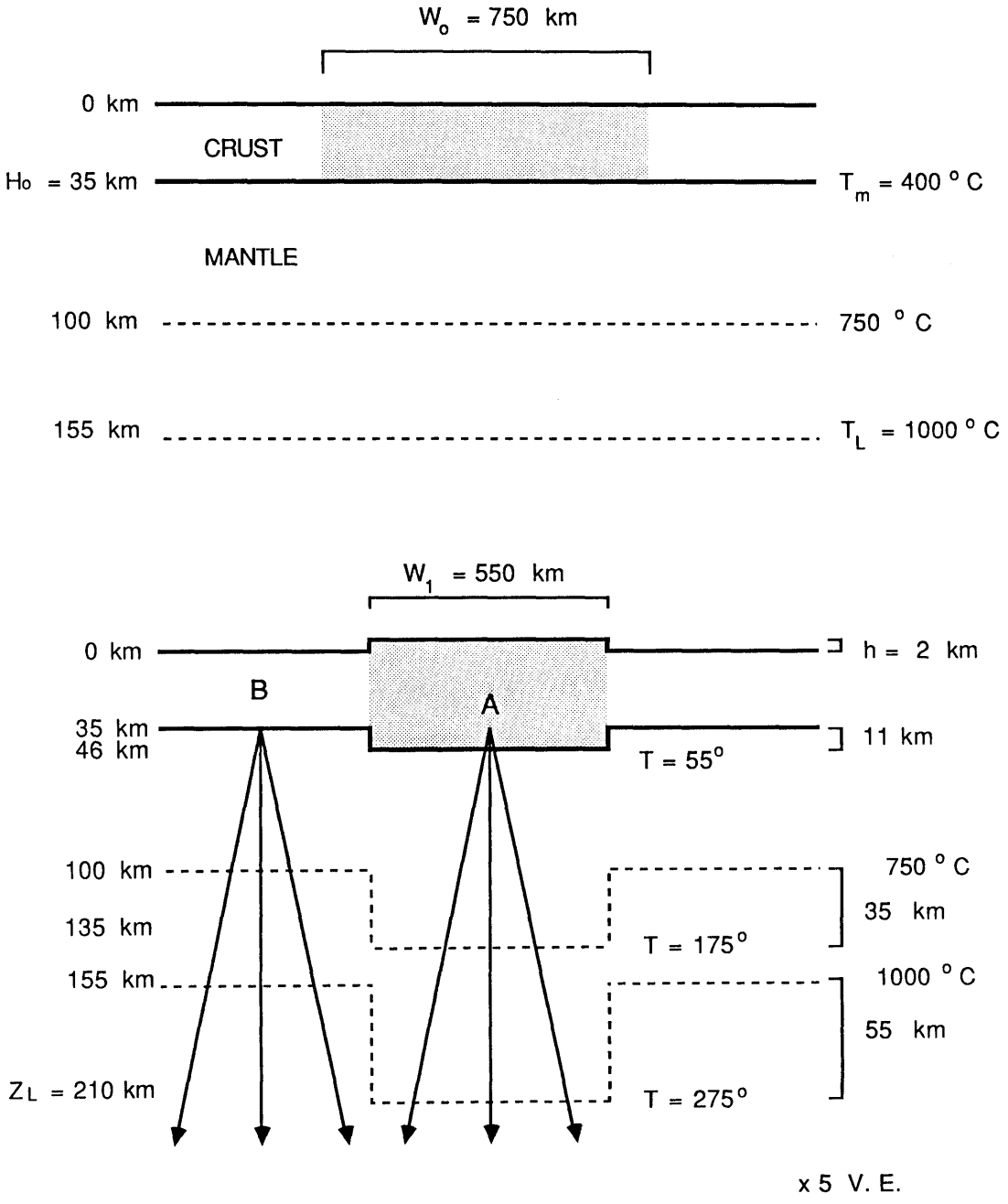
W0 = 750 km
0 km
CRUST
H0 = 35 km
Tm = 400 ° C
MANTLE
100 km
750 ° C
155 km
TL = 1000 ° C
W1 = 550 km
0 km
h = 2 km
B
A
35 km
46 km
11 km
T = 55°
100 km
750 ° C
135 km
35 km
T = 175°
155 km
1000 ° C
55 km
ZL = 210 km
T = 275°
x 5 V. E.

Figure 6

2 JUNE 73

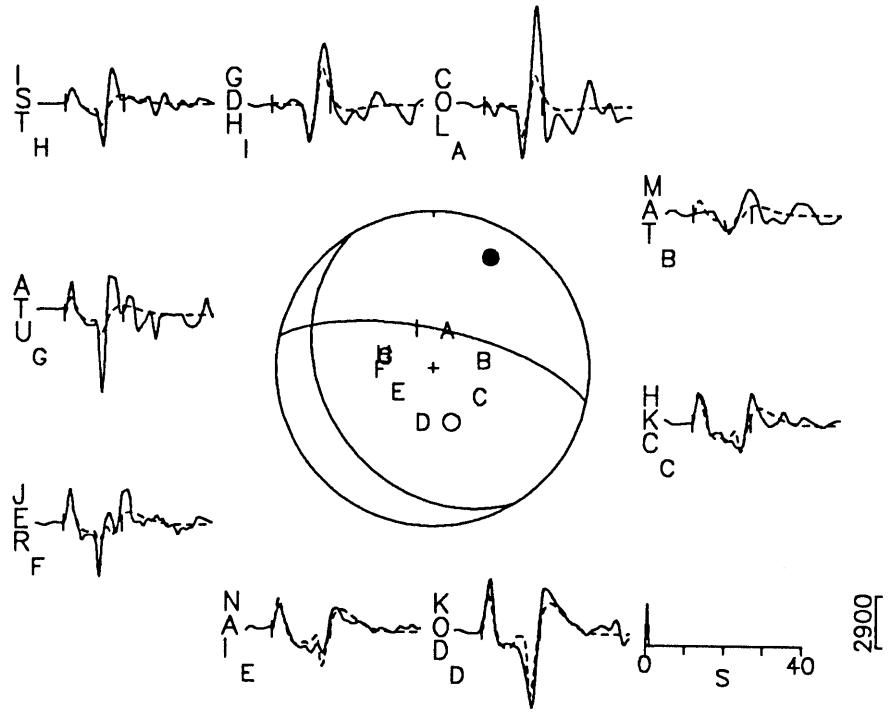

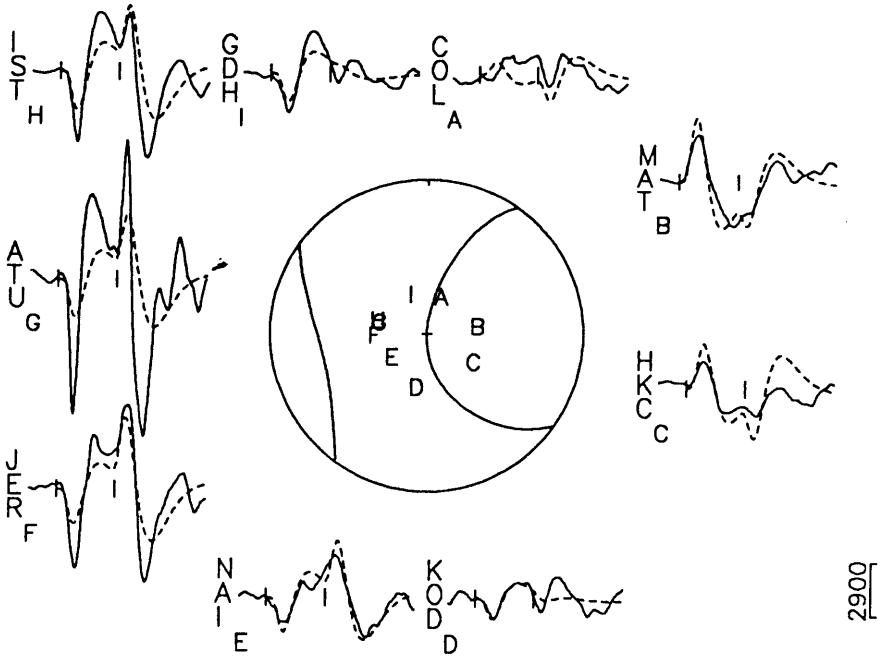

Figure 7

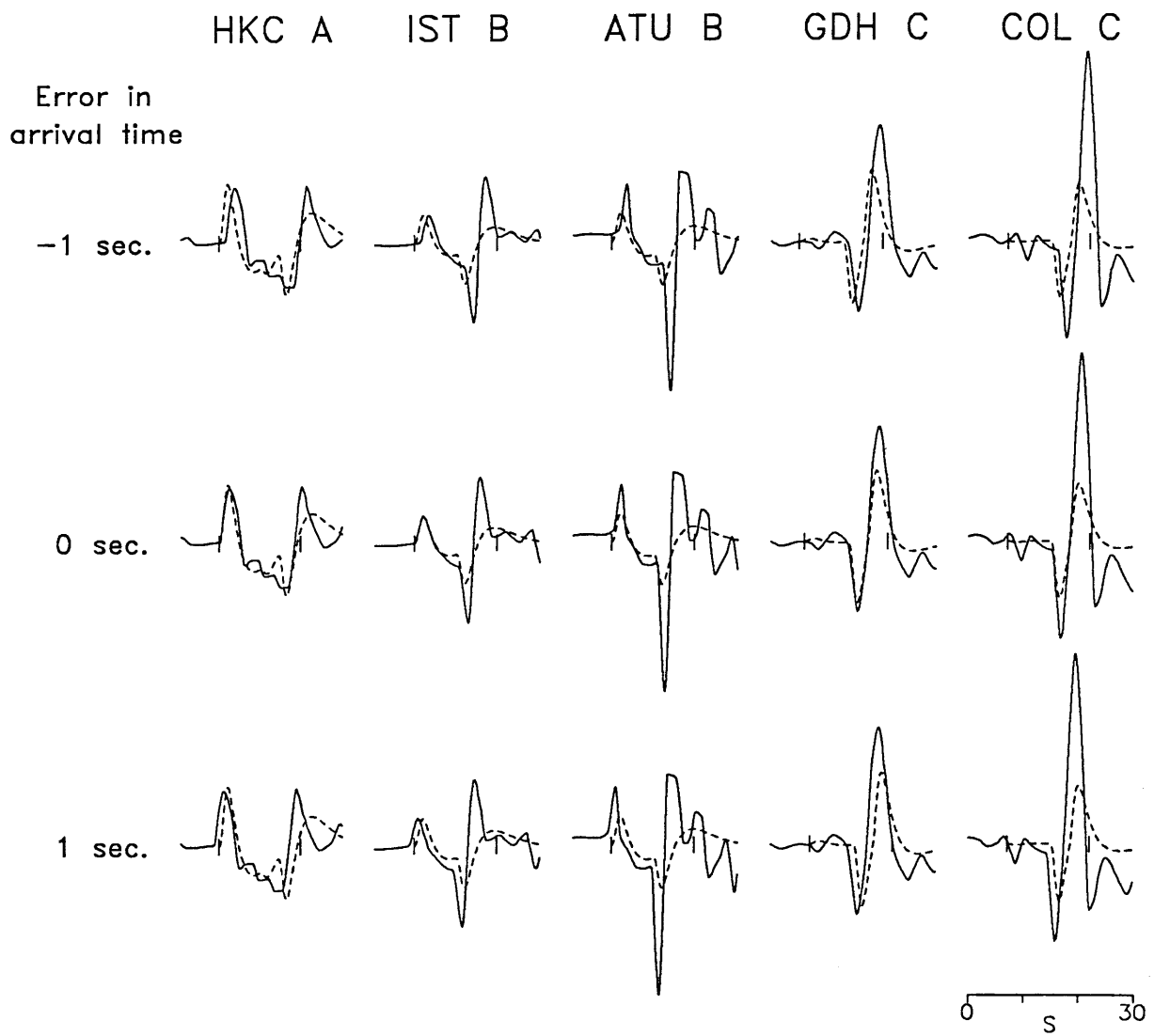
2 JUNE 1973 P WAVEFORMS
HKC A
IST B
ATU B
GDH C
COL C
Error in arrival time
−1 sec.
0 sec.
1 sec.
0
S
30

Figure 8a

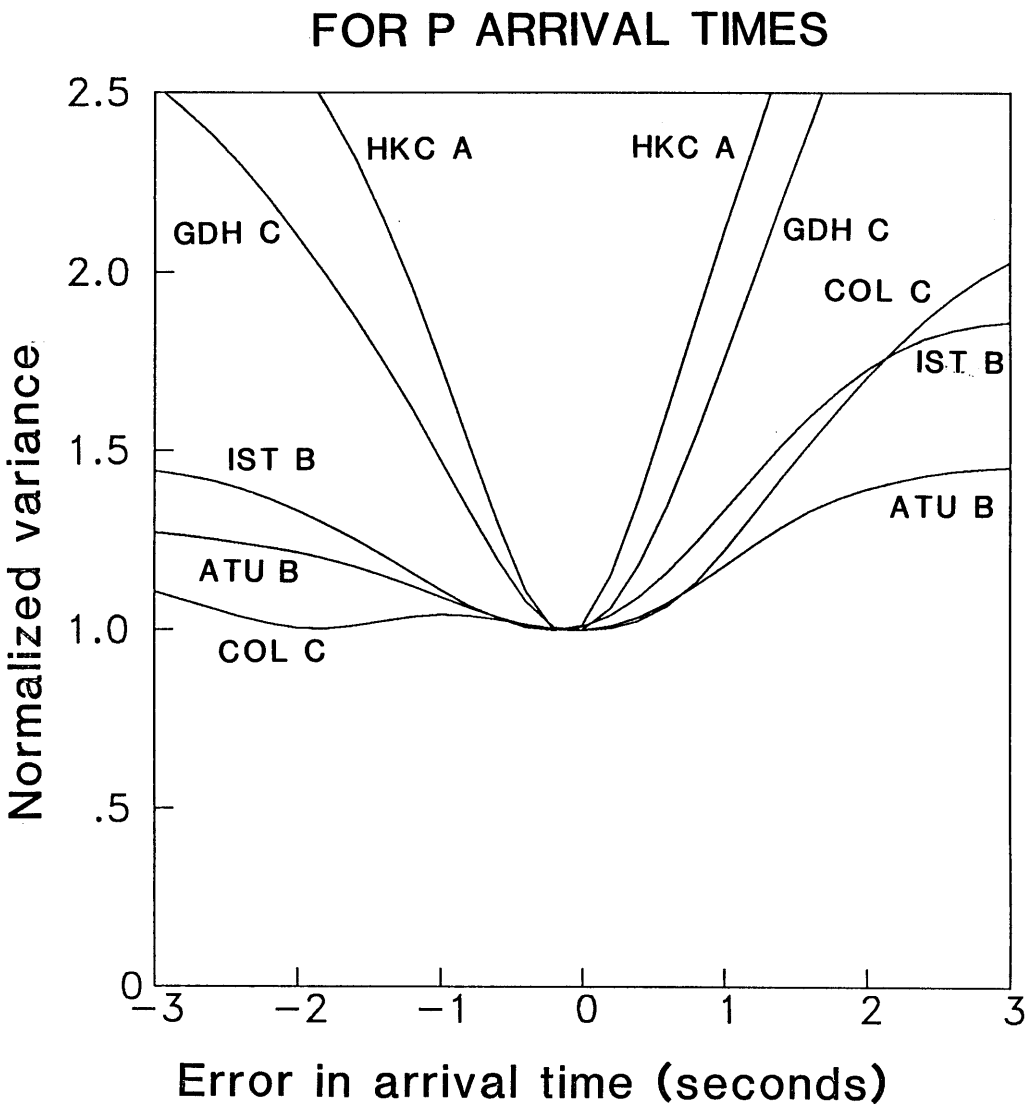
FOR P ARRIVAL TIMES
Normalized variance
2.5
2.0
1.5
1.0
.5
0
HKC A
HKC A
GDH C
GDH C
COL C
IST B
IST B
ATU B
ATU B
COL C
−3
−2
−1
0
1
2
3
Error in arrival time (seconds)

Figure 8b

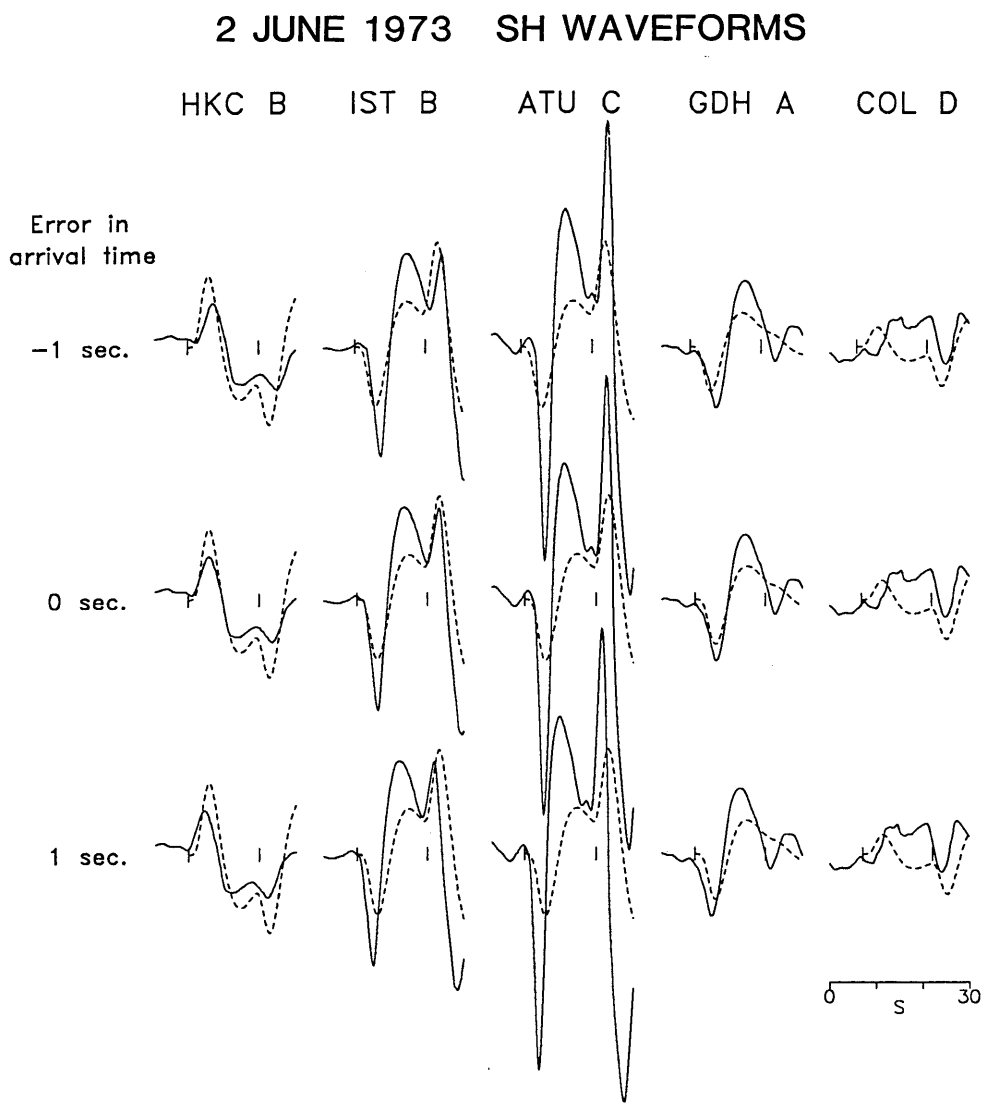
2 JUNE 1973 SH WAVEFORMS
HKC B
IST B
ATU C
GDH A
COL D
Error in arrival time
−1 sec.
0 sec.
1 sec.
0
S
30

Figure 9a

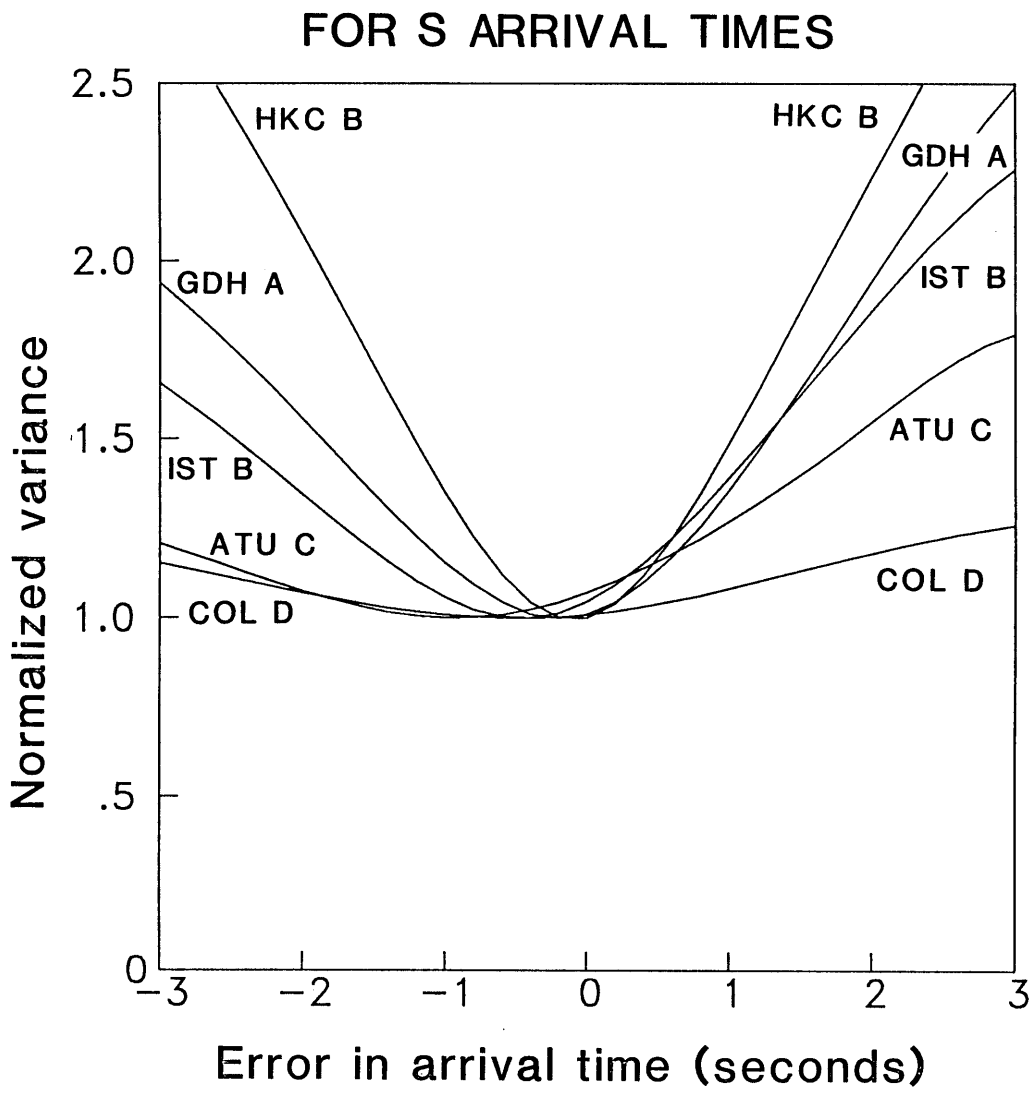
FOR S ARRIVAL TIMES
Normalized variance
2.5
2.0
1.5
1.0
.5
0
HKC B
GDH A
IST B
ATU C
COL D
HKC B
GDH A
IST B
ATU C
COL D
−3
−2
−1
0
1
2
3
Error in arrival time (seconds)

Figure 9b

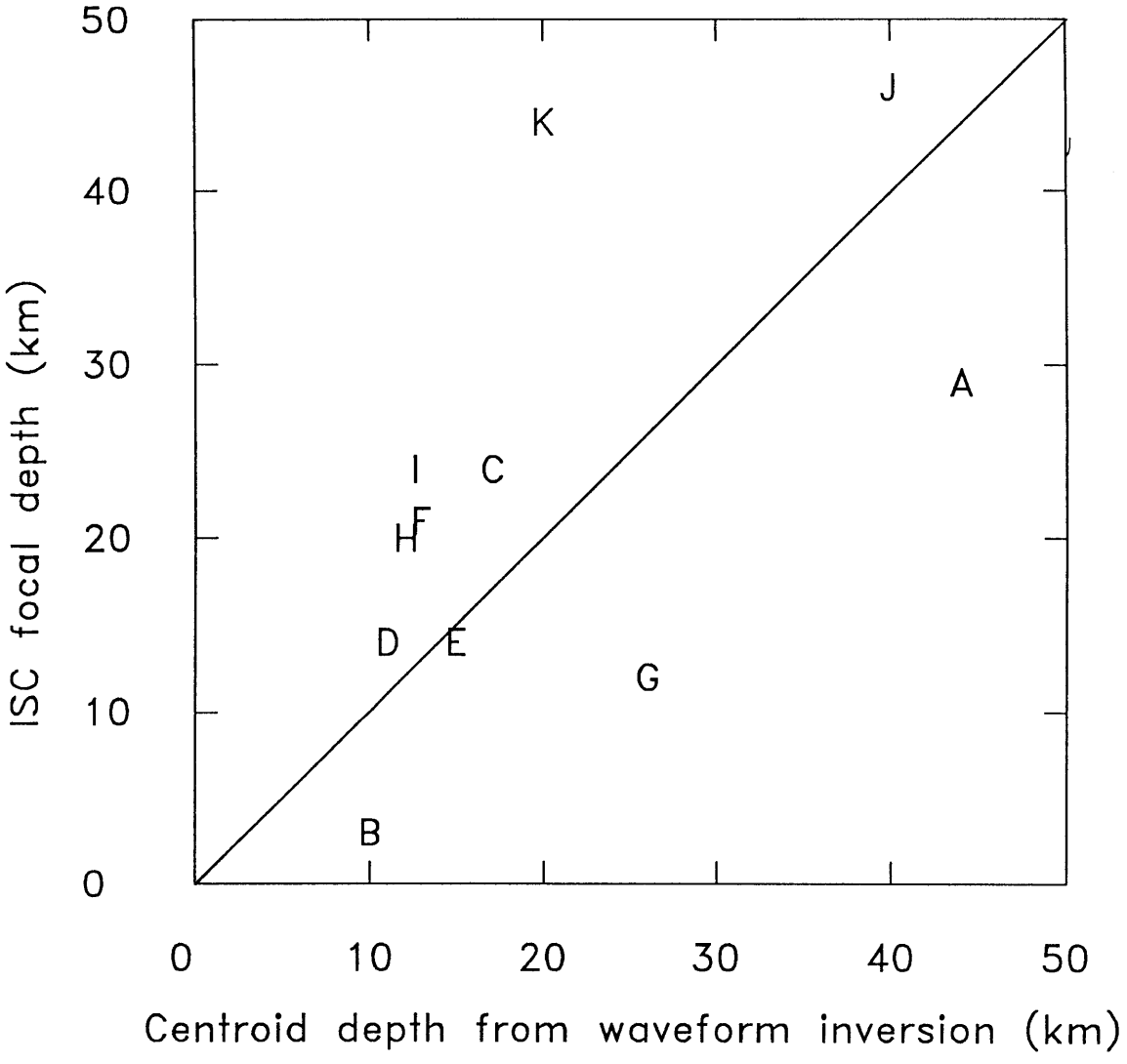
50
40
30
20
10
0
ISC focal depth (km)
0
10
20
30
40
50
Centroid depth from waveform inversion (km)
K
J
A
I
C
F
H
D
E
G
B

Figure 10

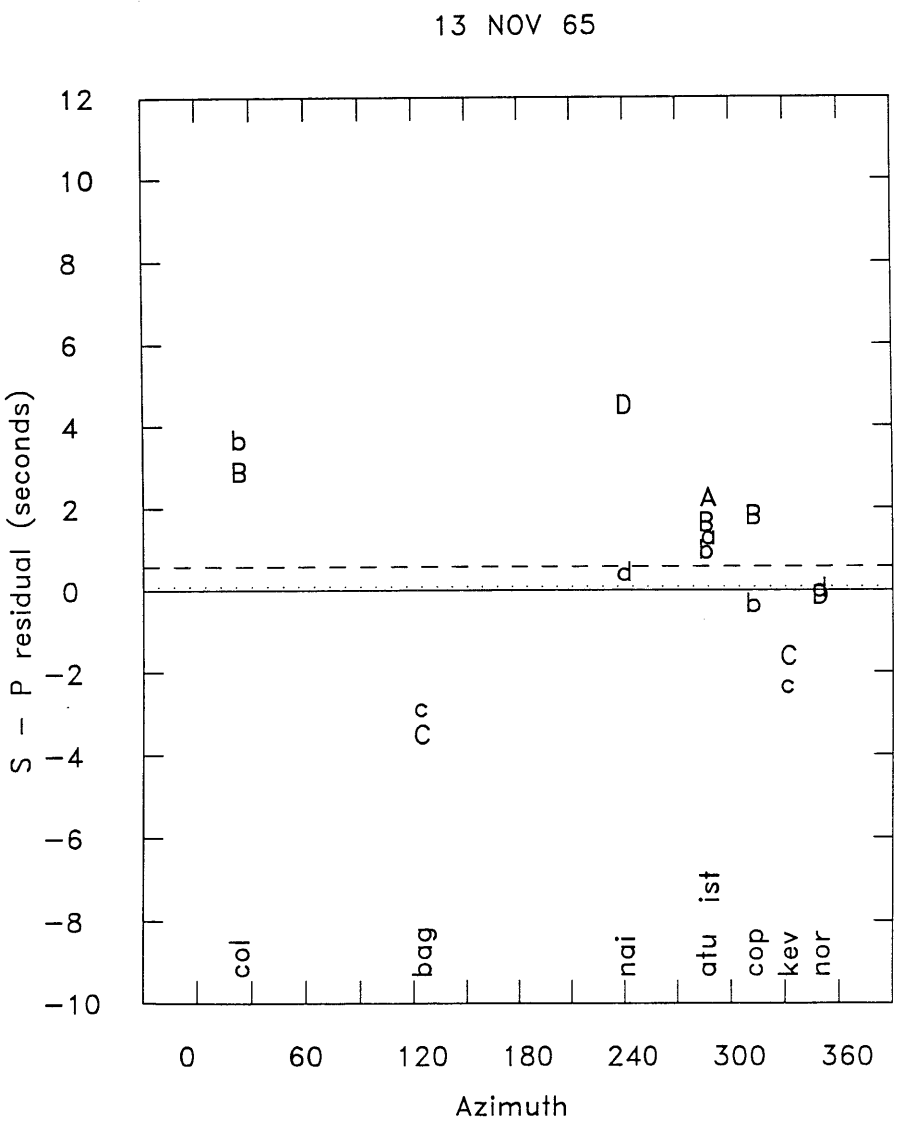

Figure 11a

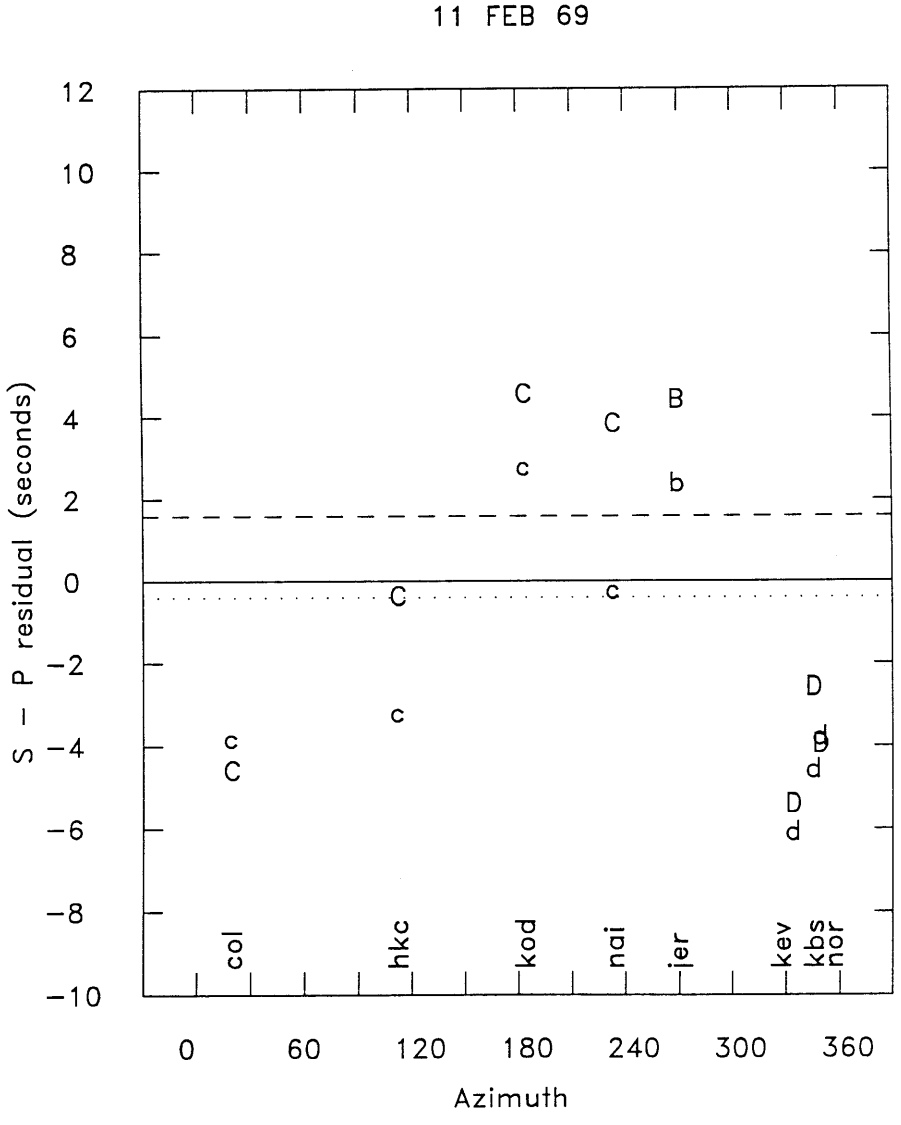

Figure 11b

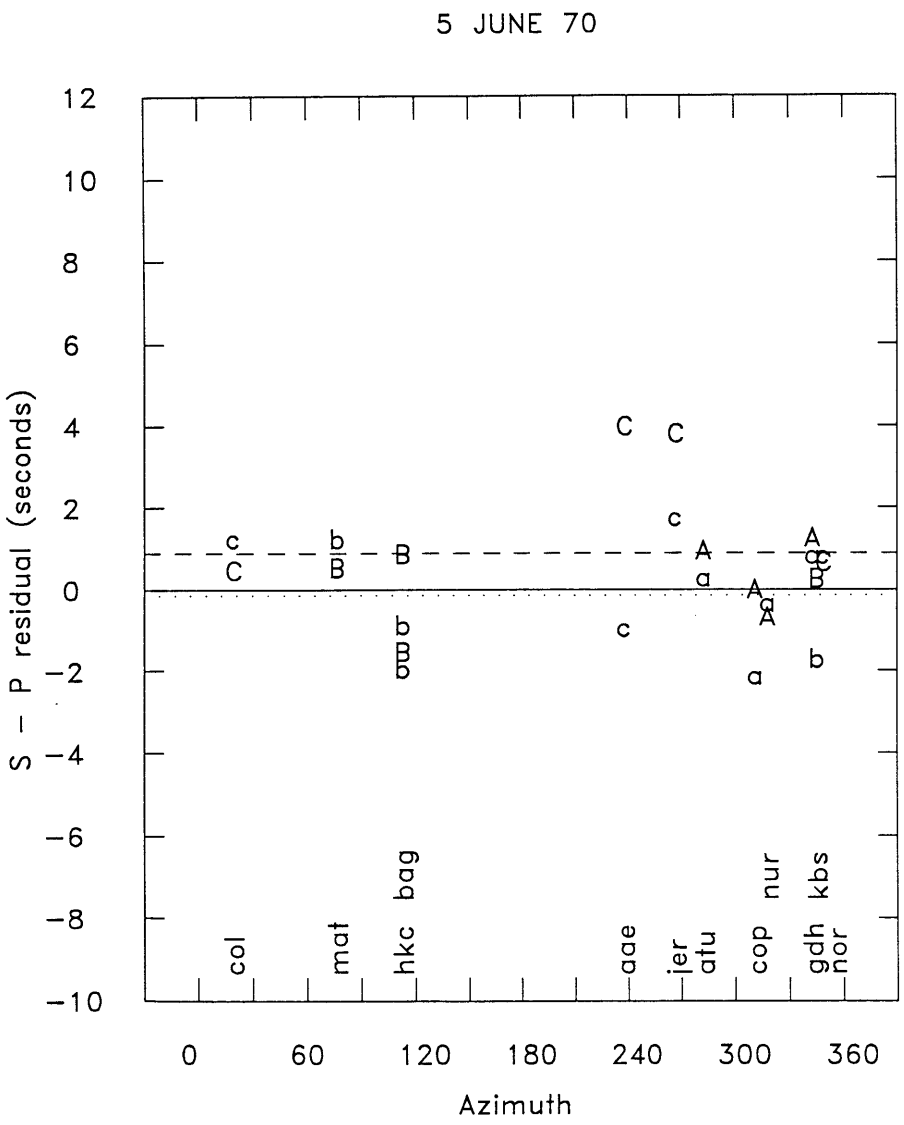

Figure 11c

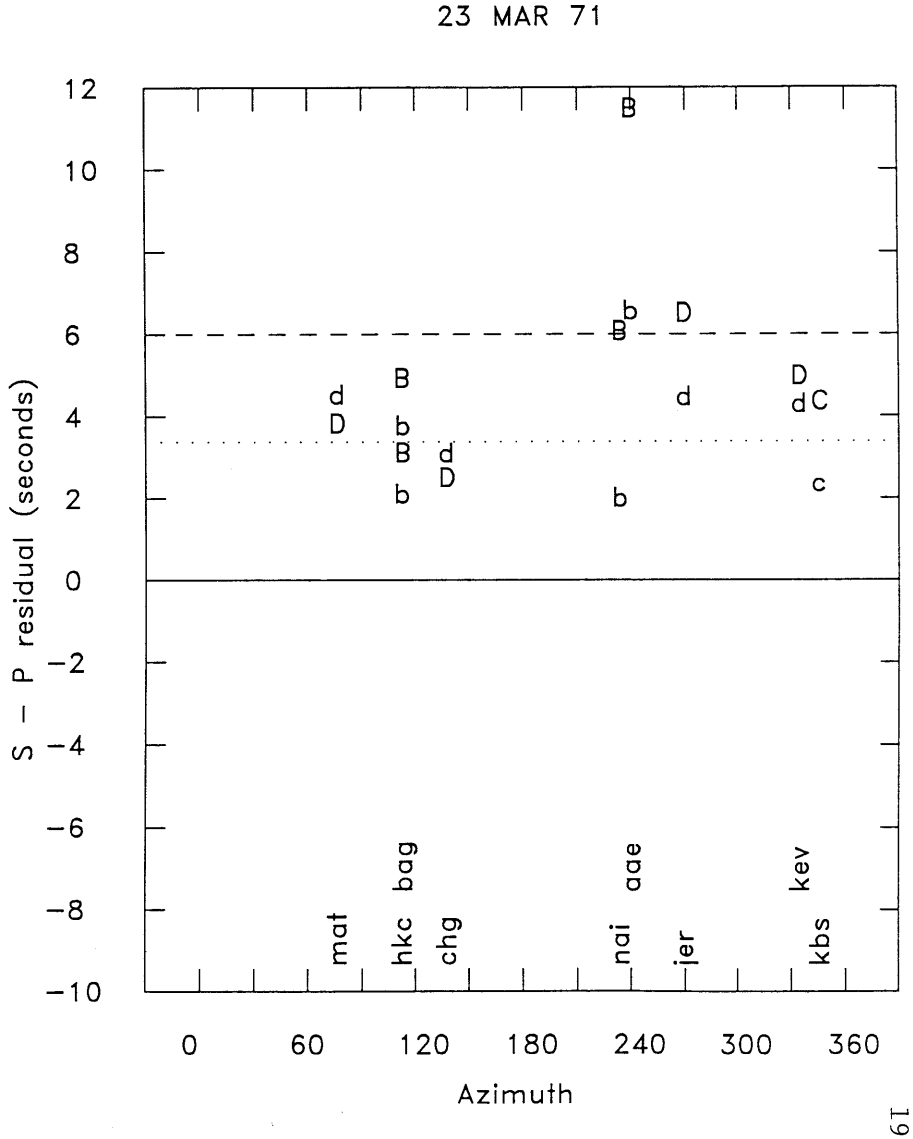

Figure 11d

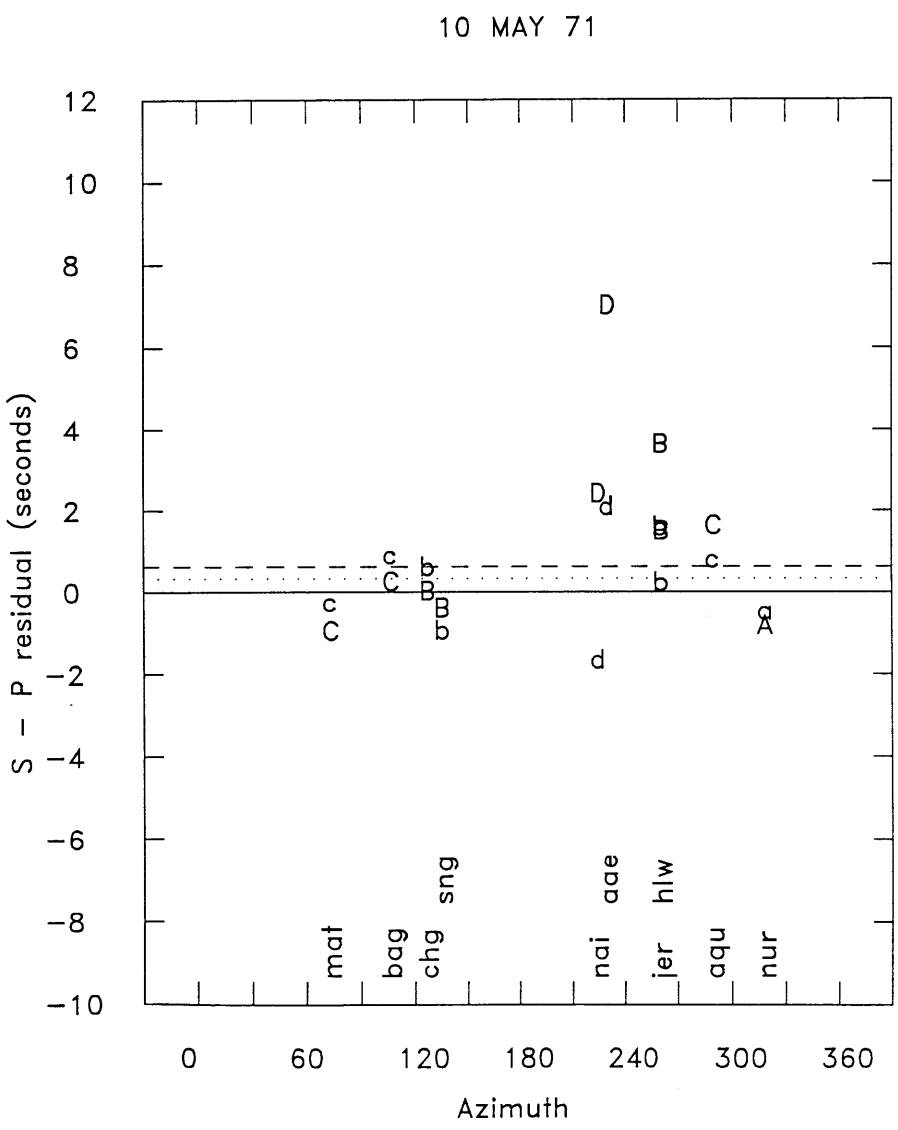

Figure 11e

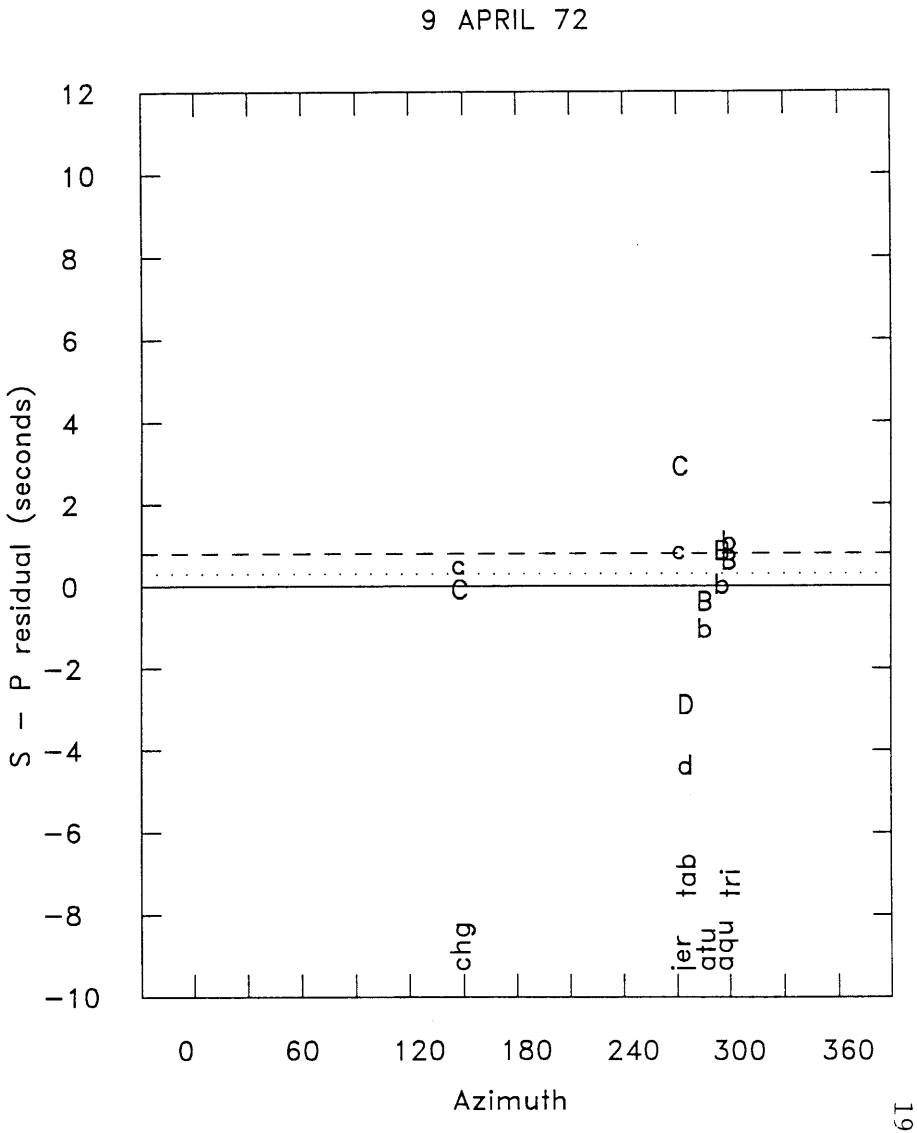

Figure 11f

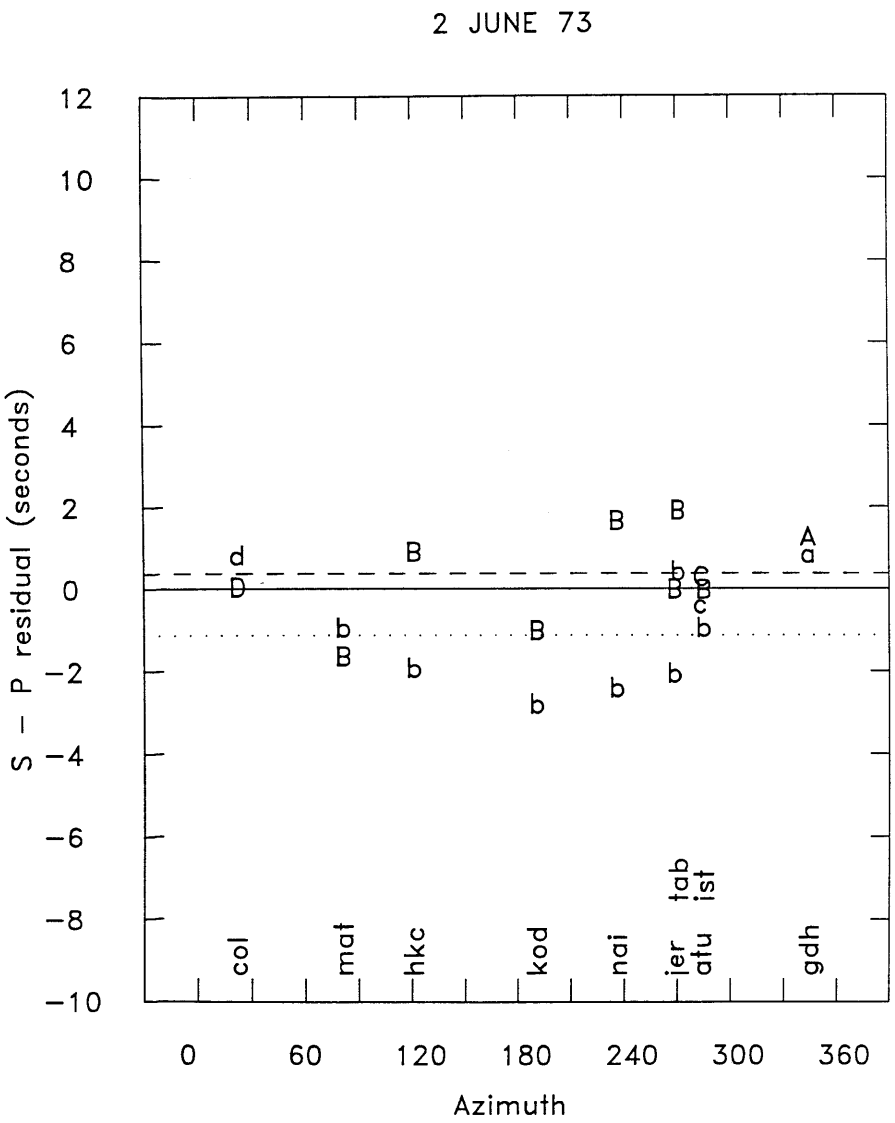

Figure 11g

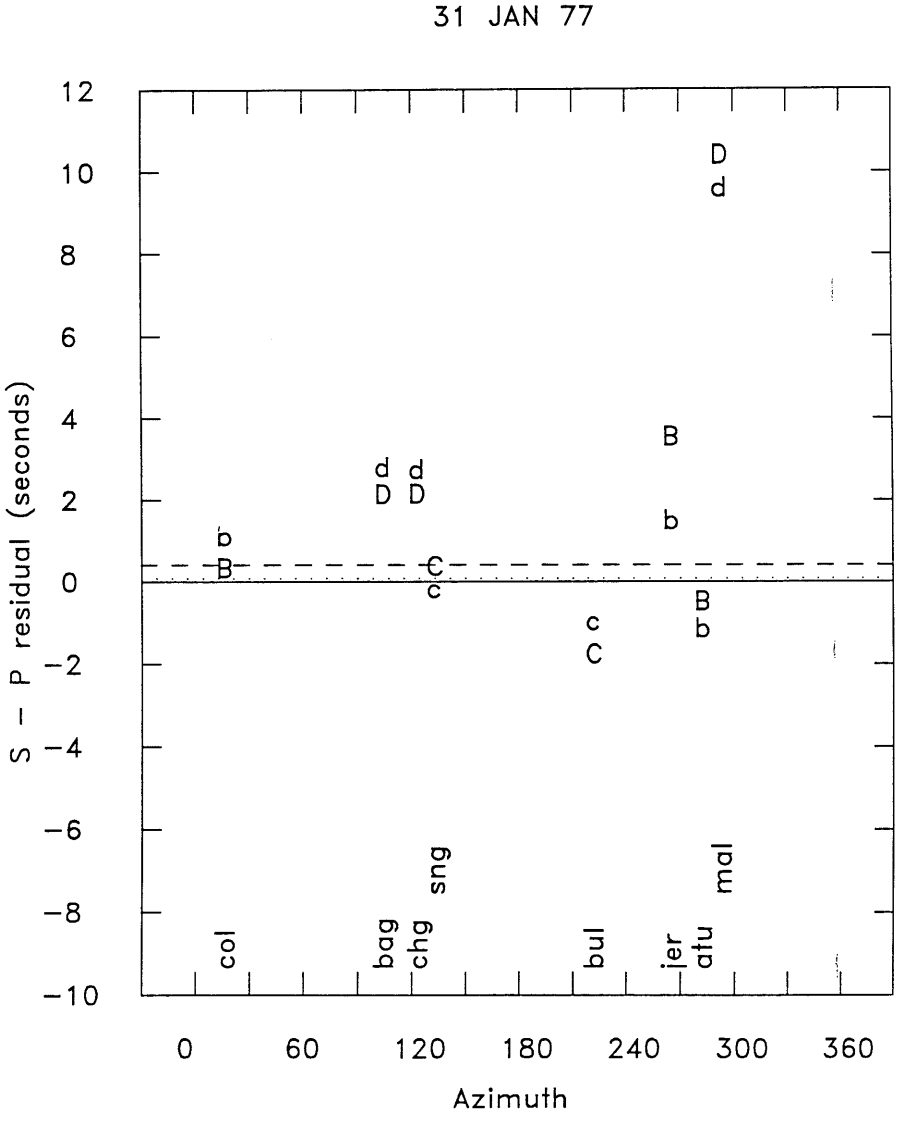

Figure 11h

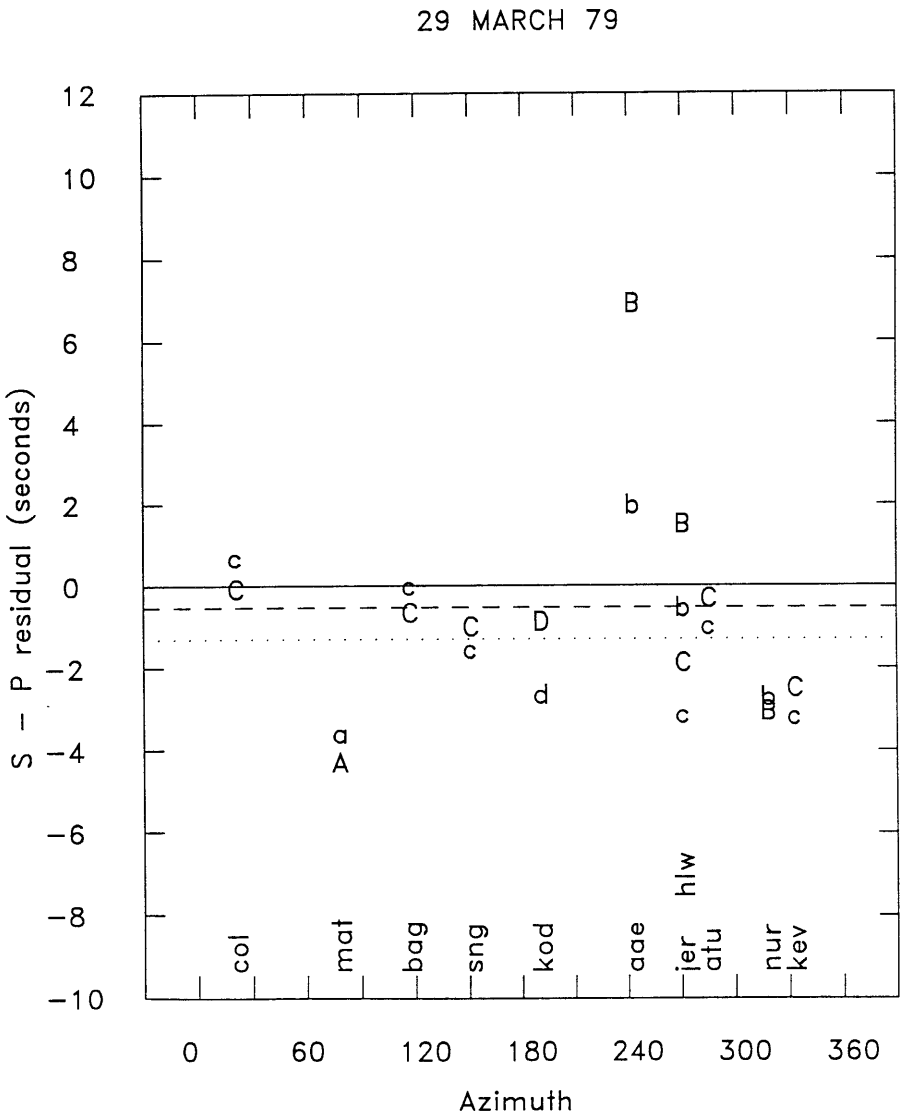

Figure 11i

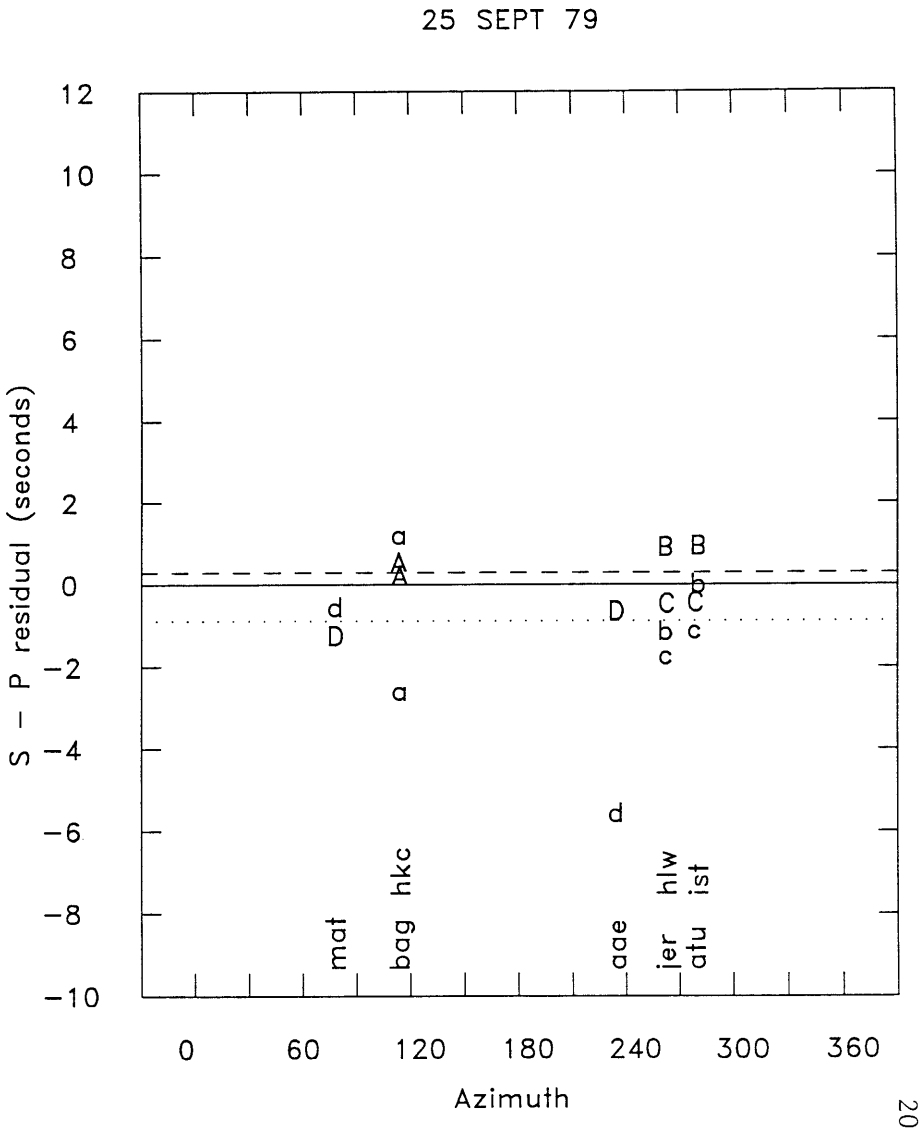

Figure 11j

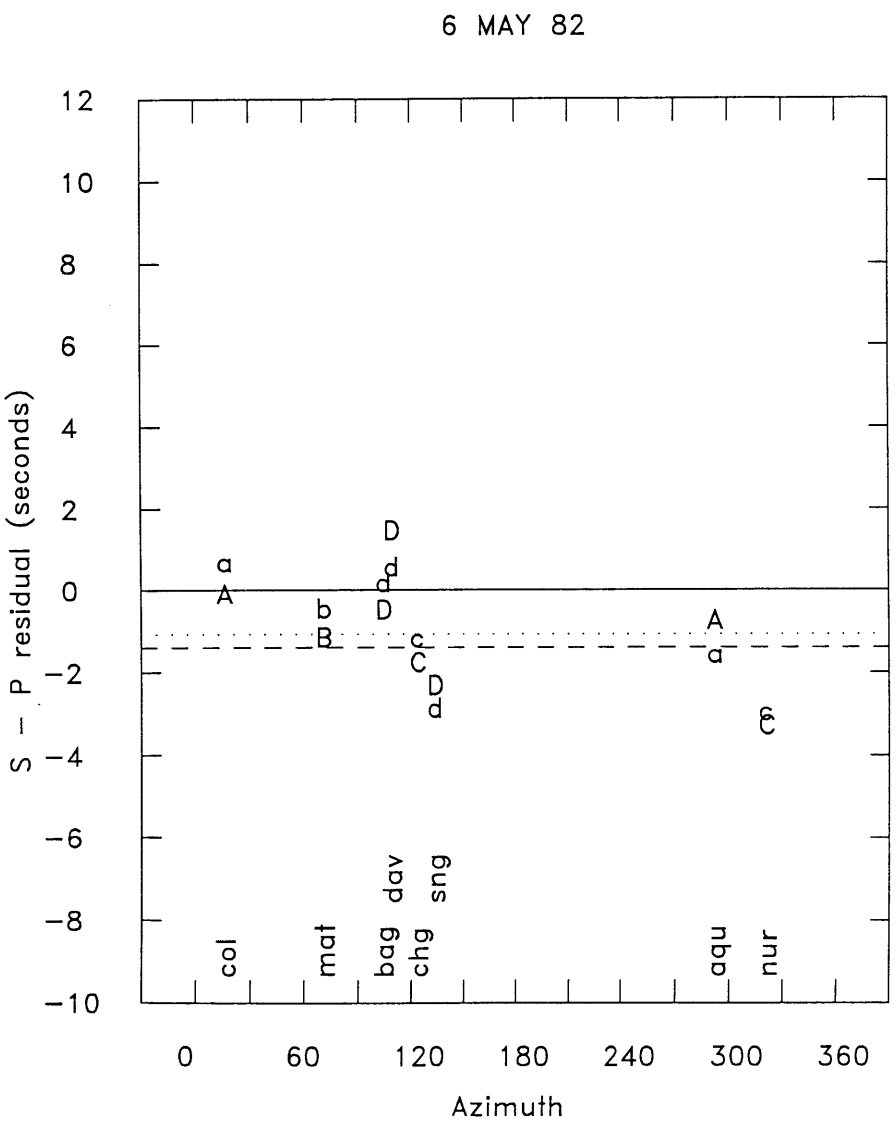

Figure 11k

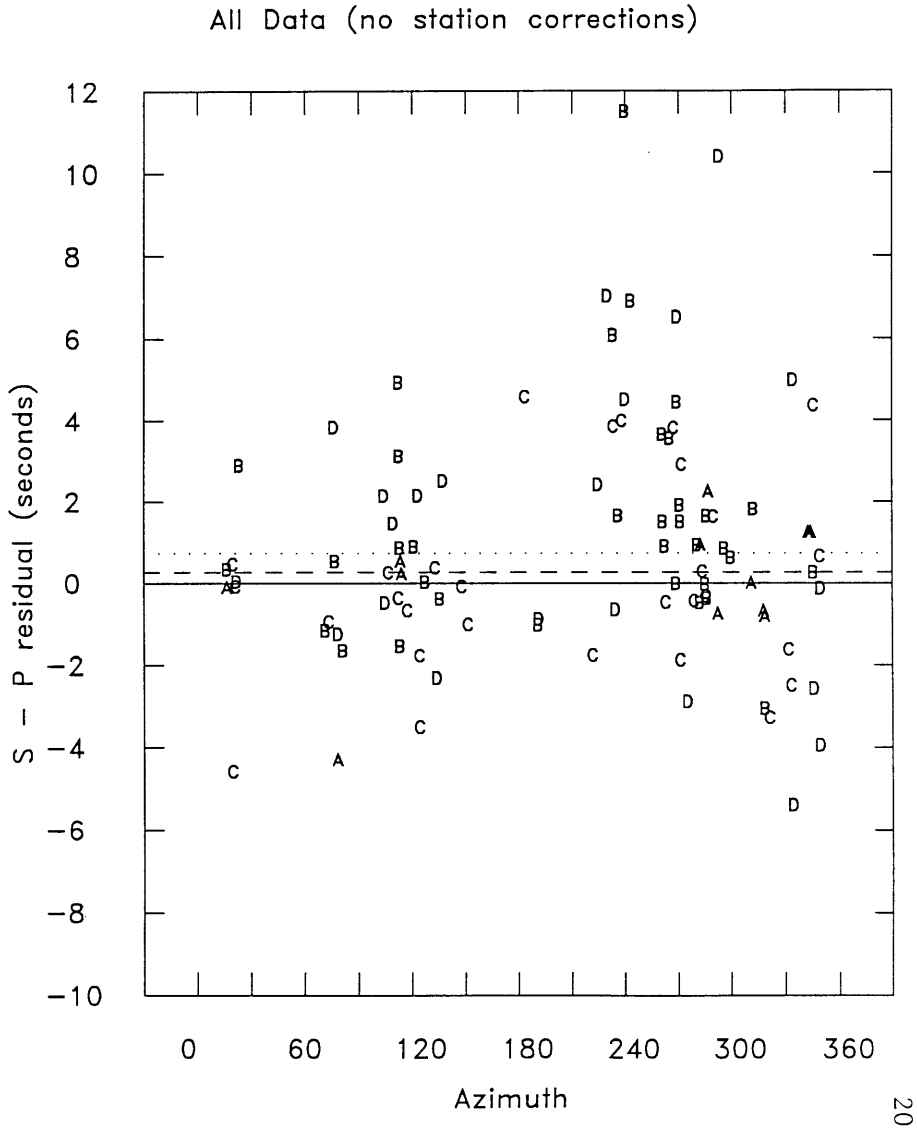

Figure 111

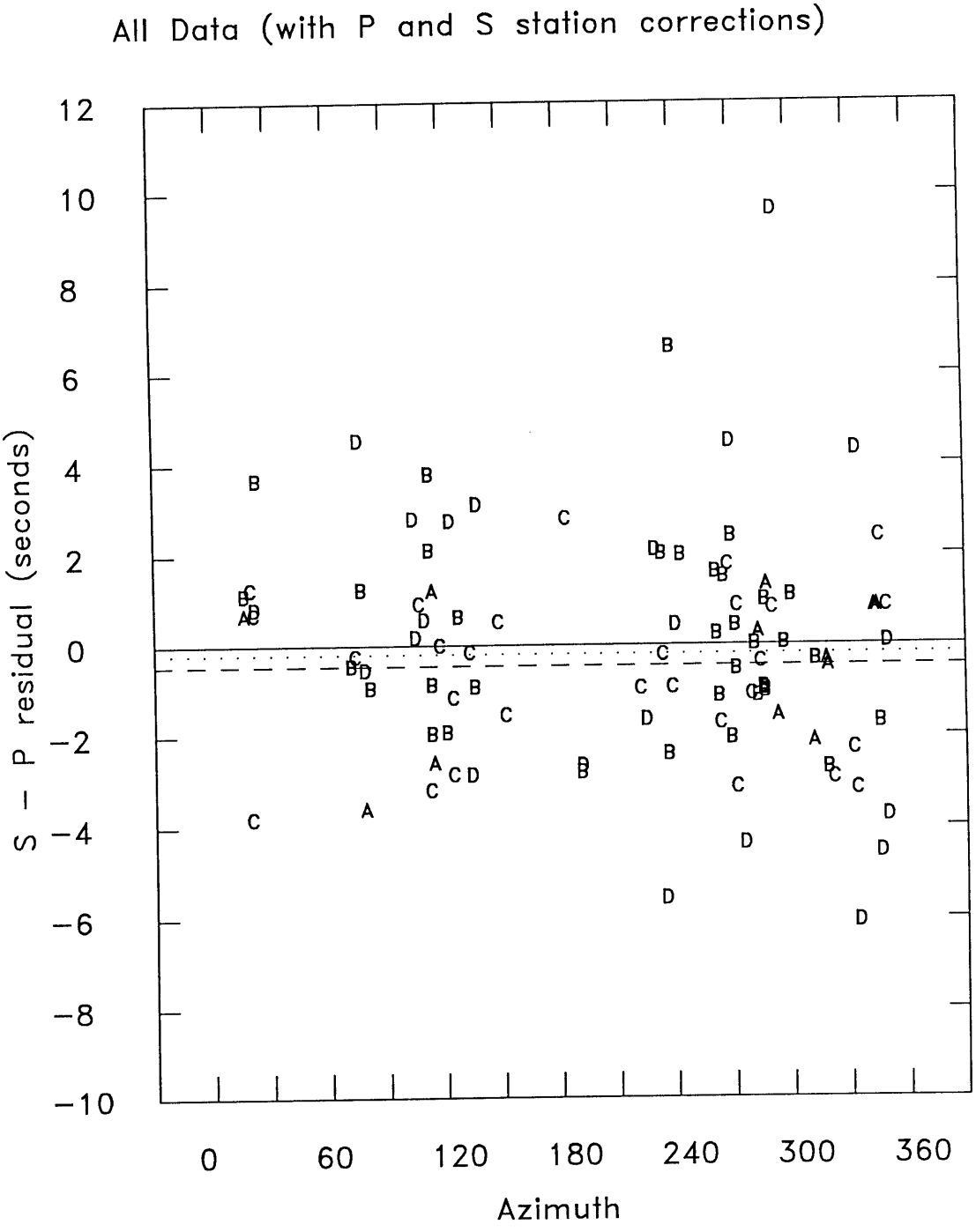
All Data (with P and S station corrections)
S - P residual (seconds)
12
10
8
6
4
2
0
−2
−4
−6
−8
−10
0
60
120
180
240
300
360
Azimuth

Figure 11m

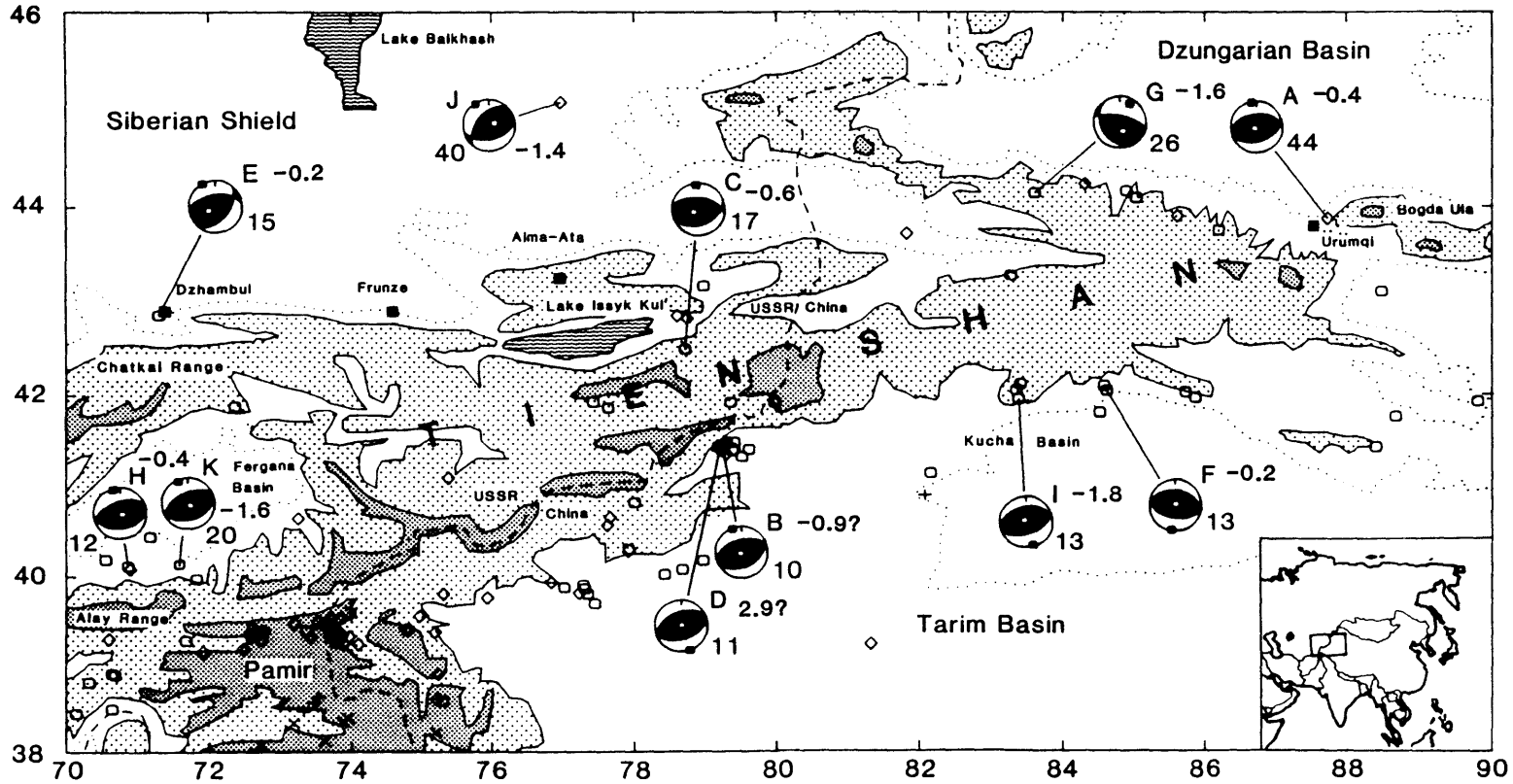
Lake Baikhash
Siberian Shield
Dzungarian Basin
J
40
-1.4
G -1.6
26
A -0.4
44
E -0.2
15
C -0.6
17
Bogda Ula
Urumqi
Alma-Ata
Dzhambul
Frunze
Lake Issyk Kul'
USSR/ China
TIEN SHAN
Chatkal Range
Kucha Basin
H -0.4
K
Fergana Basin
-1.6
12
20
USSR
China
B -0.9?
10
I -1.8
13
F -0.2
13
D 2.9?
11
Tarim Basin
Alay Range
Pamir
46
44
42
40
38
70
72
74
76
78
80
82
84
86
88
90

Figure 12

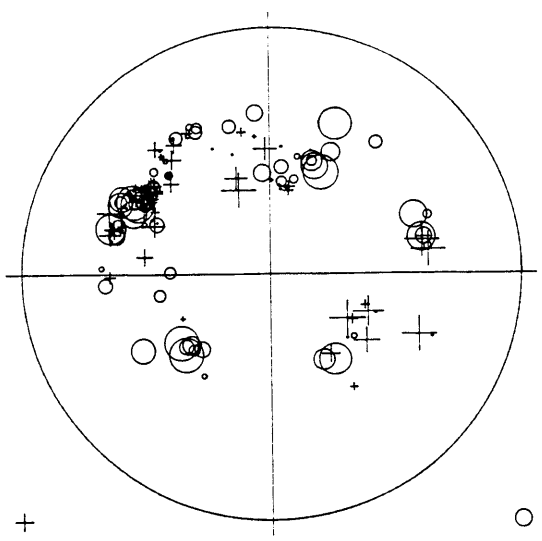

EVENT 1

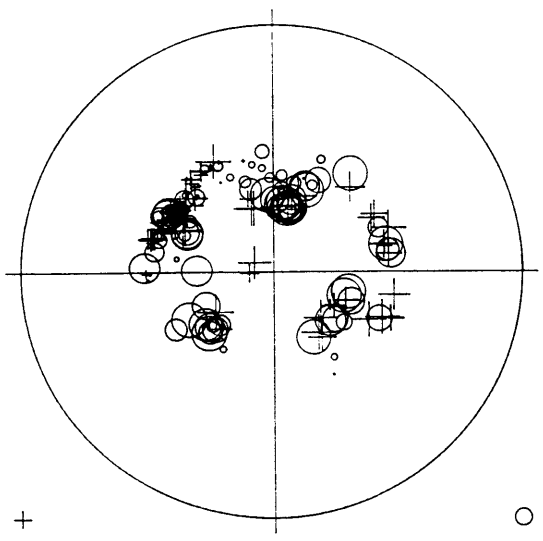

EVENT 2

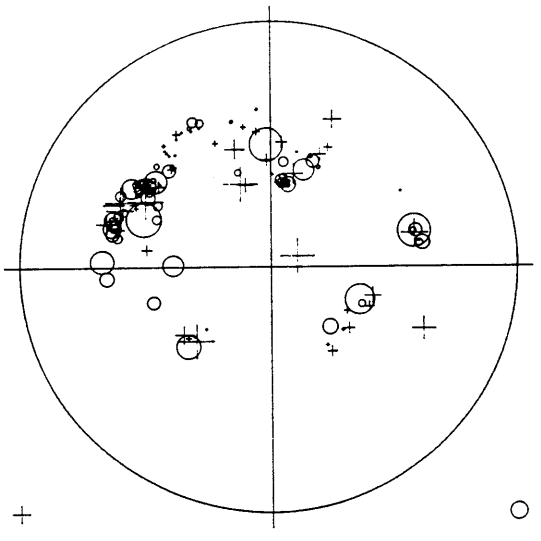

EVENT 4

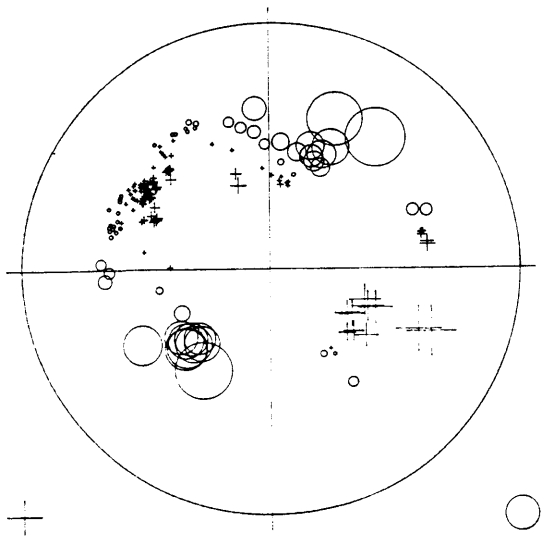

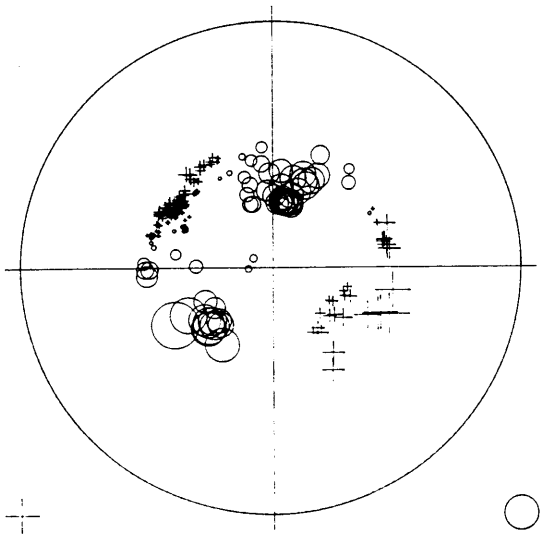

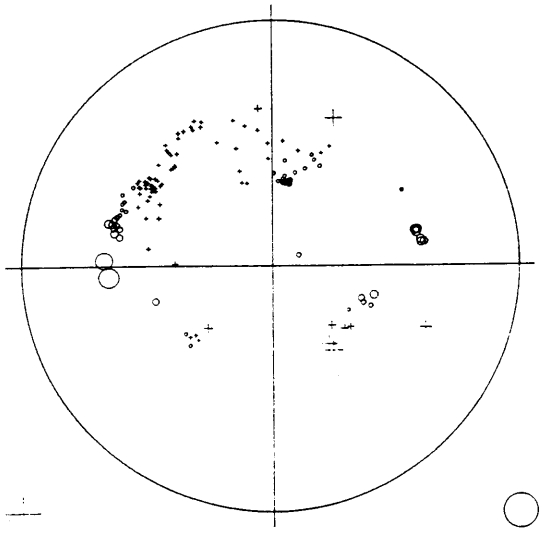

Figure 13

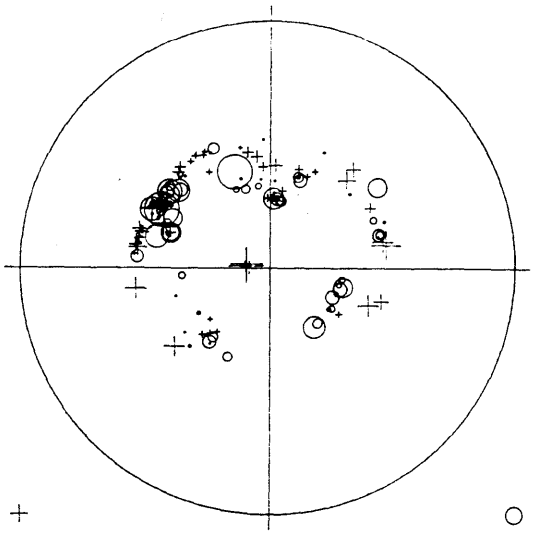

EVENT 3

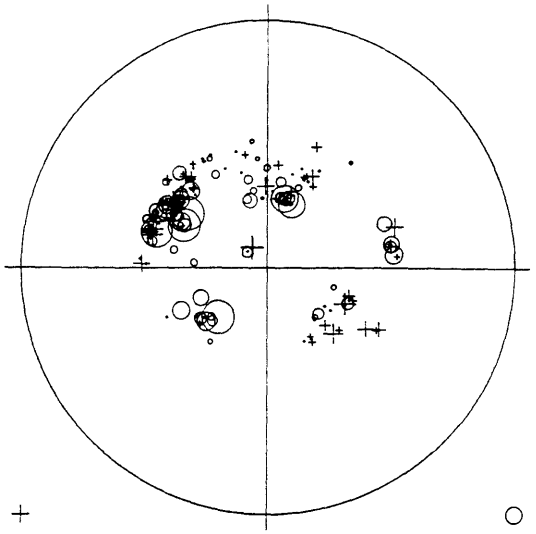

EVENT 5

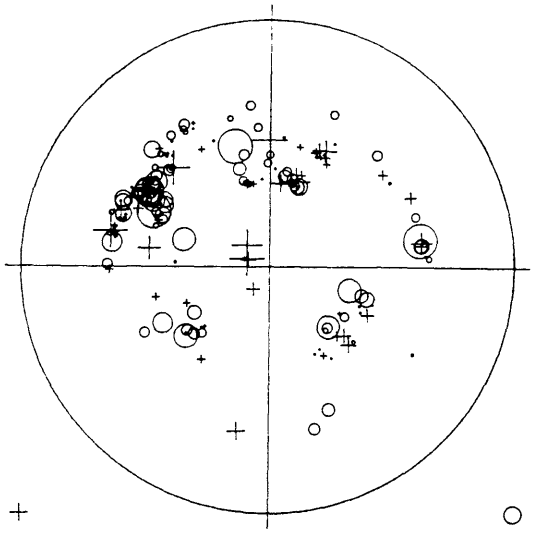

EVENT 6

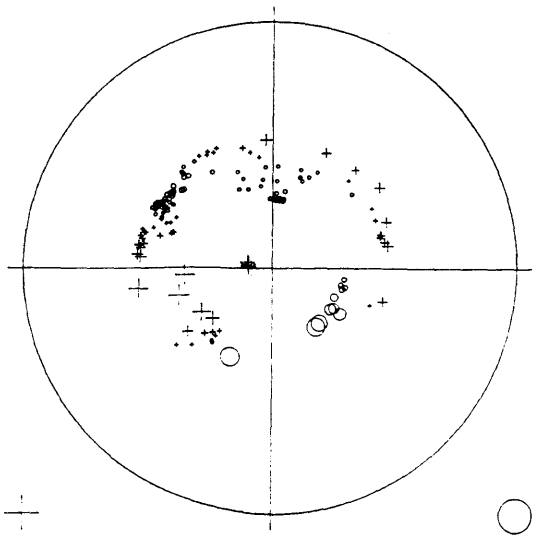

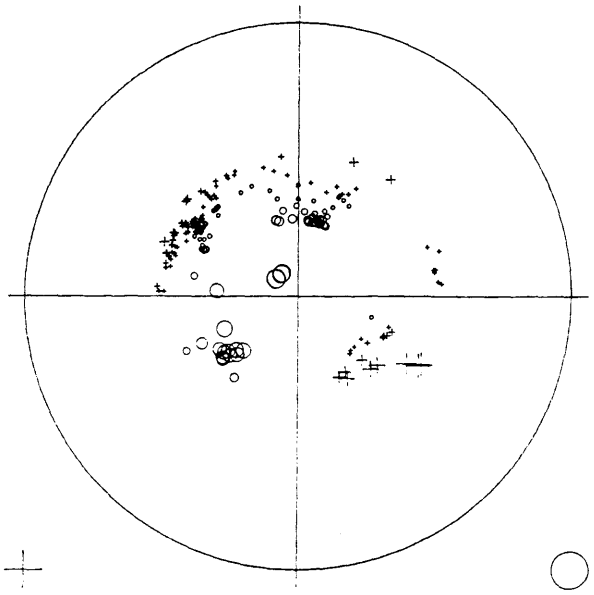

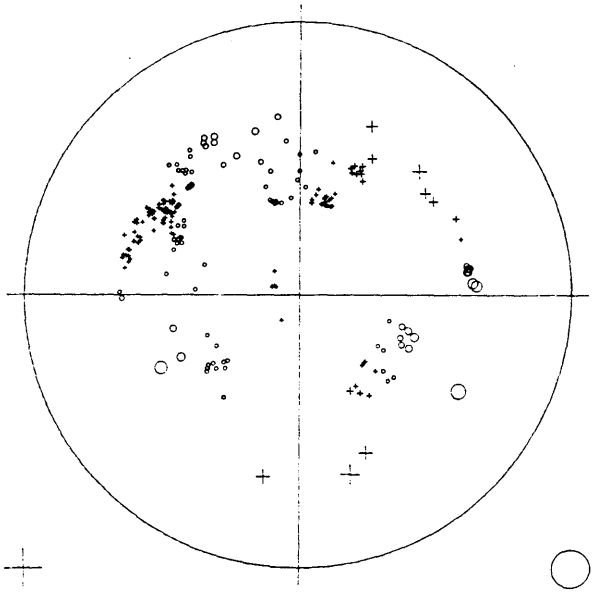

Figure 13 (cont.)

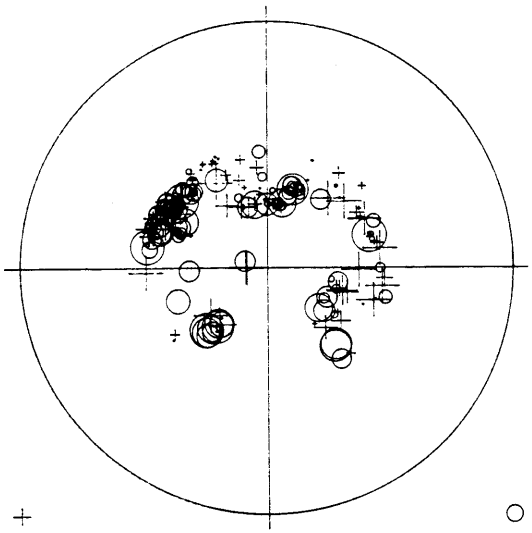

EVENT 7

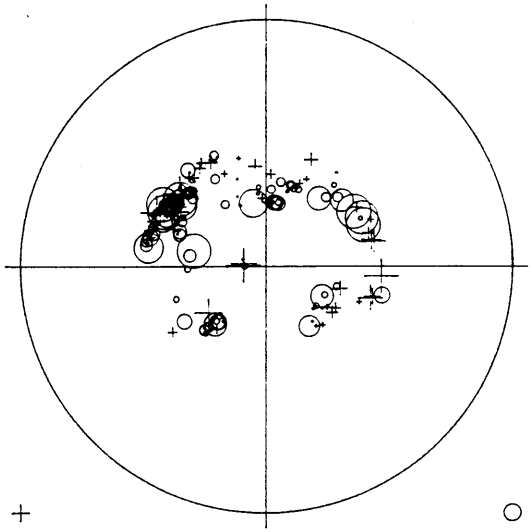

EVENT 8

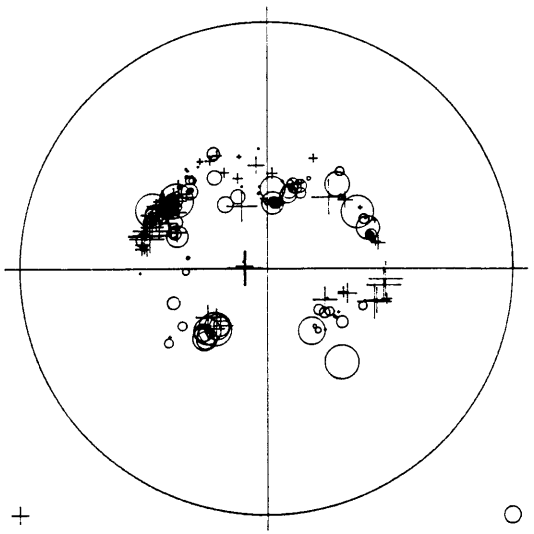

EVENT 9

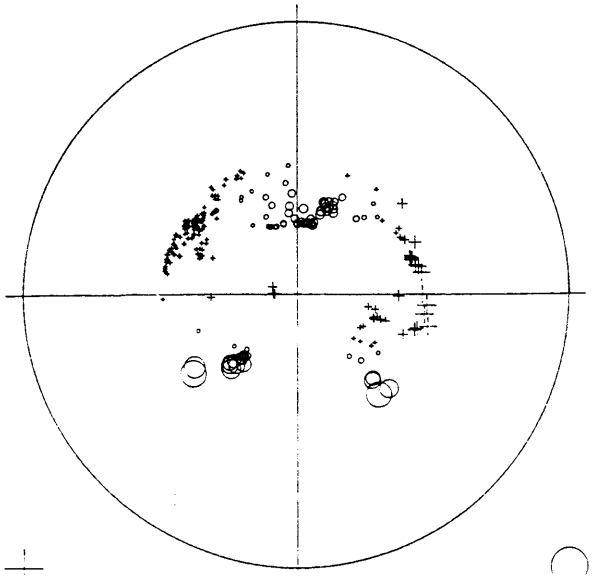

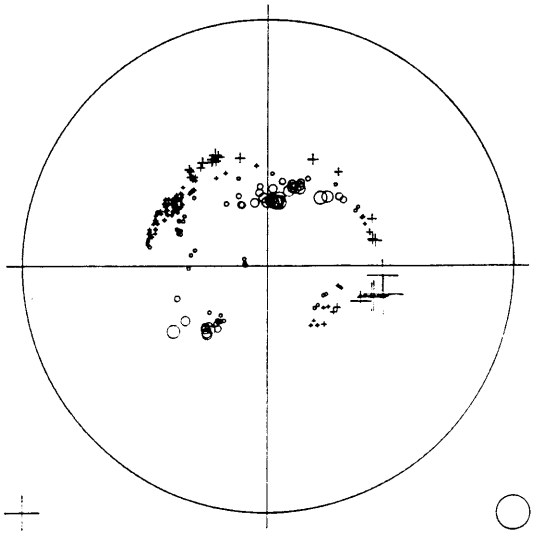

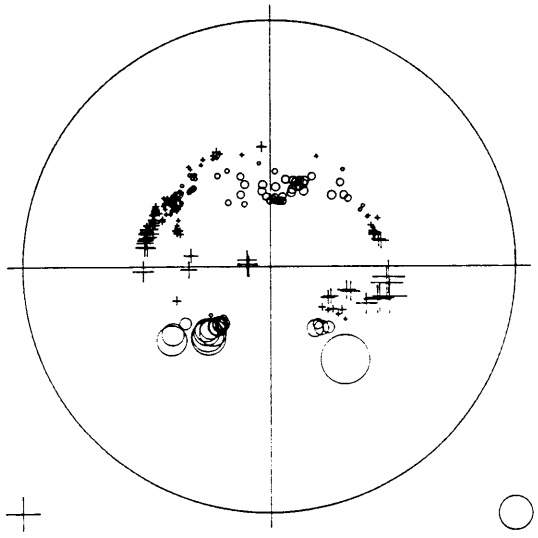

Figure 13 (cont.)

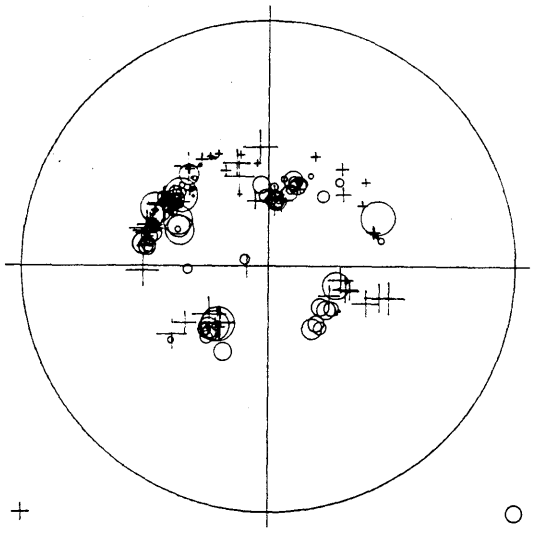

EVENT 10

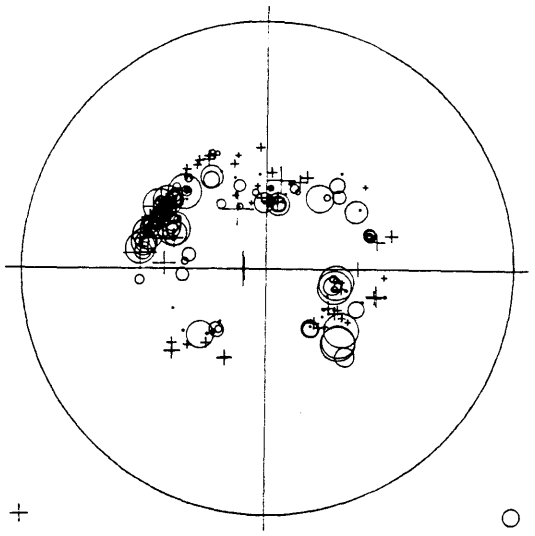

EVENT 11

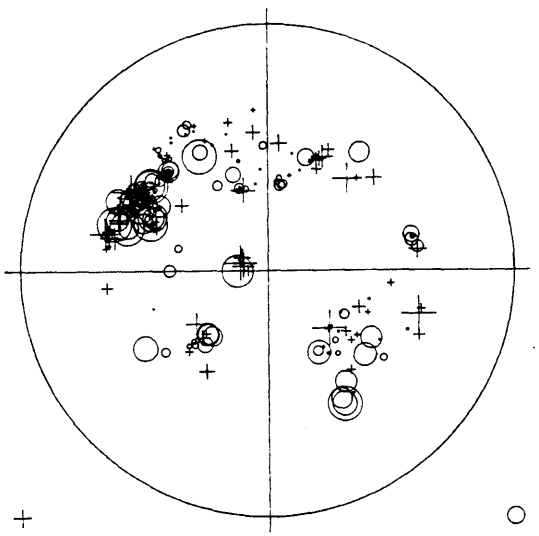

EVENT 12

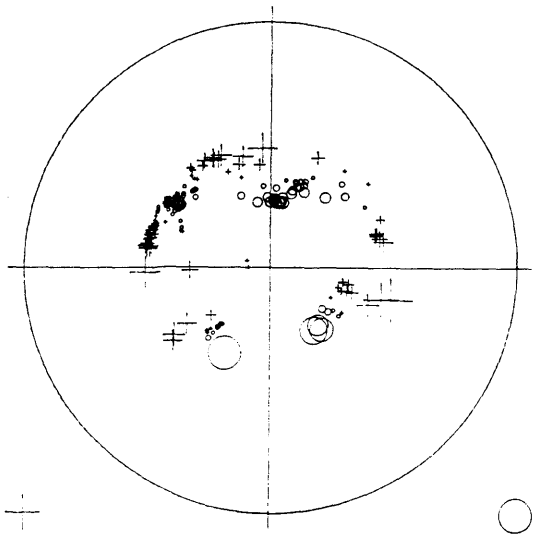

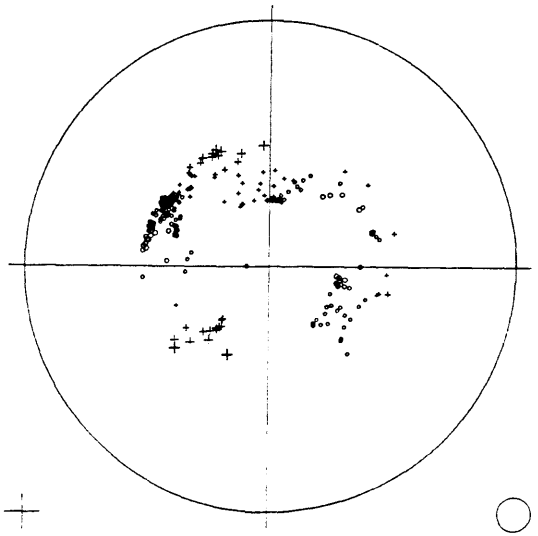

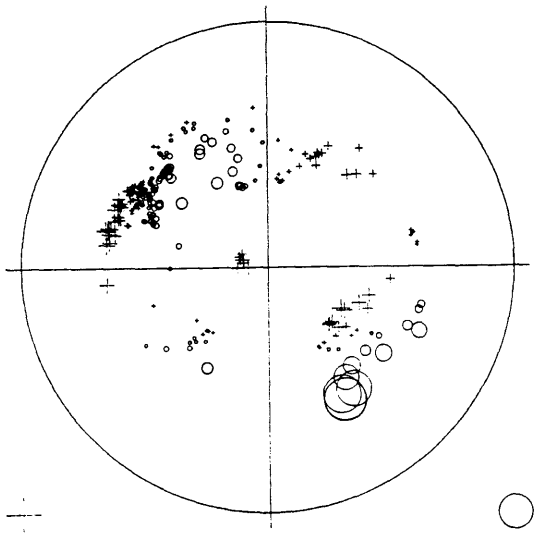

Figure 13 (cont.)

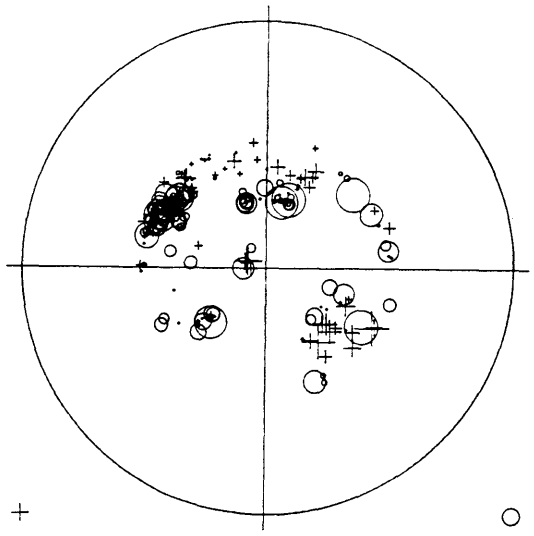

EVENT 13

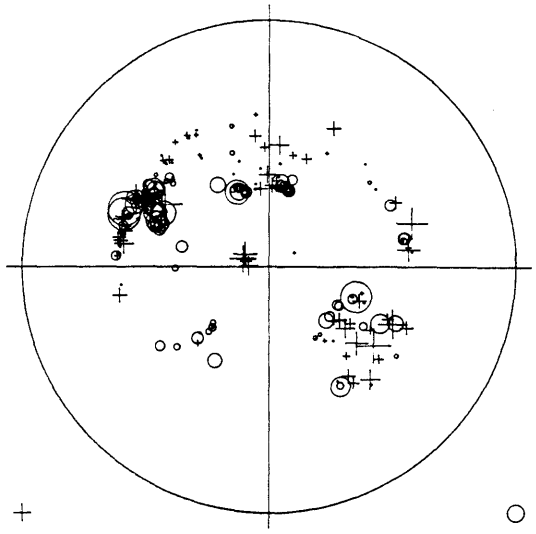

EVENT 14

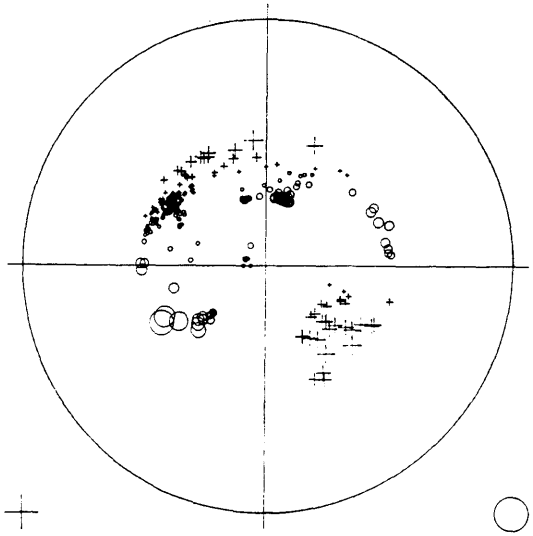

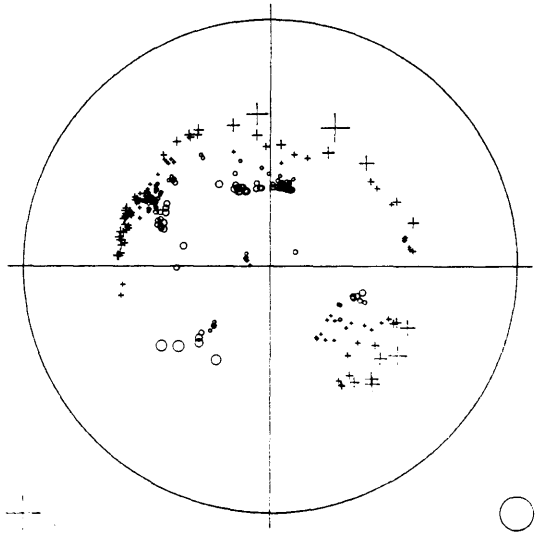

Figure 13 (cont.)

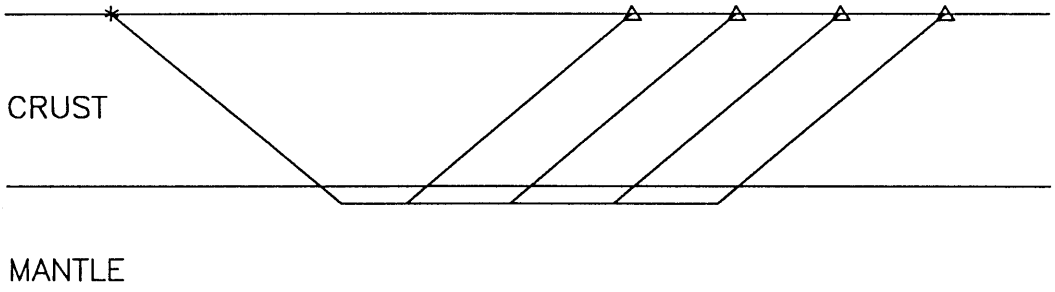

Figure 14a

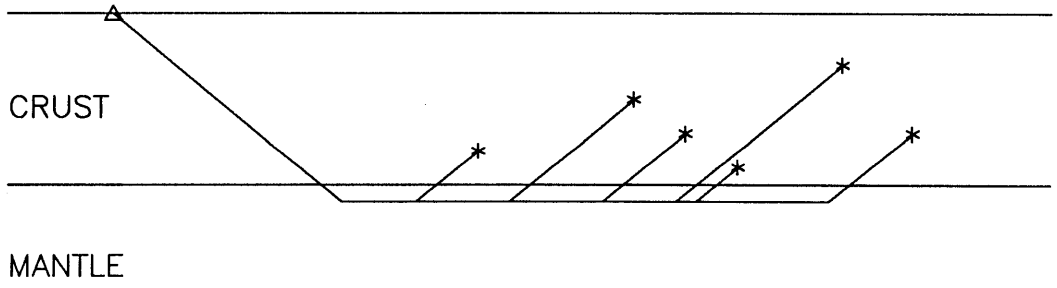

Figure 14b

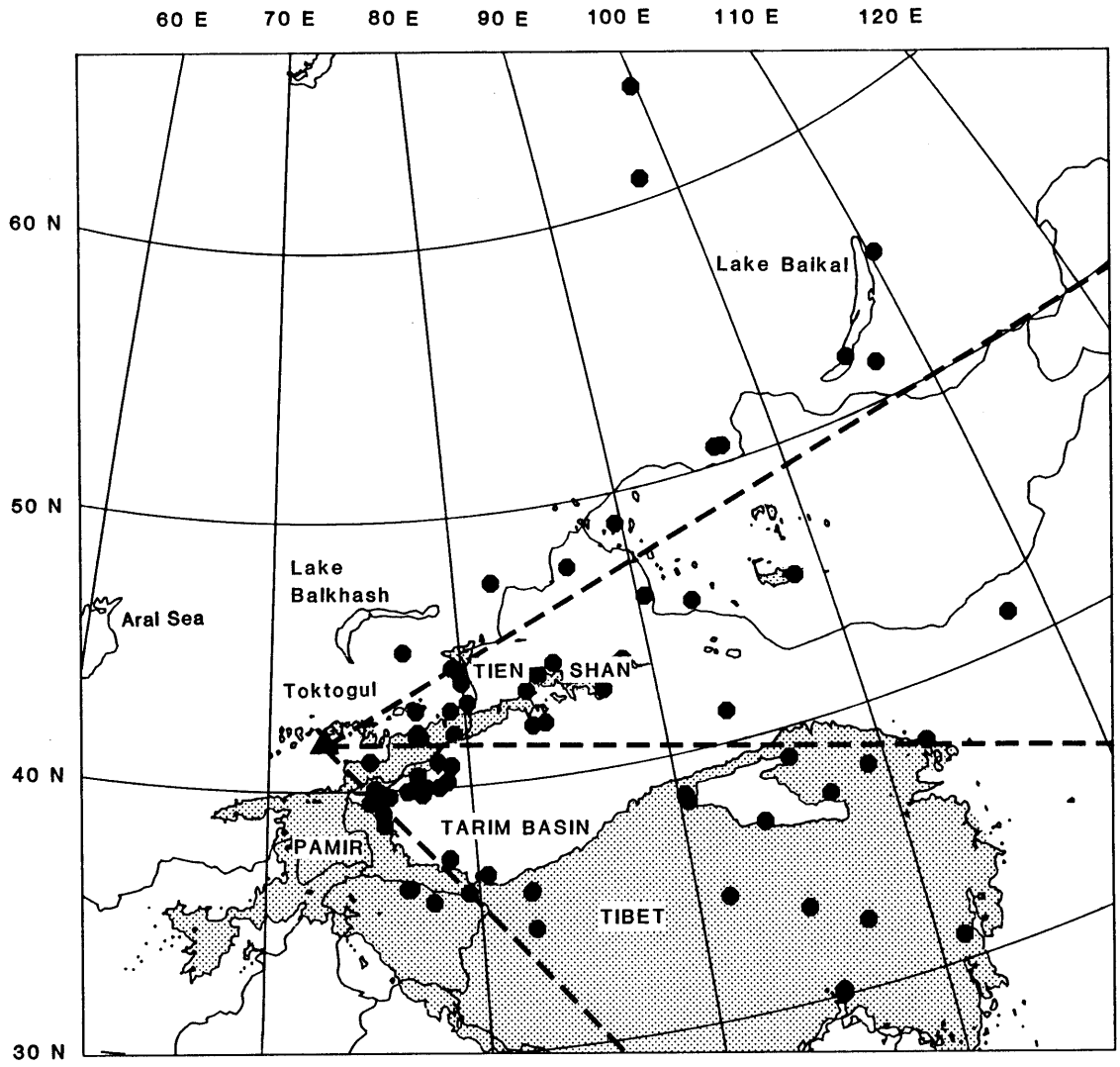
60 E
70 E
80 E
90 E
100 E
110 E
120 E
60 N
50 N
40 N
30 N
Lake Baikal
Lake
Balkhash
Aral Sea
TIEN
SHAN
Toktogul
TARIM BASIN
PAMIR
TIBET

Figure 15

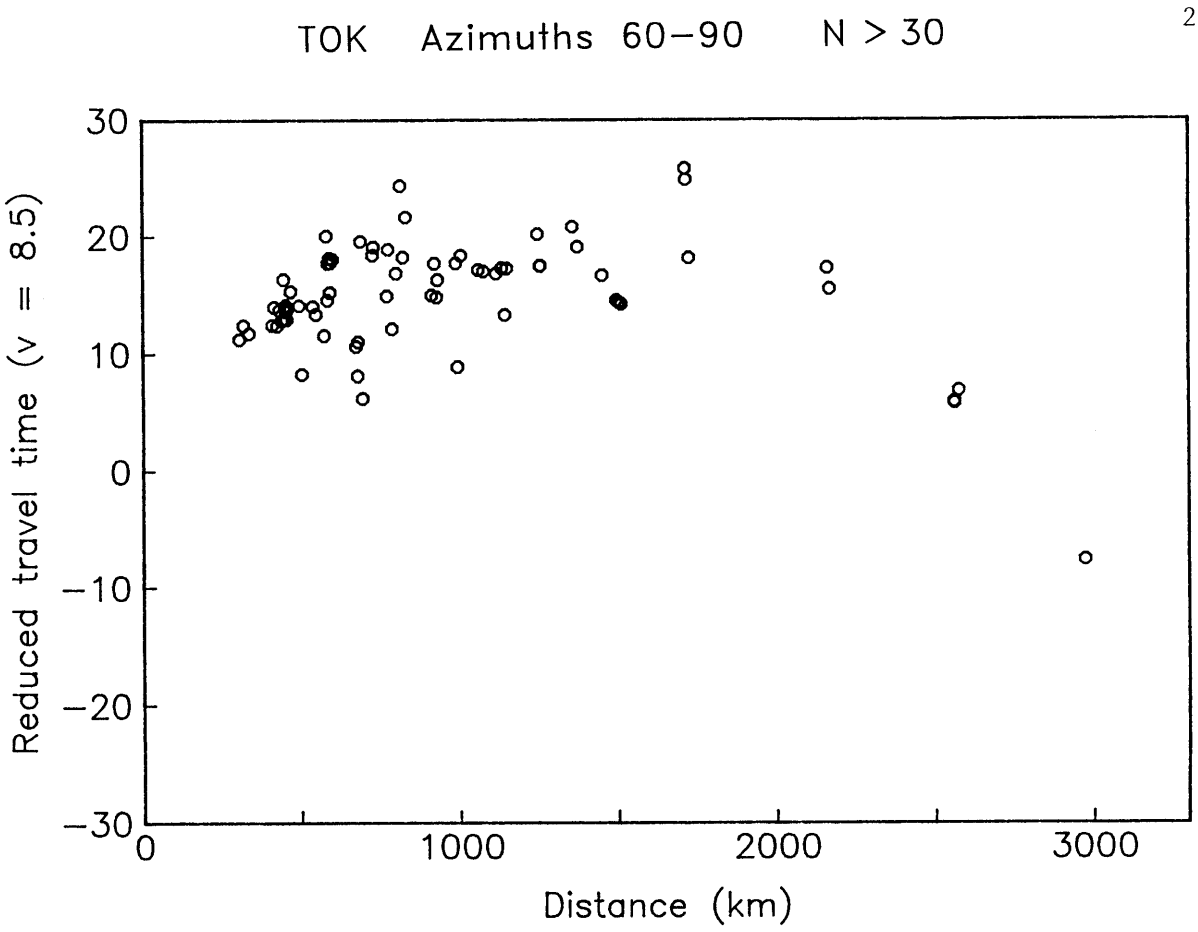

Figure 16a

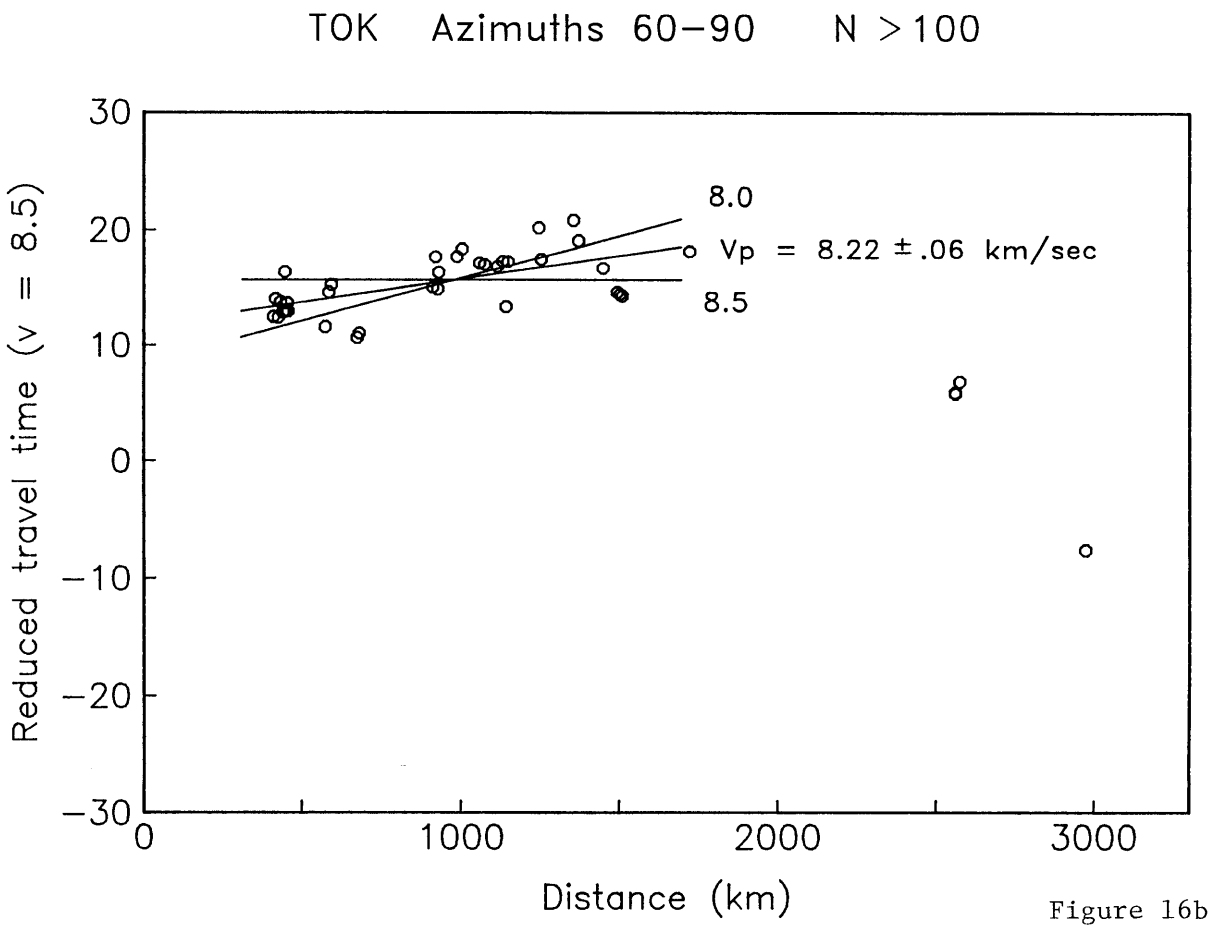

Figure 16b

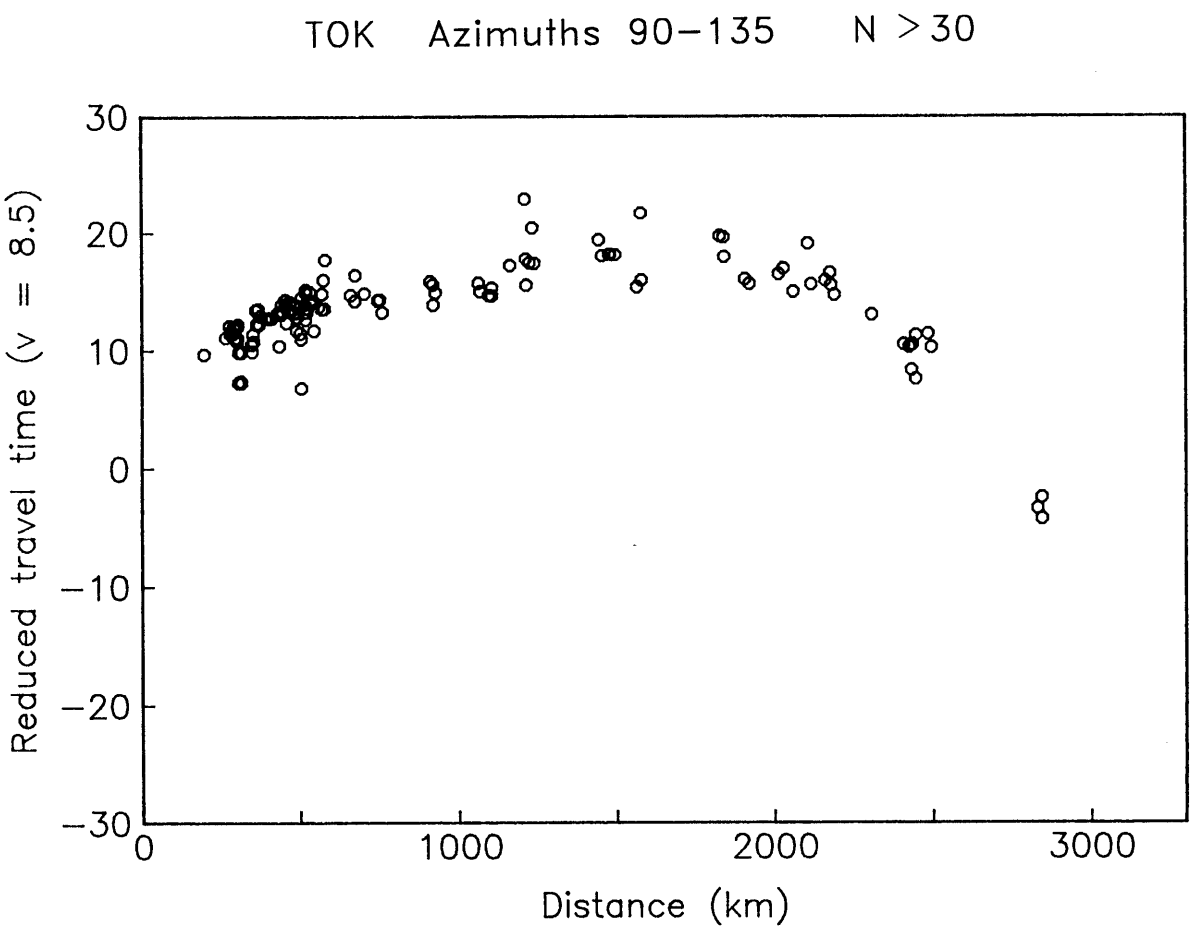

Figure 16c

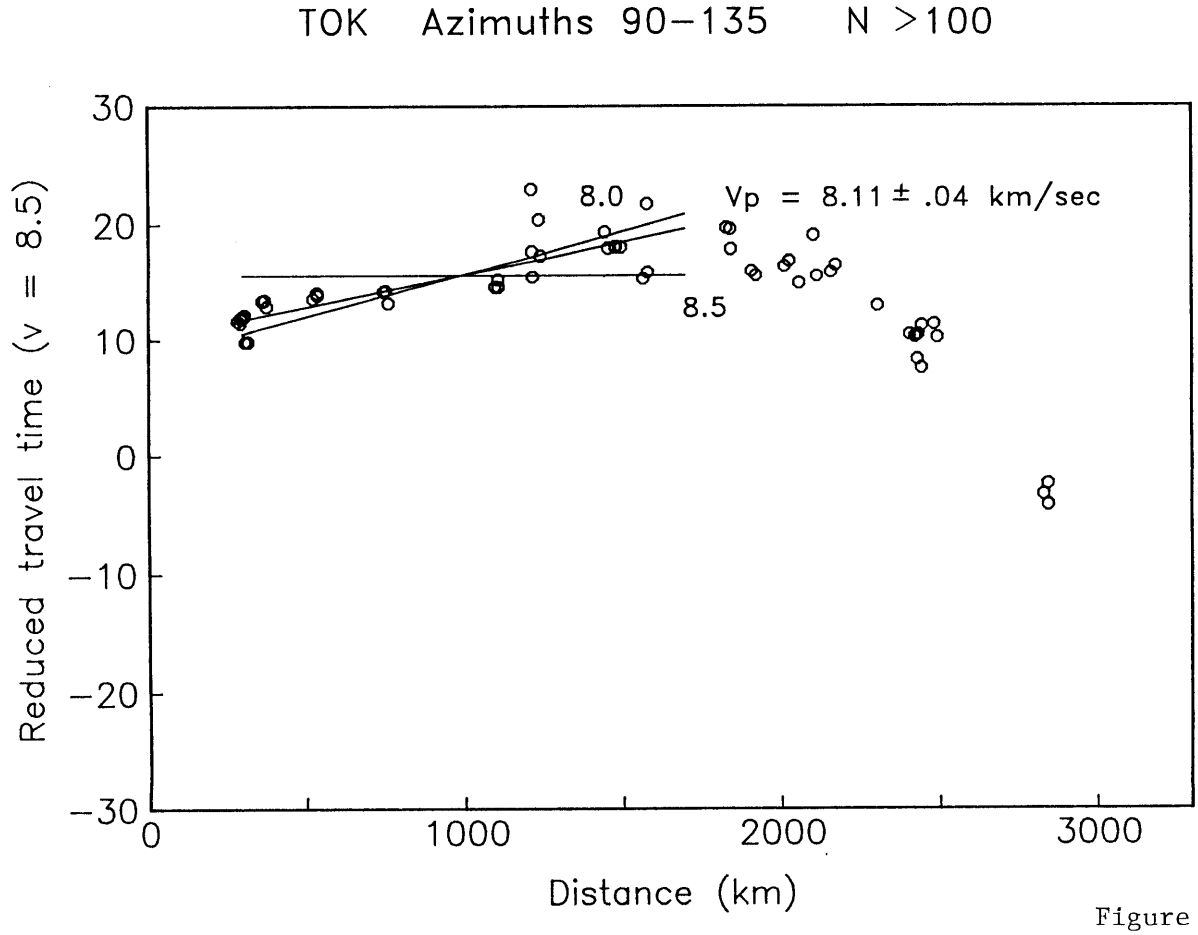

Figure 16d

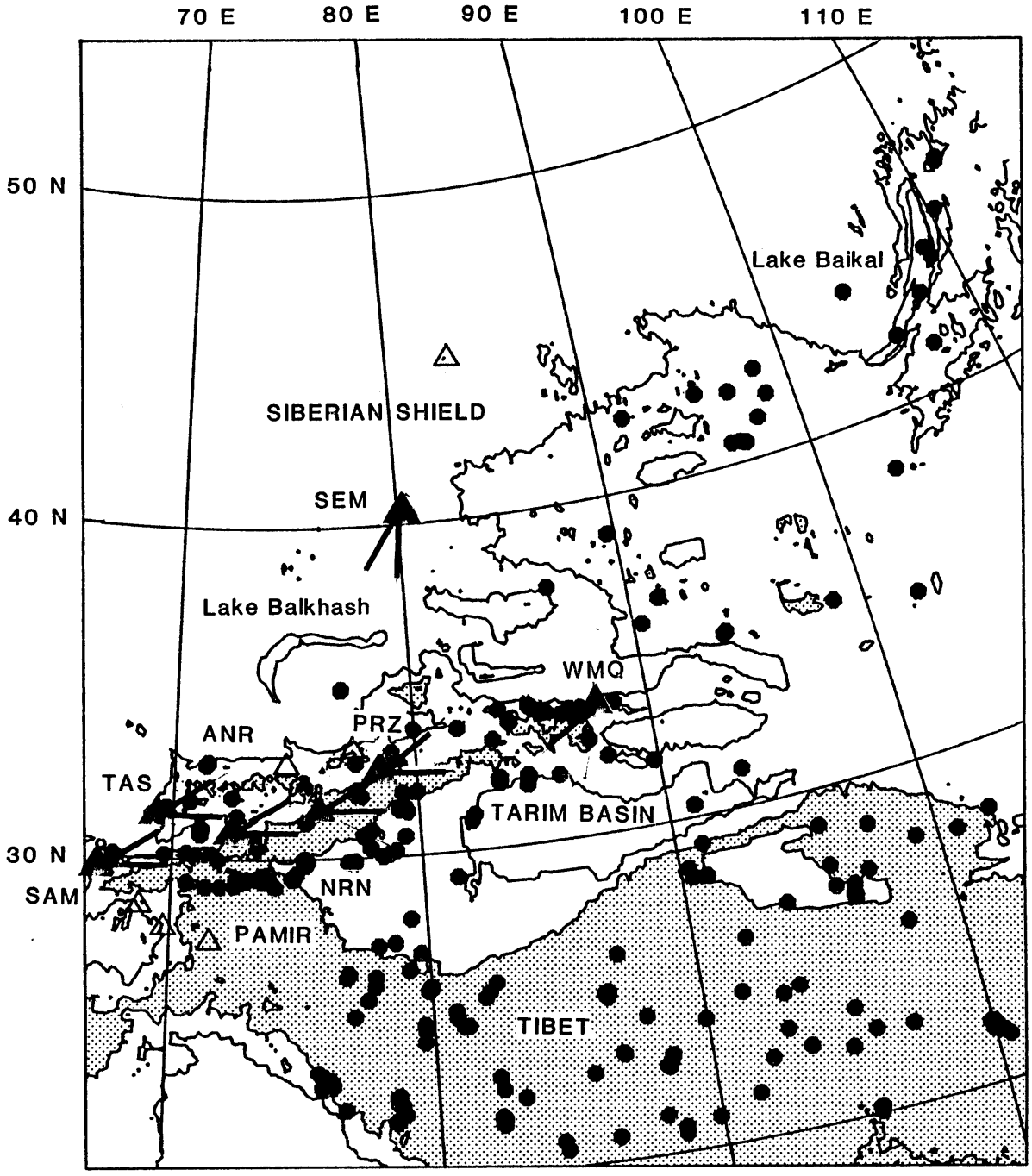
70 E
80 E
90 E
100 E
110 E
50 N
40 N
30 N
Lake Baikal
SIBERIAN SHIELD
SEM
Lake Balkhash
WMQ
PRZ
ANR
TAS
TARIM BASIN
SAM
NRN
PAMIR
TIBET

Figure 17

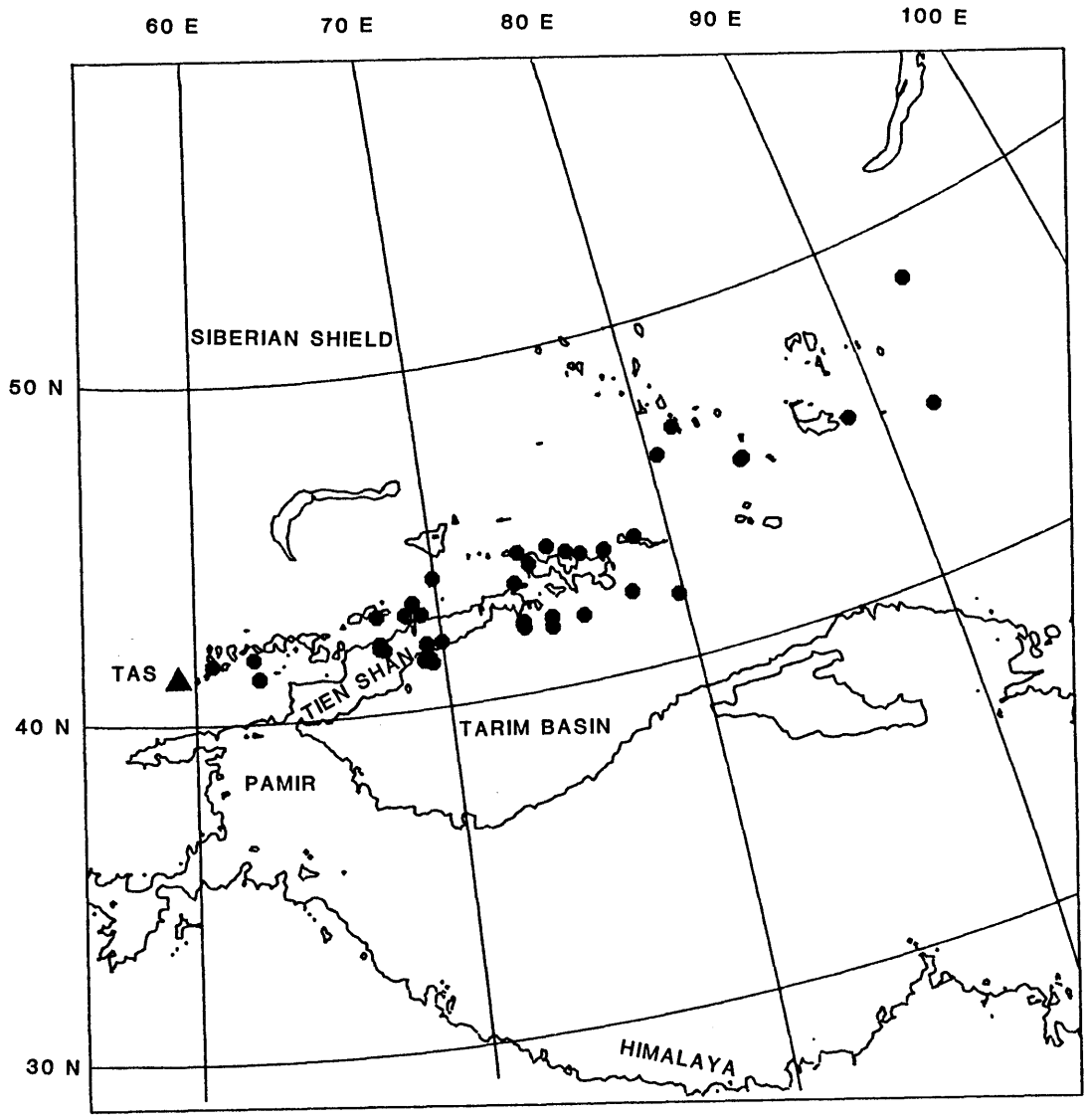
60 E
70 E
80 E
90 E
100 E
50 N
40 N
30 N
SIBERIAN SHIELD
TAS
TIEN SHAN
TARIM BASIN
PAMIR
HIMALAYA

Figure 18

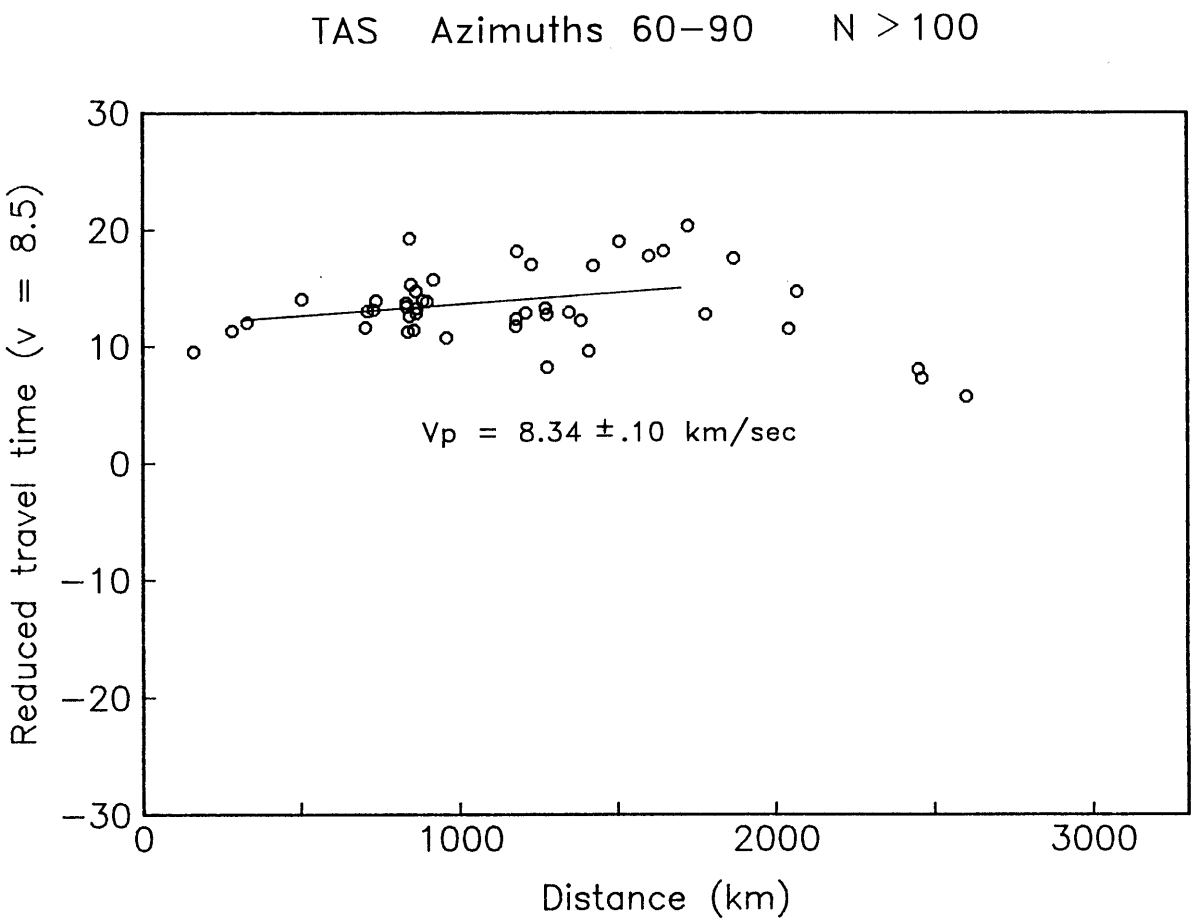
TAS Azimuths 60–90 N > 100
Reduced travel time (v = 8.5)
30
20
10
0
−10
−20
−30
0
1000
2000
3000
Distance (km)
Vp = 8.34 ±.10 km/sec

Figure 19

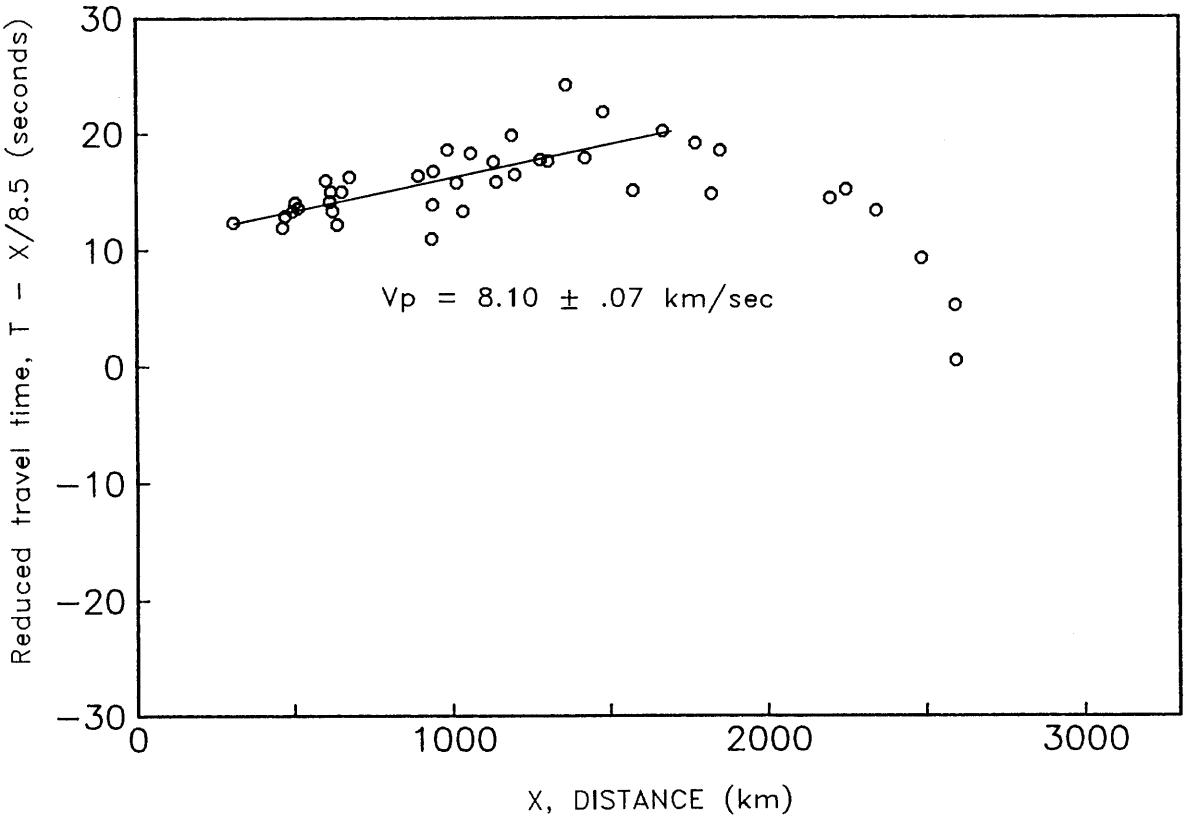

Figure 20a

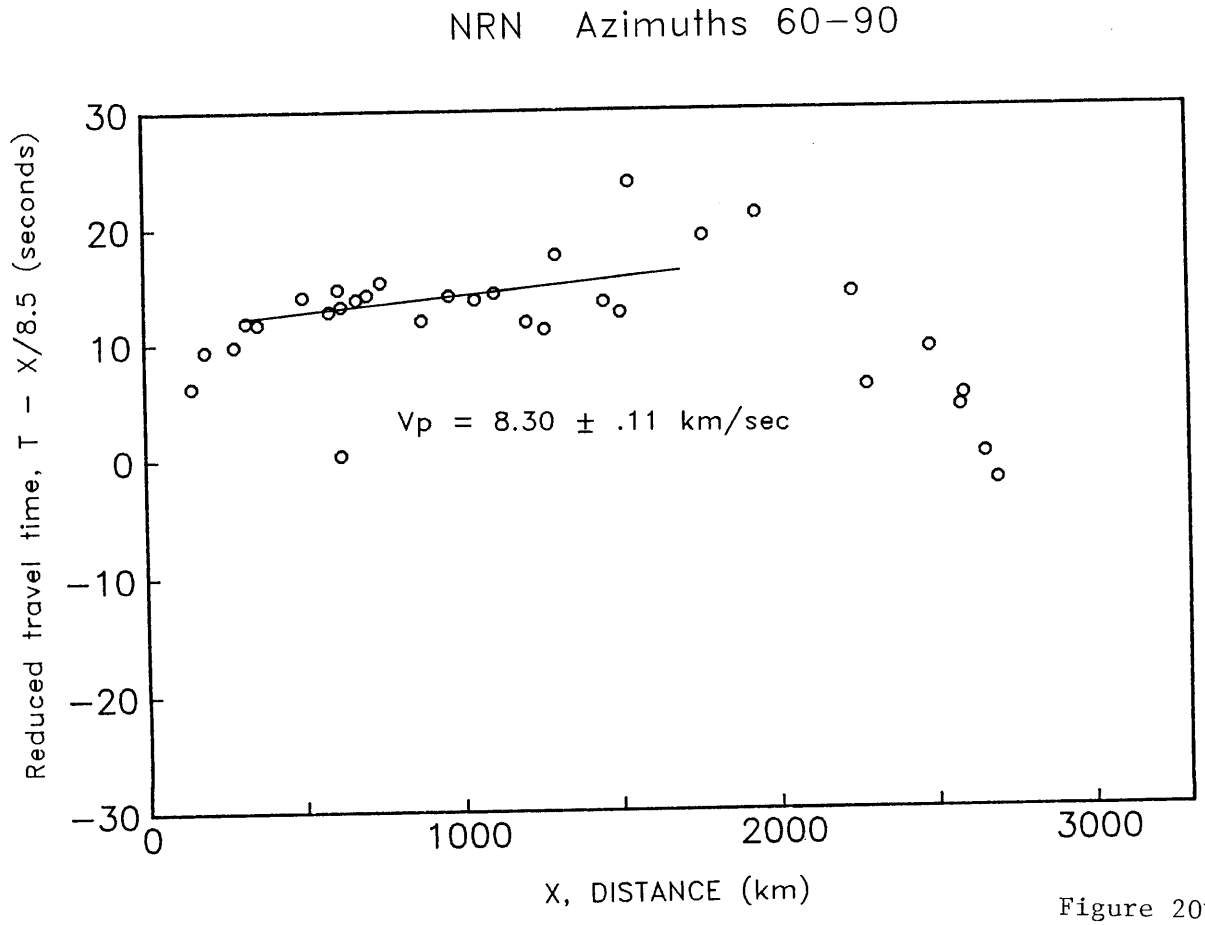

Figure 20b

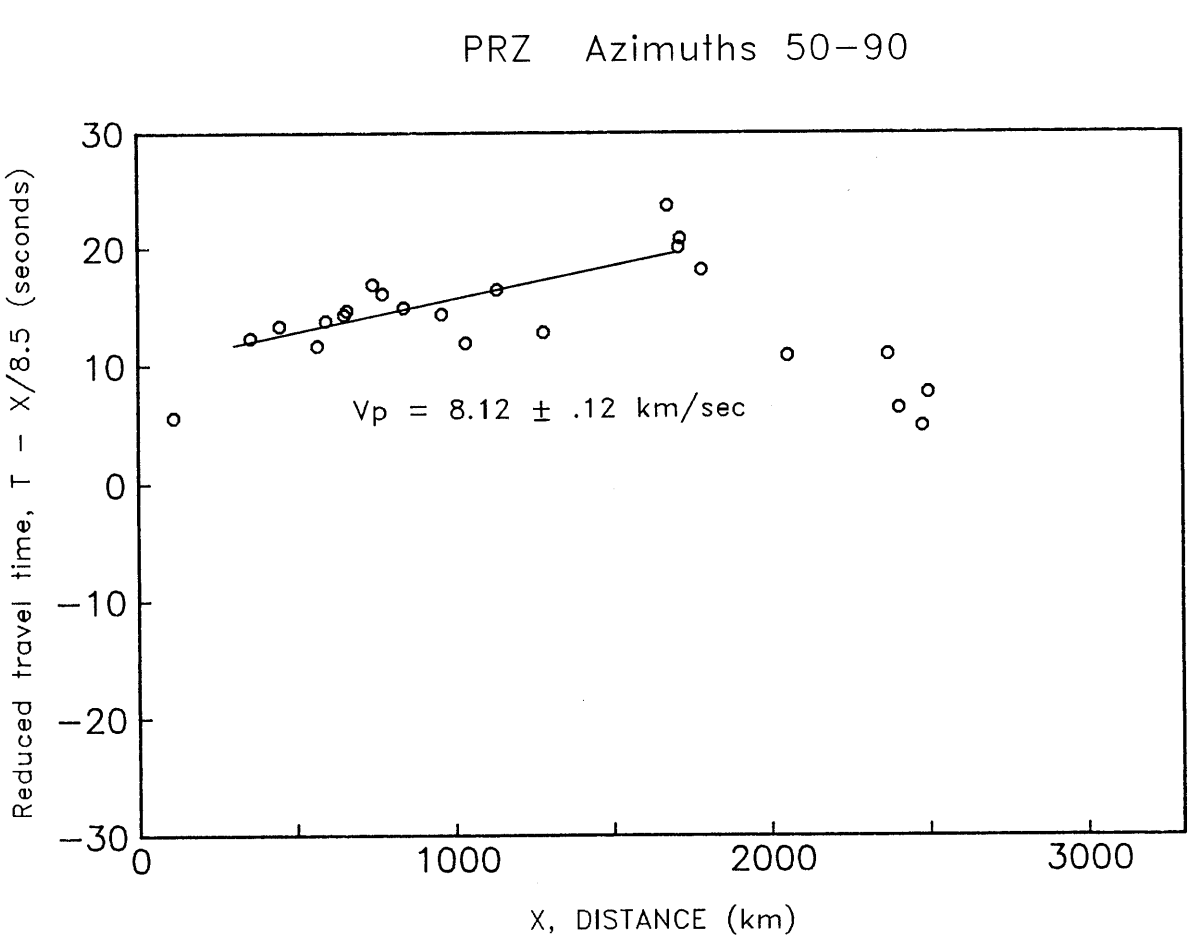

Figure 20c

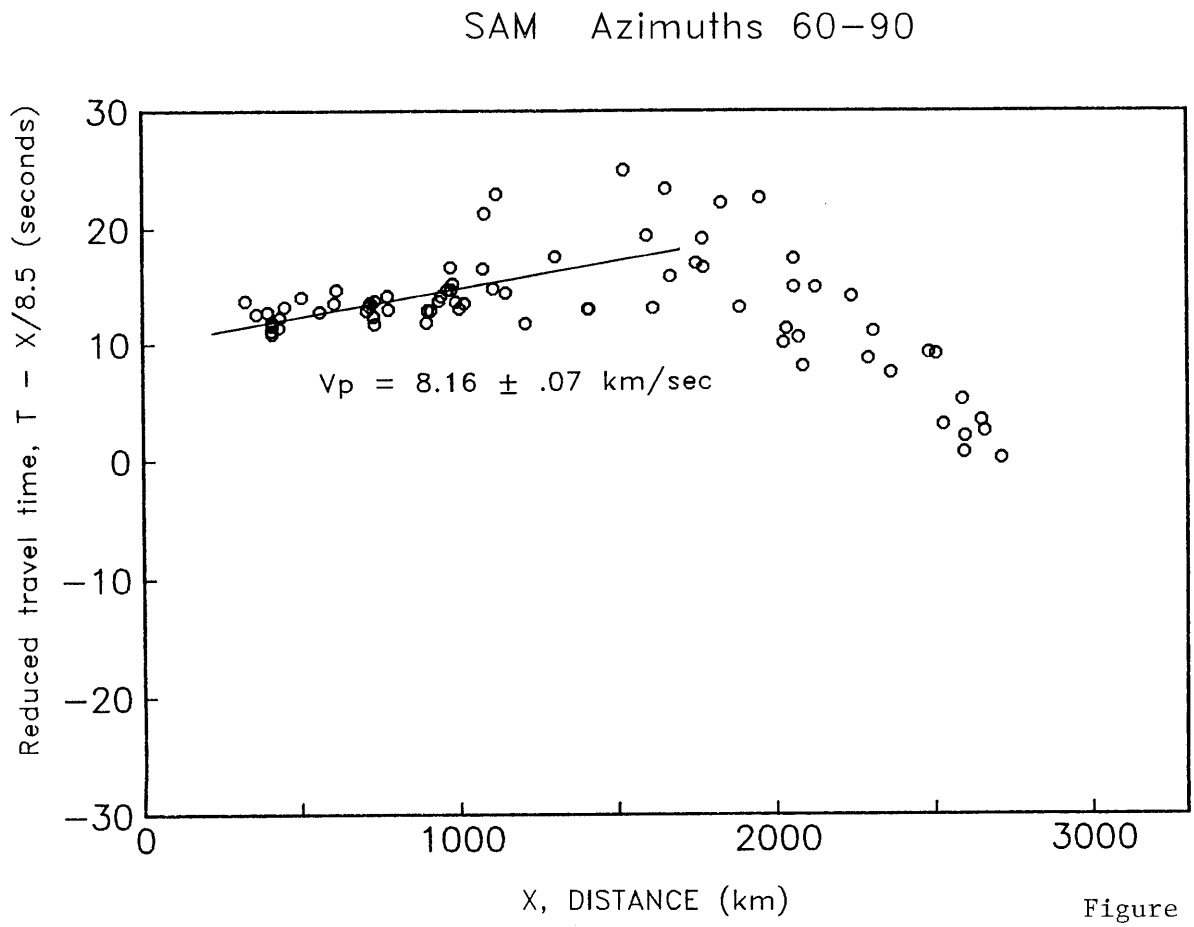

Figure 20d

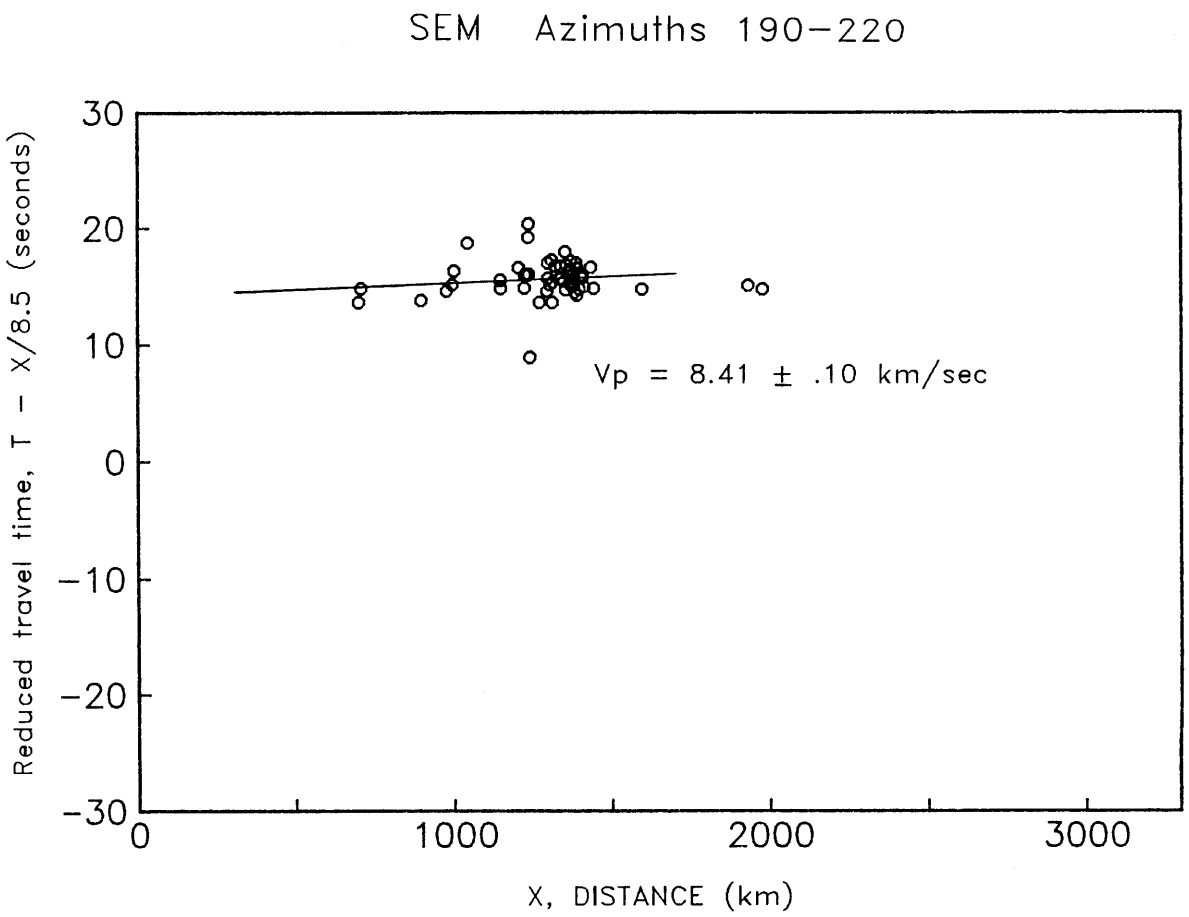
SEM Azimuths 190–220
Reduced travel time, T – X/8.5 (seconds)
30
20
10
0
–10
–20
–30
0
1000
2000
3000
X, DISTANCE (km)
Vp = 8.41 ± .10 km/sec

Figure 20e

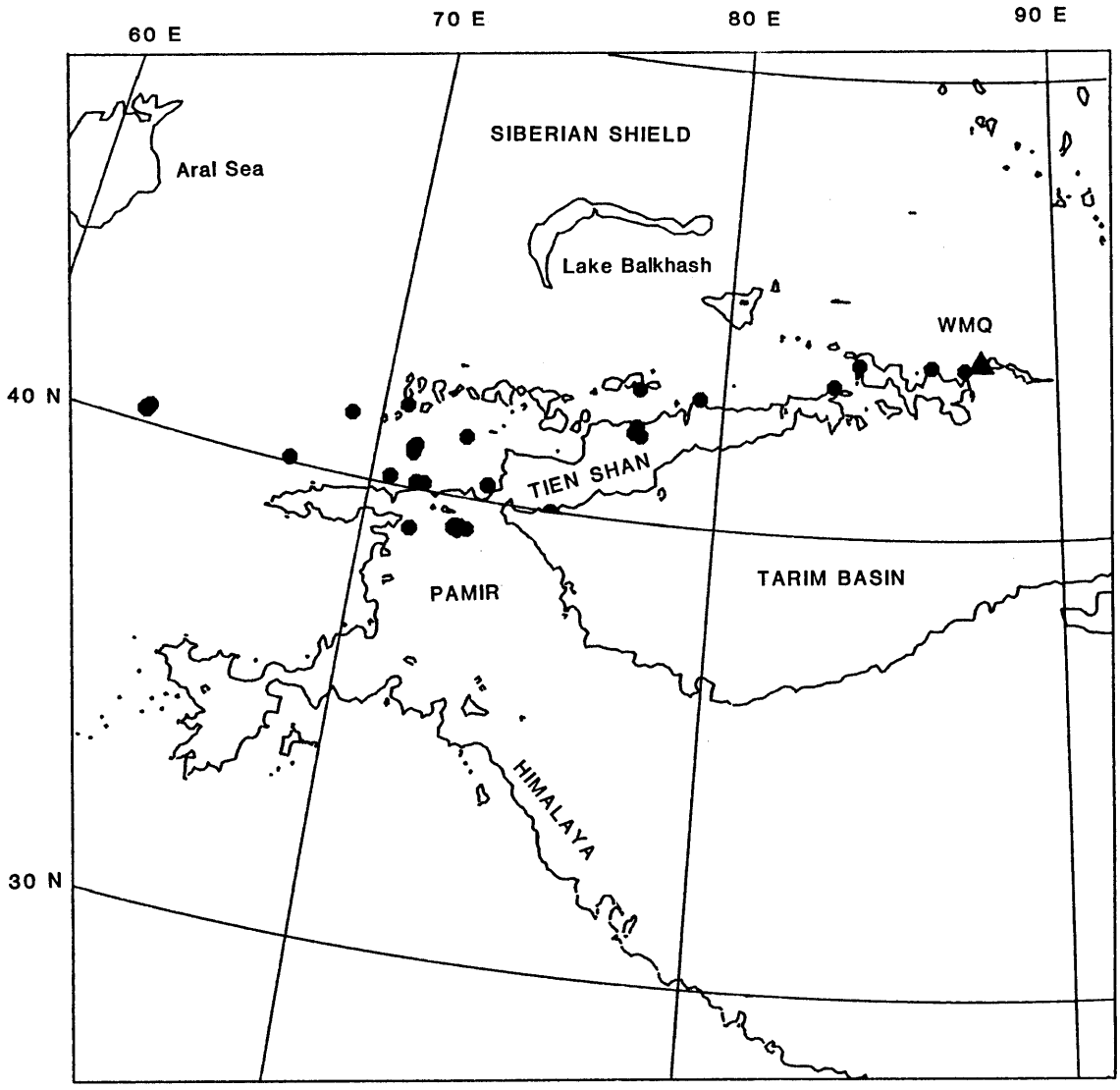
60 E
70 E
80 E
90 E
40 N
30 N
Aral Sea
SIBERIAN SHIELD
Lake Balkhash
WMQ
TIEN SHAN
PAMIR
TARIM BASIN
HIMALAYA

Figure 21

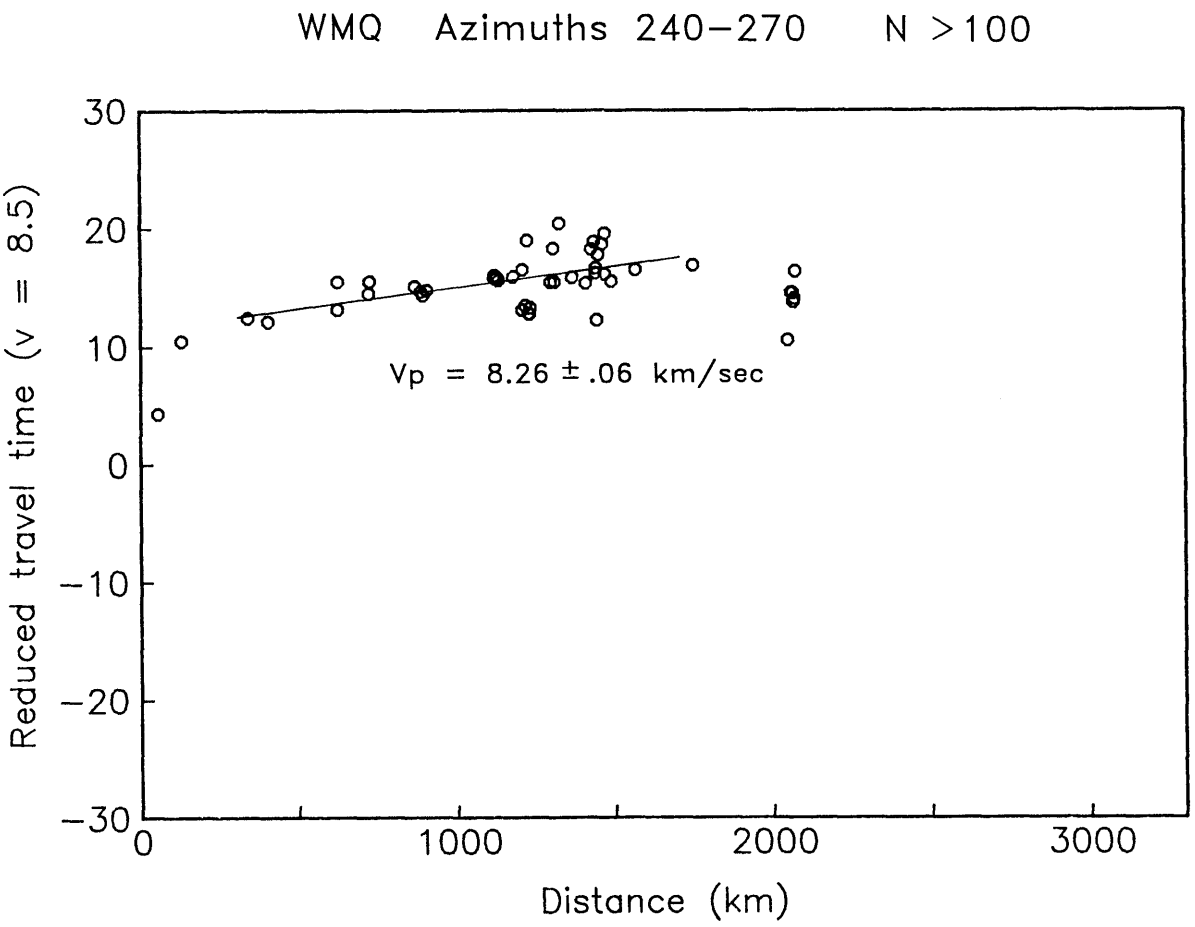
WMQ Azimuths 240–270 N >100
Vp = 8.26 ± .06 km/sec
Reduced travel time (v = 8.5)
Distance (km)
30
20
10
0
−10
−20
−30
0
1000
2000
3000

Figure 22

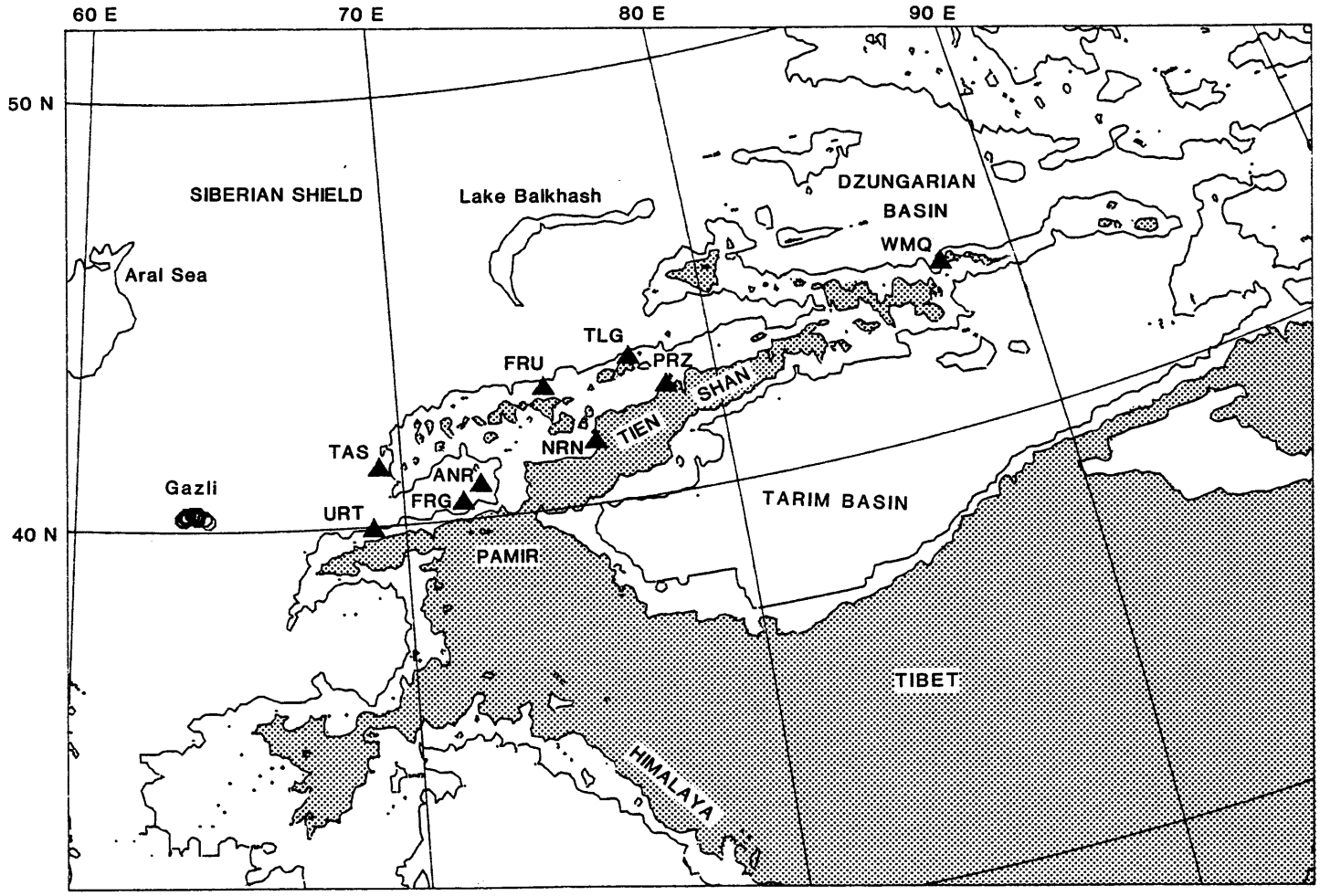
60 E
70 E
80 E
90 E
50 N
40 N
SIBERIAN SHIELD
Lake Balkhash
DZUNGARIAN
BASIN
WMQ
Aral Sea
TLG
FRU
PRZ
SHAN
TIEN
NRN
TAS
ANR
FRG
URT
Gazli
TARIM BASIN
PAMIR
TIBET
HIMALAYA

Figure 23

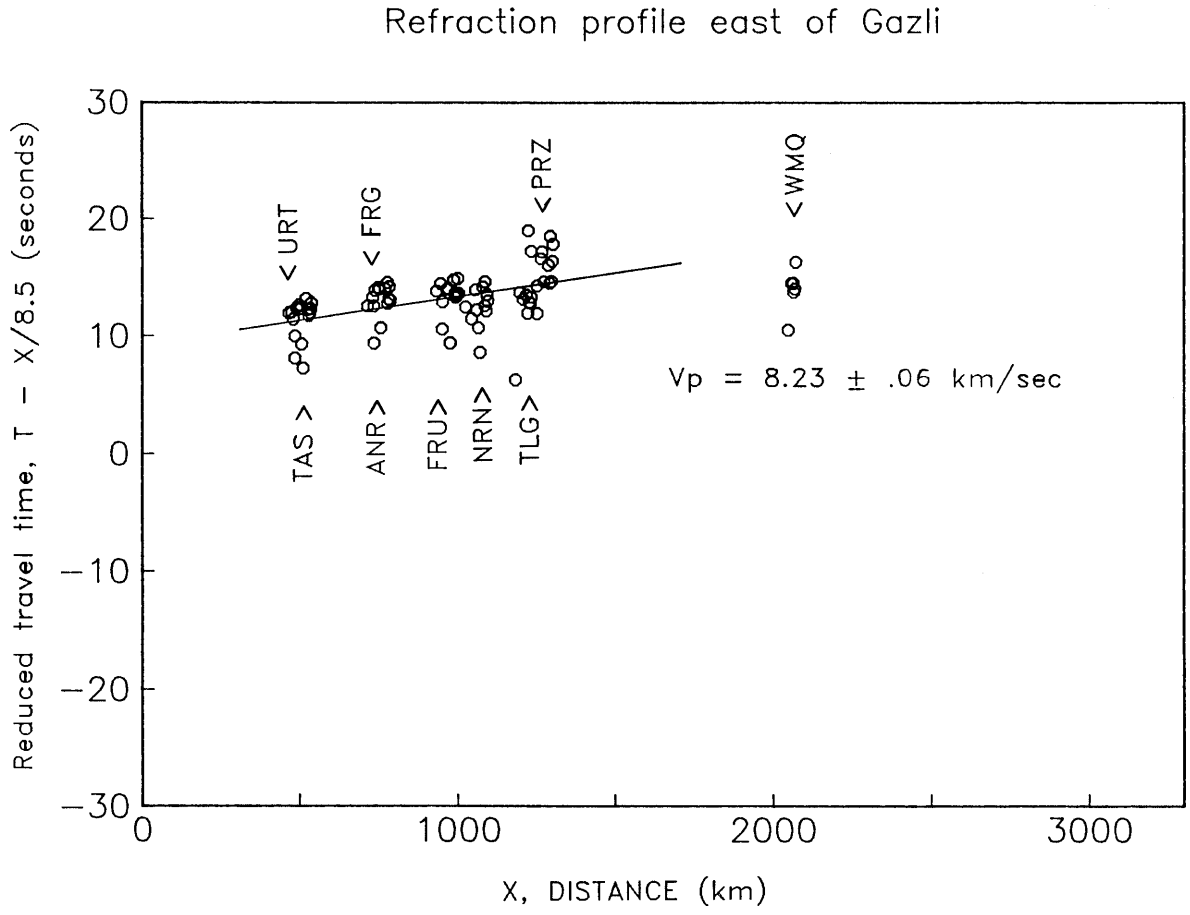

Figure 24

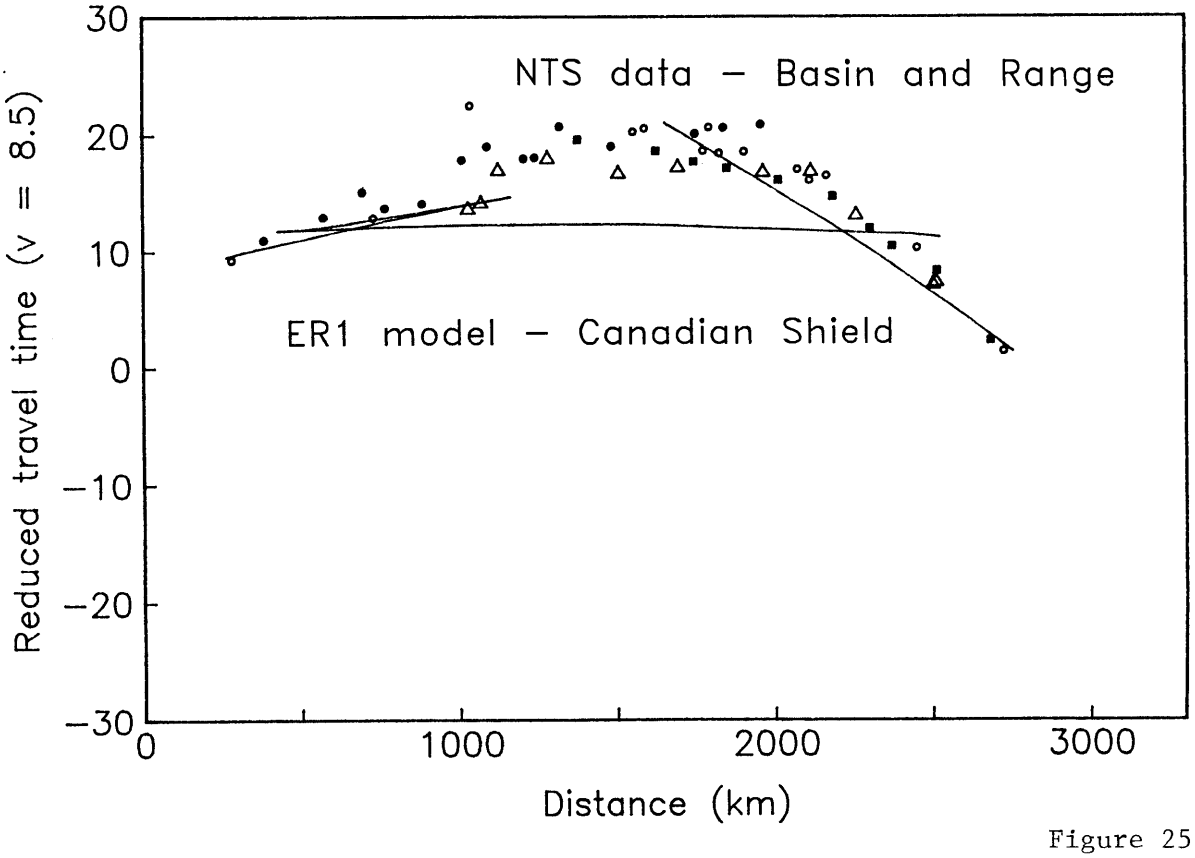

Figure 25

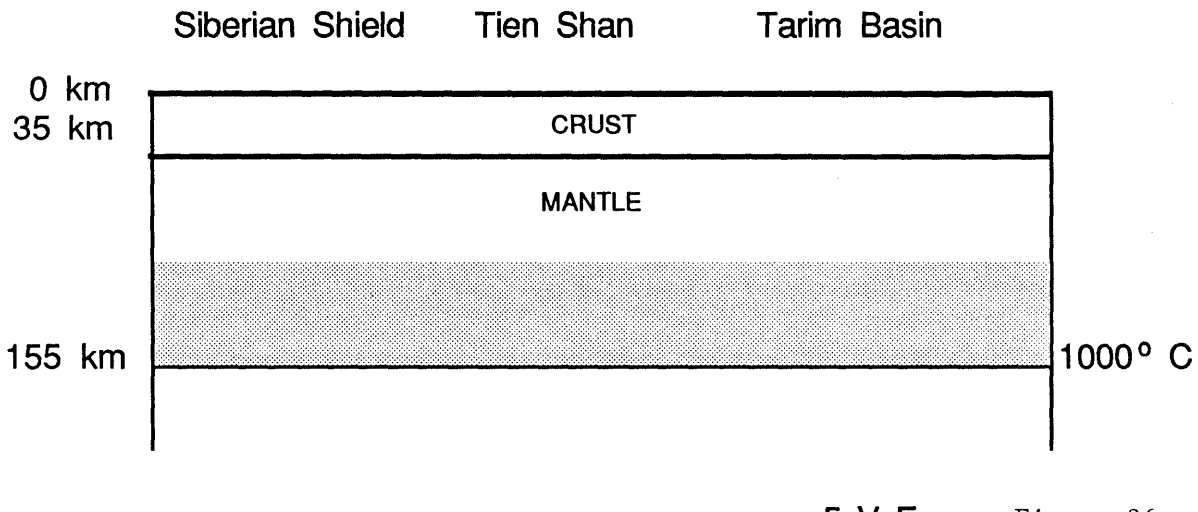

Figure 26a

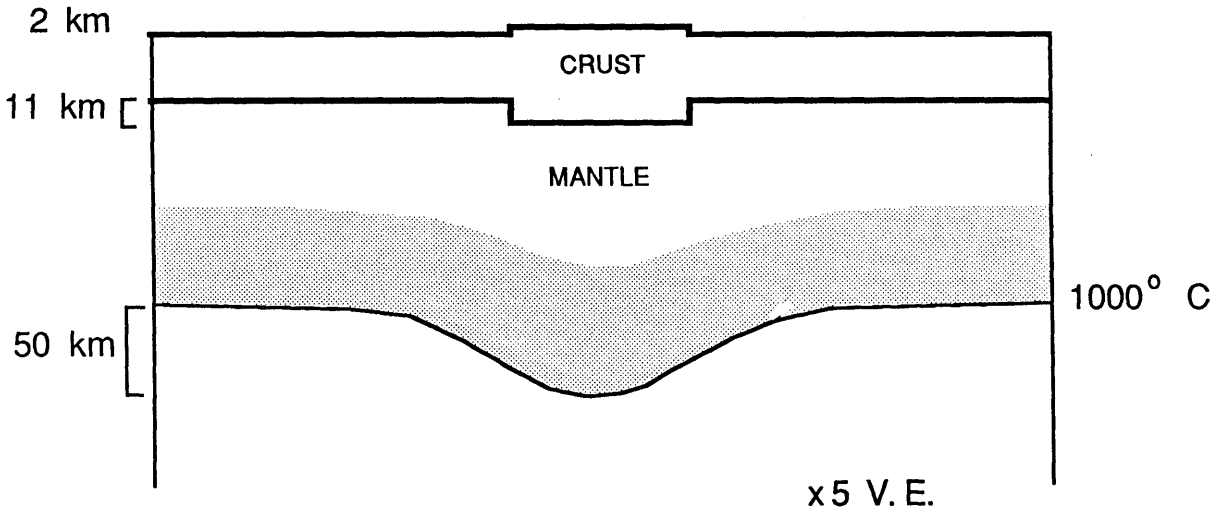

Figure 26b

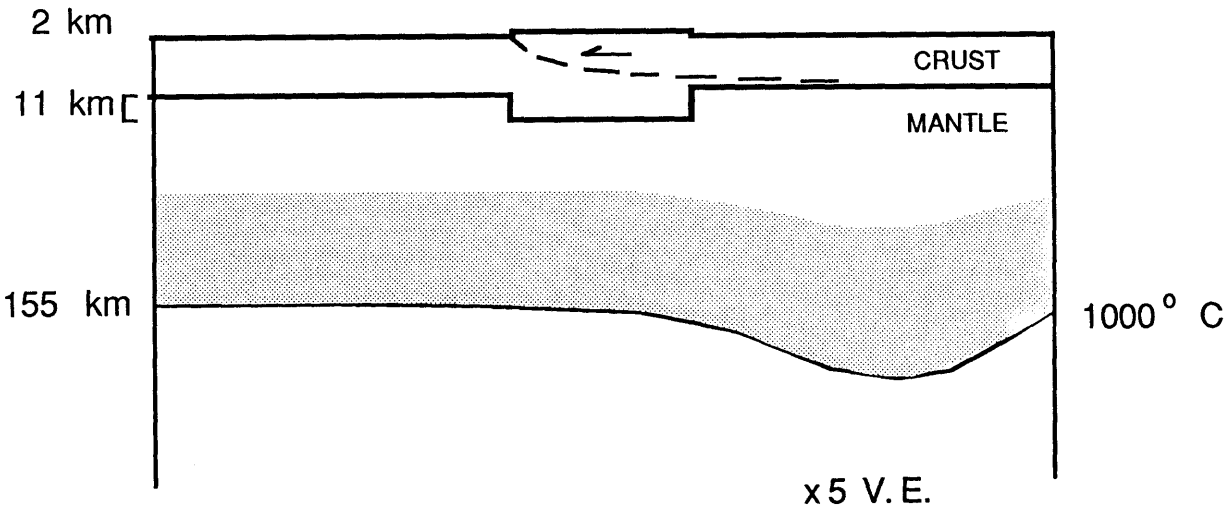

Figure 26c

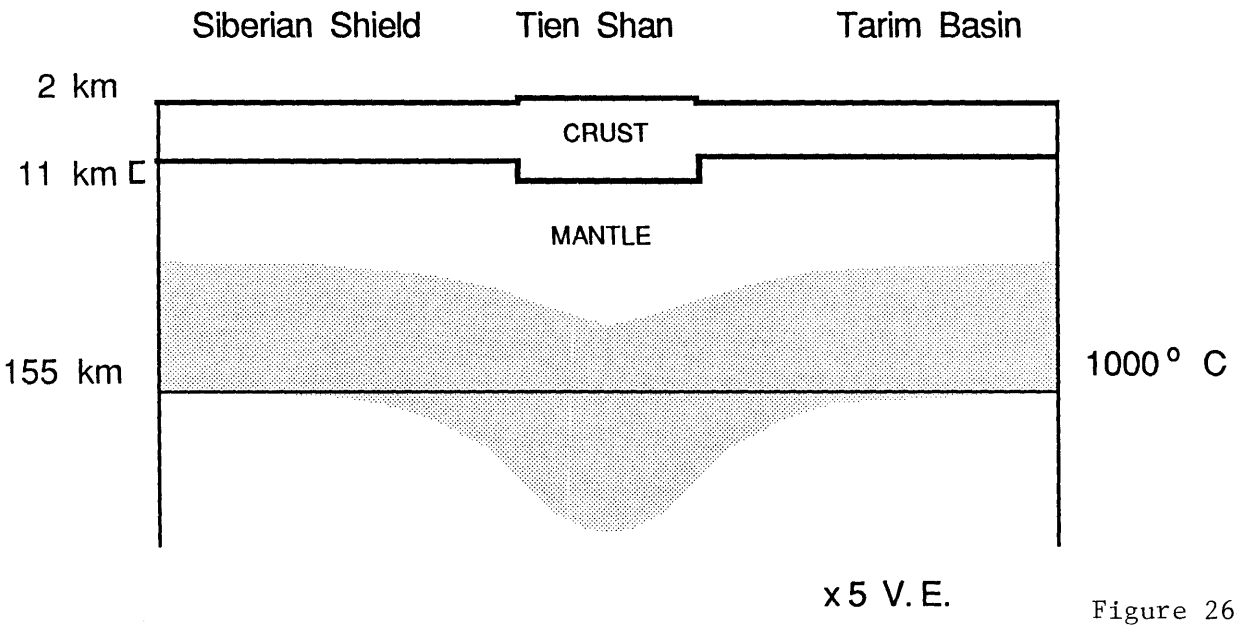

Figure 26d

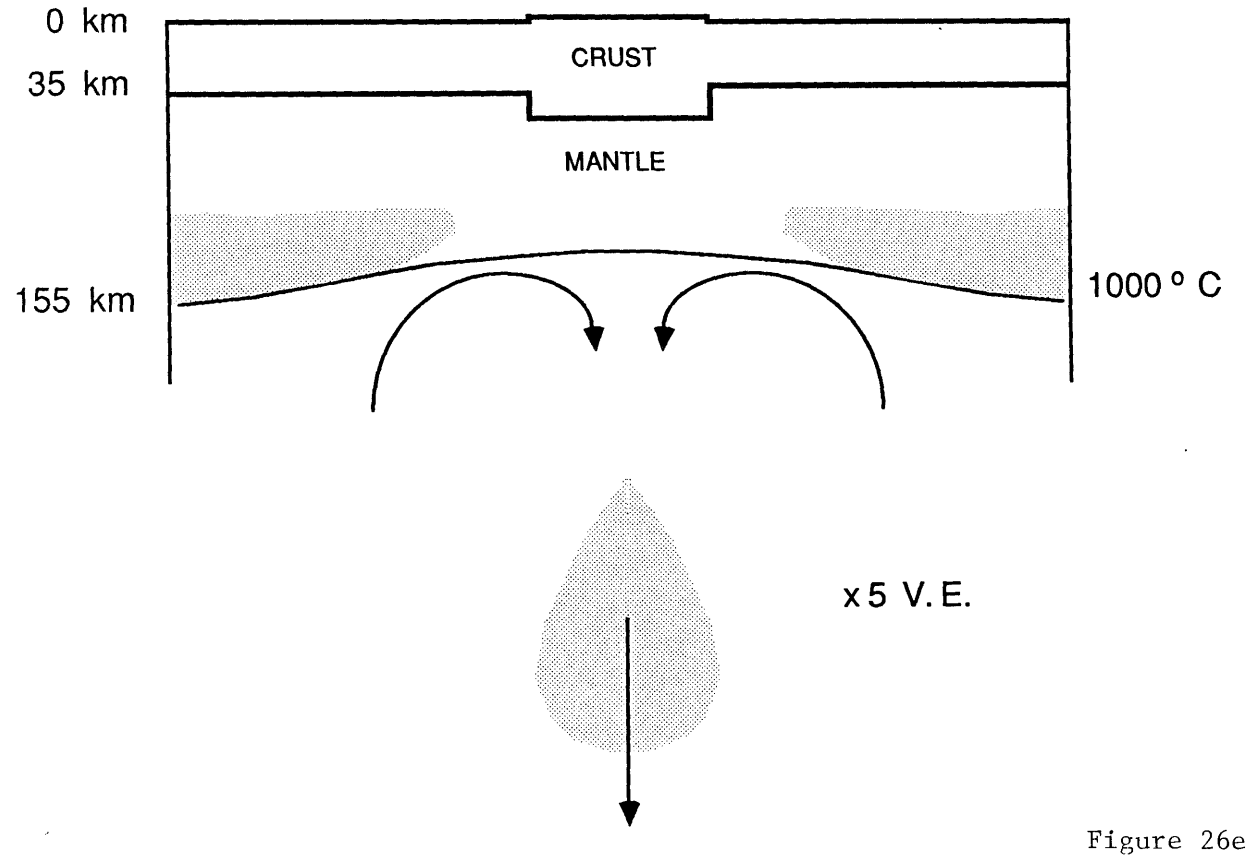

Figure 26e

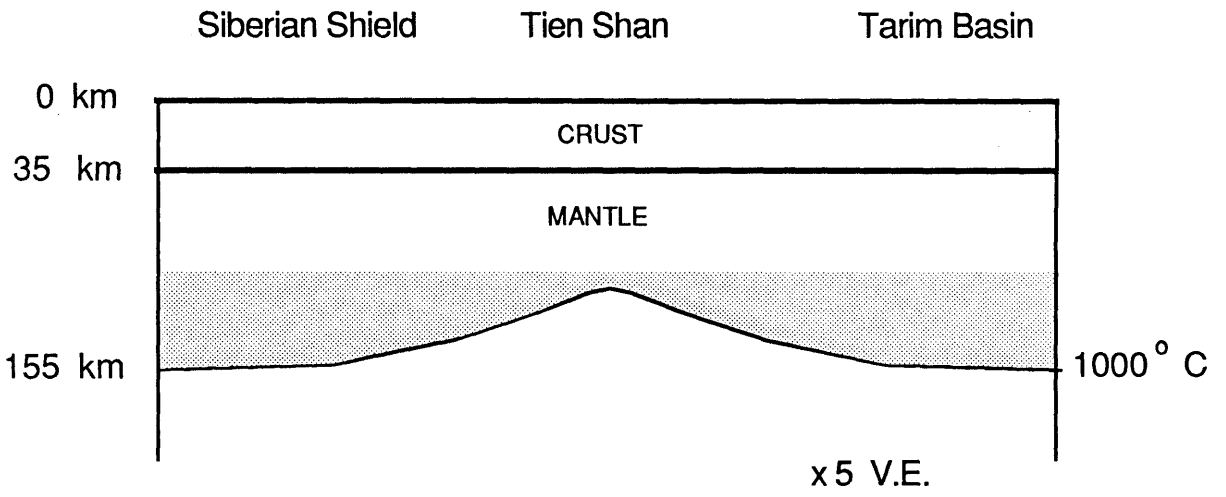

Figure 27a

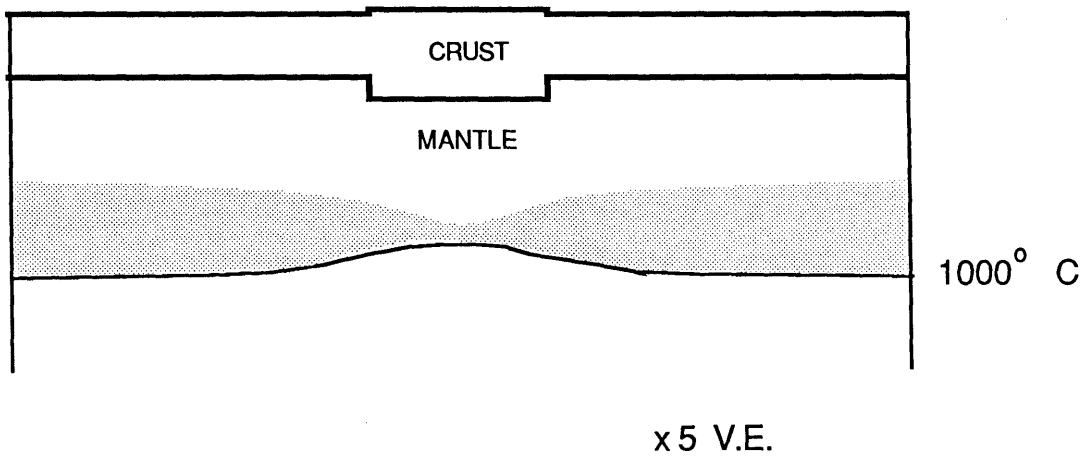

Figure 27b